UNIVERSITY OF LIVERPOOL

Stoichiometric Manipulation of Inorganic Compounds to Function as Near Infrared Absorbers

Thesis submitted in accordance with the requirements of the University of Liverpool for the degree of Doctor of Philosophy by Rachel Stephanie Coulter.

September 2015

Abstract

The synthesis, characterisation and testing of compounds to function as near-infrared (NIR) absorbers in a patented laser imaging process is presented.

Working in conjunction with industrial partner Datalase Ltd, the project has focussed on finding materials which absorb NIR radiation for use in inks. The material is required to absorb NIR radiation from a laser and transfer it to a colour-changing pigment as heat in order to form images. The application of this process is primarily to create labels on packaging.

Initially four commercial samples were analysed to provide a starting point for selecting NIR absorber candidates. Preliminary samples were synthesised and a testing procedure was established. A range of compounds were identified as potential NIR absorbers, synthesised, characterised and tested. The family of alkali metal tungsten bronzes M_xWO_3 was explored with various types of M and different values of x. The effect on laser imaging performance of factors such as solid state vs solvothermal synthesis routes and particle shape were investigated. As a family they were found to generally perform well. Sub-stoichiometric tungsten trioxides WO_{3-x} were also investigated but show inferior performance as NIR absorbers compared to the tungsten bronzes.

Molybdenum bronzes M_xMoO_3 were a natural follow-on family from the tungsten bronzes for investigation. The proved relatively difficult to synthesise in phase pure form and did not show the same level of performance as their tungsten counterparts. A phosphate tungsten bronze sample $P_4W_{12}O_{32}$ had the same issues as the molybdenum bronzes – intermediate performance and difficult synthesis which is particularly undesirable for industrial applications.

A number of copper phosphates and transparent conducting oxides were also studied. These samples generally had a lower level of NIR absorbance compared to the bronze samples which led to poor imaging. Throughout the project the main characterisation techniques used were powder X-ray diffraction, UV-vis-NIR spectrometry and scanning electron microscopy.

Acknowledgements

I would first like to thank Professor Rosseinsky for taking on this project and providing guidance throughout. My gratitude goes to Dr Troy Manning for his mentorship and availability for last-minute discussions of seemingly baffling results. Next to the photocatalysis sub-group for their discussion, suggestions and ideas over the past three years – Professor Jim Darwent, Dr John Claridge, Dr Matthew Dyer, Borbala Kiss and Tim Johnson. Thanks also to Dr Alex Cowan for the generous use of his spectrophotometer during this project. I would not have got very far without the help of all my lab and office colleagues past and present. Through asking many questions of you I have learned a lot about chemistry, synthesis techniques, data interpretation, admin and various software programs! In no particular order: Dr Michael Pitcher, Maria Diaz-Lopez, Leopoldo Enciso Maldonado, Zoe Taylor, Harry Sansom, Dr Alma Santibanez, Dr Pranab Mandal, Christos Tzitzeklis, Dr Hripsime Gasparyan, Dr Julia Payne, Wen Xu, Dr Christophe Didier, Dr Alex Corkett, Dr Chris Collins, Mike Chatterton, Dr Phil Chater, Frantisek Simo, Dr Asif Tahir, Tom Mangnall, Dr Alexandros Katsoulidis, Oliver Wilcox, Dr Dave Stewart, Dr Hongjun Niu, Dr Marco Zanella, Jibreel Haddad, Anita Peacock and Darren Hodgeman. Additional special mention goes to Dr Troy Manning and Dr Michael Pitcher for acting as my thesis proof-readers and Jane Remmer for keeping everyone organised and planning great Christmas dinners. At Datalase I am indebted to Dr Adam O'Rourke and Richard Cook for all their help in the lab and using the lasers and Dr Anthony Jarvis for his input and suggestions.

On a non-academic level I will begin with very special thanks to my parents for their continual support, love and encouragement. My woes over the course of the project must have been fairly tedious and non-comprehensible to non-scientists but you listened patiently and did your best problem-solving nevertheless. A special commendation goes to Lettice and Kat for providing reassurance and much-needed perspective on my lowest days, I'm not sure I would have made it without you! For brilliant trips and visits over the last three years, thanks go to Steff, Naeve, Katie, Maeve, Toby, Robyn, Alison, Sarah and Susan for all the memories and laughs. To my non-chemist gal pals Ellen and Julia, you have been invaluable in keeping me sane and talking about something other than work. Last but not least to the office crew with whom many nights out and after work pints have been had and made my time in Liverpool so much more interesting! Zoe, Oliver, Tom, Darren, Tim, Noemie, Alex, Jibs and Harry, it wouldn't have been the same without you.

Contents

List of Abbreviations

Units

a.u.	Arbitrary units
^{o}C	Degrees Celsius
eV	Electron volts
h	Hours
g	Grams
mol	Moles
mm	Millimetres (metres x 10^{-3})
µm	Micrometres (metres x 10^{-6})
nm	Nanometres (metres x 10^{-9})
W	Watts

Samples

rITO	$In_{2-x}Sn_xO_{3-x}$ Commercial sample 'reduced indium tin oxide'.
CHP	$Cu_2(OH)(PO_4)$ Commercial sample copper hydroxyphosphate
BTO1	Cs_xWO_3 + CsW_2O_6 Commercial sample 'blue tungsten oxide' 1
BTO2	WO_{3-x} Commercial sample 'blue tungsten oxide' 2
NaTB-ST1	Na_xWO_3 synthesised solvothermally from from $Na_2WO_4.2H_2O$ and Na_2SO_4 in water at 200 ^{o}C for 24 h then reduced in 5% H_2/N_2 at 500 ^{o}C for 2 h.
NaTB-ST2	$Na_xWO_3.yH_2O$ synthesised solvothermally from $Na_2WO_4.2H_2O$ and NaCl in water at 180 ^{o}C for 48 h.
KTB-ST	K_xWO_3 synthesised solvothermally from K_2WO_4 and K_2SO_4 in water at 200 ^{o}C for 24 h then reduced in 5% H_2/N_2 at 500 ^{o}C for 2 h.
RbTB-ST	Rb_xWO_3 synthesised solvothermally from WCl_6 and RbOH in ethanol and acetic acid at 230 ^{o}C for 20 h.
ATB-ST	$(NH_4)_xWO_3$ synthesised solvothermally from ammonium paratungstate in ethanol at 200 ^{o}C for 72 h.
TTB-ST	Sn_xWO_3 synthesised solvothermally from H_2WO_4 and Sn in water at 200 ^{o}C for 24 h.
NaTB-SS	Na_xWO_3 made by solid state synthesis using Na_2CO_3, WO_3 and W with several heating steps. SS1 x = 0.1, SS2 x = 0.2, SS3 x = 0.25, SS4 x = 0.33, SS5 x = 0.4, SS6 x = 0.6, SS7 x = 0.8.

KTB-SS	K_xWO_3 made by solid state synthesis using K_2CO_3, WO_3 and W with several heating steps. SS1 x = 0.33, SS2 x= 0.6.
RbTB-SS	$Rb_{0.33}WO_3$ made by solid state synthesis using Rb_2CO_3, WO_3 and W with several heating steps.
CsTB-ST1	Cs_xWO_3 synthesised from WCl_6 and $CsOH.H_2O$ in ethanol and water without heating.
CsTB-ST2	Cs_xWO_3 synthesised solvothermally from WCl_6 and $CsOH.H_2O$ in ethanol and water at 200 ^oC for 24 h.
CsTB-ST3	Cs_xWO_3 synthesised solvothermally from WCl_6 and $CsOH.H_2O$ in ethanol, water and benzyl alcohol in a 1:1:1 ratio at 200 ^oC for 24 h.
CsTB-ST4	Cs_xWO_3 synthesised solvothermally from WCl_6 and $CsOH.H_2O$ in ethanol, water and benzyl alcohol in a 4:2.5:1 ratio respectively at 200 ^oC for 24 h.
CsTB-ST5	Cs_xWO_3 synthesised solvothermally from WCl_6 and $CsOH.H_2O$ in ethanol, water and benzyl alcohol in a 1:2.5:4 ratio respectively at 200 ^oC for 24 h.
CsTB-ST6	Cs_xWO_3 synthesised solvothermally from WCl_6 and $CsOH.H_2O$ in ethanol, water and hydroquinone in a 4:2.5:1 ratio respectively at 200 ^oC for 24 h.
CsTB-ST7	Cs_xWO_3 synthesised solvothermally from Cs_2WO_4 and Cs_2SO_4 in water at 200 ^oC for 24 h then reduced in 5% H_2/N_2 at 500 ^oC for 2 h.
CsTB-ST8	Cs_xWO_3 synthesised from WCl_6 and $CsOH.H_2O$ in ethanol and water heated to 500 ^oC for 2 h in 5% H_2/N_2.
CsTB-SS	Cs_xWO_3 made by solid state synthesis using H_2WO_4 and Cs_2CO_3heated to 500 ^oC for 1 h in 5% H_2/N_2. SS1 x = 0.25, SS2 x = 0.33.
PTB	$P_4W_8O_{32}$ phosphate tungsten bronze made by solid state synthesis using WO_3, $(NH_4)_2HPO_4$ and W with several heating steps.
HMB	H_xMoO_3 made by reducing $MoO_3$with Zn in acidic conditions.
NaMB	$Na_xMoO_3.yH_2O$ made by reducing MoO_3 in the presence of $Na_2MoO_4.2H_2O$ and $Na_2S_2O_4$ in water.
KMB-ST	K_xMoO_3 made by solvothermal ion exchange of HMB with 0.9 M KCl solution at 180 ^oC for 48 h.
KMB-SS	K_xMoO_3 made by solid state synthesis using K_2MoO_4, MoO_3 and Mo with several heating steps at 435^oC.
RbMB	Rb_xMoO_3 made by solvothermal ion exchange of HMB with 0.9 M RbCl solution at 180 ^oC for 48 h.

CZP	$CuZr_2(PO_4)_3$ made by solid state route using CuO, ZrO_2 and $NH_4H_2PO_4$ with several heating steps.
CSCP	$Ca_{10-x/2}Na_xCu_{0.5}(PO_4)_7$ made by solid state route using $CaCO_3$, Na_2CO_3 CuO, and $NH_4H_2PO_4$ with several heating steps. x = 0, 0.5 and 1.
SZCP	$SrZn_{1-x}Cu_xP_2O_7$ made by solid state route using ZnO, CuO, $SrCO_3$ and $(NH_4)_2HPO_4$ with several heating steps. x = 0, 0.25, 0.5, 0.75 and 1.
TiO_2-AM	TiO_2 heated under flowing NH_3 at 700 ^oC for either 4 or 8 h.
TiO_2-ST	TiO_2 heated solvothermally in triethanolamine to 140 ^oC for either 24 or 48 h.
TiN-OX	TiN oxidised solvothermally in H_2O_2 solution at 170 ^oC for 24 h. Concentrations of 0.5, 1, 2 and 3 weight % H_2O_2 solution were used.
LaBSO	$Ba_{1-x}La_xSnO_3$ made by solid state synthesis using SnO_2, $BaCO_3$ and La_2O_5 with several heating steps. x = 0.05 and 0.1.

Chapter 1

Introduction

1.1 Introduction

The printing industry is one of the largest and most profitable in the world. Due to the high demand for products and large range of applications, printing companies in the US alone brought in $112 billion in revenue in 2006[1]. The process of creating words and images was revolutionised with Johannes Gutenburg's invention of the movable printing press in the 1450's. As well as enabling the mass production and circulation of books, scientific research could now be communicated much more easily across distances which led to the establishment of a scientific community in Europe. Despite being an ancient process, printing technology is still evolving and recently there has been increased interest in new ways of optimising the imaging process and reducing the number or quantity of consumables used. Environmental concerns are a motivating factor in this but there are also inherent economic benefits.

At present, two of the most widely used processes are *inkjet printing*, in which droplets of ink are forced onto the paper through a narrow nozzle onto specific areas of a substrate, and *laser printing* which uses an electrostatic charge-transfer drum system similar to that used in photocopiers. The laser is passed over the charged drum and creates an oppositely charged image to which powdered ink (toner) is attracted. This is transferred from the drum to a sheet of paper and fixed in place using heat. Both processes operate at relatively high speeds (although laser is faster than inkjet) and produce good quality images however each has its drawbacks. Inkjet printers obviously require ink and so cartridges need to be replaced or refilled regularly. In addition, the inkjet heads can become blocked requiring maintenance or replacement which adds to the cost. Laser printer toner needs to be replenished and the drums used for image transfer have a limited lifetime and so need to be replaced every so often.

This project has been partially funded by Datalase Ltd. which is a materials company with a portfolio of products and complementary intellectual property in the field of colour change technology and is a market leader in this field. Datalase have developed a novel laser

imaging system in which the substrate is coated in an ink that absorbs laser radiation and creates an image by initiating a colour-change reaction. The current Datalase pigment technology is formulated into an ink which is applied to packaging labels. A CO_2 laser is then used to irradiate the label; the pigment in the ink absorbs the radiation directly and is heated to a point where the colour change reaction occurs. The result is that the parts of the label irradiated by the laser change colour from white to black. Thus an image is rapidly created on the parts of the label targeted by the laser.

This process can operate at high speeds and is particularly suitable for individual packaging labels, such as bar codes or delivery addresses, because each image can be different and the equipment can easily be added to production lines. The lasers currently used in the process are mid-infrared continuous wave 10600 nm CO_2 lasers which are effective with the current ink formulation. The pigment is an ammonium molybdate compound (discussed below) which changes colour at around 300 ^{o}C.

This process offers several advantages over conventional inkjet or laser printing methods. There are no consumables at the point of printing: the labels or packages are pre-coated in the ink which is highly convenient on a large production line; imaging can be achieved on almost any substrate; a coating over the label such as lamination is not an obstacle; and images can be created at very high speeds with a high level of clarity.

1.2 Project Motivation

The Datalase imaging technology is currently moving away from CO_2 lasers which are relatively bulky, occasionally need re-gassing and have imaging speeds limited by the internal mirror galvanometer mechanism used to control the laser beam. There is a desire to move to smaller, higher powered solid state fibre lasers which operate in the 750-2500 nm range i.e. the near infrared (NIR) region of the electromagnetic spectrum. These alternative lasers are less bulky, require less maintenance and can be arranged in arrays to increase imaging speeds. The laser head is connected by flexible optical fibre cables so the main body of the laser does not need to be situated immediately adjacent to a production line like the rigid CO_2 lasers. The laser specifications are given in Chapter 2.

The major obstacle to overcome when using an NIR laser is that the pigment present in the Datalase ink formulation does not directly absorb radiation of this wavelength and therefore will not change colour. Therefore an intermediary is needed – another component of the ink that will absorb the NIR radiation and transfer it to the pigment as heat to trigger the thermal colour change in order to form an image. It is this compound, an NIR absorber, which is the focus of this project. A schematic overview of the Datalase process is given in Figure 1.1.

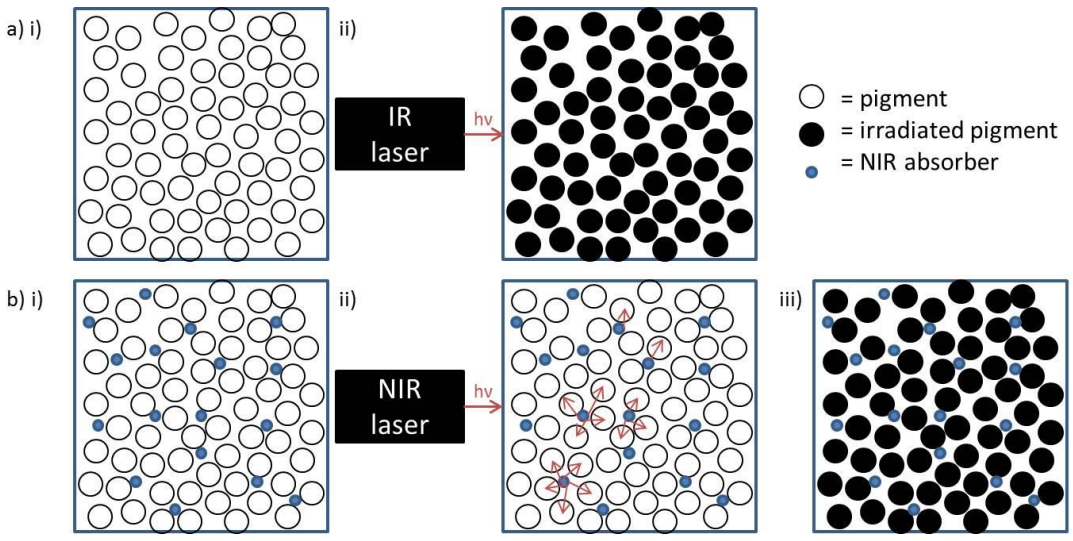

Figure 1.1 - Schematic representation of the Datalase imaging process using a) CO_2 infrared lasers: i) the label is coated in ink ii) irradiation causes pigment colour change and b) solid state NIR lasers: i) the label is coated in ink, ii) the absorber takes in the laser radiation and transfers it to the pigment iii) pigment colour change.

1.3 The Interaction of Light with Matter

The first step in the Datalase image creation process is the absorption of NIR light by the absorber compound. There are a number of ways in which condensed matter can interact with light. In simple terms, incident light irradiated upon a material can be transmitted through the material, reflected back or absorbed by it. In reality the true picture is not so straightforward and is often a combination of all three. More specifically, it is the electromagnetic field of the light wave which interacts with the local electromagnetic field of the atoms making up the material.

In the classical electrodynamic model, light is treated as an electromagnetic wave and atoms as dipole oscillators[2]. Lorentz first proposed the model in which electrons are treated as though bound to the nucleus of an atom by a spring-like force that obeys Hooke's law[†]. Applying an electric field of frequency ω interacts with the charge on the electrons and causes them to oscillate about the equilibrium position. Radiation is emitted at the resonance frequency of the oscillations ω_0. It should be noted that the field also interacts with the nucleus but it is so massive compared to the electrons that it essentially remains stationary. If $\omega = \omega_0$ then a resonance phenomenon occurs, very large oscillations are induced and energy is transferred from the electromagnetic wave to the atom. The resonant frequency depends on the mass of the atom and each atom will have several dipoles of specific frequencies which can be seen in the multiple lines of emission spectra. This is the case for a free atom but interaction behaviour is different in materials with different properties.

1.3.1 Transmission

If light passes into a material and its frequency ω does not coincide with any of the atomic resonant frequencies ω_0 in a medium, it will pass directly through it (be *transmitted*). The light wave drives the electronic oscillations but damping effects cause a phase lag which means that the speed of light in a medium is slower than it is in a vacuum. Regardless, in a transparent material the light wave propagates directly through the material and emerges on the other side. In materials like stained glass which are transparent but coloured, only light of certain frequencies is transmitted – the remainder is *absorbed* (see section1.3.3).

[†] Hooke's Law: the force *F* needed to extend or compress a spring a certain distance *y* is proportional to the distance as F(y)=-ky where *k* is the 'stiffness', a constant characteristic of each spring.

If the velocity of light reduces significantly in a medium then it is said to be *refracted*. This occurs when the light passes through a boundary between two transparent media with different refractive indices i.e. through which light passes at different speeds. When crossing the interface, the frequency of the light remains the same but the wavelength changes to account for the change in speed as the values are directly related by:

$$c = \lambda v \qquad (1)$$

Where c is the speed of light, λ is its wavelength and v is its frequency. A continuous transition is only possible with a change in direction so a beam of light will appear 'bent'. The amount that a medium 'bends' the light is known as its refractive index, n, and is equal to the ratio of the speed of light in a vacuum, c, to its speed in the medium, c_m.

$$n = \frac{c}{c_m} \qquad (2)$$

The diagram and photograph in Figure 1.2 both illustrate this effect.

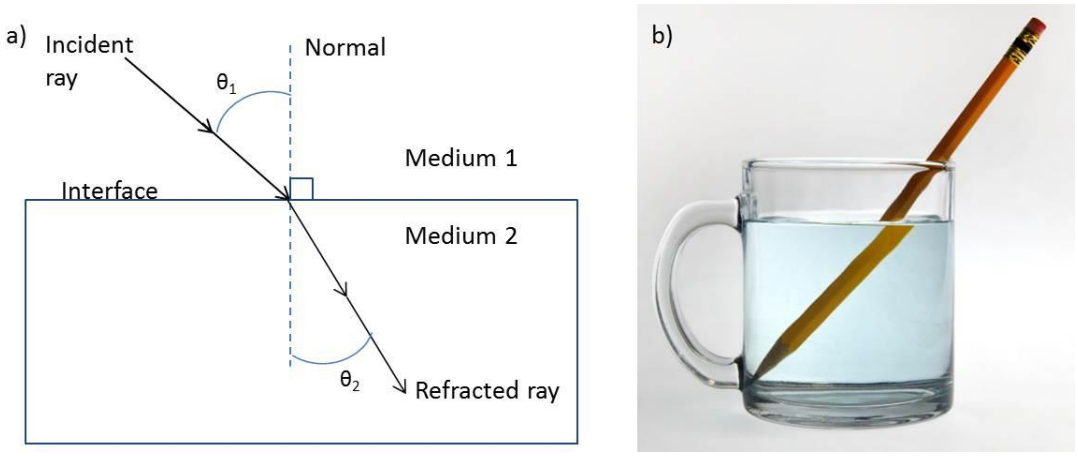

Figure 1.2 – a) Diagram representing the process of light refraction and b) a photograph showing a refracted image of a pencil seen through water. Photograph credit© 2011–2014 Florida Center for Instructional Technology / Dr. Roy Winkleman.

The sines of the angles of refraction at the interface are related to the refractive indices, n, by Snell's law:

$$\frac{sin\theta_1}{sin\theta_2} = \frac{n_2}{n_1} \qquad (3)$$

Although the velocity of the light is reduced, its intensity is not affected during refraction i.e. the light is still transmitted, just not in a straight line.

1.3.2 Reflection

When encountering a boundary between two media, a beam of light can also be *reflected*. If the interface surface between the two media is smooth, the reflection of the incident beam will be symmetrical with respect to the surface normal. This is known as *specular reflection* when the light is reflected in a specific direction at a smooth interface e.g. in a mirror. This effect is used to advantage in optic fibre technology – light entering a thin glass fibre at a steep enough angle undergoes total internal reflection at the inner surface of the fibre and so can be transmitted long distances. If the incident angle is less than the critical angle required for total internal reflection, the light will be refracted out of the glass fibre.

If a surface is curved, the reflected beams of light will diverge or converge and result in bigger or smaller specularly reflected images respectively. When light hits a rough surface (which is the case with most objects), the light is reflected back in all directions. This is known as *diffuse reflection.* A surface which reflects back all the light appears white. If only certain frequencies of the incident radiation are reflected and the rest are absorbed (see below) a surface will appeared coloured and a surface which reflects no radiation appears black.

Light which penetrates some way into a material before being reflected is said to be *scattered*. The size of the particles by which the light is being scattered affects the properties of the scattered light. The most famous example of this is the blue colour of the sky which results from the light from the sun being scattered by atmospheric molecules. The molecules in the air are much smaller than the wavelength of sunlight. These conditions are known as *Rayleigh scattering*, and the relationship between the intensity of scattering and the wavelength is described by the Rayleigh scattering law:

$$\sigma_s(\lambda) \propto \frac{1}{\lambda^4} \qquad (4)$$

Here σ_s is the scattering cross-section and λ is the wavelength of light. The full equation has many more parameters which have been omitted for clarity. The result of this is that radiation with short wavelengths (blue) is scattered more than that with long wavelengths (red). The molecules making up a cloud however are large enough for scattering to be almost independent of wavelength and so clouds appear white or grey. Objects which scatter light can appear translucent (like frosted glass) or opaque (like milk).

1.3.3 Absorption

The transmission of a material, discussed above, is closely related to its *absorption*. If light passes into a material without being reflected or scattered, that which is not absorbed is transmitted and vice versa. Absorbed light accounts for the colours of objects we see all around us. A material can absorb and transmit light of different energies simultaneously, for example in coloured glass which is both transparent and coloured. The absorption and transmittance of light through a material is described by the Beer-Lambert law:

$$I = I_0 10^{-\alpha[J]l} \quad (5)$$

I is the intensity of the transmitted radiation, I_0 is the incident intensity, α is the molar absorption coefficient. [J] is the molar concentration of the absorbing species J and l is the path length of the sample. The absorption coefficient is related to another term, the extinction coefficient κ:

$$\alpha = \frac{4\pi\kappa}{\lambda} \quad (6)$$

λ is the wavelength of light. The transmittance of light through a sample is equal to the ratio of transmitted radiation to the amount of incident radiation:

$$T = \frac{I_t}{I_0} \quad (7)$$

The absorbance, A, of a sample is given by:

$$A = log\frac{I_0}{I} = log\frac{1}{T} = \alpha[J]l \quad (8)$$

From these equations it can be seen that the amount of radiation that can pass through a sample decreases exponentially with sample thickness and molar concentration. Therefore the amount of absorbance will increase in a thicker or more concentrated sample, assuming that reflectance and/or scattering have been taken into account. The Beer-Lambert law is limited to monochromatic radiation and is generally used for liquid samples although it is also applicable to gases and in Chapter 2 it will be seen how it can also be applied to solid samples.

1.3.3.1 Absorption in atoms and molecules

In the case of absorption, a quantum approach is needed to explain the general processes. The classical model treats light as an electromagnetic wave but quantum mechanics endows it with particle-like properties while also giving matter some wave-like properties. If a particle has momentum *p,* the de Broglie relation states that it also has a wavelength λ:

$$\lambda = \frac{h}{p} \qquad (9)$$

Where *h* is Planck's constant[†]. Quantum mechanics is named after *quanta* or 'packets of energy' first proposed by Planck in 1900. Quanta of light are called photons and the electronic structure of atoms is quantised into discrete energy levels. Planck's constant also relates energy, *E*, of a species to its frequency, *v:*

$$E = h\nu \qquad (10)$$

Substituting in the frequency from equation 1 above, the energy of a photon can be expressed using its speed and wavelength as:

$$E = \frac{hc}{\lambda} \qquad (11)$$

If the energy of a photon corresponds to the gap between discrete energy levels in an atom then the photon can be absorbed by that atom.

As well as discrete electronic energy levels, molecules also have quantised rotational and vibrational energy levels (they also have translational motion but its associated energy is continuous rather than quantised). The energy of separation between levels decreases in the order electronic>vibrational>rotational. The rotational states correspond to the angular momentum of a molecule and the energy separation of these levels is small so transitions occur in the microwave region of the electromagnetic spectrum and do not contribute to optical properties in the visible or NIR regions which are of interest in this work. Higher energy vibrational transitions occur in the IR region and it will be seen that these contribute more to the overall properties than the rotational levels. Each electronic state in a molecule will have associated vibrational states which correspond to the molecule vibrating about its bonds.

When a photon of appropriate energy is absorbed by a molecule, the molecule is promoted into a higher energetic state. These excited states have a limited lifetime and inevitably decay via either a *non-radiative* or *radiative* process. If the molecule is promoted to a higher vibrational state, the energy can be transferred to surrounding molecules as heat as the molecule returns to a lower vibrational state in a non-radiative decay event. Radiative decay happens when the excitation energy is discarded as photons of lower energy. If this occurs immediately after irradiation it is called *fluorescence* or if the emission continues for some time after the event, it is known as *phosphorescence*. The timescales of these

[†] Planck's constant $h=6.626\times10^{-34}$ J.s or 4.136×10^{-15} eV.s

processes are shown in the Jablonski diagram Figure 1.3 with an illustration of the possible transitions between electronic and vibrational states. Other fates of an excited molecule include triggering a photochemical reaction, as in photosynthesis, or breaking bonds resulting in dissociation of the molecule. Another possibility is that an electron is excited so strongly that it is expelled from a material. Then *photoionisation* has occurred and this is the basis for a number of spectroscopic techniques.

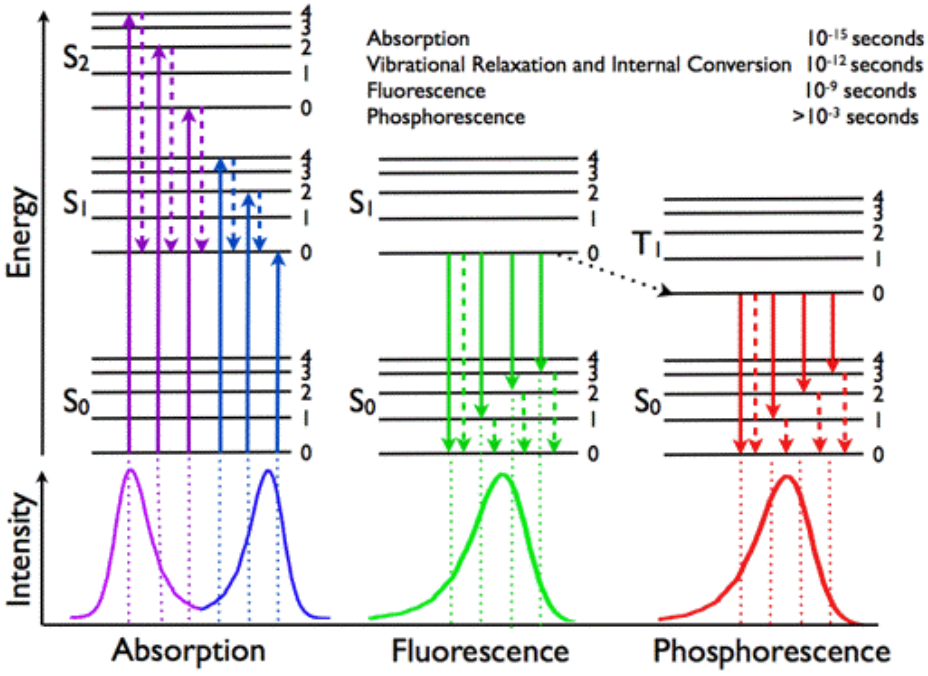

Figure 1.3 - Jablonski diagram representing transitions between electronic energy levels and associated vibrational levels. Solid arrows indicate radiative transitions as occurring by absorption (violet, blue) or emission (green for fluorescence; red for phosphorescence) of a photon. Dashed arrows represent non-radiative transitions (violet, blue, green, red). Representative spectra are shown below. From reference 3.

The energy loss processes have been described but the energy is initially gained by one of a number of known light absorption mechanisms. In transition metal compounds, the outer electrons reside in the five *d*-orbitals. In a free atom these orbitals are degenerate but in a complex the field applied by the surrounding ligand species removes the degeneracy. The orbitals reside at different energy levels depending on the relative position, number, and nature of surrounding ligands. In the ground state the *d* electrons will be located in the lowest energy orbitals but a photon of appropriate energy can excite an electron to a *d*-orbital of higher energy. This is known as a *d-d transition* and since the energy separation corresponds to the visible region of the electromagnetic spectrum, these compounds are usually coloured. From an incident beam of white light such as sunlight, photons which

have the energy matching the *d*-orbital energy 'gap' will be absorbed and photons of other energies will be reflected back causing the material to have the complementary colour to the wavelength which is absorbed. For example, if photons of energy corresponding to the red wavelength of light are absorbed the material will appear green and vice versa.

The aforementioned vibrational levels are also involved in *d-d* transitions. The Laporte selection rule for centrosymmetric complexes forbids transitions that do not have an accompanying change in parity (symmetry with respect to an inversion centre). However vibrational motion of the transition metal complexes eliminates the centre of symmetry and the *d-d* transitions become weakly allowed. This type of transition is known as *vibronic* i.e. a combination of electronic and vibrational contributions.

Absorption can also occur when an electron is transferred to or from a metal orbital to an orbital on a ligand, known as a *charge-transfer transition*. Unlike the d-d transitions, charge-transfer transitions are not bound by the Laporte selection rule so have much greater intensity. Conjugated molecules such as aromatic hydrocarbons or conjugated polymers are also strongly coloured. Their electrons are delocalised across the whole molecule in overlapping π orbitals and incoming light can promote these π electrons to an excited state – a π* anti-bonding orbital. This is known as a $\pi^* \leftarrow \pi$ *transition*. These conjugated systems are commonly present in dyes.

1.3.3.2 Absorption in solids - electrons

Unlike molecular solids, crystalline materials have strong bonds between all atoms which are packed closely together and this affects their optical properties. As in the conjugated molecular systems previously discussed, electrons which are not tied up in bonds will be delocalised. However unlike the molecular example, the electrons are not limited to a specific molecule but are delocalised throughout the whole solid. The strong interaction between neighbouring atoms means the outer electronic orbitals overlap to form *bands* of energy (see Figure 1.4). The core orbitals are not involved in this and remain discrete.

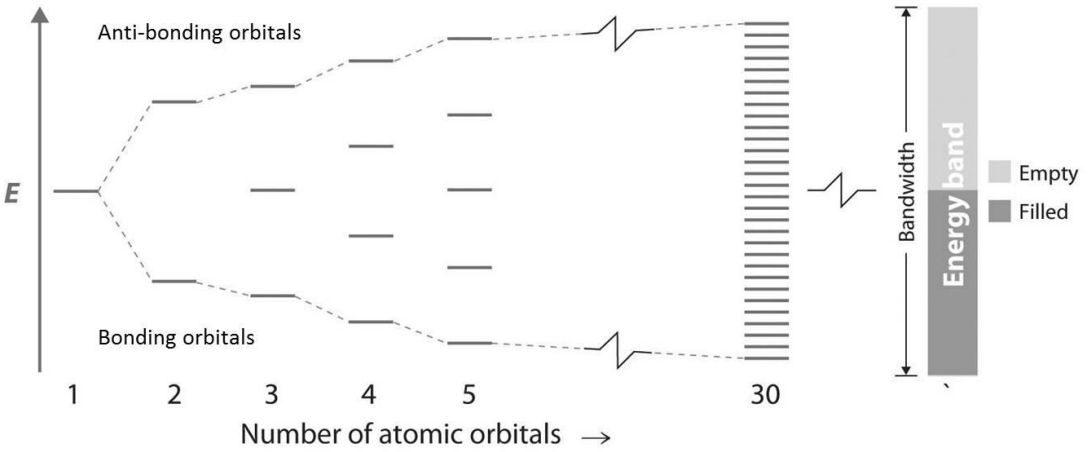

Figure 1.4 - Representation of the formation of electronic bands from overlapping atomic orbitals.

The bands which are important for the chemistry of a material are the *valence band* which is the highest energy filled band and the *conduction band* which is the lowest energy vacant band. The energy gap between these is known as the *band gap, E_g,* and its value defines whether a material is a metal ($E_g = 0$), a semiconductor (small E_g) or an insulator (large E_g). The bands do not have discrete energies like atomic energy levels but a range of energies which results in broad bands of absorption. Electrons fill the bands up to a point known as the Fermi energy, E_F, which can lie in the valence or conduction band, or in the band gap. The position of E_F depends on the density of states of a material i.e. the number of states available within a given energy range.

The optical properties of metals and semiconductors are defined by their *dielectric function* which is dependent on their electronic band structure. Using the classical Drude-Lorentz model for a free gas of electrons, the frequency-dependent dielectric constant ε(ω) (also known as the relative permittivity) is defined by the following relation:

$$\varepsilon(\omega) = 1 - \frac{\omega_p^2}{\omega^2 - i\omega\gamma} \qquad (12)$$

ω_p is the plasma frequency and γ is the damping parameter caused by the scattering of electrons. ω_p in turn is dependent on a number of factors:

$$\omega_p = \sqrt{\frac{Ne^2}{\varepsilon_0 m_0}} \qquad (13)$$

N is the number of electrons per unit volume, *e* is the magnitude of the charge on the electron, ε_0 is the permittivity of a vacuum and m_0 is the mass of an electron. The associated mathematical derivations will not be detailed here but the important points to

note are that the relative dielectric function (and therefore the optical properties) of a material depend on the free carrier concentration and the amount of damping of electronic motion. Also an interesting point to note is that the refractive index *n* encountered in section 1.3.1 is related to the relative dielectric constant: $n = \sqrt{\varepsilon(\omega)}$. In a metal ω_p is high and since frequencies below ω_p will be reflected, this gives many metals their shiny appearance.

In semiconductors, a photon can promote an electron across the band gap if it has sufficient energy ($\geq E_g$). This is known as an *interband transition* and the photon is absorbed in the process. Electrons can also be thermally excited across the band gap so semi-conductors become more conducting as their temperature increases. The conductivity of semi-conductors can also be increased by doping i.e. introducing foreign atoms into the material. These add an extra small band into the band gap either just above the valence band (p-type doping) or just below the conduction band (n-type doping) and so reduce E_g.

Two types of *intraband transition* can also take place – *free carrier absorption* and *plasmon absorption*. The electrons in the conduction band act as free charge carriers. They have only weak interactions with atomic nuclei in the crystal so can move freely. The dipole oscillator model does not apply here so the electrons have no natural resonant frequency ($\omega_0 = 0$). The energy levels of the conduction band are only partially filled by electrons so higher empty levels are available for occupation. Absorption of light can promote electrons within the conduction band. The position of the absorption edge is dependent upon the number and mobility of free charge carriers. For a metal the absorption occurs in the UV region but for a semiconductor it appears in the infrared region. This is due to the much smaller carrier concentration in the semiconductor and it can be tuned with doping.

The plasma of free electrons in the conduction band of a semiconductor or a metal can be driven to oscillate collectively with the plasma frequency, ω_p, by the electric field of applied light. Quantisation of these oscillations forms a quasiparticle known as a *plasmon* (plasma oscillation) which can be visualised as the cloud of free electrons oscillating back and forth with respect to the lattice ions. Interaction of the oscillating electrons with incident light of similar momentum and wavelength to that of the plasmons causes a resonant excitation and the light is absorbed. The plasma frequency of oscillation of unbound free electrons (ω_p) decreases when boundaries are introduced, for example in a nanoparticle[4].

The particle size affects how much of the incident radiation is absorbed and how much is scattered, however in small particles absorption is dominant[5]. In bulk materials the surface plasmon oscillates only a short distance into the material as a thin surface layer but in nanoparticles, *localised surface plasmon resonance* (LSPR) involves all the free electrons in the particle[6]. Since their size is smaller than the wavelength of the incident light the effect of the electric field is felt evenly throughout the particle[7].

In particles with diameters <100 nm the resonance frequency is in the visible-to-infrared range. Optical absorption peaks that are observed are centred on the LSPR frequency[8]. The optical properties are also influenced by a number of factors such as the particle size and shape, the surrounding medium and the free charge carrier concentration. The free carrier concentration can be readily changed in metal oxides by doping which is not possible in metal nanoparticles. Figure 1.5 shows the LSPR extinction coefficients for a range of metals and metal oxides and the variation in frequency (wavelength) can be seen along with different peak shapes.

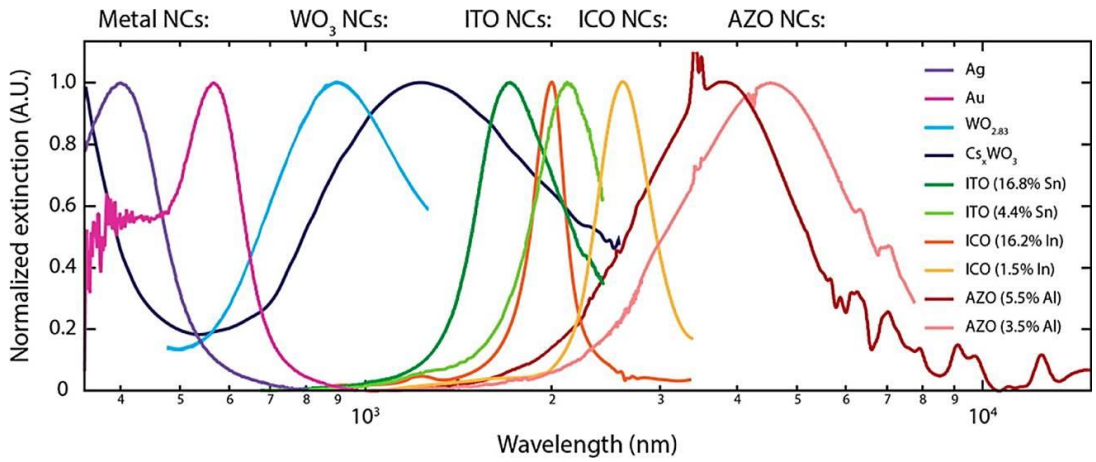

Figure 1.5 - Normalized optical extinction coefficients vs wavelength due to LSPR's in solution and films of metal and metal oxide nanocrystals (NC's). Taken from Lounis et. al.[6]; ITO=indium tin oxide, ICO=indium cadmium oxide, AZO=aluminium-doped zinc oxide.

Damping caused by collisions or structural defects[9] reduces the intensity of LSPR interaction and broadens the optical line width – therefore this can also be tuned by doping. The 'tunability' of these materials gives them a broad range of applications, from biosensing[10] (most widely used in home pregnancy tests[7]) to 'smart windows'[11]. The field of nanoplasmonics has developed dramatically in recent years as better synthetic routes to nanoparticles are discovered[7].

In a bulk crystalline material, charge carriers moving through the ionic lattice can cause the formation of *polarons*. The charge carrier attracts neighbouring species with opposite charges and repels those with like charges – it is the charge carrier plus the surrounding area of lattice deformation that constitute the polaron. A small polaron is the strong interaction of a charge carrier with the surrounding lattice in such a way that the charge carrier is essentially localised to one site in the lattice. Or in the words of Emin[12], electrons or holes that become *"trapped in potential wells of their own creation".* If the spatial extent of the wavefunction of the trapped species is comparable to the spacing of atoms in the lattice then the polaron is considered 'small'. A large polaron on the other hand has a weaker interaction and is spread over a larger area of the lattice. Applying energy induces a transition (or "hopping") from one site to another, overcoming the energy barrier. The hopping is typically thermally-activated but light can also act as an initiator. If this is the case, broad absorption bands are observed in the near-infrared region of the electromagnetic spectrum[13]. Because of the electron (or hole) localisation to one lattice site, materials need to have at least a small amount of site inequivalency to be polaronic – e.g. neighbouring metal sites with different valencies.

1.3.3.3 Absorption in solids - phonons

In order for a colour change to occur in the Datalase imaging process, the absorbed NIR radiation has to be transferred to the pigment molecules as heat. Heat is simply a term for the transfer of thermal energy which is the amount of atomic vibration in a material - the greater the vibration the hotter the material. In a crystalline material, rotational energy states like those in molecular materials do not exist since the atoms in a lattice are not free to rotate but vibrational energy levels are present. The quantum of wave-like thermal vibrations of the lattice at a certain frequency is known as a phonon and is sometimes treated as a particle. In addition to the electronic absorptions discussed above, a framework lattice can interact with incident radiation by *phonon absorption*.

Phonon (or lattice) absorption occurs at lower energies than most electronic absorptions as the phonon resonance frequencies are in the mid- to far-infrared range. In order to transfer energy from photon to phonon, both energy and momentum must be maintained and a coupling mechanism is needed. Photon momentum $p = {}^{h}/_{\lambda}$ and phonon momentum $p = {}^{h}/_{a}$ will be conserved if λ=a i.e. if the de Broglie wavelength of the incident radiation λ is equal to the lattice constant a (h is Planck's constant). Coupling occurs when there is a

change in the electric dipole moment of the lattice. The absorption coupling mechanism can involve single or multiple phonons[14]. In ionic crystals with alternating cations and anions, the oscillation of photons in an electromagnetic wave can cause the formation of a single phonon which absorbs strongly in the infrared region (also known as Reststrahl absorption). When two or more phonons interact in such a way to cause dipole moments with which a photon can couple then it is classified as multi-phonon absorption. The range of combinations of vibrational modes during multi-phonon absorption is complex and the intensity of these interactions is weaker than for single-phonon absorption.

A photon can transfer all of its energy to the phonon system and be fully absorbed. However if only part of the energy is transferred, or if the photon loses or gains energy then it is said to be inelastically scattered. Both infrared and Raman spectroscopy are used to gain information from these photon-phonon interactions. Photons of IR wavelength are used to induce vibrational transitions in solids which have either permanent or dynamic dipole moments and the frequency of these phonons can be detected. Inelastic photon scattering events from optical phonons are used in Raman spectroscopy to gain information about the phonons, such as their energy and momentum. Since the probability of this type of scattering is relatively low, high intensity lasers are used as the light sources in these experiments. Chapter 2 gives more detail on these techniques.

Following laws of thermodynamics, when two bodies are in contact heat will flow from the hotter one to the cooler in order to achieve thermal equilibrium. In the Datalase process, the near infrared (NIR) absorber particles absorb energy from the NIR laser and will transfer this energy as heat to the surrounding ink including the ammonium octamolybdate pigment particles. This pigment colour change takes place at around 300 ^{o}C so this is the minimum amount of heat that needs to be transferred to cause image formation. The fundamental physical processes of thermal conductivity are rather complex and dependent on many variables so a full description of these is considered to be outside the scope of this project. However, in simple terms, heat can be either conducted or transferred radiatively between materials. Conduction involves the transfer of heat by rapid collisions of vibrating atoms or electrons with their neighbours and by propagation, collision or scattering of phonons. Radiative heat transfer is distinctly different in that it is the emission of a photonic electromagnetic wave with a frequency in the infrared region which is generated by dipole oscillations within the material.

1.4 Target Material Considerations

The target compound(s) must first and foremost absorb radiation in the near infrared (NIR) region of the electromagnetic spectrum (750-2500 nm). Ideally the absorption profile will peak at around 1000-1100 nm because solid state Yb:glass lasers that operate at 1070 nm have relatively cheap diodes for the NIR range, although Er:glass 1550 nm lasers are also being considered as an option. In addition to NIR absorbance, Datalase have a number of other criteria for NIR absorbers. Organic compounds tend to be expensive and not often commercially available in large quantities so the focus will be on inorganic compounds. Expensive platinum group metals (PGMs) are undesirable for this project as the associated cost is too high for a small business like Datalase. Potentially toxic metals such as cadmium or lead are also to be avoided in case of application of labels to food packaging.

The current leading NIR absorbing material for this application is indium tin oxide $In_{2-x}Sn_xO_3$ (ITO). It performs well but indium has no significant known ores and is produced as a by-product of zinc production requiring complex (and often proprietary) procedures to purify it[15]. This means that clear production data is not readily available so predicting future supplies is difficult. The prevalence of indium-containing compounds, including ITO, in display technologies and photovoltaic applications means that it is in high demand. As yet it is not widely recycled so resources are dwindling and this has led to price fluctuations which are unfavourable for small businesses like Datalase. According to one estimation, there will only be enough indium to last around 10 years at current consumption and recovery rates[16]. In 2010 an EU study listed indium as a "critical raw material" and cites limited recycling as one of the reasons for this[17]. However the increased price means that companies are now developing processes to extract the metal from base metal concentrates that have as little as 100 ppm (parts per million) indium[18]. Reclaiming indium, from sputtering targets used to make ITO films for example, is also an area where improvements in efficiency are being made and measures like this should mean that indium is relatively sustainable in the long term. However the time-lag in bringing these processes to capacity means there will still be short-term instabilities and price fluctuations.

Datalase are seeking replacement absorbers that do not contain indium to act as an alternative NIR absorbing material for use in the Datalase NIR laser imaging process. The compound should have the ability to be easily formulated into inks i.e. not dissolve in the chosen solvent system or react with any other ink components. It should provide efficient

heat transfer to the pigment for rapid image formation. As well as NIR absorption, the absorber should be relatively transparent in the visible region (390-750 nm) so that coatings applied to labels are not dark in colour. Transparency can be achieved more easily if the absorber is effective at low concentrations (<5% ink overall) and has a small particle size (<500 nm) – this would also help give an even dispersion in ink provided there is little aggregation.

The target material criteria are summarised as follows:

- Absorb electromagnetic radiation in the NIR region (ideally at 1070 nm)
- Transparent as possible in the visible region
- Inorganic compound (but no PGMs)
- Non-toxic, sustainable metals (no indium)
- Inert with respect to the ink formulation
- Transfer heat effectively

1.5 The Pigment

The pigment used in the Datalase laser imaging process is ammonium octamolybdate $(NH_4)_4Mo_8O_{26}$, known as AOM, in the form of a white powder. The molybdenum atoms form a cluster structure in which they are linked together by oxygen atoms[19], shown in Figure 1.6.

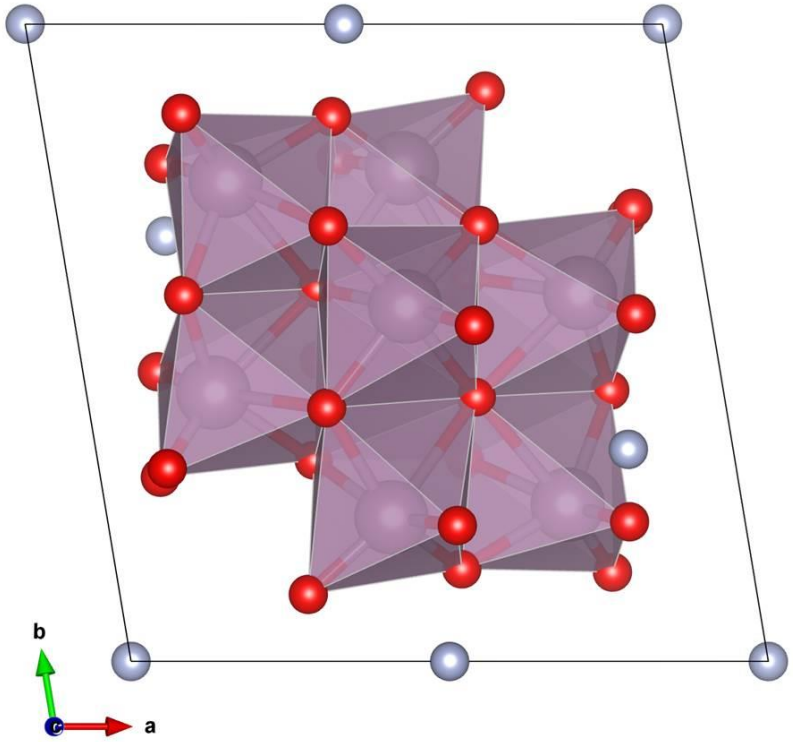

Figure 1.6 – Polyhedral representation of the structure of $(NH_4)_4Mo_8O_{26}$: O=red, Mo=purple and N=grey.

The cluster is an anion with an overall charge of -4 and the compound has triclinic symmetry in space group P-1. This is one of a large family of polyoxomolybdates[20] and water molecules are usually present in the structure. When irradiated directly with mid-infrared radiation (around 10600 nm), the pigment changes colour from white to black. The colour change is irreversible. The thermal decomposition has been studied by Ma[21] who found that MoO_3 forms at 370 ^oC and up to this point the only change is dehydration. However when heated under vacuum, an irreversible black colour change is observed above 250 ^oC and attributed to the formation of a number of oxygen deficient molybdates MoO_{3-x}. It is thought that incorporation of the AOM pigment into the ink formulation prevents contact with air and so the oxygen-deficient phases result from the indirect laser heating via the NIR absorber to give the black colouration of images thus created.

1.6 Near Infrared Absorbing Materials

Compounds that absorb radiation in the near infrared (NIR) region of the electromagnetic spectrum (750-2500 nm) have a range of applications. Coatings have been used on 'smart windows' in order to modulate heat to maintain comfortable temperatures inside buildings or automobiles in summer and therefore reduce the energy consumption from air conditioning[22]. Medically they are used in photothermal therapy for specific targeting of tumours. When the absorber is inserted to the diseased area and irradiated with NIR light it will then heat up and kill the diseased cells without harming healthy tissue[23]. Other uses include IR cut-off optical filters[24], laser welding, stealth technology and solar harvesting[25]. This range of uses means there is some considerable research interest in this area.

Metal nanoparticles, particularly gold[23a], and lanthanum hexaboride[22, 26] are commonly used as NIR absorbers. Both these species absorb NIR radiation via localised surface plasmon resonance (discussed above) and the absorption peak can be tuned by changing the particle size[26] and shape[27]. Transparent conducting oxides often show absorbance outside the visible range, due to plasmon resonance of electrons in the conduction band. Doped metal oxides are well known for displaying excellent NIR absorption properties, for example tin-doped indium oxide (ITO)[28] or antimony-doped tin oxide (ATO)[24, 29]. Titanium nitride, TiN, has strong absorbance in the visible region and some NIR absorption[30]. A range of organic molecules are also known to have NIR absorbing properties. These molecules typically have extended delocalised electrons in aromatic systems so the absorbance arises from $\pi^* \leftarrow \pi$ transitions. However these compounds all have their drawbacks for application in laser imaging. LaB_6 and TiN are very darkly coloured so would produce poor coatings. The limitations of indium have been discussed previously, as have toxicity issues with elements such as antimony. The focus of this project is on inorganic compounds for reasons mentioned in section 1.4 so organic candidates are ruled out. The ideal compound would be colourless but these materials are usually coloured due to extension of the absorbance peak from the NIR region to at least the adjacent red region visible region of the electromagnetic spectrum. The choice of prospective candidates is discussed further below.

1.7 A Starting Point: Analysis of Commercial Samples

Datalase provided four commercially available samples that perform reasonably well as near infrared absorbers so these were thought to be a practical starting point for the research project. The samples were obtained from overseas suppliers and very little was known about their synthesis or composition. The first stage of the project was to characterise these samples and use information thus gained to guide the choice of future candidate materials. Details of techniques and equipment used can be found in Chapter 2 and results of analysis are shown in full in Appendix 1. The samples are outlined in Table 1.1.

Table 1.1 - Summary of commercial NIR absorber compounds

Sample	Full name	Colour	Formula
rITO	Reduced indium tin oxide	Blue	$In_{2-x}Sn_xO_{3-x}$
CHP	Copper hydroxyphosphate	Pale green	$Cu_2(OH)(PO_4)$
BTO1	'Blue tungsten oxide' 1	Dark blue	$Cs_xWO_3 + CsW_2O_6$
BTO2	'Blue tungsten oxide' 2	Dark blue	WO_{3-x}

The abbreviations shown in Table 1.1 will be used in subsequent discussions. It was initially thought that BTO1 and BTO2 were the same compound with different particle sizes. However after analysis it was clear that this was not the case. The results of analysis showed that the commercial samples all have different compositions, crystal structures, morphologies and NIR light absorption mechanisms - all factors which will need to be considered during the project. The compositions of rITO and CHP were as expected but the 'mystery' BTO compounds consisted of a caesium tungsten bronze and caesium tungstate mixture (BTO1) and a reduced form of tungsten trioxide (BTO2).

Based on this information, four types of compound related to the commercial samples were chosen as potential NIR absorber candidates:

1. Tungsten bronzes
2. Sub-stoichiometric tungsten oxides
3. Copper phosphates
4. Transparent conducting oxides.

The existing work on these families of materials is summarised below in section 1.8.

1.8 Literature Background

After analysis of commercial samples in Appendix 1, tungsten bronzes, reduced tungsten oxide, copper phosphates and transparent conducting oxides were chosen as potential candidate materials. The research carried out on these materials to date is summarised in this section.

1.8.1 Tungsten Bronzes

1.8.1.1 History

The first tungsten bronze was discovered by Friedrich Wohler in 1823 when he heated sodium tungstate with tungsten trioxide in a reducing atmosphere of hydrogen[31]. The result was a sodium-tungsten compound with a lustrous yellow colour hence the name 'bronze' (the tungsten bronzes should not be confused with metal alloys of the same name). Potassium analogues were found by Laurent in 1838[32] and some early investigations of the compounds were undertaken by Spitzin[33] and Brunner[34]. Their properties were not studied in more detail until the 1930's onward, most notably by Hagg, Straumanis and Magneli. Hagg showed that the sodium tungsten bronzes, previously thought to be distinct compounds, actually form a solid solution[35] with the composition varying with the amount of incorporated sodium as Na_xWO_3. The valence of the tungsten atoms changes to accommodate the sodium cations – at the upper limit (x = 1) all the tungsten is in the +5 state but as vacancies are introduced in the sodium lattice a corresponding amount of tungsten atoms are oxidised to the +6 valence state. Straumanis measured the chemical and electrical properties of the sodium bronzes[36]. Early optical studies were done on the sodium tungsten bronzes in the form of both single crystals[37] and compacted powders[38]. Optical properties of nanoparticle dispersions of a range of bronzes were only investigated more recently by Takeda and Adachi in 2007 and they were found to be excellent NIR absorbers[39].

1.8.1.2 Structure

The first sodium bronzes to be studied were found to have a cubic (perovskite) crystal structure[40] and Magneli reported the structure of the tetragonal potassium bronze in 1949[41]. He also reported potassium, rubidium and caesium bronzes that were found to have a hexagonal unit cell[42] and subsequently published their crystal structures[43] giving the hexagonal bronzes a general formula of M_xWO_3. M is traditionally an alkali metal cation but

can be a range of other elements[44] including barium[45], thallium[46], copper[47], tin[48], lead[49], antimony[49] or lanthanides[50]. Analogous bronzes also exist with molybdenum, vanadium, niobium or titanium in place of tungsten[51] however they are not isostructural to the tungsten bronzes or to each other [52]. Molybdenum bronzes are discussed in more detail in Chapter 6.

The building units of the tungsten bronzes are corner-sharing WO_6 octahedra[44], arranged either in a regular or distorted network, with metal cations situated in the spaces in between. The structure adopted depends on the nature and amount of the metal cation M. The cubic bronzes have the perovskite structure consisting of WO_6 octahedra corner-linked to six others leaving square channels in which the M^+ ions reside. For M_xWO_3, when x = 1 the sodium A sites are fully occupied but vacancies appear as x approaches 0. As the amount of M^+ decreases, phase changes occur to less symmetrical structures. Two tetragonal structures are known, 'Tetragonal I' which is a distorted version of the perovskite structure and 'Tetragonal II' which is a different structural type altogether. The Tetragonal I structure is pseudo-cubic and very similar to the perovskite structure shown in Figure 1.7a but with the tungsten atoms shifted off centre in the octahedra to form a zigzag arrangement relative to each other. The Tetragonal II bronze structure also consists of corner-linked WO_6 octahedra but they are connected in such a way as to leave pentagonal, square and triangular channels (Figure 1.7b). The triangular channels are too small to be occupied but cations can be inserted into both the larger channels, giving a maximum value of x = 0.6.

The hexagonal tungsten bronze (HTB) has the WO_6 octahedra corner-linked to form 6-membered rings in the *ab* plane and these *ab* layers are then stacked in the *c*-direction to form channels along the [001] axis. The hexagonal channels are larger than in the tetragonal or cubic structures and so species with larger cations can stabilise this structure more effectively while species with smaller M^+ ions like Li^+ or Na^+ tend to adopt structures with smaller channels[44]. There are three W atoms for each M site in the HTB structure so the maximum value of x = 0.33 when all sites are filled. The lower limit is thought to be around x = 0.13[53]. Below this value, intergrowth tungsten bronze (ITB) phases are known to form which consist of alternating layers of HTB phase and a ReO_3-type structure. First found by Hussain and Kihlborg[53], these ITB phases form with larger alkali metals and relatively low

x values (x < 0.15). Varying the thickness of the 'slabs' results in a homologous series of different phases. The four structural types are shown in Figure 1.7.

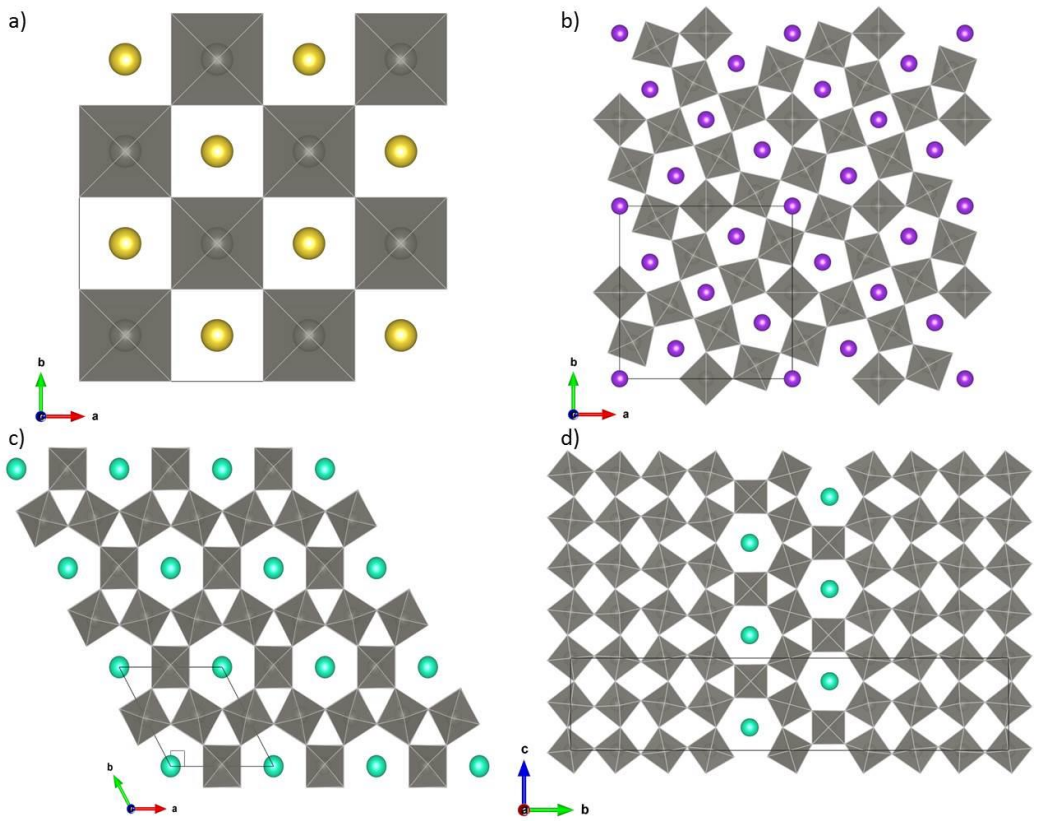

Figure 1.7 – Polyhedral representation of four possible crystal structures of tungsten bronzes: a) cubic perovskite, b) tetragonal II, c) hexagonal and d) intergrowth.

1.8.1.3 Synthesis

Traditional solid state routes were originally used to synthesise the bronzes, generally by reducing polytungstates with tungsten and tungsten trioxide at high temperatures. Electrolytic reduction was performed on the molten precursors by Scheibler[54] and also by Magneli[42], growing crystals of the product on the cathode. Vapor-phase reactions can be used if the metal cation M is volatile enough but this method is not suitable for alkali metal bronzes[44]. Takeda and Adachi mixed aqueous solutions of alkali metal salts and ammonium tungstate before drying and heating to 800 ^{o}C under a reducing atmosphere[39]. Mamak *et. al.* successfully used a thermal plasma method to make nanoparticles of Na, K and Cs bronzes in large quantities with strong NIR absorption[55].

In more recent years the high temperature routes have been superseded by hydro- or solvothermal approaches, in particular for the fabrication of nanoparticles. Nanoparticles are particularly desirable for optical applications as they are more highly absorbing in the

NIR region than the bulk material due to LSPR effects but with limited absorbance in the visible region of the electromagnetic spectrum[39], ideal properties for a NIR absorber. Solvothermal routes are highly tuneable so a range of crystal structures and morphologies can be obtained by simple adjustments to factors such as the pH, the solvent, the reaction time or the temperature. Guo *et. al.* have successfully utilised solvothermal methods to produce a range of tungsten bronzes, firstly as nanoparticles[56] then as one dimensional nanorods[25, 57]. More recently, Liu *et. al.* have developed an "electrostatically induced synthesis" procedure in which they treat the tungstate starting materials with a mild reducing agent ethylenediamine (EDA, $C_2H_4(NH_2)_2$)[58]. The protonated EDA has a strong interaction with the WO_6 octahedra and forms a local reducing environment to form one dimensional nanoparticles of the bronze. Mattox *et. al.* have recently used a colloidal route to obtain distinct nanoshapes of Cs_xWO_3 to directly investigate the effect of shape on LSPR properties[59]. Solvothermal and solid state routes will be used in this work.

1.8.1.4 Properties

Chemically, the tungsten bronzes are very inert compounds – they are insoluble in water and resistant to most acids. This has been attributed to the high energy of activation for diffusion of the alkali metal through the oxide lattice[44]. Single crystals of the alkali metal tungsten bronzes (TBs) show metallic conductivity when $x > 0.25$[44] and below this value behave as semiconductors. The charge carriers are free electrons introduced into the conduction band of the WO_3 host lattice by the dopant alkali metals. They also exhibit superconductivity, particularly the rubidium tungsten bronzes which have a T_c of 7.5 K[60].

The TBs are known for their distinctive optical properties. The sodium TBs exhibit a characteristic range of colours depending on the sodium content of the sample, from dark blue when $x = 0.2$ to lustrous yellow when $x = 0.9$. Brown and Banks measured the reflection spectra of the sodium TBs and show that the position of the absorption peak is dependent on the value of x (as could be expected from the observed colours) and that the optical spectra show a distinct change when the crystal structure changes[38]. Takeda and Adachi were the first to report on the NIR absorbing properties of the hexagonal tungsten bronzes in 2007 when they found that nanoparticle dispersions of HTBs had dramatically increased NIR absorption compared to bulk WO_3 while maintaining high transmittance in the visible range[39]. They also note that the nature of cation M^+ does not have a strong effect on the position of the absorption band indicating that the band structure of a HTB is

independent of the cation. However the absorption increases with increasing amounts of Cs in a series of Cs-HTB samples, showing that the electrons donated to the conduction band from the alkali metal cations play a direct role in the NIR absorption mechanism. As the amount of dopant is directly correlated with the amount of absorption, it follows that the maximum absorption will be achieved for samples with the maximum value of x in M_xWO_3 which is 0.33 for HTB's as there are 3 tungsten atoms for every one potential M atom in the hexagonal unit cell.

In the past there has been some debate over the mechanism of NIR absorption in the tungsten bronzes. Local surface plasmon resonance (LSPR) is thought to be the dominant absorption mechanism in the tungsten bronzes, with a smaller contribution from polaron effects[61]. At low dopant concentrations, localised electronic levels are created below the conduction band and NIR light causes polaron 'hopping' from W^{5+} centres to an adjacent W^{6+} site or promotion to the conduction band. However when the amount of intercalated M^+ approaches the maximum value of x, there are more electrons occupying the conduction band and LSPR becomes the major absorption mechanism. This means that smaller particle size will lead to higher absorption due to the higher surface area available for interaction with the incident NIR radiation hence the recent focus on nanoparticles. Additionally those particles with a high aspect ratio i.e. with one dimensional nanostructures will lead to higher absorption as there will be both transverse and longitudinal plasmon resonances and a higher defect level due to the faster growth rate[62].

The photothermal transmission rate is an important factor in the Datalase imaging process as the NIR absorber has to pass on the laser radiation to the pigment in the ink. The transmission efficiency results from surface plasmon resonance[23a, 61] which is another reason to try and enhance this effect. It can be shown that free electrons are essential for NIR absorption by looking at the hexavalent tungstates which have the same crystal structure as the tungsten bronzes but show no NIR absorption. This is due to the fact that there are no free electrons present in the conduction band to absorb NIR radiation by promotion.

1.8.2 Sub-stoichiometric WO_3

1.8.2.1 History

The so-called "blue tungsten oxides" were known for nearly as long as the tungsten bronzes but were not well understood until the development of the field of non-stoichiometry from 1914. They have the general formula WO_{3-x} and are sometimes known as Magneli phases, named for Arne Magneli who was the first to propose a crystallographic shear arrangement of the WO_6 octahedra to account for the oxygen deficiencies in the structure.

1.8.2.2 Structure

Like the tungsten bronzes, the building blocks of the tungsten sub-oxides are corner-sharing WO_6 octahedra. The WO_3 parent phase structure varies with temperature but at room temperature it has a perovskite-like ReO_3 structure[63] made up of corner-sharing WO_6 octahedra (known as the γ-phase which is stable from 17-330 ^oC). It can be considered as the perovskite ABO_3 structure without the large A cation. Each octahedron is connected to 6 neighbours to form a 3-dimensional network of W-O bonds, shown in Figure 1.8. Tilting of the octahedra means that there is deviation from cubic symmetry to become monoclinic with the $P2_1/n$ space group. The tilting means that infinite zig-zag chains of W-O bonds are formed in all three directions with W-O-W angles of 158^o and O-W-O angles of 166^o. The off-centre W positions give W-O bonds lengths varying from 1.72 to 2.16 Å[63].

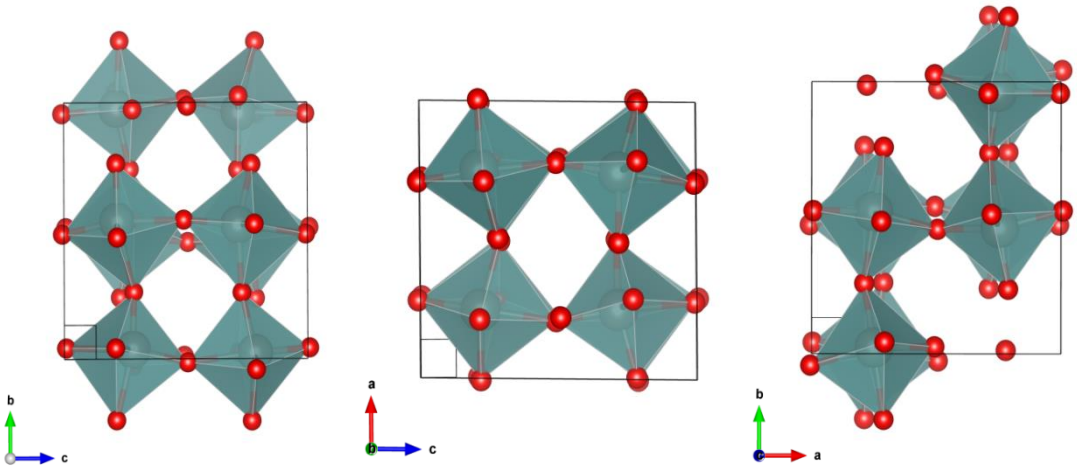

Figure 1.8 – Polyhedral representation of the crystal structure of WO_3 showing tilted WO_6 octahedra along all 3 crystallographic axes.

When oxygen atoms are removed from this structure, a number of tungsten atoms will have fewer than the ideal number of corner-sharing bonds and will be left 'under-bonded'. As Magneli first described[64], this issue is resolved by a shift of units of octahedra in order to form bonds with the 'exposed' tungsten atoms once again. These octahedra are now edge-

sharing and these distinct sections of edge-sharing octahedra form at regular intervals parallel to each other throughout the bulk corner-sharing structure to give the crystallographic shear (CS) structure (Figure 1.9). They become closer together as the level of reduction increases i.e. the less oxygen present in the structure the more frequently the shear planes occur. Booth *et. al.* have identified two structural families in this composition range[65]. These are phases in which the CS planes lie along either the [102] or [103] plane within the structure and form homologous series with general formulas of W_nO_{3n-1} and W_nO_{3n-2} respectively[66]. The limit of this CS structure is thought to be at a O:W ratio of 2.85 i.e. when x = 0.15.

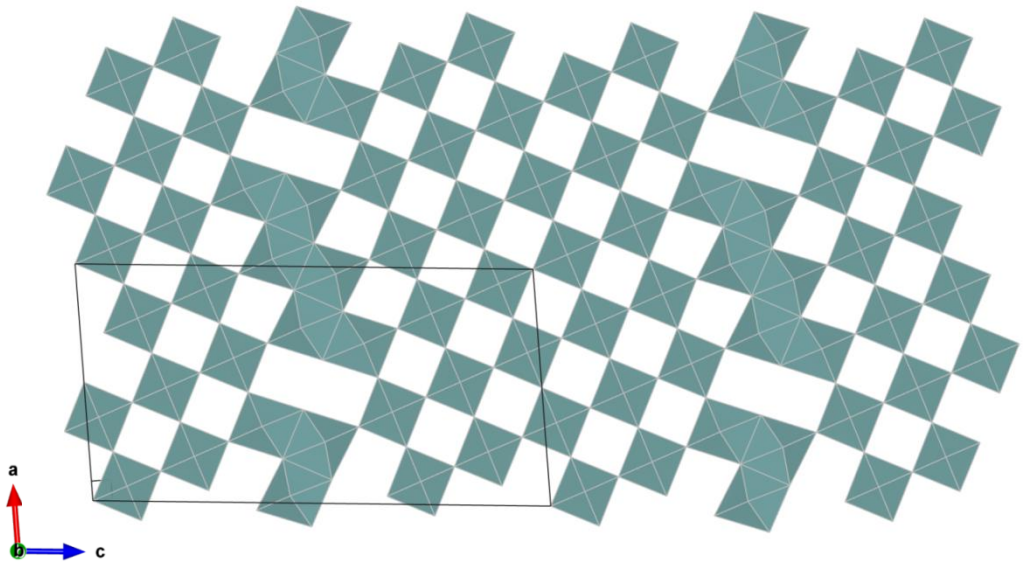

Figure 1.9 - Polyhedral representation of the crystal structure of $WO_{2.9}$ viewed along the b-axis showing [102] crystallographic shear planes.

At greater degrees of reduction, the shear plane structure is destabilised and columnar structure forms. Only two phases with this structure are known, $W_{24}O_{68}$ and $W_{18}O_{49}$ corresponding to x values of 0.166 and 0.28 respectively[65]. The range of x in WO_{3-x} is thought to be $0.08 < x < 0.375$[67] although there are reports of phases with x as low as 0.03[68]. $W_{18}O_{49}$ is reportedly the only phase in the WO_{3-x} family which can be isolated in pure form[69] and so will be concentrated on in this work. Like the previous CS phases, this phase is also made up of both corner- and edge-sharing distorted octahedra but they are linked in such a way to form pentagonal columns which are linked together laterally leaving hexagonal tunnels along the *b*-axis parallel to the columns. The pentagonal columns and hexagonal channels are both evident in the structure in Figure 1.10 viewed along the *b*-axis.

The one dimensional structure makes this phase highly anisotropic and when synthesised - it tends to crystallise as needles or rods with the *b*-axis (010) as the growth direction.

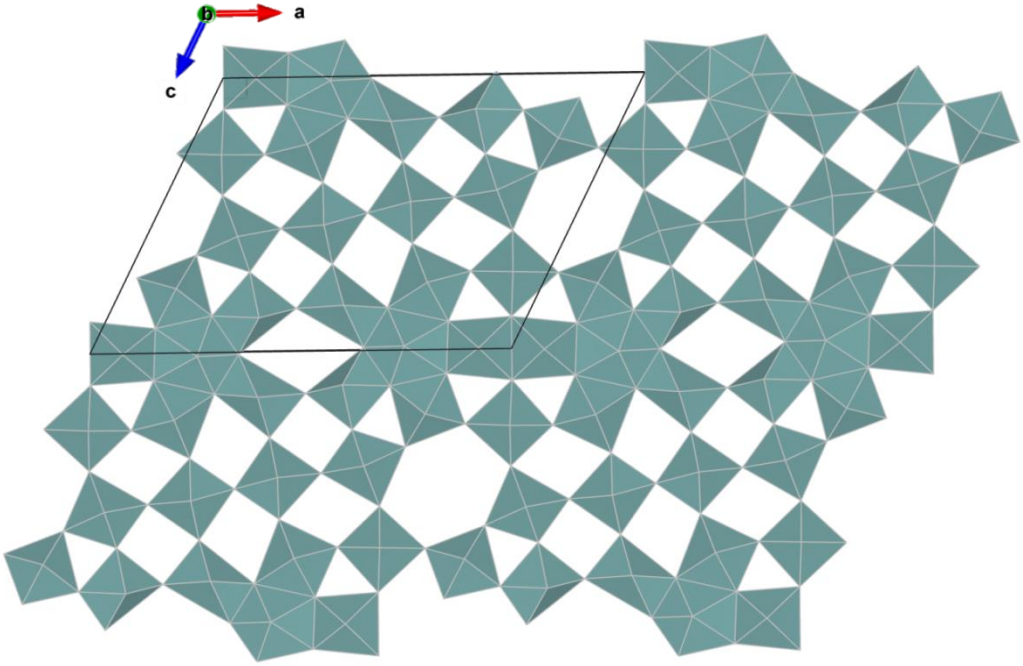

Figure 1.10 - Polyhedral representation of the structure of $W_{18}O_{49}$ viewed along the b-axis showing pentagonal columns and hexagonal channels.

1.8.2.3 Synthesis

Many different synthetic approaches have been used over the years to make tungsten sub-oxides, particularly $W_{18}O_{49}$. High temperature vapour phase routes were used by Berak and Sienko in 1970 to produce single crystals of WO_{3-x} phases by heating tungsten trioxide at 1320 ^{o}C for eight days then at 1022 ^{o}C for a further five days under a reducing atmosphere[70]. Chen *et. al.* thermally treated sputter-deposited tungsten films at 700-850 ^{o}C to obtain dense nanowires[71]. A number of other groups have also used tungsten metal as a precursor[72].

There has been interest in nano-structured $W_{18}O_{49}$ for use in a range of applications including electrochromic windows, gas sensors, optical devices and photocatalysts[73]. A microwave-enhanced chemical vapour deposition technique was used by Hsieh and co-workers in 2011[74] resulting in $W_{18}O_{49}$ "nanoslabs". In the same year Liu *et. al.* used a thermal evaporation method at 800-900 ^{o}C to obtain dense nanowires[75]. Zhu *et. al.* produced "microtrees" of impure $W_{18}O_{49}$ by heating a tungsten foil to 1600 ^{o}C under an applied current in an argon atmosphere[76]. A colloidal route by Lee and co-workers using

$W(CO)_6$, $Me_3NO{:}2H_2O$ and oleylamine heated to 270 ^oC in a Schlenk vessel yielded thin nanowires[62a]. Wang *et. al.* annealed and oxidised sputter-deposited WC_x films to produce small nanorods[77].

More attention has also been given to solvothermal routes in recent years. In 2003 Lou and Zeng used an inorganic route to obtain single crystalline nanorods[73]. Choi *et. al.* used a simple route using WCl_6 as a starting material and heating it at 200 ^oC in an autoclave for 10 h with ethanol acting simultaneously as the solvent and mild reducing agent to form $W_{18}O_{49}$ nanorods. Guo *et. al.* used a two-step hydrothermal process by synthesising ammonium tungsten oxide at 200 ^oC then annealing the product at 500 ^oC under a reducing atmosphere to form $W_{18}O_{49}$[78]. More recently they have developed a simpler route using alcohols and the morphology of the $W_{18}O_{49}$ products was controlled by adjusting the amount and nature of the reactants[79]. Bai *et. al.* have also used a simple alcohol-based route combined with a cooling step to give networks of $W_{18}O_{49}$ nanowires[80]. Clearly these mild, simple one-step synthetic routes are extremely promising for larger scale applications and are more environmentally friendly. They also allow for facile nanostructure tuning – as well as the common nanorods, nanospheres[79] and even 'nanourchins'[81] have been made. However one-dimensional nanostructures offer the greatest number of practical applications. Both solvothermal and solid state routes will be used in this project.

1.8.2.4 Properties

Optically the same colour change is observed when WO_3 is doped with an alkali metal or reduced to WO_{3-x}. In each case an amount of the W^{6+} cations are reduced to W^{5+} which acts as a chromophore so the pale green WO_3 turns deep blue. This dramatic colour change has led to applications in electrochromic materials[82]. The blue colour can been seen somewhat as an indication of NIR absorption because the absorption peak in the NIR region extends some way out into the red and green regions of the visible spectrum making the compounds appear blue.

WO_3 has a large band gap of 2.6-3.6 eV and so can be used for photocatalytic applications. Introducing oxygen vacancies reduces the band gap and shifts the absorption edge to lower energies i.e. from the visible into the near infra-red[83]. $W_{18}O_{49}$ is found to have much stronger absorption than the less reduced phases like $W_{25}O_{73}$[39]. As the oxygen deficiencies

are introduced, defects are created and electrons are introduced into the conduction band (two electrons for each missing oxygen).

The mechanisms of NIR absorption are similar in nature to those of the tungsten bronzes. There was much discussion in the past but now the generally accepted models are those of small polaron absorption and LSPR. It has been widely known that charge carriers form polarons in tungsten suboxide phases[84]. However in 1981 Iguchi *et. al.* calculated that the maximum degree of reduction that can occur before overlap of polaron wavefunctions is $W_{20}O_{58}$ ($WO_{2.9}$)[85] and Salje and Guttler[86] state that the maximum concentration of polarons corresponds to a composition of $WO_{2.85}$. For more reduced compounds, half the charge carriers are densely packed polarons and the rest exist as free carriers so both polaron hopping and LSPR occur when samples are irradiated.

Nanorods of $W_{18}O_{49}$ also have high mechanical strength which makes them suitable for applications like scanning tunnelling microscope tips[72a]. The presence or absence of oxygen in the WO_x structure has a large effect on conductivity which leads to use of these materials as sensors for oxygen-containing gases[87].

1.8.3 Copper Phosphates

Phosphates are commonly found in nature, for example in minerals or in bones. They are biologically important and form a wide range of salts and acids. Phosphate compounds are built up of the basic $[PO_4]^{3-}$ tetrahedron arranged into different structural units. Compounds containing lone tetrahedra are known as orthophosphates and $[P_2O_7]^{4-}$ diphosphate units form so-called 'pyrophosphates'. Cyclic phosphates (also known as metaphosphates) contain larger groups of corner-linked tetrahedra but are relatively rare, as are species that have had an oxygen atom substituted by fluorine[88] or units containing boron[89]. Examples of phosphate structural units are shown in Figure 1.11.

Phosphate 'polymers' are also known with the tetrahedra corner-linked into long chains. The counter-ion can be almost any cation and there is often more than one in a given compound. Compounds can be amorphous or crystalline, hydrated or anyhydrous. With such structural variation it is unsurprising that many hundreds of phosphate compounds are known. This report will be limited to copper phosphates.

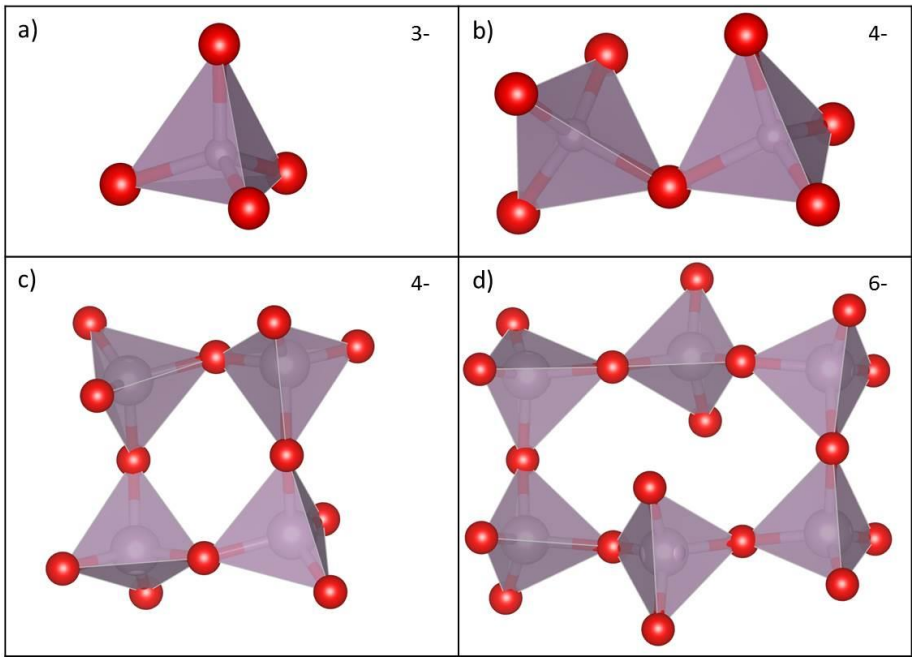

Figure 1.11 - a) the basic PO_4 tetrahedron arranged into b) diphosphate c) and d) some cyclic phosphate structural units. Overall unit charges are shown.

There are known copper phosphates which contain all the structural units mentioned above. In the more common ortho- and diphosphate families, there are a few copper-only compounds (namely $Cu_2(PO_4)(OH)$, $Cu_3(PO_4)_2$ and $Cu_2P_2O_7$) but many contain additional cation species. The majority contain Cu in the 2+ oxidation state, although $CuPO_3$ containing Cu+ has been synthesised[90]. Although many phosphates occur in nature, they have also been synthesised by solid state[91] and solution-based routes[92].

1.8.4 Transparent Conducting Oxide (TCO) materials

Indium tin oxide (ITO) falls into the category of TCO materials. TCO's combine the properties of electrical conductivity and optical transmission, previously thought to be incompatible. Their unique characteristics have resulted in a wide range of applications, particularly in displays, electronics, photovoltaics and smart window technologies[93] which has in turn resulted in an explosion of research in this area. The first known TCO was cadmium oxide, reported in 1907 by Badeker[94] but the majority of modern TCO's are composed of zinc, tin or indium oxide semiconductors which can be heavily doped to give high electronic conductivities. The majority of commercially used TCO's exhibit n-type conductivity with dopant atoms creating donor energy levels below the conduction band. However efforts are also being made to develop viable p-type conductors in order to create transparent semiconductors by overcoming the low hole mobility through the conduction

band[95] and creating p-n junctions. Optical absorbance typically occurs in the ultraviolet region where radiation has enough energy to excite an electron across the bandgap and in the infrared region by interaction of free charge carriers with incident radiation which results in the high visible transmittance. The Handbook of Transparent Conductors[96] gives an excellent overview of the history, applications and properties of TCO's.

1.8.4.1 Tin oxides

ITO is the most widely used TCO material, particularly in optoelectronic devices in which it plays the role of a transparent electrode, typically in the form of a thin film. Doping In_2O_3 with Sn increases its conductivity by contributing an electron to the conduction band for each In^{3+} replaced by a Sn^{4+} cation. There are many more detailed reviews on the properties and synthesis of ITO, for example the one by Granqvist and Hultaker from 2002[28] and references therein. However the sample of ITO characterised in Appendix 1 was a reduced form – i.e. it was non-stoichiometric. While ITO is colourless (or pale green in bulk powder form), the rITO sample was a mid-blue colour so its optical properties are clearly different to those of fully stoichiometric ITO. Reduction introduces more charge carriers in the form of oxygen vacancies so the plasmon edge is shifted to the higher energy NIR range but also overlaps the visible region somewhat giving rise to the blue colour. Despite some desirable properties, the indium oxides will be disregarded for reasons outlined in section 1.4 pertaining to the desire to avoid the use of indium in this project.

SnO_2 is a widely used semiconductor with a wide direct band gap of 3.6 eV and high transmission in the visible range[97]. Doping with species like F^- on the oxygen site or Sb^{5+} on the tin site introduce more charge carriers and increase conductivity. SnO_2 can also be intrinsically doped by the introduction of interstitial Sn cation or oxygen vacancies[98]. The multi-valence of Sn means SnO_2 can tolerate a relatively large amount of non-stoichiometry and this results in electronic conductivity. Fully stoichiometric SnO_2 is an insulator. If SnO_2 can be reduced in the same way as rITO it could be a potential indium-free NIR absorber candidate.

1.8.4.2 Zinc oxides

Zinc oxide has a wide range of uses[99] and zinc is a suitable element for this project as it is abundant, relatively non-toxic and inexpensive. Pure ZnO is largely reflective in the NIR region but like other TCO's, doping alters the optical properties. Intrinsic defects can be

introduced but unlike SnO_2, samples are unstable in ambient conditions so they are unsuitable for most applications[100]. In transparent electrode research, extrinsic dopants are commonly +3 oxidation state metals on the metal lattice sites or -1 oxidation state halogens on the oxygen lattice sites. Looking at trivalent cations, boron-doped ZnO is largely transparent in the NIR region[101]. Aluminium zinc oxide (AZO) has increased IR absorbance compared to ZnO, due to the greater amount of charge carriers available to interact with incident radiation[102] but one sample has been found to be ineffective in Datalase tests. The level of doping could be altered to see if this changes the results. Ga-doped ZnO thin films are essentially transparent, at least up to 850nm[103]. Indium zinc oxide has a lower indium content than ITO but it is also NIR transparent[104].

As for halogen doped materials, one sample of fluorine-doped ZnO has been found to be ineffective by Datalase. Doping with chlorine has been found to blue-shift the absorption peaks even further away from the NIR region[105]. This change is attributed to the Burstein-Moss effect which can cause a blue shift when all the microstates near the conduction band are filled e.g. on addition of a dopant. The Fermi level moves into the conduction band and so more energy is needed to cross the band gap which appears increased[106]. Work on doping with larger halogens is more limited but bromine and iodine appear to have a similar effect on ZnO to chlorine when used as dopants[107].

There have been suggestions that ZnO doped with transition metals could have interesting optical properties[108]. Mn, Cd, and Fe as well as Mg have been used to adjust the bandgap in ZnO nanoparticles[109]. Doping with Mn, Mg and Fe increased the band gap and blue-shifted the absorption spectra into the near-UV region of the spectrum. Cd on the other hand decreases the band gap and causes a red-shift of the absorption peaks. The absorption shifts as far as the visible region of the spectrum using 10% Cd however no information is given beyond 2.2 eV. Conversely another study found that doping ZnO nanorods with Mn caused a red-shift of the UV absorption peak[110]. It is possible that the morphology of the samples has affected the optical properties in this case and lower levels of the dopant were used. In both cases however the absorption edge still does not appear to be near the NIR region although the UV-vis data does not extend into that part of the spectrum so it is difficult to say with certainty.

These materials will all be investigated in more detail in up-coming chapters. Tungsten bronzes are dealt with in Chapters 3 and 4, non-stoichiometric tungsten oxides in Chapter 5, some copper phosphates in Chapter 7 and a number of TCO-like materials in Chapter 8.

1.9 References

1. Walker, T. The History of Print: From Phaistos to 3D. http://www.cartridgesave.co.uk/news/the-history-of-print-from-phaistos-to-3d/. Accessed May 2015.
2. Fox, M., Classical Propagation. In *Optical Properties of Solids*, Oxford University Press: Oxford, 2001.
3. Antonie J.W.G. Visser, O. J. R. Basic Photophysics. http://www.photobiology.info/Visser-Rolinski.html. Accessed April 2015.
4. Bohren, C. F., How can a particle absorb more than the light incident on it? *American Journal of Physics* **1983,** *51* (4), 323-327.
5. Pillai, S.; Catchpole, K. R.; Trupke, T.; Green, M. A., Surface plasmon enhanced silicon solar cells. *J Appl Phys* **2007,** *101* (9), 093105.
6. Lounis, S. D.; Runnerstrom, E. L.; Llordés, A.; Milliron, D. J., Defect Chemistry and Plasmon Physics of Colloidal Metal Oxide Nanocrystals. *The Journal of Physical Chemistry Letters* **2014,** *5* (9), 1564-1574.
7. Stockman, M., Nanoplasmonics: The physics behind the applications. *Physics Today* 2011.
8. Mendelsberg, R. J.; Garcia, G.; Li, H.; Manna, L.; Milliron, D. J., Understanding the Plasmon Resonance in Ensembles of Degenerately Doped Semiconductor Nanocrystals. *The Journal of Physical Chemistry C* **2012,** *116* (22), 12226-12231.
9. Gerlach, E., Carrier scattering and transport in semiconductors treated by the energy-loss method. *Journal of Physics C: Solid State Physics* **1986,** *19* (24), 4585.
10. Anker, J. N.; Hall, W. P.; Lyandres, O.; Shah, N. C.; Zhao, J.; Van Duyne, R. P., Biosensing with plasmonic nanosensors. *Nat Mater* **2008,** *7* (6), 442-453.
11. Llordes, A.; Garcia, G.; Gazquez, J.; Milliron, D. J., Tunable near-infrared and visible-light transmittance in nanocrystal-in-glass composites. *Nature* **2013,** *500* (7462), 323-326.
12. Emin, D., Small Polarons. *Physics Today* 1982.
13. (a) Schirmer, O. F.; Salje, E., The W5+ polaron in crystalline low temperature WO_3 ESR and optical absorption. *Solid State Communications* **1980,** *33* (3), 333-336; (b) Granqvist, C.-G. In *Electrochromic oxides: microstructures and optical properties*, 1993; pp 84-94.
14. Lattice Absorption. http://www.reading.ac.uk/infrared/library/absorptiontheory/ir-absorptiontheory-latticeabsorption.aspx. Accessed July 2015.
15. Alfantazi, A. M.; Moskalyk, R. R., Processing of indium: a review. *Minerals Engineering* **2003,** *16* (8), 687-694.
16. Rhodes, P. C. Indium Shortage Creates problems For Solar Cell Manufacturers. http://oilprice.com/Alternative-Energy/Solar-Energy/Indium-Shortage-Creates-Problems-For-Solar-Cell-Manufacturers.html. Accessed August 2015.
17. Industry, E. C. f. E. a. Critical raw materials for the EU. http://ec.europa.eu/enterprise/policies/raw-materials/files/docs/report-b_en.pdf. Accessed August 2015.
18. Phipps, G.; Mikolajczak, C.; Guckes, T., Indium and Gallium: long-term supply. *Renewable Energy Focus* **2008,** *9* (4), 56-59.
19. Weakley, T. J. R., The crystal structure of ammonium β-octamolybdate pentahydrate. *Polyhedron* **1982,** *1* (1), 17-19.
20. Ma, E., The Thermal Decomposition of Ammonium Polymolybdates. I. *Bulletin of the Chemical Society of Japan* **1964,** *37* (2), 171-175.
21. Ma, E., The Thermal Decomposition of Ammonium Polymolybdates. II. *Bulletin of the Chemical Society of Japan* **1964,** *37* (5), 648-653.
22. Takeda, H.; Kuno, H.; Adachi, K., Solar Control Dispersions and Coatings With Rare-Earth Hexaboride Nanoparticles. *J Am Ceram Soc* **2008,** *91* (9), 2897-2902.

23. (a) Tang, H.; Shen, S.; Guo, J.; Chang, B.; Jiang, X.; Yang, W., Gold nanorods@mSiO_2 with a smart polymer shell responsive to heat/near-infrared light for chemo-photothermal therapy. *J Mater Chem* **2012,** *22* (31), 16095-16103; (b) Guo, C.; Yin, S.; Yu, H.; Liu, S.; Dong, Q.; Goto, T.; Zhang, Z.; Li, Y.; Sato, T., Photothermal ablation cancer therapy using homogeneous Cs_xWO_3 nanorods with broad near-infra-red absorption. *Nanoscale* **2013,** *5* (14), 6469-6478.
24. Wang, L.; Hang, J.; Shi, L.; Sun, X.; Xu, F., Preparation and characterization of NIR cutoff antimony doped tin oxide/hybrid silica coatings. *Mater Lett* **2012,** *87* (0), 35-38.
25. Guo, C.; Yin, S.; Huang, L.; Yang, L.; Sato, T., Discovery of an excellent IR absorbent with a broad working waveband: Cs_xWO_3 nanorods. *Chemical Communications* **2011,** *47* (31), 8853-8855.
26. Adachi, K.; Miratsu, M.; Asahi, T., Absorption and scattering of near-infrared light by dispersed lanthanum hexaboride nanoparticles for solar control filters. *J Mater Res* **2010,** *25* (03), 510-521.
27. Cooper, C. T.; Rodriguez, M.; Blair, S.; Shumaker-Parry, J. S., Mid-Infrared Localized Plasmons through Structural Control of Gold and Silver Nanocrescents. *The Journal of Physical Chemistry C* **2015,** *119* (21), 11826-11832.
28. Granqvist, C. G.; Hultaker, A., Transparent and conducting ITO films: new developments and applications. *Thin Solid Films* **2002,** *411* (1), 1-5.
29. (a) Dawar, A. L.; Joshi, J. C., Semiconducting transparent thin films: their properties and applications. *Journal of Materials Science* **1984,** *19* (1), 1-23; (b) Russo, D. A.; McKown, C. S.; Roger, C.; Stricker, J. L. Solar-control coating on glass. EP1201616A2, 2002.
30. Cortie, M. B.; Giddings, J.; Dowd, A., Optical properties and plasmon resonances of titanium nitride nanostructures. *Nanotechnology* **2010,** *21* (11), 115201.
31. Wohler, F., *Pogg. Ann.* **1824,** *2*, 350.
32. Laurent, A., *Ann. chim. phys.* **1838,** *67*.
33. Spitzin, *Z. anorg. allgem. Chem.* **1925,** (148).
34. Brunner, Beitrage zur Kenntis der Wolframbronzen. *Dissertation, Zurich* **1903**.
35. (a) Hagg, G., *Z. physik. Chem.* **1935,** *B29*; (b) Hagg, G., *Nature* **1935,** *135*.
36. Straumanis, M. E., *Journal of the American Chemical Society* **1949,** *71*.
37. Lynch, D. W.; Rosei, R.; Weaver, J. H.; Olson, C. G., The optical properties of some alkali metal tungsten bronzes from 0.1 to 38 eV. *J Solid State Chem* **1973,** *8* (3), 242-252.
38. Brown, B. W.; Banks, E., The Sodium Tungsten Bronzes1,2. *Journal of the American Chemical Society* **1954,** *76* (4), 963-966.
39. Takeda, H.; Adachi, K., Near Infrared Absorption of Tungsten Oxide Nanoparticle Dispersions. *J Am Ceram Soc* **2007,** *90* (12), 4059-4061.
40. De Jong, W. F., *Z. Krist.* **1932,** *81*.
41. Magneli, A., Crystal structure of tetragonal potassium bronze. *Arkiv foer Kemi* **1949,** *1*.
42. Magneli, A., Blomberg, B., Contribution to the Knowledge of the Alkali Tungsten Bronzes. *Acta Chem. Scand.* **1951,** *5*.
43. Magneli, A., studies on the Hexagonal Tungsten Bronzes of Potassium, Rubidium and Cesium. *Acta Chem. Scand.* **1953,** *7*.
44. Dickens, P. G.; Whittingham, M. S., The tungsten bronzes and related compounds. *Quarterly Reviews, Chemical Society* **1968,** *22* (1), 30-44.
45. Conroy, L. E.; Yokokawa, T., The Preparation and Properties of a Barium Tungsten Bronze. *Inorganic Chemistry* **1965,** *4* (7), 994-996.
46. Sienko, M. J., Thallium-Tungsten Bronze: A Solid State Defect Structure1. *Journal of the American Chemical Society* **1959,** *81* (21), 5556-5559.
47. Conroy, L. E.; Sienko, M. J., A Copper Analog of the Alkali Tungsten Bronzes. *Journal of the American Chemical Society* **1957,** *79* (15), 4048-4051.

48. McColm, I. J.; Steadman, R.; Howe, A., Preparation, structure, and Mössbauer spectra of tin tungsten bronzes. *J Solid State Chem* **1970,** *2* (4), 555-562.
49. Dobson, M. M.; Hutchison, J. L.; Tilley, R. J. D.; Watts, K. A., The structures of intergrowth tungsten bronzes of Ba, Sn, Pb, and Sb. *J Solid State Chem* **1987,** *71* (1), 47-60.
50. Shipunova, N. T. K., V. V.; Serebrennikov, V. V.; Finkel'shtein, L. D.; Efremova, N. N., *Zhurnal Neorganicheskoi Khimii* **1988,** *33* (11), 2732-2735.
51. Banks, E., Wold, A., Oxide Bronzes. *Preparative Inorganic Reactions* **1968,** *4*.
52. (a) Marley, P. M.; Banerjee, S., Reversible Interconversion of a Divalent Vanadium Bronze between δ and β Quasi-1D Structures. *Inorganic Chemistry* **2012,** *51* (9), 5264-5269; (b) Sasaki, T.; Watanabe, M.; Fujiki, Y., Structure of $K_{1.0}Ti_8O_{16}$ and $K_{0.0}Ti_8O_{16}$. *Acta Crystallographica Section B* **1993,** *49* (5), 838-841; (c) Wadsley, A. D.; Andersson, S., Alkali Metal Titanium Oxide Bronzes. *Nature* **1961,** *192* (4802), 551-552.
53. Hussain, A.; Kihlborg, L., Intergrowth tungsten bronzes. *Acta Crystallographica Section A* **1976,** *32* (4), 551-557.
54. Scheibler, C., *J. Prakt. Chem.* **1861,** *83*.
55. Mamak, M.; Choi, S. Y.; Stadler, U.; Dolbec, R.; Boulos, M.; Petrov, S., Thermal plasma synthesis of tungsten bronze nanoparticles for near infra-red absorption applications. *J Mater Chem* **2010,** *20* (44), 9855-9857.
56. (a) Gu, Z.; Ma, Y.; Zhai, T.; Gao, B.; Yang, W.; Yao, J., A Simple Hydrothermal Method for the Large-Scale Synthesis of Single-Crystal Potassium Tungsten Bronze Nanowires. *Chemistry – A European Journal* **2006,** *12* (29), 7717-7723; (b) Guo, C.; Yin, S.; Dong, Q.; Sato, T., Near-infrared absorption properties of Rb_xWO_3 nanoparticles. *CrystEngComm* **2012,** *14* (22), 7727-7732.
57. (a) Guo, C.; Yin, S.; Huang, L.; Sato, T., Synthesis of One-Dimensional Potassium Tungsten Bronze with Excellent near-Infrared Absorption Property. *ACS Applied Materials & Interfaces* **2011,** *3* (7), 2794-2799; (b) Guo, C.; Yin, S.; Zhang, P.; Yan, M.; Adachi, K.; Chonan, T.; Sato, T., Novel synthesis of homogenous Cs_xWO_3 nanorods with excellent NIR shielding properties by a water controlled-release solvothermal process. *J Mater Chem* **2010,** *20* (38), 8227-8229.
58. Liu, G.; Wang, S.; Nie, Y.; Sun, X.; Zhang, Y.; Tang, Y., Electrostatic-induced synthesis of tungsten bronze nanostructures with excellent photo-to-thermal conversion behavior. *Journal of Materials Chemistry A* **2013**.
59. Mattox, T. M.; Bergerud, A.; Agrawal, A.; Milliron, D. J., Influence of Shape on the Surface Plasmon Resonance of Tungsten Bronze Nanocrystals. *Chem Mater* **2014,** *26* (5), 1779-1784.
60. Stanley, R. K.; Morris, R. C.; Moulton, W. G., Conduction properties of the hexagonal tungsten bronze, Rb_xWO_3. *Physical Review B* **1979,** *20* (5), 1903-1914.
61. Adachi, K.; Asahi, T., Activation of plasmons and polarons in solar control cesium tungsten bronze and reduced tungsten oxide nanoparticles. *J Mater Res* **2012,** *27* (06), 965-970.
62. (a) Lee, K.; Seo, W. S.; Park, J. T., Synthesis and Optical Properties of Colloidal Tungsten Oxide Nanorods. *Journal of the American Chemical Society* **2003,** *125* (12), 3408-3409; (b) Guo, C.; Yin, S.; Dong, Q.; Sato, T., Simple route to $(NH_4)_xWO_3$ nanorods for near infrared absorption. *Nanoscale* **2012,** *4* (11), 3394-3398.
63. Loopstra, B. O.; Boldrini, P., Neutron diffraction investigation of WO_3. *Acta Crystallographica* **1966,** *21* (1), 158-162.
64. Magneli, A., Structures of the ReO_3-type with recurrent dislocations of atoms: `homologous series' of molybdenum and tungsten oxides. *Acta Crystallographica* **1953,** *6* (6), 495-500.
65. Booth, J.; Ekström, T.; Iguchi, E.; Tilley, R. J. D., Notes on phases occurring in the binary tungsten-oxygen system. *J Solid State Chem* **1982,** *41* (3), 293-307.

66. Pickering, R.; Tilley, R. J. D., An electron microscope study of tungsten oxides in the composition range $WO_{2.90}$-$WO_{2.72}$. *J Solid State Chem* **1976,** *16* (3–4), 247-255.
67. Migas, D. B.; Shaposhnikov, V. L.; Borisenko, V. E., Tungsten oxides. II. The metallic nature of Magneli phases. *J Appl Phys* **2010,** *108* (9).
68. Magneli, A., Non-stoichiometry and Structural Disorder in some families of inorganic compounds. *Pure and Appl. Chem.* **1978,** *50*.
69. Remškar, M.; Kovac, J.; Viršek, M.; Mrak, M.; Jesih, A.; Seabaugh, A., W_5O_{14} Nanowires. *Advanced Functional Materials* **2007,** *17* (12), 1974-1978.
70. Berak, J. M.; Sienko, M. J., Effect of oxygen-deficiency on electrical transport properties of tungsten trioxide crystals. *J Solid State Chem* **1970,** *2* (1), 109-133.
71. Chao-Hsuing, C.; Shui-Jinn, W.; Rong-Ming, K.; Yi-Cheng, K.; Kai-Ming, U.; Tron-Min, C.; Bor-Wen, L.; Hao-Yi, T., The influence of oxygen content in the sputtering gas on the self-synthesis of tungsten oxide nanowires on sputter-deposited tungsten films. *Nanotechnology* **2006,** *17* (1), 217.
72. (a) Gu, G.; Zheng, B.; Han, W. Q.; Roth, S.; Liu, J., Tungsten Oxide Nanowires on Tungsten Substrates. *Nano Lett* **2002,** *2* (8), 849-851; (b) Kun, L.; David, T. F.; Lawrence, S., Easy growth of undoped and doped tungsten oxide nanowires with high purity and orientation. *Nanotechnology* **2005,** *16* (1), 10; (c) Jin, Y. Z.; Zhu, Y. Q.; Whitby, R. L. D.; Yao, N.; Ma, R.; Watts, P. C. P.; Kroto, H. W.; Walton, D. R. M., Simple Approaches to Quality Large-Scale Tungsten Oxide Nanoneedles. *The Journal of Physical Chemistry B* **2004,** *108* (40), 15572-15577; (d) Cho, M. H.; Park, S. A.; Yang, K. D.; Lyo, I. W.; Jeong, K.; Kang, S. K.; Ko, D. H.; Kwon, K. W.; Ku, J. H.; Choi, S. Y.; Shin, H. J., Evolution of tungsten-oxide whiskers synthesized by a rapid thermal-annealing treatment. *Journal of Vacuum Science & Technology B: Microelectronics and Nanometer Structures* **2004,** *22* (3), 1084-1087.
73. Lou, X. W.; Zeng, H. C., An Inorganic Route for Controlled Synthesis of $W_{18}O_{49}$ Nanorods and Nanofibers in Solution. *Inorganic Chemistry* **2003,** *42* (20), 6169-6171.
74. Yun Tsung, H.; Sen Hung, H.; Uei Shin, C.; Meng Wen, H.; Han, C. S., Synthesis of Tungsten Oxide Nanoslab Bundles by Microwave Plasma-Enhanced Chemical Vapor Deposition. *Jpn J Appl Phys* **2011,** *50* (1S1), 01AB05.
75. Liu, F.; Mo, F. Y.; Jin, S. Y.; Li, L.; Chen, Z. S.; Sun, R.; Chen, J.; Deng, S. Z.; Xu, N. S., A novel lift-off method for fabricating patterned and vertically-aligned $W_{18}O_{49}$ nanowire arrays with good field emission performance. *Nanoscale* **2011,** *3* (4), 1850-1854.
76. Zhu, Y. Q.; Hu, W.; Hsu, W. K.; Terrones, M.; Grobert, N.; Hare, J. P.; Kroto, H. W.; Walton, D. R. M.; Terrones, H., Tungsten oxide tree-like structures. *Chemical Physics Letters* **1999,** *309* (5–6), 327-334.
77. Wang, S.-J.; Chen, C.-H.; Ko, R.-M.; Kuo, Y.-C.; Wong, C.-H.; Wu, C.-H.; Uang, K.-M.; Chen, T.-M.; Liou, B.-W., Preparation of tungsten oxide nanowires from sputter-deposited WC_x films using an annealing/oxidation process. *Appl Phys Lett* **2005,** *86* (26), 263103.
78. Guo, C.; Yin, S.; Huang, Y.; Dong, Q.; Sato, T., Synthesis of $W_{18}O_{49}$ Nanorod via Ammonium Tungsten Oxide and Its Interesting Optical Properties. *Langmuir* **2011,** *27* (19), 12172-12178.
79. Guo, C.; Yin, S.; Yan, M.; Kobayashi, M.; Kakihana, M.; Sato, T., Morphology-Controlled Synthesis of $W_{18}O_{49}$ Nanostructures and Their Near-Infrared Absorption Properties. *Inorganic Chemistry* **2012,** *51* (8), 4763-4771.
80. Bai, H.; Su, N.; Li, W.; Zhang, X.; Yan, Y.; Li, P.; Ouyang, S.; Ye, J.; Xi, G., $W_{18}O_{49}$ nanowire networks for catalyzed dehydration of isopropyl alcohol to propylene under visible light. *Journal of Materials Chemistry A* **2013,** *1* (20), 6125-6129.
81. Guo, C.; Yin, S.; Dong, Q.; Sato, T., The near infrared absorption properties of $W_{18}O_{49}$. *RSC Advances* **2012,** *2* (12), 5041-5043.
82. Granqvist, C. G., Electrochromic tungsten oxide films: Review of progress 1993–1998. *Solar Energy Materials and Solar Cells* **2000,** *60* (3), 201-262.

83. Migas, D. B.; Shaposhnikov, V. L.; Rodin, V. N.; Borisenko, V. E., Tungsten oxides. I. Effects of oxygen vacancies and doping on electronic and optical properties of different phases of WO_3. *J Appl Phys* **2010,** *108* (9).
84. Viswanathan, K.; Brandt, K.; Salje, E., Crystal structure and charge carrier concentration of $W_{18}O_{49}$. *J Solid State Chem* **1981,** *36* (1), 45-51.
85. Iguchi, E.; Salje, E.; Tilley, R. J. D., Polaron interaction energies in reduced tungsten trioxide. *J Solid State Chem* **1981,** *38* (3), 342-359.
86. Salje, E.; Güttler, B., Anderson transition and intermediate polaron formation in WO_{3-x} Transport properties and optical absorption. *Philosophical Magazine Part B* **1984,** *50* (5), 607-620.
87. Galatsis, K.; Li, Y. X.; Wlodarski, W.; Comini, E.; Sberveglieri, G.; Cantalini, C.; Santucci, S.; Passacantando, M., Comparison of single and binary oxide MoO_3, TiO_2 and WO_3 sol–gel gas sensors. *Sensors and Actuators B: Chemical* **2002,** *83* (1–3), 276-280.
88. Begley, M. J.; Dove, M. F. A.; Hibbert, R. C.; Logan, N.; Nunn, M.; Sowerby, D. B., Crystal structures of the difluorophosphate complexes, $Co(O_2PF_2)_2.2MeCN$ and $Cu(O_2PF_2)_2$. *Journal of the Chemical Society, Dalton Transactions* **1985,** (11), 2433-2436.
89. Zheng, J.; Zhang, A., An open-framework borophosphate, $LiCu_2BP_2O_8(OH)_2$. *Acta Crystallographica Section E* **2009,** *65* (5), i40.
90. Ball, M. C., Phase-equilibrium relationships in the systems $CuO-P_2O_5$ and $Cu_2O-P_2O_5$. *Journal of the Chemical Society A: Inorganic, Physical, Theoretical* **1968,** (0), 1113-1115.
91. (a) Shoemaker, G. L.; Anderson, J. B.; Kostiner, E., Copper(II) phosphate. *Acta Crystallographica Section B* **1977,** *33* (9), 2969-2972; (b) Bamberger, C. E.; Specht, E. D.; Anovitz, L. M., Crystalline Copper Phosphates: Synthesis and Thermal Stability. *J Am Ceram Soc* **1997,** *80* (12), 3133-3138.
92. Robertson, B. E.; Calvo, C., The crystal structure and phase transformation of α-$Cu_2P_2O_7$. *Acta Crystallographica* **1967,** *22* (5), 665-672.
93. Ginley, D. S.; Perkins, J. D., Transparent Conductors
Handbook of Transparent Conductors. Ginley, D. S., Ed. Springer US: 2010; pp 1-25.
94. Badeker, K., *Ann. Phys. (Leipzig)* **1907,** *22*, 749.
95. Hosono, H., Non-conventional Materials
Handbook of Transparent Conductors. Ginley, D. S., Ed. Springer US: 2010; pp 313-351.
96. Kykyneshi, R.; Zeng, J.; Cann, D. P., Transparent Conducting Oxides Based on Tin Oxide
Handbook of Transparent Conductors. Ginley, D. S., Ed. Springer US: 2010; pp 171-191.
97. Moharrami, F.; Bagheri-Mohagheghi, M. M.; Azimi-Juybari, H.; Shokooh-Saremi, M., Structural, electrical, optical, thermoelectrical and photoconductivity properties of the SnO_2–Al_2O_3 binary transparent conducting films deposited by the spray pyrolysis method. *Physica Scripta* **2012,** *85* (1), 015703.
98. Kılıç, Ç.; Zunger, A., Origins of Coexistence of Conductivity and Transparency in SnO_2. *Phys Rev Lett* **2002,** *88* (9), 095501.
99. Ozgur, U.; Alivov, Y. I.; Liu, C.; Teke, A.; Reshchikov, M. A.; Dogan, S.; Avrutin, V.; Cho, S. J.; Morkoc, H., A comprehensive review of ZnO materials and devices. *J Appl Phys* **2005,** *98* (4).
100. Ellmer, K., Transparent Conductive Zinc Oxide and Its Derivatives
Handbook of Transparent Conductors. Ginley, D. S., Ed. Springer US: 2010; pp 193-263.
101. (a) Kumar, V.; Singh, R. G.; Singh, F.; Purohit, L. P., Highly transparent and conducting boron doped zinc oxide films for window of Dye Sensitized Solar Cell applications. *J Alloy Compd* **2012,** *544* (0), 120-124; (b) Lokhande, B. J.; Patil, P. S.; Uplane, M. D., Studies on structural, optical and electrical properties of boron doped zinc oxide films prepared by spray pyrolysis technique. *Physica B: Condensed Matter* **2001,** *302–303* (0), 59-63.

102. Li, C. D.; Lv, J. P.; Liang, Z. Q., Effects of Al doping on the optical and electrical properties of pre-synthesized ZnO powders by solid state method. *J Mater Sci-Mater El* **2012,** *23* (9), 1673-1677.
103. Shinde, S. S.; Shinde, P. S.; Oh, Y. W.; Haranath, D.; Bhosale, C. H.; Rajpure, K. Y., Structural, optoelectronic, luminescence and thermal properties of Ga-doped zinc oxide thin films. *Appl Surf Sci* **2012,** *258* (24), 9969-9976.
104. Kumar, B.; Gong, H.; Akkipeddi, R., High mobility undoped amorphous indium zinc oxide transparent thin films. *J Appl Phys* **2005,** *98* (7).
105. Yousefi, R.; Jamali-Sheini, F., Effect of chlorine ion concentration on morphology and optical properties of Cl-doped ZnO nanostructures. *Ceram Int* **2012,** *38* (7), 5821-5825.
106. (a) Burstein, E., Anomalous Optical Absorption Limit in Insb. *Phys Rev* **1954,** *93* (3), 632-633; (b) Moss, T. S., The Interpretation of the Properties of Indium Antimonide. *P Phys Soc Lond B* **1954,** *67* (418), 775-782.
107. Tao, Z.; Yu, X.; Fei, X.; Liu, J.; Zhao, Y.; Wu, H.; Yang, G.; Yang, S.; Yang, L., Synthesis and optical properties of halogen-doped ZnO phosphor. *Mater Lett* **2008,** *62* (17–18), 3018-3020.
108. (a) Jin, Z. W.; Yoo, Y. Z.; Sekiguchi, T.; Chikyow, T.; Ofuchi, H.; Fujioka, H.; Oshima, M.; Koinuma, H., Blue and ultraviolet cathodoluminescence from Mn-doped epitaxial ZnO thin films. *Appl Phys Lett* **2003,** *83* (1), 39-41; (b) Liu, M.; Kitai, A. H.; Mascher, P., Point defects and luminescence centres in zinc oxide and zinc oxide doped with manganese. *Journal of Luminescence* **1992,** *54* (1), 35-42.
109. Wang, Y. S.; Thomas, P. J.; O'Brien, P., Optical Properties of ZnO Nanocrystals Doped with Cd, Mg, Mn, and Fe Ions. *The Journal of Physical Chemistry B* **2006,** *110* (43), 21412-21415.
110. Guo, Y.; Cao, X.; Lan, X.; Zhao, C.; Xue, X.; Song, Y., Solution-Based Doping of Manganese into Colloidal ZnO Nanorods. *The Journal of Physical Chemistry C* **2008,** *112* (24), 8832-8838.

Chapter 2

Methodology

2.1 Introduction

A range of experimental techniques have been used during the course of this project for sample synthesis, characterisation and analysis. These will be described here, as will the development of the commercial laser imaging testing protocol used to assess the performance of samples as near infrared absorbers.

2.2 Synthesis

2.2.1 Solid State Synthesis

The solid state synthesis technique is one of the most traditional but also the most reliable in modern chemistry[1]. Reactants are usually metal oxides or carbonates which are carefully weighed before being mixed together in powder form - commonly by milling or hand grinding - then heated in an electric furnace. Mixing is important to encourage sample homogeneity and powders are often pressed into pellets in order to promote reaction via close proximity of reactants. Alumina crucibles are generally used to hold samples during heating but crucibles of other materials like platinum or zirconia are available for samples that would react with alumina. The heating step can take place in a range of atmospheres – in air, in vacuum or in the presence of a gas that is inert, oxidising or reducing. Gas atmospheres can be static or flowing depending on the design of furnace used. Box furnaces are used for static air heating while tube furnaces are employed for reactions requiring flowing gas. Frequently subsequent remixing and reheating steps are required to obtain a pure product.

This technique offers excellent control over product stoichiometry – the amount of reactants can be calculated precisely from balanced chemical equations and measured out accordingly. A series of samples with increased levels of doping for example can be accurately made this way. Drawbacks of this method include the high temperatures and long heating times required, multiple steps which can be time consuming and the need for reagents of high purity which can be expensive. The method is inherently slow due to the huge amount of inhomogeneity at an atomic level even if the reactant particles seem well

mixed. Nucleation of the crystals of the product phase can occur readily at reactant interfaces however formation of the product creates a barrier to further product formation[1]. Reactants are now separated by a product layer and have further to diffuse in order to react so the rate of reaction slows. It is often necessary to regrind and reheat mixtures several times to ensure a reaction goes to completion.

In this work, all furnaces were electric Carbolite tube or box furnaces depending whether a gas flow was required or not. When vacuum conditions were required, samples were placed into either quartz or Pyrex tubes which were evacuated using a high vacuum line with a turbo pump. The tubes were sealed closed using a gas-oxygen blow torch and then placed into furnaces. When required, pellets were formed using cylindrical Specac pellet dies of required diameter and a Specac hydraulic press using 1-3 tons of pressure for a short amount of time. When required, planetary ball milling was carried out using a Fritsch Pulverisette 7 mill with zirconia balls.

2.2.2 Solvothermal Synthesis

Solvothermal synthesis has been defined as "a chemical reaction in a closed system in the presence of a solvent (aqueous and non-aqueous solution) at a temperature higher than that of the boiling point of such a solvent"[2]. Using this method in practice, one takes reactants which are placed in a solvent and heated under autogenous or applied pressure in a steel autoclave. Water is commonly used as the solvent and thus hydrothermal synthesis forms a significant subset of solvothermal synthesis. Metal oxides can be synthesised using water as a solvent but for non-oxides such as chalcogenides or sulphides it is necessary to use non-aqueous solvents. A number of chemical and thermodynamic parameters can be easily varied, for example reactant concentration, solvent mixture, oven temperature, reaction time, pressure etc. so these routes can lead to control of product size, shape, crystallinity, composition and so on. Solvothermal synthesis routes have become more popular in recent decades as advantages such as lower synthesis temperatures and novel particle morphologies have become apparent. New material applications have resulted from known compounds being synthesised in new forms, usually on the nanoscale. Solvothermal synthesis is an increasingly viable way of making homogeneous crystalline nanoparticulate products via 'one pot' reactions using green solvents and low reaction temperatures.

All solvothermal syntheses in this work were carried out in general purpose steel reaction vessels (4750 series) from Parr Instrument Company used with Teflon liners of 120ml internal volume. Unless stated otherwise, the ovens used were Carbolite electric convection ovens. These were used for both reactions and drying of products. All H_2O used was distilled. Centrifugation was carried out using a Thermo Scientific Heraeus Multifuge X1 at 12000 rpm for 10 minutes and repeated three times.

2.3 Characterisation

2.3.1 Powder X-ray Diffraction (PXRD)

PXRD is one of the most important characterisation techniques for crystalline materials. The data resulting from these measurements contain a wealth of information about sample composition, phase, purity, crystallinity and crystallite size. X-rays are generated by bombarding a metal target with a high-energy electron beam. It collides with and expels electrons from the inner shells of atoms causing another electron to drop down from a higher level to fill the gap and in the process it emits excess energy as X-ray radiation. The wavelength of X-rays (around 10^{-10} m) is comparable to the spacing between lattice planes within a crystal so it was realised in the early twentieth century that they could be used to probe crystalline structures.

One of the key relations for XRD is Bragg's Law, written as:

$$\lambda = 2d_{hkl}\, sin\, \theta \qquad (14)$$

This relates the separation of the lattices planes, d_{hkl}, to the angle, ϑ, and wavelength, λ, of an incoming X-ray beam. If the angle of incidence results in constructive interference of X-rays reflected off different lattice planes then a bright reflection will be observed. Rays that interfere destructively are not observed.

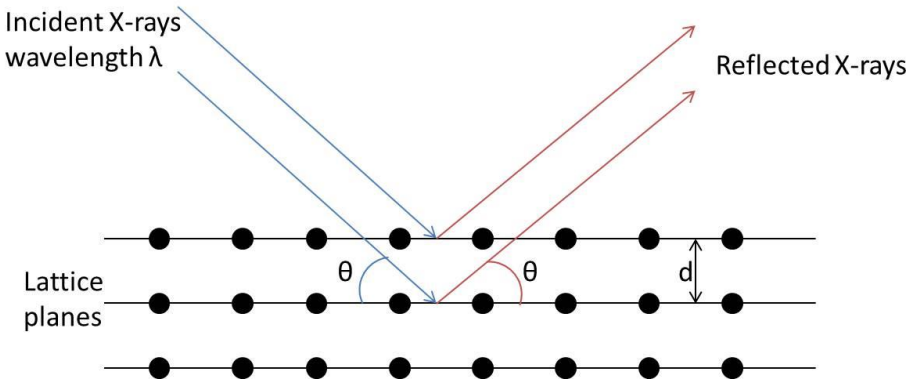

Figure 2.1 - Illustration of the principles behind Bragg's Law.

Parallel lattice planes are labelled by Miller indices hkl which define the reciprocal of the axial intercepts of the planes with the unit cell. X-rays diffracted by a single crystal form a pattern of spots on a detector resulting from individual reflections whereas polycrystalline powder samples have crystallites lying at all possible angles so the diffracted beams form a cone of intensity for each plane (hkl). Data are presented as peaks of certain intensity at a corresponding angle, 2θ. Bragg's Law is used to determine the plane of atoms which has given rise to each diffraction peak. Indexing the peaks in this way gives the dimensions of the unit cell. The intensity of the peaks gives information about constructive and destructive interference of beams diffracted from different lattice planes which is dependent on individual scattering strengths of atoms in the crystal. Heavier atoms with more electrons will diffract more strongly than smaller ones.

For PXRD, the Debye-Scherrer method is commonly used and involves using monochromatic radiation and rotating the detector in the plane of the incident beam to give full cones of diffraction. Comparison of X-ray patterns to a large international database of Powder Diffraction Files (PDFs) provides a straightforward method for phase identification. PXRD measurements in this work were performed on a Bruker D8 diffractometer with monochromated Cu Kα radiation of 1.54 Å in transmission mode from 10-60^{o} 2θ. Graphical representations of crystal structures were created using Vesta (Visualisation for Electronic and STructural Analysis) software[3]. Rietveld and Pawley refinements were carried out using jEdit software to input code to Topas Academic V5[4].

2.3.2 UV-vis-NIR Spectroscopy

Optical spectroscopy is a key analytical technique in this project to assess whether potential NIR absorber materials can absorb in the NIR region of the electromagnetic spectrum (750-2500 nm). UV-vis-NIR data were collected on a Shimadzu UV-vis 2600 single monochromator spectrophotometer between 300 and 1400nm with $BaSO_4$ as a standard and reference. 1400 nm was the upper limit of this machine. Incident light is monochromated by a diffraction grating and a cylindrical quartz powder cell was used to measure samples as dry powders.

A two-detector ISR-2600 integrating sphere attachment was used. This is a hollow sphere with the interior coated in a white diffuse reflective material, in this case $BaSO_4$. The surface exhibits almost perfect Lambertian reflectance i.e. total isotropic diffuse reflectance. This means that all the light reflected from the sample will 'bounce' around the

interior of the sphere and will reach the detector. The detector is positioned so it is never directly irradiated. Two detectors are used – one in the visible region from 300-850 nm and one in the NIR region from 850-1400 nm. Compared to other configurations, the intensity of detected light is reduced when using an integrating sphere which can increase the amount of noise in a measurement. To prevent this, the widest slit width (5nm) on the spectrophotometer was used. A representation of the spectrophotometer set-up is shown in Figure 2.2, taken from the Shimadzu website[5].

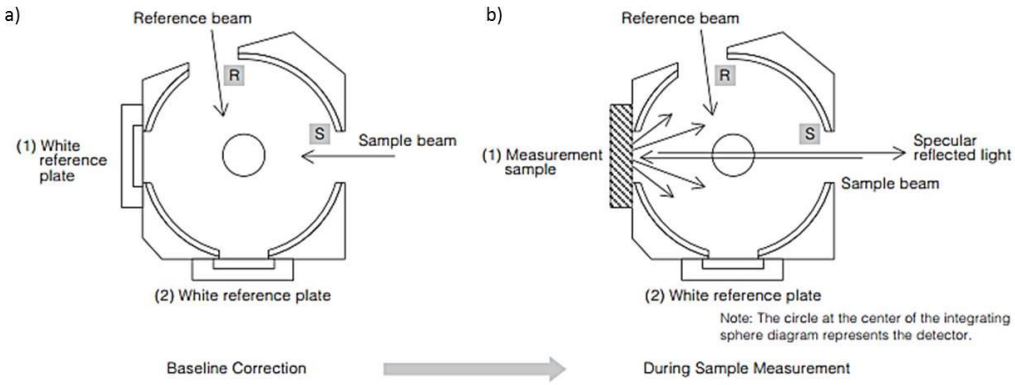

Figure 2.2 - Representation of the diffuse reflectance measurement set-up using an integrating sphere: a) A $BaSO_4$ white reference is attached at position (1) and the baseline is measured b) the white reference plate is replaced by the sample and diffuse reflectance is measured. Any specularly reflected light exits via the inlet port and is not detected. Adapted from reference 5.

Transmittance is defined as the amount of incident light (I_0) that passes through a sample and is detected (I_t) so can be defined:

$$T = \frac{I_t}{I_0} \qquad (15)$$

Values are usually given as percentages. Transmittance through an opaque solid sample is assumed to be negligible but the light reflectance can be defined in the same way: the amount of the incident light that is reflected off the sample into the detector (I_r).

$$R = \frac{I_r}{I_0} \qquad (16)$$

Reflectance is also given as percentage values. The Beer-Lambert law (discussed in section 1.3.3) defines absorbance as:

$$A = log\frac{I_0}{I} = \varepsilon cl \qquad (17)$$

Where I is the transmitted (or reflected) intensity, ε is the molar absorption (or extinction) coefficient, c is the molar concentration of the absorbing species and l is the path length of

the sample. However substituting R into the equation means that optical absorbance values can be determined indirectly from the reflectance measurements using the relation:

$$A = log\frac{1}{R} = -logR \qquad (18)$$

Absorbance is a dimensionless quality and so arbitrary units (a.u.) are used throughout.

2.3.3 Scanning Electron Micrscopy (SEM)

Microscopy techniques are commonly used to visualise particle size and morphology. During SEM, a focussed electron beam is scanned across the sample and secondary electrons emitted by the sample are detected to create an image. SEM images were recorded with a Hitachi S-4800 field emission scanning electron microscope on samples attached to 15 mm aluminium stubs with sticky carbon tape. A sputter coater was used to deposit a thin layer of gold (5-10 nm) over the samples to improve conductivity in the electron beam. Voltages of 3-5 kV were used with a current of 10 μA.

2.3.4 Energy-dispersive X-ray Spectroscopy (EDX)

An X-ray detector attachment from Oxford Instruments was used in conjunction with the Hitachi S-4800 field emission scanning electron microscope to record EDX data on gold-coated powder samples attached to 15 mm aluminium stubs with sticky carbon tape. The electron beam causes the emission of X-rays from the sample and by recording their characteristic energy, the elements present can be detected.

2.3.5 Thermogravimetric analysis (TGA)

TGA records the mass of a sample as a function of temperature. It can give information about oxidation, reduction or decomposition of a sample as well as desorption of water or other solvents. TGA measurements were taken in an alumina pan using a TA Instruments SDT Q600 thermogravimetric instrument from room temperature to 600-900 ^{o}C with a ramp rate of 10 ^{o}C/min under flowing bottled air. An empty pan was used as a reference and data are plotted as the weight % against temperature.

2.3.6 Fourier transform infrared spectroscopy (FTIR)

Vibrational energy levels were discussed briefly in section 1.3.3. For molecular vibrations to be infrared active and therefore detectable by FTIR, they need to obey a selection rule. Namely, when atoms are displaced relative to each other, there must be a change in the electric dipole moment of the molecule. For example, a symmetric stretch in a symmetric molecule (e.g. N_2) is inactive as there is no overall change in dipole moment but the same

stretch would be active in a non-symmetric molecule (like NO). A non-linear molecule composed of N atoms will have 3N-6 independent vibrational modes. These correspond to different stretches and 'wagging' of atoms around the equilibrium position of their bonds. Each active mode has a characteristic frequency which can be detected and assigned. A JASCO FT-IR-4200 was used to collect data from powder samples in this project.

2.3.7 BET method for measuring surface area

The BET technique is commonly used for measuring the surface area of solid samples and is named Brunauer-Emmett-Teller after its inventors[6]. It is based on the idea of gas molecules adsorbing to a surface and makes a number of assumptions: firstly that gas molecules adsorb onto a material surface in infinite layers; secondly that there is no interaction between layers and thirdly; that each layer can be treated with Langmuir monolayer adsorption theory. Assuming an infinite amount of layers, the BET equation takes the form:

$$\frac{p}{v(p_0 - p)} = \frac{1}{v_m c} + \frac{c-1}{v_m c}\frac{p}{p_0} \qquad (19)$$

Where p_0 is the saturation pressure of the adsorptive gas, v_m is the volume of monolayer coverage and c is the BET constant. A plot of $\frac{p}{v(p_0-p)}$ against $\frac{p}{p_0}$ should be linear over the pressure range measured, and the y intercept of $\frac{1}{v_m c}$ and the gradient $\frac{c-1}{v_m c}$. The value of v_m can therefore be obtained from the intercept and gradient, in addition to c, which must be positive. From v_m, the surface area can be calculated.

In this work, powder samples were placed in a vessel, weighed and degassed overnight at 120 ^{o}C. They were transferred to a Micromeritics Tristar II instrument and nitrogen was used as the sorption gas. An isotherm was recorded for relative partial pressures $\frac{p}{p_0}$ between 0 and 1.

2.4 Laser Image Testing

'Laser' is an acronym for Light Amplification by Stimulated Emission of Radiation. A populated metastable excited state is created by *pumping* atoms by one of several methods such as using a flash lamp or a diode laser until there are more species in an excited state than in the ground state (population inversion). The material in which this occurs is known as the *gain medium* and it can be a solid, liquid, gas or plasma. The laser medium is confined to a cavity bounded by mirrors which has a specific resonant frequency. Photons

with wavelengths corresponding to the resonant frequency are amplified while others undergo destructive interference. When excited atoms are stimulated by an emitted photon to emit, the resulting emitted radiation is coherent with very little divergence. Different gain media give rise to lasers with fixed or variable emission wavelengths that can operate in pulses or in a continuous wave mode. Solid state lasers are used in this project. The gain medium consists of glass doped with lanthanide cations.

2.4.1 Laser specifications

Sample testing for laser imaging performance was performed in industrial laboratories at Datalase Ltd., Widnes. Near infrared solid state lasers were used for irradiating sample coatings. A 40 W continuous wave laser with ytterbium hosted in glass as the gain medium emits radiation of 1070 nm while a 5 W erbium:glass operates at 1550 nm.

2.4.2 Ink formulation

Firstly the near infrared absorber prepared at the University of Liverpool was added to a solvent-based ink formulation at a certain weight per cent loading. The ink composition was a follows: 43% ethanol, 15% ethyl acetate, 22% ammonium octamolybdate pigment, 19% “Elvacite 2028” binder, and 1% “Aerosil 200” a form of fumed silica, where % values are measured by weight. The components were added together in the order given above and mixed to homogeneity using an overhead Silverson mixer. Homogeneity was tested using a Hegman gauge (also known as a grind gauge) which a steel block is containing a channel or groove that decreases steadily in depth from 100 µm to zero. The ink is pooled at the deep end and pulled towards the shallower end of the groove using a flat edged blade. Scratches in the ink in the groove indicate the presence of large particles so the ink is considered homogenous when no scratches are observed. The ink is then passed once through a bead mill before use.

The absorber was added to this base ink formulation and mixed in using an overhead Silverson mixer for 5-10 minutes. The mixture was passed continuously through a bead mill. The viscosity of the ink was then adjusted using a ‘Zahn 2’ cup which is commonly used in the ink and paints industry. It is a metal cup with a hole in the bottom of a defined size and the time taken for the ink to drain out of a full cup is measured. The timer is stopped when the stream of flowing ink is broken and becomes droplets. The more viscous the ink the more time it will take to drain from the cup. The ink viscosity was adjusted by adding more

solvent (3:1 mixture of ethanol:ethyl acetate) until the draining time was 20 seconds at room temperature.

Once the viscosity was satisfactory, a K Control Coater was used to draw down the ink onto a polyethylene terephthalate (PET) substrate using a 16 µm k-bar. This is a metal rod with wire of a certain thickness wrapped tightly around it which should give a consistent coating when pulling ink across a flat surface. The ink is distributed in front of the bar which attached to the 'arms' of the coating machine, the machine is activated and pulls the bar forward at a steady speed in order to distribute the ink across the substrate. The speed settings ranged from 1-10 and a setting of 9 was always used. A hairdryer was then used to dry the coating after which it was ready for laser irradiation.

2.4.3 Laser Imaging

Initially both 1070 and 1550 nm lasers were used for imaging however so few samples imaged at 1550 nm that the results from 1070 nm irradiation will be used throughout. The PET sheet coated in the ink was placed under the laser head at a distance of 168 mm. The laser imaging control software was set to create a double row of 5 squares, each 5x5mm in size. The fluence values varied across the set of squares and values are listed in Table 2.1. Fluence is calculated using the equation:

$$Fluence = \frac{Laser\ pulse\ energy\ [J]}{Image\ area\ [cm^2]} = \frac{Laser\ power\ [W] x\ Pulse\ time\ [s]}{Image\ Area\ [cm^2]} \qquad (20)$$

The measured laser power was 30.8 W used at a setting of 50%. Fluence is commonly given in units of Jcm^{-2} (which is equal to $Wscm^{-2}$).

Table 2.1 - Fluences used during laser imaging tests in units of Joules per cm²

	Square#	1	2	3	4	5	6	7	8	9	10
Laser wavelength	1070nm	2.2	2.3	2.5	2.6	2.9	3.2	3.5	3.7	4.0	4.6
	1550nm	0.7	0.9	1.1	1.6	1.8	2.3	2.6	3.1	3.5	3.9

Once the laser was activated, after appropriate ventilation and safety measures were in place, images were created in a matter of milliseconds. A handheld Spectro-Eye spectrometer was used to measure the optical density of the coatings. Optical density (OD) is defined as

$$OD = -log_{10}\left(\frac{I(l)}{I_0}\right) \quad (21)$$

Where $I(l)$ is the intensity of reflected light from sample of length l and I_0 is the intensity of incident radiation. Values were recorded for the background coating (un-irradiated area) and for each square laser image (irradiated area). Figure 2.3 shows an example of the set of squares produced when the coating is irradiated.

Figure 2.3 - Photograph of an example of the squares printed during laser irradiation. Top left square is lowest laser fluence and bottom right is the highest.

For ease of analysis, the highest OD reached for each sample was plotted along with the background OD. The highest OD values often occurred at the highest fluence value but this was not the case for all samples. However any fluence value below 5 Jcm^{-2} is considered commercially viable so this is not an issue that will be discussed further.

2.4.4 Possible sources of error

Steps were taken to control potential sources of error during testing. In order to eliminate possible uneven coating distribution across the substrate, images were irradiated onto two areas of each PET film with each laser, on the left and right sides respectively. Each coating was also made in duplicate so in total 4 sets of images were measured for each sample and then an average value was taken. The error values used were therefore the standard deviation of the range of 4 values. A double layer of white printer paper was placed behind the substrate for all spectrometer measurements to ensure there was no possible optical contribution from background surfaces and that measurements were comparable. All other steps were carried out by the researcher in the same way so should not vary significantly.

2.4.5 Standardising the Testing Procedure

A consistent testing procedure is needed in order to assess sample performance and compare them to each other. There are a number of possible variables in the procedure – how much absorber should be added into the ink? For how long should the ink be milled? Is the absorber evenly distributed throughout the ink coating?

Firstly a large batch of potassium tungsten bronze K_xWO_3 (KTB) was prepared in order to carry out tests (synthetic details can be found in Chapter 3). This sample was chosen as it was one of the earliest synthesised in the project and could be made reliably. Processing conditions can make a difference to the performance of the material and one of the main variables in this process is the amount of time the ink spends being passed through the bead mill. To investigate this, an ink formulation was made up with 2.5 wt% KTB mixed in with a Silverson mixer. Portions of this mixture were then passed through the bead mill for 5, 10 20 and 30 minutes before the coating and irradiation steps of the procedure. The imaging results are shown in Figure 2.4 and it can be seen that the background optical density (OD) is not significantly affected across the range of samples, apart from getting slightly darker after 30 minutes of milling. The ΔOD of the images themselves begins at a relatively high value for the 5 minute sample, increases slightly for the 10 minute sample then progressively decreases for the 20 and 30 minute samples. Although the ΔOD value is higher for the 10 minute sample it should be noted that the error values are considerably higher so the imaging is less consistent. It was concluded that 5 minutes of milling gave the best results and is sufficient to achieve a good mixture of the absorber and components of the ink.

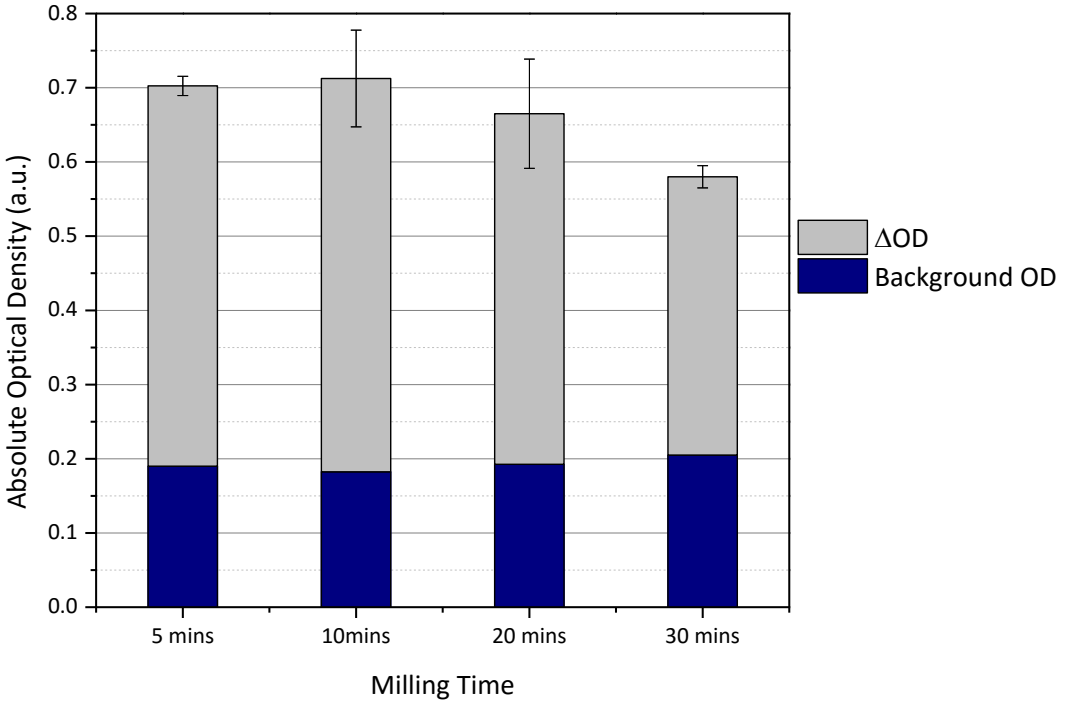

Figure 2.4 - Results of laser imaging coatings of K_xWO_3-containing ink milled for different times.

Another variable to be considered is the loading amount of absorber into the ink i.e. the concentration of the sample present in the coating. The standard amount of absorber mixed into the ink formulation is 2.5 weight per cent (wt%) for reduced indium tin oxide (rITO), the current industry leading material for this application. As the majority of NIR absorber samples are dark blue, this value will affect the colour of the coating. The ink formulation on its own is white so adding more absorber will result in a darker coloured coating. However having too little absorber present will lead to poor imaging because there won't be sufficient laser radiation absorbed to cause a colour change in the pigment. Therefore a balance between these two considerations is needed.

KTB was tested at 2.5 wt% and also at 0.75 and 0.5 wt%. The imaging results are shown in Figure 2.5.

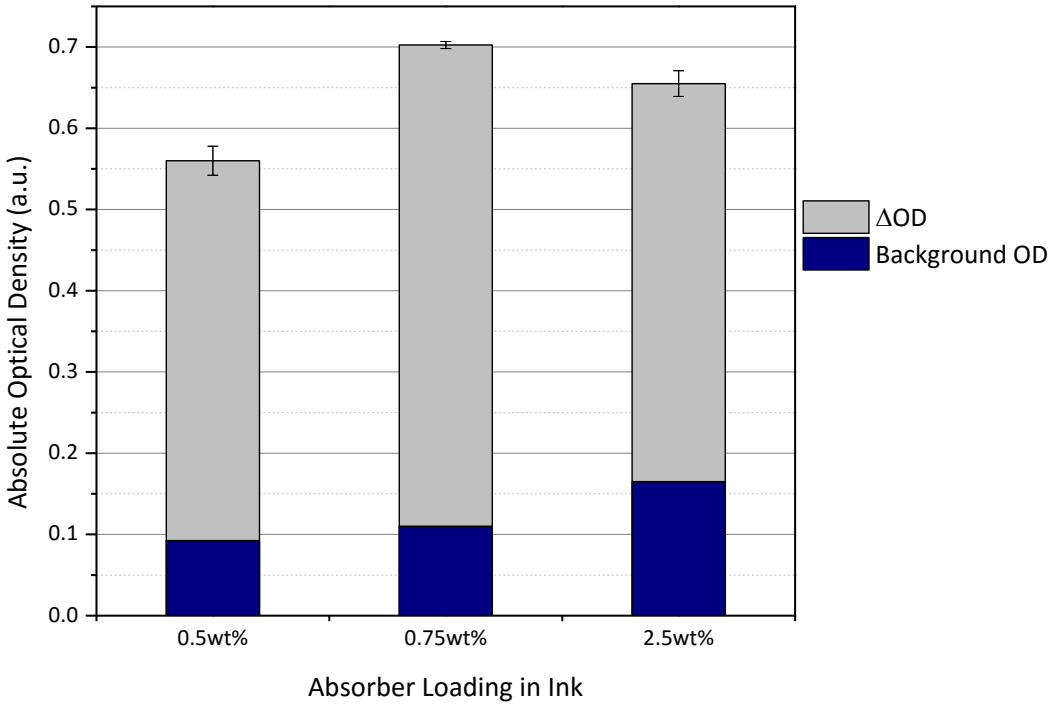

Figure 2.5 - Results of laser imaging coatings containing different concentrations of K_xWO_3 absorber.

As expected, it can be seen that the background OD of the coatings increases with increasing KTB concentration. A value of around 0.1 is desirable – the PET substrate without a coating has a value of 0.09 – so the coatings with 0.5 and 0.75 wt% loading are both acceptably low whereas the 2.5 wt% coating is darker than ideal. The OD of the images is quite good for all loading values but the darker background colour of the 2.5 wt% film means the contrast between the background and the images is not as good. Therefore the

ΔOD values of the irradiated images are slightly lower than those of the 0.75 wt% coating. The 0.5 wt% coating also has lower values than the 0.75 wt% because less of the absorber is present to transfer laser radiation to the pigment. It was decided that 0.75 wt% was the best option for future testing.

In order to evaluate the distribution of the absorber particles throughout the coating EDX mapping was used. An un-irradiated section of the KTB 2.5 wt% film was cut out and prepared for EDX analysis by being mounted on an aluminium stub with carbon tape and sputter-coating with a layer of gold. The mapping images are shown in Figure 2.6. There are larger clumps visible in the SEM image and the corresponding EDX maps show that these are the pigment particles since they match the location of Mo signal and the pigment is an ammonium octamolybdate (AOM). The signals for K and W originating from the KTB absorber are present around and among the pigment particles so it is clear that both the AOM pigment and the KTB absorber are evenly distributed across the film. Therefore they are in close proximity to each other and laser radiation can be transferred as heat to cause the pigment colour change.

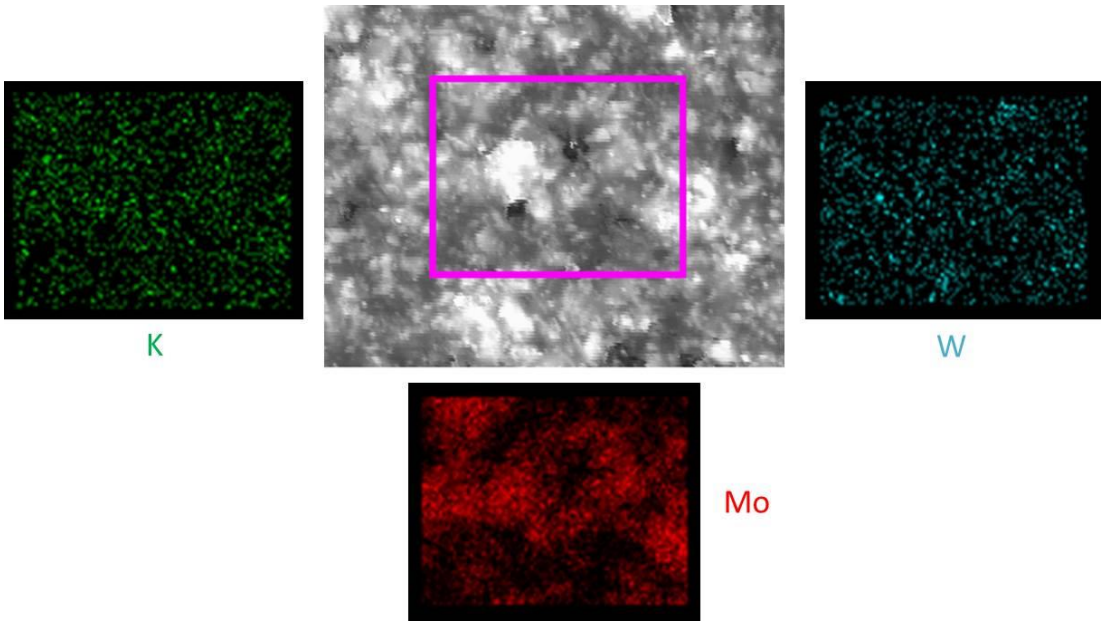

Figure 2.6 - EDX mapping of a section of coating showing the location of K (green), W (blue) and Mo (red) signals. Both the K_xWO_3 absorber and $(NH_4)_4Mo_8O_{26}$ pigment particles are evenly distributed.

The standard testing procedure to be used subsequently was to load 0.75 wt% of the absorber, mix it into the ink and then bead mill the mixture for 5 minutes before adjusting the viscosity and coating the PET substrate.

2.5 References

1. West, A. R., Synthesis Methods. In *Basic Solid State Chemistry*, Second Edition ed.; John Wiley & Sons Ltd: New York, 2000.
2. Demazeau, G., Solvothermal reactions: an original route for the synthesis of novel materials. *Journal of Materials Science* **2008,** *43* (7), 2104-2114.
3. Momma, K.; Izumi, F., VESTA 3 for three-dimensional visualization of crystal, volumetric and morphology data. *Journal of Applied Crystallography* **2011,** *44* (6), 1272-1276.
4. Coelho, A. A., Indexing of powder diffraction patterns by iterative use of singular value decomposition. *Journal of Applied Crystallography* **2003,** *36* (1), 86-95.
5. Sugioka, M. Solid Sample Reflectance Measurements. http://www.shimadzu.com/an/uv_talk/index.html, Volume 14.
6. Brunauer, S.; Emmett, P. H.; Teller, E., Adsorption of Gases in Multimolecular Layers. *Journal of the American Chemical Society* **1938,** *60* (2), 309-319.

Chapter 3

The Tungsten Bronzes

3.1 Introduction

Following analyses of commercial samples (detailed in Appendix 1), the family of tungsten bronzes M_xWO_3 were chosen as promising candidates for near infrared (NIR) absorbers in laser imaging applications. M is usually an alkali metal but analogues have been made with M = Ba, Tl, Cu, Sn, Pb, Sb and lanthanides. This chapter will concentrate on bronzes with M = Na, K, Rb, (NH_4) and Sn with the Cs-containing bronzes dealt with in the following chapter in more detail. The synthesis and characterisation of samples will be described followed by the sample performance in laser imaging tests and discussion of results.

3.2 Synthesis of Tungsten Bronzes

As can be seen from the background literature (see Chapter 1), the tungsten bronzes are not a new family of compounds but since their discovery in 1823[1] there have been two resurgences in academic interest. Firstly the vast majority of initial structural characterisation was carried out by Hagg, Straumanis and Magneli in the 1950's-60's[2] and in more recent years, the publication of the paper by Takeda and Adachi[3] which demonstrated their potential as NIR absorbers created renewed research. Subsequent publications by Guo *et. al.*[4] show that the tungsten bronzes can be made by simple hydrothermal synthesis routes. In this work both solvothermal and traditional solid state synthesis routes have been used and will be compared.

3.2.1 Solvothermal Synthesis

All heating and cooling rates were 10 ^oC per minute unless otherwise specified. Dry samples were ground with a pestle and mortar before analysis. All starting materials were used as purchased without further purification and purities are given on a trace metals basis. Water is distilled and ethanol is absolute.

3.2.1.1 Potassium Tungsten Bronze K_xWO_3

Potassium tungsten bronzes were made following the route by Guo *et. al.*[4c]. K_2WO_4 (Sigma Aldrich 99.99%, 1.9562 g, 0.006 mol) and K_2SO_4 (Sigma Aldrich 99.99%, 2.0911 g, 0.012 mol)

were dissolved in 60 ml H_2O in a Teflon liner. The pH was adjusted to ≈1.5 using 70% HNO_3 which formed a white suspension in the colourless solution. The liner was placed in a steel autoclave and heated to 200 ^oC for 24 h. The pale yellow product was isolated by centrifugation and washed with H_2O before being dried in air at 60 ^OC. The dry product was ground using a pestle and mortar then heated in a tube furnace at 500 ^oC for 2 h under a flow of 5% H_2 in N_2 during which a colour change to dark blue occurred.

3.2.1.2 Sodium Tungsten Bronze Na_xWO_3

1) The sodium tungsten bronze synthesis was adapted from that of the potassium tungsten bronze sample, above. $Na_2WO_4.2H_2O$ (Sigma Aldrich ≥ 99%, 1.5592 g, 0.005 mol) and Na_2SO_4 (Sigma Aldrich ≥ 99%, 1.4204 g, 0.01 mol) were dissolved in 50 ml H_2O in a Teflon liner of 125 ml volume. The pH was adjusted to ~1.5 using 70% HNO_3. The liner containing the pale yellow solution was transferred to a steel autoclave and heated to 200 ^oC for 24 h. The white product was isolated by centrifugation and washed with water before being dried in air at 60 ^OC. The dry product was ground using a pestle and mortar then heated in a tube furnace at 500 ^oC for 2h under a flow of 5% H_2 in N_2 during which a colour change to dark blue occurred.

2) A second route from a paper by Wang *et. al.*[5] was also used in an attempt to obtain samples with a 'nanowire bundle' morphology. $Na_2WO_4.2H_2O$ (Sigma Aldrich ≥ 99%,) and NaCl (Sigma Aldrich ≥ 99%,) were dissolved in 70 ml H_2O in Teflon liners. The mixtures were acidified with 37% HCl until the pH≈2 when measured with a pH meter and transferred to steel autoclaves. They were heated for 48 h at 180 ^oC. The blue products were separated by centrifugation and washed with distilled H_2O then dried at 80 ^oC for 4 h in air.

3.2.1.3 Rubidium Tungsten Bronze Rb_xWO_3

Rubidium tungsten bronze was synthesised using the route outlined by Guo *et. al.*[6]. WCl_6 (Sigma Aldrich ≥ 99%, 0.3569 g, 9 x 10^{-4} mol) was dissolved in 48 ml C_2H_5OH and RbOH (Alfa Aesar 99%, 0.0461 g, 4.5 x 10^{-4} mol) was added. The Rb:W ratio was 0.5. 12 ml acetic acid CH_3COOH was added (20 volume % of the total solution) and the Teflon liner was transferred to a steel autoclave and heated to 230 ^oC for 20 h. The blue products were separated by centrifugation, washed with distilled H_2O and dried at 60 ^oC in air.

3.2.1.4 Ammonium Tungsten Bronze $(NH_4)_xWO_3$

The ammonium tungsten bronze can be considered a member of the alkali metal series and was initially synthesised following the route by Guo *et. al.*[4a]. Ammonium paratungstate (APT, $(NH_4)_{10}(H_2W_{12}O_{42}).4H_2O$, Sigma Aldrich 99.99%, 0.2500 g, 8.2 x 10^{-5} mol) was dissolved in ethylene glycol $C_2H_6O_2$ at 190 ^oC. Once the solution was cool, 30 ml acetic acid CH_3COOH was added and the solution transferred to a Teflon-lined autoclave. This was heated to 200 ^oC for 72 h. The blue product was collected by centrifugation, washed with H_2O and C_2H_5OH and dried in air at 60 ^oC.

This route yielded low amounts of product from each synthesis so it was scaled up to get enough sample for testing. The route from Guo *et. al.*[4a] was modified to use ethanol as a solvent instead of ethylene glycol to eliminate the extra heating step. APT (1.000 g, 3.28 x 10^{-4} mol) was added to 60 ml C_2H_5OH in a Teflon liner in a steel autoclave and heated to 200 ^oC for 72 h. The dark blue solid product was collected by centrifugation, washed with ethanol and dried in air at 80 ^oC. When a lower temperature and reaction time were used (180 ^oC, 24 h) some starting material remained in the final product.

3.2.1.5 Tin Tungsten Bronze Sn_xWO_3

Tin tungsten bronze has not previously been prepared by a solvothermal route and differs from the others by having a metal cation charge of 2+, as shown by McColm, Steadman and Howe using Mossbauer spectroscopy[7]. Xu *et. al.* have used relatively low temperature routes[8] however these require further steps for product crystallisation or purification. In this work, the tin tungsten bronze was prepared by adding stoichiometric amounts of elemental tin (Sigma Aldrich ≥ 99%, 0.1466 g, 1.23 x 10^{-3} mol) and tungstic acid H_2WO_4 (Sigma Aldrich 99.99%, 0.9269 g, 3.71 x 10^{-3} mol) to 53 ml deionised water to form a yellow suspension in a Teflon liner. This was placed into a steel autoclave and heated for 24 h at 200 ^oC. The dark blue solid product was collected by centrifugation, washed with water and dried in air at 80 ^oC. Using a shorter reaction time of 12 h at the same temperature resulted in WO_3 impurities.

3.2.2 Solid State Synthesis

Traditional high temperature solid state routes were also used to prepare tungsten bronzes of the alkali metals (Na, K and Rb) and compared to the solvothermal samples. Following the paper by Leonova *et. al.*[9] appropriate alkali metal carbonates were reacted with

tungsten trioxide to give the metal tungstate. This was then reacted with further WO_3 and W to give tungsten bronzes.

$$1.\ M_2CO_3 + WO_3 \rightarrow M_2WO_4 + CO_2$$

$$2.\ xM_2WO_4 + \left(2 - {}^{4x}/_{3}\right)WO_3 + {}^{x}/_{3}W \rightarrow 2M_xWO_3$$

The carbonate precursors were 99.9% pure (trace metals basis), purchased from Sigma Aldrich and dried in an oven overnight. In step 1, the reactants were ground using a pestle and mortar then pressed into pellets of 20 mm diameter. These were heated in air in Al_2O_3 crucibles. The products were ground and analysed before use in step two. The tungstates and other precursors for reaction 2 were ground together using a pestle and mortar. The mixtures were sealed into quartz tubes under vacuum and heated. The tubes were cut open and the products ground with a pestle and mortar before analysis. Different values of x were used and heating conditions are shown in Table 3.1. Heating and cooling rates were 5 ^{o}C/min. It was necessary to repeat either step 1 or step 2 for all samples.

Table 3.1 - Heating conditions used in the solid state synthesis of tungsten bronzes M_xWO_3

M_xWO_3 Samples		**Step One**		**Step Two**	
M	x	Temp (^{o}C)	Time (h)	Temp (^{o}C)	Time (h)
Na	0.1, 0.20, 0.25, 0.33, 0.4, 0.6, 0.8	600	4	i) 650	8
				ii) 650	24
K	0.33, 0.6	i) 600	4	700	10
		ii) 650	5		
Rb	0.33	i) 600	5	700	10
		ii) 650	5		

A list of sample names to be used throughout the rest of the chapter is given in Table 3.2.

Table 3.2 - Summary of tungsten bronze samples

Name	**Compound**	**Synthesis Route**	**Relevant Paper**
NaTB-ST1	Na_xWO_3	Solvothermal, two step	N/A
NaTB-ST2	$Na_xWO_3.yH_2O$	Solvothermal, one step	Wang *et. al.,* 2010[5]
KTB-ST	K_xWO_3	Solvothermal	Guo *et. al.*, 2011[4c]
RbTB-ST	Rb_xWO_3	Solvothermal	Guo *et. al.*, 2012[6]
ATB-ST	$(NH_4)_xWO_3$	Solvothermal	Guo *et. al.*, 2012[4a]

TTB-ST	Sn_xWO_3	Solvothermal	N/A
NaTB-SS1,2, 3,4,5, 6,7	Na_xWO_3	Solid State	Leonova *et. al.*, 2009[9]
KTB-SS1,2	K_xWO_3	Solid State	Leonova *et. al.*, 2009[9]
RbTB-SS	Rb_xWO_3	Solid State	Leonova *et. al.*, 2009[9]

3.3 Characterisation

3.3.1 Powder X-ray Diffraction (PXRD)

PXRD was used to determine the crystallinity and phase composition of the products.

3.3.1.1 Solvothermal Samples

The diffractograms of the solvothermal NaTB samples are shown in Figure 3.1.

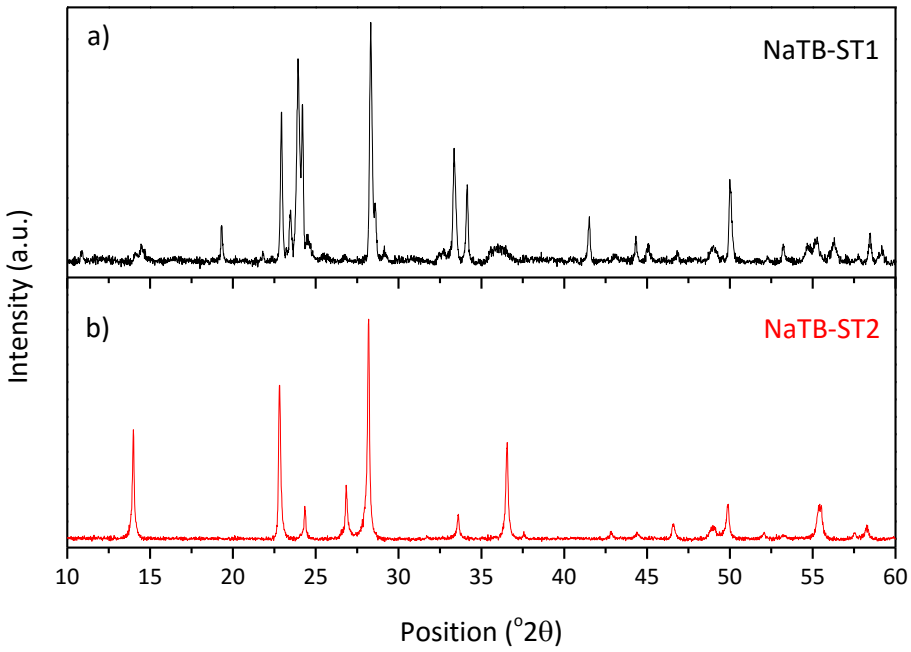

Figure 3.1 - PXRD diffractograms of Na_xWO_3 samples made by solvothermal synthesis.

Two different crystal structures are adopted by the NaTB-ST compounds made by different synthetic routes. The two-step procedure used to make NaTB-ST1 results in a tetragonal product. Tungsten bronzes with larger alkali metals have a hexagonal crystal structure with channels running parallel to the *c*-axis (see Figure 3.4) but due to the smaller size of the Na^+ cation compared to other alkali metal cations, it is not usually stable in the relatively large channels. NaTB-ST1 adopts a pseudo-cubic tetragonal structure with smaller M sites

available for occupation. Bartha and co-workers[10] calculated the sizes of channels available in different tungsten bronze structures and the tetragonal (4-sided) channels have a maximum diameter of 0.129 nm. Considering the radius of un-hydrated Na^+ is 0.099 nm[10] it can fit comfortably in these channels whereas the next alkali metal cation K^+ has an ionic radius of 0.137 nm so is too big.

The tetragonal structure adopted by the NaTB-ST1 sample is shown in Figure 3.2.

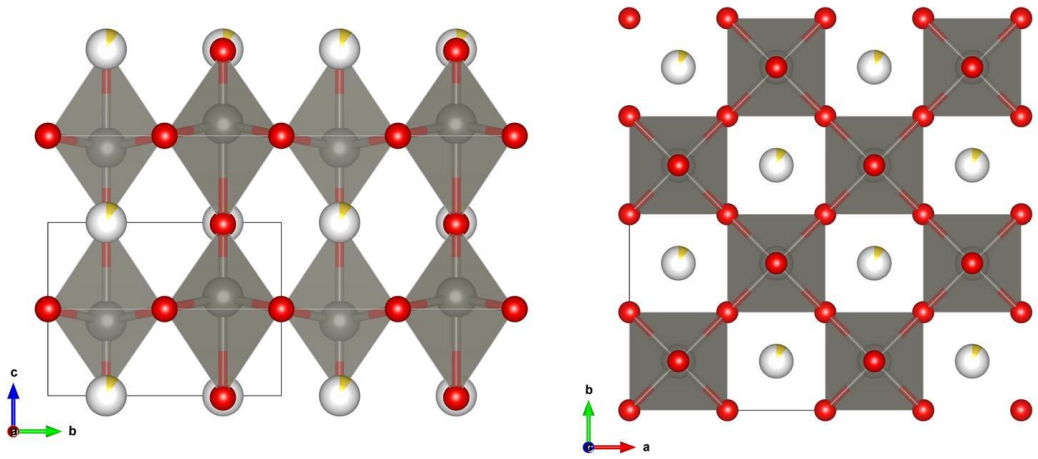

Figure 3.2 - Polyhedral representation of the tetragonal sodium bronze $Na_{0.1}WO_3$ structure viewed along the a and c axes. Known as 'Tetragonal I'. W=grey, O=red, Na=yellow.

It is a distorted version of the well-known cubic Perovskite structure. WO_6 octahedra are corner-sharing but the W atoms are displaced from the octahedral midpoint, alternating up and down with respect to the *ab* plane. This creates zigzag O-W-O-W chains running parallel to (001). The dopant Na^+ cations reside in the interstitial sites between WO_6 octahedra. As mentioned previously, this structure is only found in alkali metal tungsten bronzes with small cations i.e. lithium and sodium and with values of $x < 0.3$. Since two tetragonal bronze structures are known in the literature, care should be taken to avoid confusion. The one shown in Figure 3.2 is designated as "Tetragonal I" by Ribnick *et. al.*[11] and the second phase, known as the 'tetragonal tungsten bronze' or 'TTB' structure is designated "Tetragonal II". They are numbered in order of increasing M content unlike Magneli's original chronological numbering[12] which was the other way around. Unlike Tetragonal I, Tetragonal II is not a derivative of the Perovskite structure but assumes a completely different structural type (see Figure 3.7).

The NaTB-ST1 sample is not phase pure –an amount of $Na_5W_{14}O_{44}$ is also present. This is a triclinic phase composed of layers similar to those in the hexagonal tungsten bronze structure but they are displaced relative to each other rather than superimposed to form

channels (see Figure A.2.1 in Appendix 2). The tungsten species are all thought to be W^{6+} so the optical properties of the NaTB-ST1 sample (which will be discussed in more detail below) should not be affected.

The NaTB-ST2 sample has a hexagonal crystal structure, closely related to but distinct from the hexagonal tungsten bronze (HTB) structure. It can be considered to be the hexagonal form of WO_3 with guest species in the channels[13]. As in the Tetragonal I structure, the W atoms form WO_6 octahedra which are corner-sharing but they are linked in a way that forms 6-sided hexagonal channels along the *c*-axis. Reis *et. al.* were the first to synthesise and characterise this structure[14]. The small Na^+ cations are stabilised in the large channels by the presence of water molecules. It is likely that the second heating step in the synthesis of NaTB-ST1 would drive off any water present and make the formation of this phase by that route impossible.

Interstitial oxygens are also present in the channels giving a general formula of $Na_xWO_{3-x/2}.yH_2O$ and therefore different stoichiometry to the other HTB phases. The sodium cations are located in the centre of the hexagonal windows in the (0,0,0) position unlike the HTB phases in which the M^+ cations are located in the anionic cavities between hexagonal windows rather than in the plane of tungsten sites. The tungsten atoms in NaTB-ST2 are not displaced along the *c*-axis so the *c* lattice parameter is not doubled as it is in the HTB structure. Both this structure and the HTB structure are shown in Figures 3.3 and 3.4 respectively and the difference in the M site positions can be seen as well as the extra water and oxygen sites in $Na_xWO_{3-x/2}.yH_2O$.

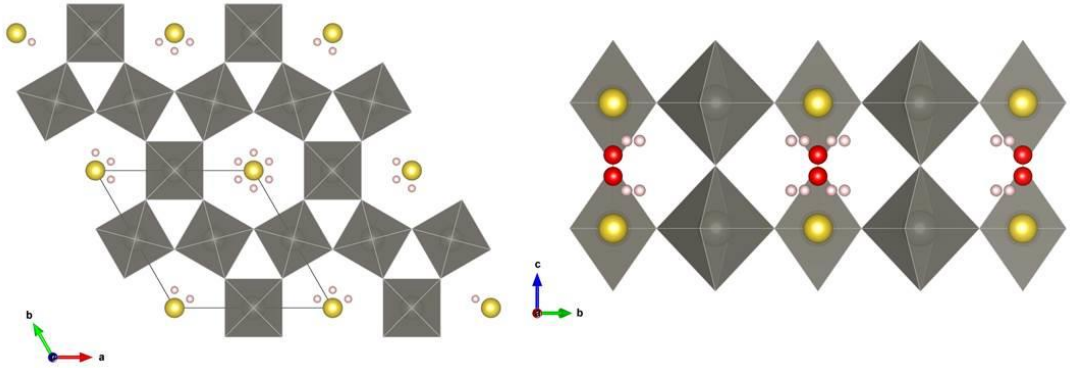

Figure 3.3 - Polyhedral representation of the crystal structure of $Na_xWO_{3-y/2}.zH_2O$ viewed along the c and a axes. W=grey, Na=yellow, O=red and H=pink.

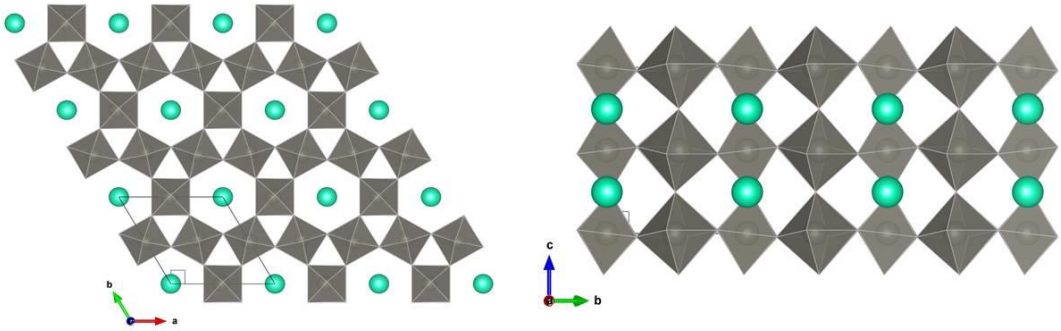

Figure 3.4 - Polyhedral representation of the crystal structure of hexagonal tungsten bronzes M_xWO_3 where M is an alkali metal. W=grey, M=green.

The non-sodium samples with larger alkali metal cations all adopt the HTB structure shown in Figure 3.4 and their PXRD diffractograms are shown in Figure 3.5.

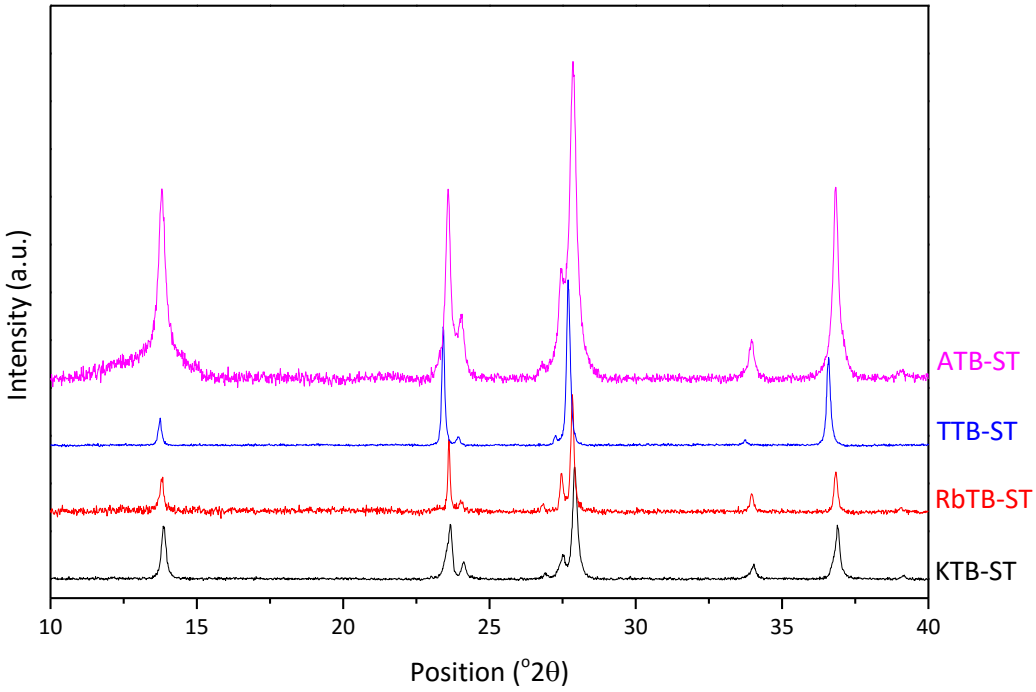

Figure 3.5 - PXRD diffractograms of hexagonal tungsten bronzes M_xWO_3 synthesised solvothermally with M=K, Rb, Sn and (NH_4).

Unlike the NaTB-ST2 structure, the M atoms reside in the hexagonal channels in out of plane positions with regard to the tungsten sites. Since the M site:W ratio in a unit cell is 1:3 the maximum value of x in the overall formula M_xWO_3 is 0.33 when all the M sites are filled. The maximum hexagonal channel diameter calculated by Bartha *et. al.*[10] is 0.189 nm which is larger than the ionic radii of alkali metal cations K^+, Rb^+ and Cs^+ as well as $(NH_4)^+$ and Sn^{2+} so these ions can all be accommodated without disrupting the framework. The

difference in lattice parameters is the cause of small shifts in peak positions in Figure 3.5. The lattice parameters were determined via Rietveld refinements and are shown in Table 3.3. According to Bragg's Law (see Chapter 2), an increase in lattice parameters should lead to a decrease in 2θ values and this trend is observed, most obviously for the TTB-ST sample which has the largest *a* value.

Table 3.3 - Crystallographic details of solvothermal tungsten bronze samples M_xWO_3

M	Space Group	a (Å)	c (Å)	x
Na	P4/nmm	5.260(4)	3.883(4)	0.05(4)
Na	P6/mmm	7.312(3)	3.896(2)	0.14(3)
K	$P6_3/22$	7.384(3)	7.536(4)	0.187(9)
Rb	$P6_3/mcm$	7.393(2)	7.525(3)	0.32(1)
NH_4	$P6_3/mcm$	7.387(2)	7.533(3)	0.31*
Sn	P6/mmm	7.428(1)	3.7928(7)	0.318(2)

*value determined from TGA data rather than refinement of PXRD data

The HTB structure as originally determined by Magneli[2c] had a space group of P6/mmm. More sensitive techniques found slight discrepancies in Magneli's structure and it was found that HTB's with different M species had small structural differences.

The Na-HTB structure has been discussed above. Using powder neutron diffraction on K_xWO_3 samples Pye and Dickens[15] found that distortions of the WO_6 octahedra lead to puckering of the ring of oxygens forming the hexagonal windows. Also the smaller size of K^+ means that the cations do not reside in the centre of the channel site but are randomly distributed between two sites (see Figure A.2.2). These modifications removed the glide and mirror planes within the structure but added a screw axis changing the space group from P6/mcm to $P6_3/22$. The Rb^+ and $(NH_4)^+$ cations occupy the centre of the channel sites and the WO_6 octahedra are not as distorted as in the KTB structure. In general the guest cations stabilise the W-O framework – hexagonal WO_3 is only formed at room temperature when made by specific synthesis routes[13]. The structure adopted by the TTB-ST sample does not contain the three-fold symmetry axis of the other alkali metal samples but is in the same space group as the NaTB-ST2 sample. The Sn^{2+} cations do not reside in the centre of the hexagonal channels but are distributed statistically among six possible off-centre sites[8b]

(see Figure A.2.3). The interaction of the stereoactive Sn 5s lone pair with neighbouring atoms is thought to be the cause of this[16]. As in NaTB-ST2, the *c*-axis is not doubled.

The M site occupancy values were also calculated from PXRD data and are given in Table 3.3. It should be noted that the value for ATB-ST was calculated from TGA data since light N atoms are difficult to detect by X-ray techniques in the presence of a much heavier atom like W. The nominal composition used during synthesis for all samples was x = 0.33 so there is some deviation from this value.

The presence of a second impurity phase in the NaTB-ST1 sample can account for the lower amount of Na present in the tetragonal phase. Also according to Takusagawa and Jacobson[17] the Tetragonal I structure only forms when x < 0.2. The hexagonal structure of the NaTB-ST2 phase also contains water molecules and extra oxygens in the structure so it is unlikely that the interstitial sites are fully occupied by Na in this case. The Na that was not intercalated into this structure could have easily formed soluble side products such as NaCl and been washed away during sample work-up so do not appear in the PXRD spectrum. This could also have been the case for the KTB-ST synthesis although the reason for less than maximum occupation in this case is less clear. However the three larger Rb^{+}, $(NH_4)^{+}$ and Sn^{2+} cations achieve site occupancies close to the maximum value (Table 3.3). However the occupancy values are closely related to the thermal parameters in the tungsten bronzes so values should be treated with some caution. The M content for all samples has also been investigated using energy-dispersive X-ray spectroscopy – see section 3.3.4.

It should be noted that this is the first example of phase pure hexagonal tin tungsten bronze Sn_xWO_3 being prepared by a one-pot hydrothermal route. Gier *et. al.* were the first to prepare the hexagonal tin tungsten bronze[18] and they used a hydrothermal route which required reactants being sealed into gold tubes under external pressure of 3000 atm of argon and heated to at least 400 ^{o}C. A milder route was used in 1995 by Xu, Smalle and Günter[8b] yet this requires long reactions times of at least 55 h to obtain the hexagonal phase. A year earlier Xu and Günter used a peroxo-polytungstic method[8a] which, despite an initial room temperature precipitation reaction, requires further reduction steps at 500 ^{o}C to obtain the tungsten bronze. The starting material also needs to be synthesised beforehand. The method presented in this work has the benefit of only requiring two commercially available starting materials – tungstic acid and elemental tin - with water as

the solvent. The use of an isobaric autoclave means that relatively large quantities (~1 g) of a crystalline phase pure hexagonal product can be obtained after reaction for 24 h at 200 °C without the need for any additional steps. A shorter reaction time of 12 h was also tried but resulted in a WO_3 impurity phase.

3.3.1.2 Solid State Samples

The alkali metal tungsten bronzes (M=Na, K, Rb) were also prepared by solid state synthesis. For Na_xWO_3, x values of 0.1, 0.2, 0.25, 0.33, 0.4, 0.6 and 0.8 were used and will be referred to as SS1-SS7 respectively. Sodium is the only alkali metal cation to form the full solid solution of tungsten bronzes from x = 0 to x = 1 and as the value of x increases, so does the symmetry of the crystal structure from hexagonal to cubic via a number of tetragonal phases[11, 19].

The PXRD diffractograms are shown in Figure 3.6.

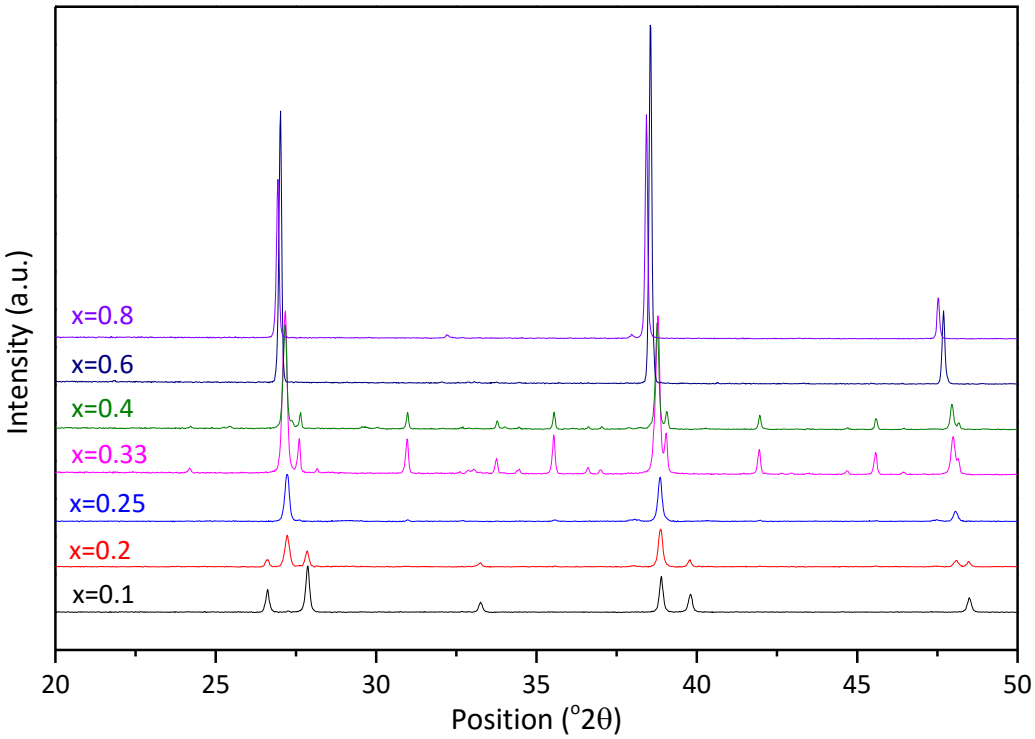

Figure 3.6 - PXRD diffractograms of Na_xWO_3 samples prepared by solid state synthesis with different nominal values of x.

NaTB-SS1 with the lowest Na content forms the Tetragonal I structure shown in Figure 3.2, the same structure adopted by NaTB-ST1. As *x* increases to 0.2 a mixture of the pseudo-cubic Tetragonal I and a fully cubic structure is seen. When x = 0.25 only the cubic phase is seen but at higher values of *x* (0.33, 0.4) the cubic phase is mixed with the Tetragonal II

structure, discussed below. At the highest values of *x* only the cubic structure is seen. As discussed above, sodium analogues do not form the HTB structure as readily as the larger cations due to the instability of the small Na^+ cation in the relatively large hexagonal channels. As shown by Dickens and Whittingham[19], the tetragonal and cubic phases co-exist between 0.25 < x < 0.45 so the formation of both phases for SS4 and SS5 with x = 0.33 and x = 0.4 respectively is unsurprising.

The tetragonal structure seen in NaTB-SS4 and SS5 is different to the 'Tetragonal I' structure adopted by the NaTB-ST1 sample – it is the 'Tetragonal II' phase. Takusagawa and Jacobsen[17] found that the space group differs slightly with the value of x due to deviations in the tungsten atom positions and structural distortions. It is P-42_1m for x = 0.33 and P4/mbm for values of x≥0.4. The Tetragonal II structure is not pseudo-cubic like Tetragonal I, but contains trigonal, square and pentagonal columns created by corner-linking WO_6 octahedra. Although the structure was first solved by Magneli for $K_{0.57}WO_3$, there are many compositional variations because of the three channels available for occupation by differently sized ions[20]. The trigonal sites are too small for sodium occupation but it can reside in the tetragonal or pentagonal sites, giving a maximum value of x = 0.6 when all sites are occupied[21]. The larger pentagonal sites are preferentially occupied first – in the x = 0.33 phase the majority of the tetragonal sites are unoccupied which leads to octahedral tilting[17].

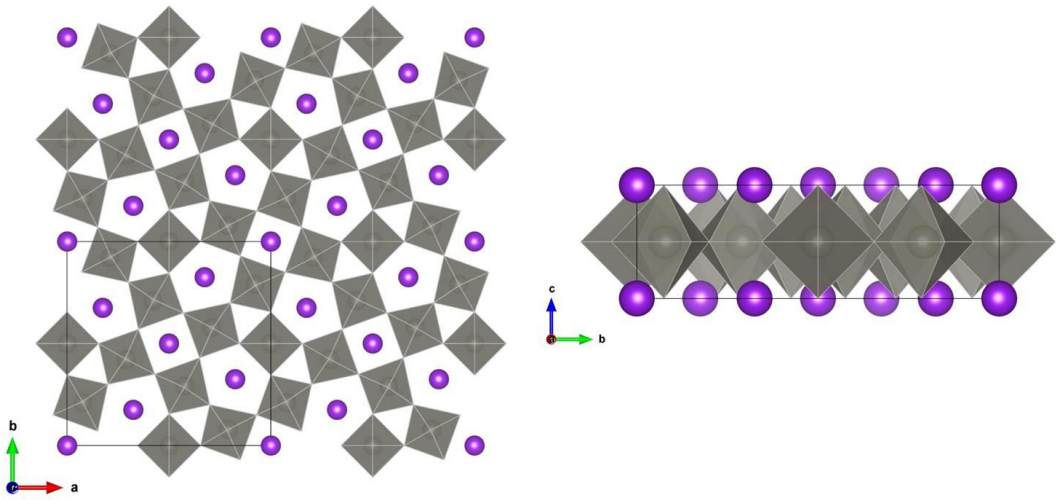

Figure 3.7 - Polyhedral representation of the tetragonal tungsten bronze M_xWO_3 structure "Tetragonal II" which exists for 0.2<x<0.6. W=grey, M=purple.

The SS4 and SS5 samples also contain a cubic perovskite bronze phase, the structure which is also adopted by the SS6 and SS7 samples with space group Pm-3m. It is built up of corner-sharing octahedra, a feature shared with the other tungsten bronze structures. In

this case the octahedra are each corner-linked to six others to form a regular three dimensional network. The cavities between octahedra are available for occupation by sodium cations. The structure is the same as that shown in Figure 3.2 but without the zigzag distortion of the W atoms in the *ab* plane. This structure is generally formed by bronzes with x > 0.4 although under certain conditions, like those used by Brown and Banks[22], it can form with lower sodium content.

In the solid state synthesis of KTB-SS x values of 0.33 and 0.6 were used, resulting in hexagonal and tetragonal bronze structures respectively. Both samples are highly crystalline and phase pure as shown in Figure 3.8 with the solid state sample of RbTB. Rb is not known to form a tetragonal tungsten bronze phase due to the larger cation radius so only a value of x = 0.33 was used in its synthesis. The HTB structure has already been discussed and is shown in Figure 3.4. The tetragonal structure is the 'Tetragonal II' phase seen in NaTB-SS5 with space group P4/mbm shown in Figure 3.7. As with sodium, the potassium cations occupy only the pentagonal and tetragonal channels giving a maximum of x=0.6. The lower limit is around x=0.4 – below this, phases of mixed HTB and tetragonal structures were found and below x=0.33 only the hexagonal bronze phase is seen.

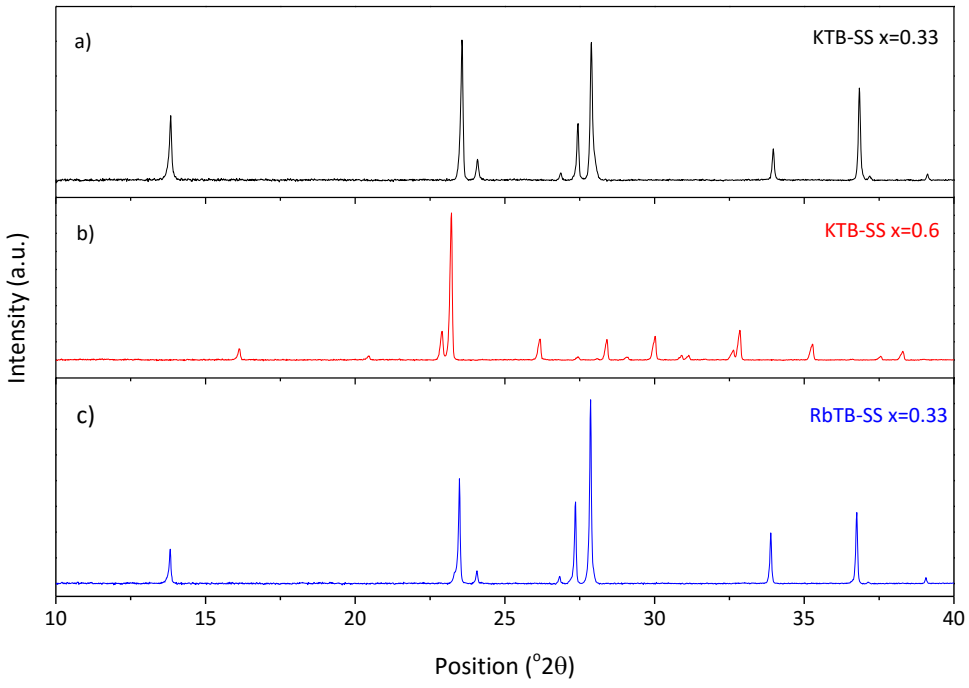

Figure 3.8 - PXRD diffractograms of tungsten bronzes M_xWO_3 made by solid state synthesis with a) M=K, x = 0.33, b) M=K, x = 0.6 and c) M=Rb, x = 0.33.

It can be noted that the solid state samples are all highly crystalline and do not show the size-related peak broadening that can be seen in the PXRD patterns of the solvothermal samples.

3.3.2 UV-vis-NIR Spectroscopy

3.3.2.1 Solvothermal Samples

The optical absorbance profiles for the ST samples can be seen in Figure 3.9.

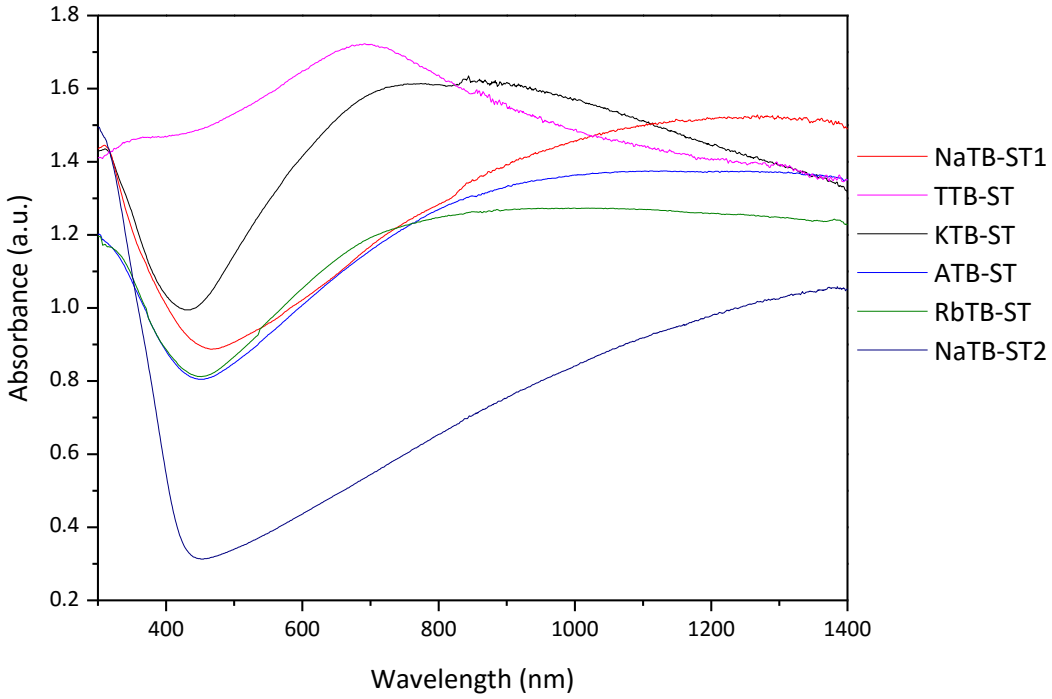

Figure 3.9 - Optical absorbance profiles of tungsten bronzes M_xWO_3 synthesised by a solvothermal route.

The NaTB-ST1, RbTB-ST and ATB spectra all show a large broad peak in absorbance in the NIR region between 800 and 1300 nm. They also display a minimum in the visible region around 450 nm – this type of profile is highly desirable for an absorber candidate in this project. The combination of high NIR absorbance with low visible absorbance is relatively rare yet essential for laser imaging application. The low visible absorbance should lead to ink coatings that have light background colours once the absorber is mixed in – as close to white as possible. The high NIR absorbance should mean that the NIR laser irradiation is absorbed efficiently and will cause the pigment in the ink to heat up and change colour from white to black to form an image.

The profile for NaTB-ST2 takes the same form but at lower intensity. It is possible that the lower absorbance in the visible region could offset the lower NIR absorbance by providing a very pale background coating colour which would give good contrast with darker images. The absorption mechanisms are discussed extensively in the literature and summarised in section 1.8.1.4. When alkali metals are doped into WO_3, each contributes an electron into the conduction band giving the tungsten bronzes metallic behaviour due to this band of free electrons. They can interact with radiation in the form of localised surface plasmon resonance (LSPR). Polaron hopping is another proposed mechanism for absorbance of NIR radiation by the tungsten bronzes. The incident radiation causes hopping of localised charge (a polaron) between non-equivalent W^{5+} and W^{6+} neighbouring sites. It is thought that both mechanisms play a role but it is likely that for samples composed of smaller particles which have a higher surface-to-bulk ratio that the LSPR mechanism will be dominant[23].

The position and intensity of the absorbance peak is dependent on the number of charge carriers which is related to the amount of alkali metal present. The KTB-ST peak is considerably shifted towards the visible region compared to the other monovalent tungsten bronzes. This suggests a greater level of W^{6+} reduction. The KTB-ST sample is reduced in a tube furnace after the solvothermal reaction step which is not the case with the NaTB-ST2, RbTB-ST and ATB-ST samples which are made via a one-pot solvothermal reaction. The tube furnace reduction has perhaps reduced the KTB-ST sample more than the other TB's or it could be an effect of particle size, discussed below. The TTB-ST sample is the only one with a divalent cation and as a result two W^{6+} are reduced for each Sn^{2+} to maintain charge neutrality. The higher W^{5+} content and therefore larger number of free electrons causes the shift of the absorbance peak into the visible region.

3.3.2.2 Solid state samples

The optical absorbance spectra of the sodium tungsten bronzes NaTB-SS4, SS5, SS6 and SS7 are shown in Figure 3.10. There is a clear change in optical properties with the change in crystal structure. The mixed phase SS4 and SS5 samples are both blue in colour and have an absorbance peak at around 700 nm. The absorbance edge is slightly red-shifted for the SS5 sample which has a higher nominal Na content than SS4. The cubic SS6 and SS7 samples are less absorbing in the NIR region and have main absorbance peaks between 500-600 nm. SS6 is red in colour while SS7 is orange. Again the absorbance edge of the sample with

higher Na content is red-shifted – this is in accordance with what is seen in the literature. For example, Brown and Banks saw a linear relationship between the position of the absorbance peak and the value of x in Na_xWO_3 samples[22] and the same trend is seen here (see Figure A.2.4).

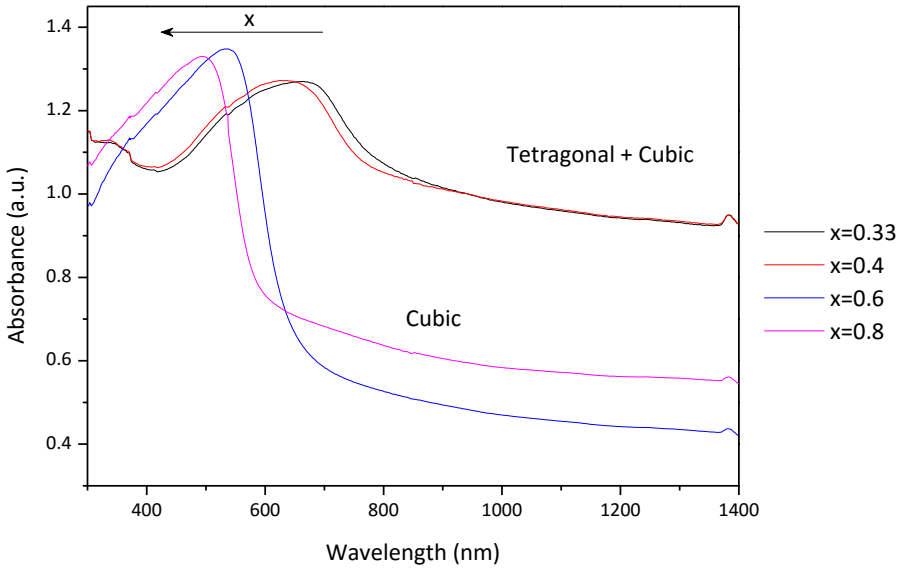

Figure 3.10 - Optical absorbance profiles of Na_xWO_3 samples SS4 x = 0.33, SS5 x = 0.4, SS6 x = 0.6 and SS7 x = 0.8 synthesised by a solid state route.

The origin of the optical absorbance is excitation of plasmons of free electrons in the conduction band. As each Na^+ cation contributes one electron to the conduction band which is primarily made up of tungsten orbitals, the number of available charge carriers for light interaction increases with increasing x and the light is absorbed at higher energies i.e. at lower wavelengths. This correlates with work by Xue and co-workers[23] who have carried out a theoretical study of the origin of colours of the sodium tungsten bronzes.

Due to instrument breakdown, NIR data is not available for NaTB-SS1, SS2 and SS3 samples. However their visible spectra were recorded and are shown in Figure 3.11 with the visible portion of the NaTB-SS4 spectrum for comparison.

Although the NIR region cannot be seen, the same trend is observed as for Figure 3.10 i.e. absorbance peak being red-shifted with decreasing values of *x*. The SS4 with x = 0.33 is more red-shifted than SS3 with x = 0.25 which does not follow the trend but this could be

due to the different spectrometers used to take measurements or be a structurally-related feature.

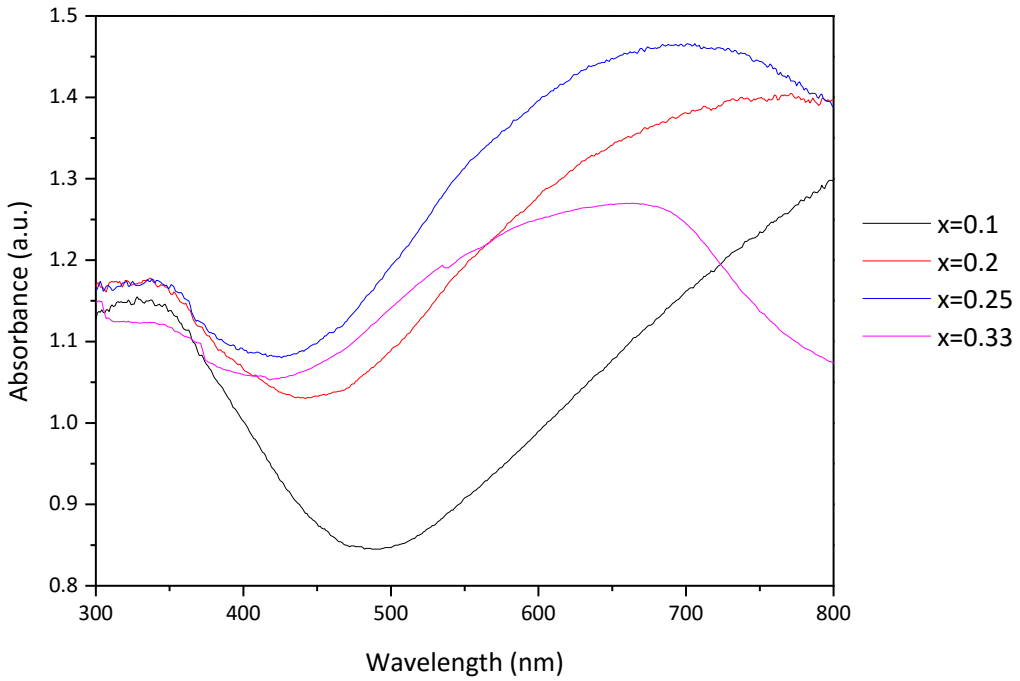

Figure 3.11 - Optical absorbance spectra in the visible region of Na_xWO_3 samples NaTB SS x = 0.1, SS2 x = 0.2, SS3 x = 0.25 and SS4 x = 0.33 synthesised by a solid state route.

The optical absorbance profiles of the solid state KTB and RbTB samples are shown in Figure 3.12.

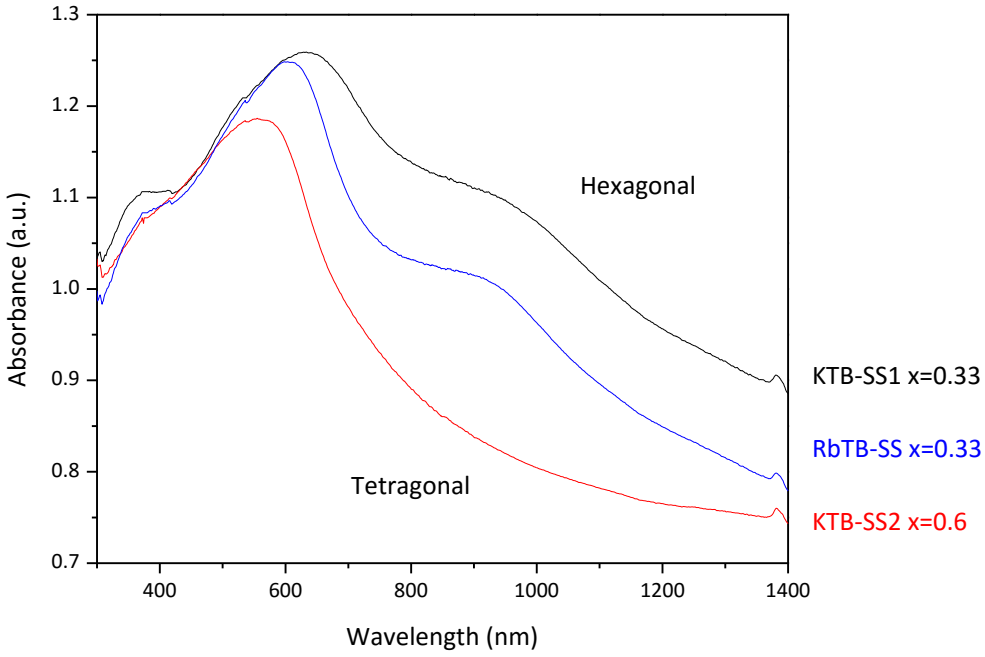

Figure 3.12- Optical absorbance profiles of tungsten bronzes M_xWO_3 with M=K, Rb made by a solid state route.

Again there is a difference in the optical absorbance profiles between different crystal structures. The samples with the hexagonal TB structure have two absorbance peaks whereas the tetragonal K sample only has one, with the main peak located in the visible region of the spectrum. The two absorbance peaks seen for the hexagonal KTB-SS1 and RbTB-SS samples arise from a combination of plasmon absorption, as discussed for the NaTB-SS samples above and polaron absorption. Polarons are localised charges which 'hop' to non-equivalent neighbouring sites on irradiation with light. The dominant peak is due to plasmon resonance as for the NaTB samples above.

The smaller 'shoulder' peaks seen in the hexagonal samples arise from polaron absorption. It is possible that this peak is not seen in the tetragonal sample because its higher *x* value of 0.6 provides too great a number of charge carriers to form localised polarons without their wavefunctions overlapping significantly. In order for polaron hopping to occur there must be neighbouring inequivalent sites which would not be the case if a large number of the electrons were localised. It is possible that there is a small contribution from polaron absorption that is hidden under the large broad plasmon peak. The KTB-SS1 sample profile differs from the KTB-ST sample (Figure 3.9) by having a less broad absorbance peak that decreases in intensity in the NIR region compared to the KTB-ST one which decreases much more gradually.

3.3.3 Scanning Electron Microscopy (SEM)

3.3.3.1 Solvothermal samples

The particle morphology of the samples was investigated using SEM of gold-coated powders on carbon tape attached to aluminium stubs. The resulting images are shown in Figure 3.13 and the scale bars on all images represent 500 nm. It can be seen that there is a range of different morphologies present in the samples however all are composed of relatively small particles (<100 nm in at least one direction).

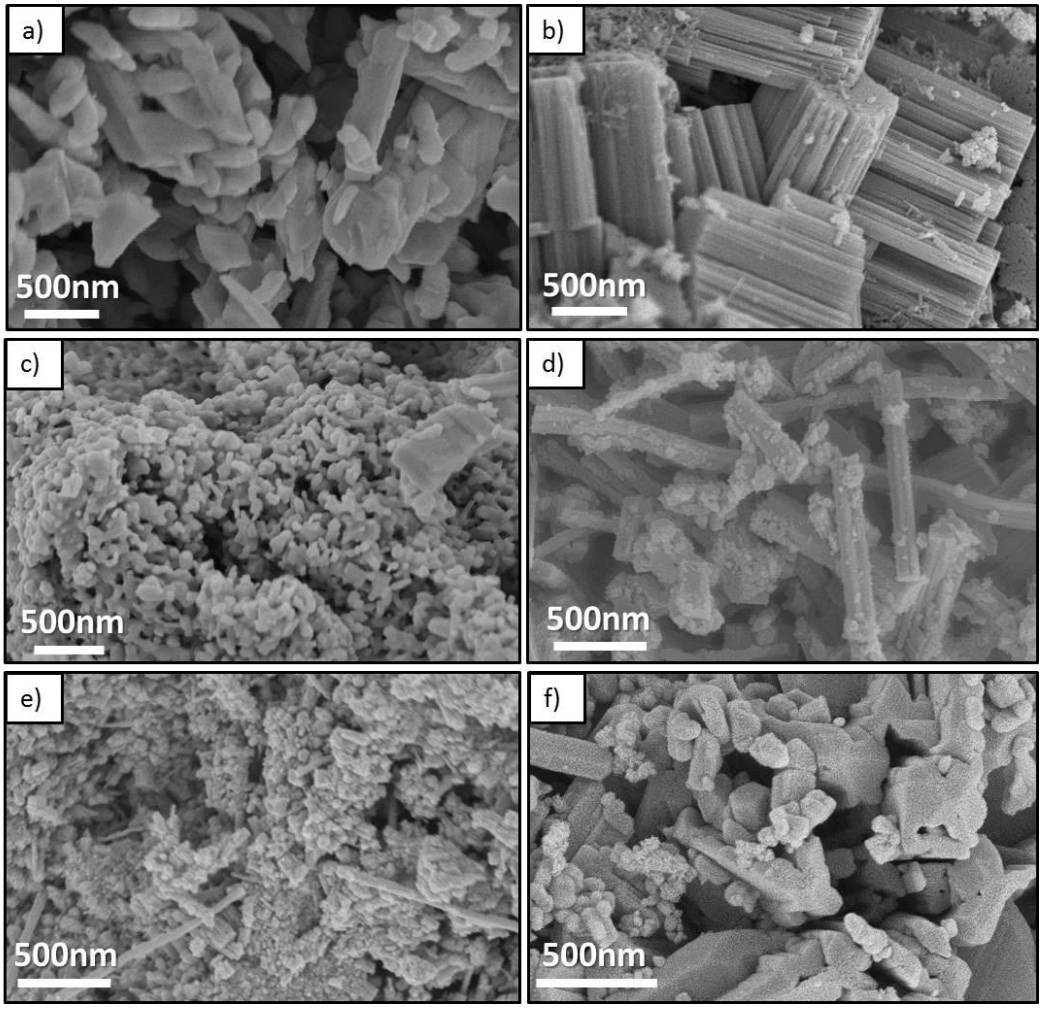

Figure 3.13 - SEM images of solvothermal tungsten bronzes a) NaTB-ST1, b) NaTB-ST2, c) KTB-ST, d) RbTB-ST, e) ATB-ST and f) TTB-ST.

Table 3.4 shows the crystallite size of the solvothermal samples calculated from PXRD data using the Scherrer equation along with the particle sizes estimated from SEM images. The surface areas were also measured using the BET method.

Table 3.4 - Particle sizes and surface area of solvothermal tungsten bronze samples

Sample	Scherrer crystallite size (nm)	SEM particle size (nm)	S.A. (m^2g^{-1})
NaTB-ST1	57.4 ± 19.7	50-1000	4.4
NaTB-ST2	61.9 ± 21.0	20-1200	24.9
KTB-ST	60.6 ± 14.9	100-800	4.8
RbTB-ST	63.8 ± 17.2	50-4000	34.0
ATB-ST	50.8 ± 13.6	50-2000	2.8
TTB-ST	64.7 ± 16.4	50-500	5.3

The Scherrer crystallite size values are an average of the values calculated from the full-width half-maximum of the peaks in the X-ray diffractograms. The error values represent the standard deviation of the range and are noticeably large. However this is indicative of the inhomogeneity of the samples. From the SEM images it can be seen that none of the samples are fully uniform in size and shape. The Scherrer equation is also based on a number of assumptions such as spherical particle shape which do not apply here. The range given in the SEM sizes is that of the smallest visible particles or the smallest dimension of a particle to the largest (e.g. the width and the length of the NaTB-ST2 nanowires). The surface area measurements have similar values for all samples apart from the NaTB-ST2 and RbTB-ST ones which are an order of magnitude higher. These are the two samples which display clear nanorod morphology in Figure 3.13. Although they do not have such defined morphology, the KTB-ST particles are the smallest overall but are arranged into larger agglomerates.

3.3.3.2 Solid state samples

The SEM images of the solid state NaTB samples are shown in Figure 3.14. NaTB-SS1-SS5 samples in Figure 3.14a-e are all composed of large agglomerates of small particles. They are relatively homogeneous in the 100nm size region but do not have any clearly defined shape apart from some rod-shaped particles visible in the NaTB-SS3 sample. The NaTB-SS6 and SS7 cubic phases in Fig 3.14f and 3.14g are clearly different. The agglomerated particles are much larger with a range of sizes and are well-defined cube shapes, reflecting the underlying crystal structure.

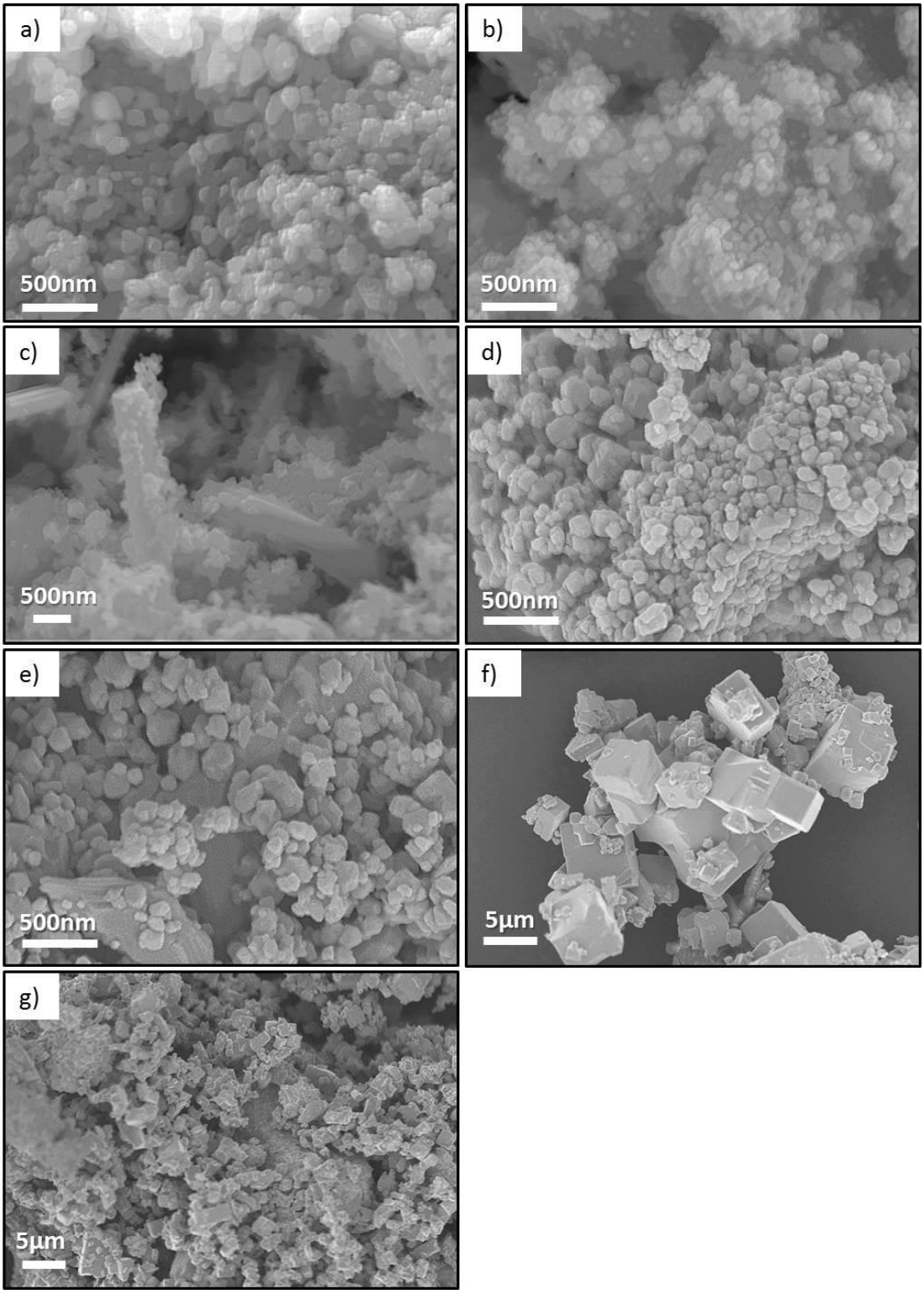

Figure 3.14 - SEM images of solid state Na_xWO_3 samples with different values of x a) SS1 x=0.1, b) SS2 x=0.2, c) SS3 x=0.25, d) SS4 x=0.33, e) SS5 x=0.4, f) SS6 x=0.6 and g) SS7 x=0.8.

The images of the KTB and RbTB-SS samples are shown in Figure 3.15. These three samples all show an elongated morphology with a mixture of large rods and smaller particles. Unlike the NaTB-SS samples, there is not a clear change in particle size or shape between the

different crystal structures of KTB-SS1 (hexagonal) and KTB-SS2 (tetragonal) although the SS2 particles are perhaps slightly larger. Like the NaTB-SS6 and SS7 samples, the particles are much larger than those seen in the other NaTB samples with lower values of *x*. The KTB-SS particles are much larger than those of KTB-ST. The small particles of KTB-ST have much more significant surface-to-bulk ratio so LSPR absorption is seen and shifts the main absorbance peak towards the NIR region.

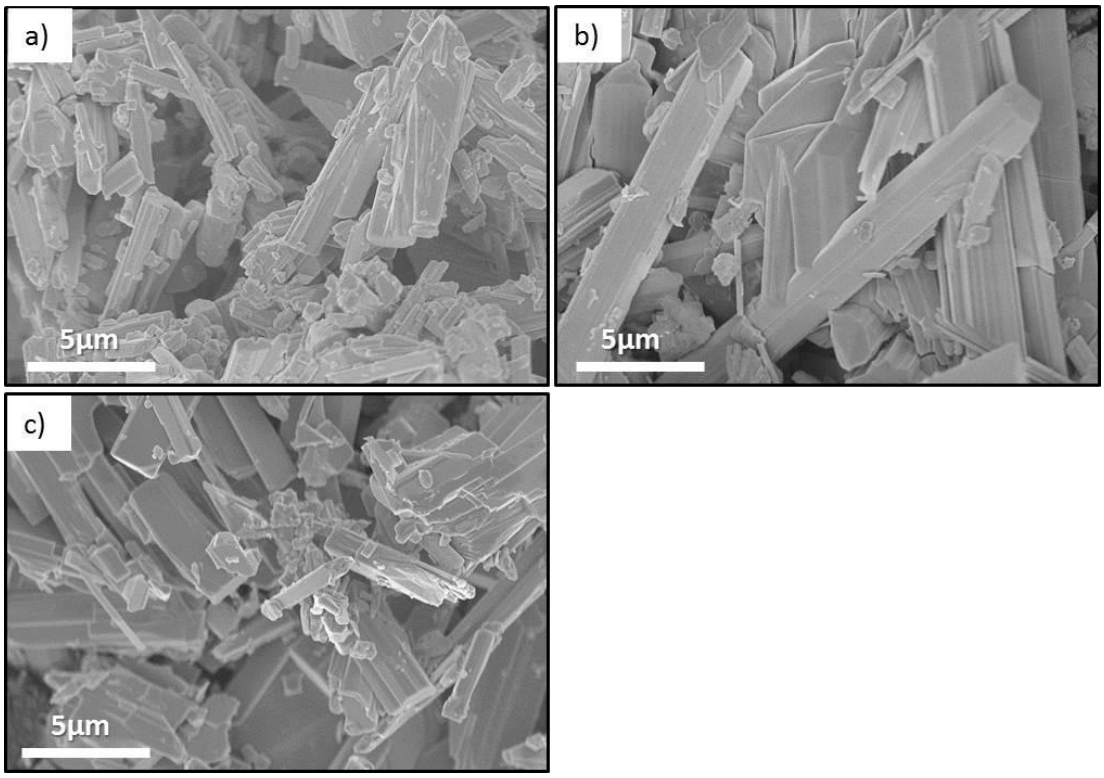

Figure 3.15 - SEM images of tungsten bronzes a) KTB-SS1, b) KTB-SS2 and c) RbTB-SS.

3.3.4 Energy Dispersive X-ray Spectroscopy Elemental Analysis (EDX)

Since the tungsten bronzes are chemically inert, they are difficult to dissolve. Inductively coupled plasma mass spectroscopy (ICP-MS) was attempted but the results thought to be unreliable. To investigate sample composition EDX was used as it can be performed on solid samples, in this case powder samples mounted on carbon tape on aluminium holders and coated with a thin layer of gold. Measurements were taken on a range of sites in each sample. The average ratio of W to M in M_xWO_3 is shown in Table 3.5 with standard deviation values as the error for each sample.

Table 3.5 - M content in tungsten bronzes M_xWO_3 taken from M:W atomic ratios from SEM EDX measurements. Around 10 areas were measured for each sample and the error represents the standard deviation of M:W ratio across the range of areas.

Sample	Nominal x	Average x	Sample	Nominal x	Average x
NaTB-ST1	0.33	0.21 ± 0.016	NaTB-SS1	0.1	0.10 ± 0.008
NaTB-ST2	0.33	0.22 ± 0.021	NaTB-SS2	0.2	0.19 ± 0.033
KTB-ST	0.33	0.29 ± 0.034	NaTB-SS3	0.25	0.21 ± 0.066
RbTB-ST	0.33	0.27 ± 0.016	NaTB-SS4	0.33	0.31 ± 0.016
TTB-ST	0.33	0.30 ± 0.018	NaTB-SS5	0.4	0.37 ± 0.025
KTB-SS1	0.33	0.34 ± 0.065	NaTB-SS6	0.6	0.58 ± 0.022
KTB-SS2	0.6	0.86 ± 0.068	NaTB-SS7	0.8	0.73 ± 0.022
RbTB-SS	0.33	0.31 ± 0.016			

The measured value of x is close to the nominal value, within error, for the majority of samples. The exceptions are the NaTB-ST1 and ST2 samples which were discussed in section 3.3.1. The lower Na content is attributed to the presence of an impurity phase in ST1, the presence of water molecules in the channels in ST2 and the possibility of the formation of soluble side products in both syntheses. KTB-SS2 is the only sample to show a considerably higher measured x value compared to the nominal value. The cause of this is unclear.

3.4 Results of Laser Imaging

The NIR absorber samples were tested for laser imaging performance at the Datalase laboratories. The testing procedure is detailed in Chapter 2, section 4. Optical density values are indicators of performance - the darker the created image compared to the background colour, the better the performance. The OD of the uncoated PET is 0.09 so the closer the background OD to this value the better.

3.4.1 Solvothermal samples

Figure 3.16 shows the background OD and highest ΔOD (OD of the images) values for each sample. The irradiation was repeated four times so the values represent the average of the four repeats and the error bars show the standard deviation of the range.

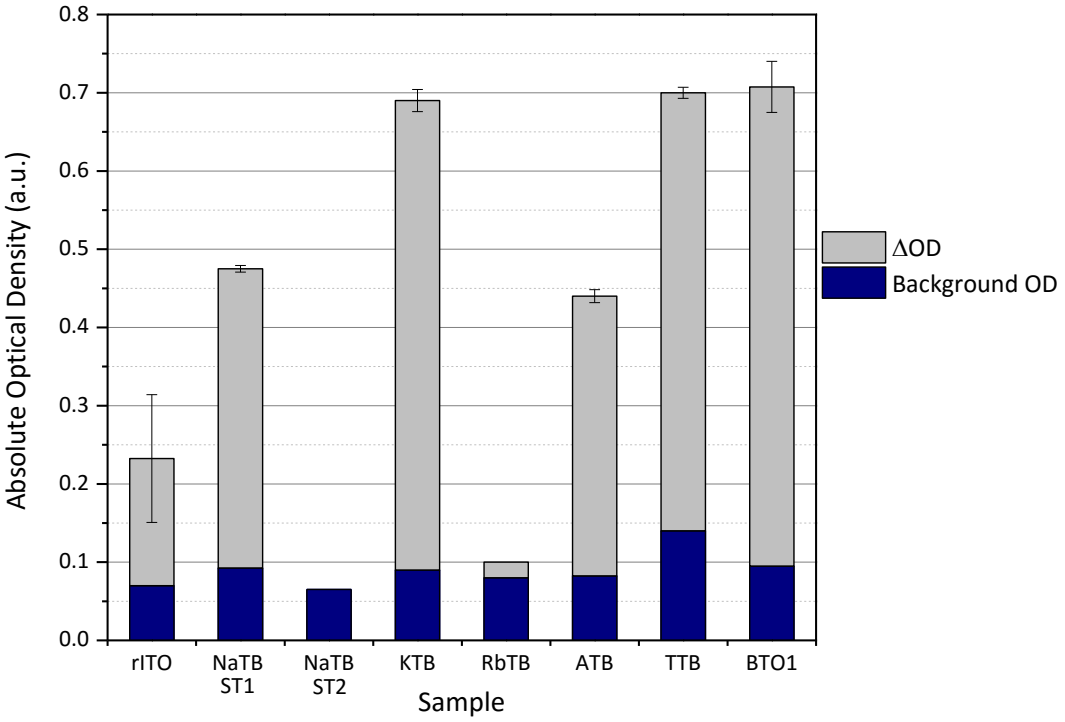

Figure 3.16 - Optical density values resulting from laser imaging tests of M_xWO_3 samples synthesised solvothermally. Commercial samples rITO and BTO1 are shown for comparison. All samples reached the highest ΔOD at 4.6 Jcm^{-2}.

It can be seen for this series of samples that there is variation in both background colour and the best optical density values (ΔOD) between samples. The values for reduced indium tin oxide rITO (the material to be replaced) and BTO1 (the tungsten bronze based commercial sample) under the same conditions have also been included for comparison. At first glance the highest ΔOD of images made using rITO as the NIR absorber would seem to be very low for a leading material but these results were created using a 1070 nm laser and rITO performs better at 1550 nm. Also in commercial applications more of the sample is used i.e. a higher concentration of the absorber in the ink which improves performance for rITO. However testing conditions in this work were standardised (see Chapter 2) in order to find a reliable way to compare samples so the rITO sample was also subject to these conditions. Therefore it is perhaps not surprising that all tungsten bronze samples show improved performance compared to rITO. The BTO1 sample however shows comparable performance to the best solvothermal samples albeit with a higher error value indicating less reproducible results.

The samples made in this work have extremely varied performance. It can be seen that the background colours are all relatively low – as mentioned above the OD of the PET substrate

alone is 0.09. The sample that gives the darkest background coating is tin tungsten bronze (TTB-ST) and this affects its performance. The TTB-ST sample had the strongest visible absorbance in Figure 3.9. Although the absolute OD value is relatively high, the high background OD contributes to this and the images created do not have as good a contrast with the background as other samples. The NaTB-ST1 and ATB-ST samples have pale background coatings with intermediate ΔOD values. The NaTB-ST2 and RbTB-ST samples hardly image at all. The reason for its particularly poor performance of RbTB-ST is unclear since it showed similar NIR absorbance to NaTB-ST1 and ATB-ST samples. The NaTB-ST2 sample had the lowest NIR absorbance of all the samples so poorer performance could be expected. The KTB-ST sample clearly shows the best performance with an acceptably low background coupled with high ΔOD. Its small particle size and high NIR absorbance are likely to be contributing factors to its performance.

3.4.2 Solid state samples

Figure 3.17 shows the results for the series of solid state NaTB samples.

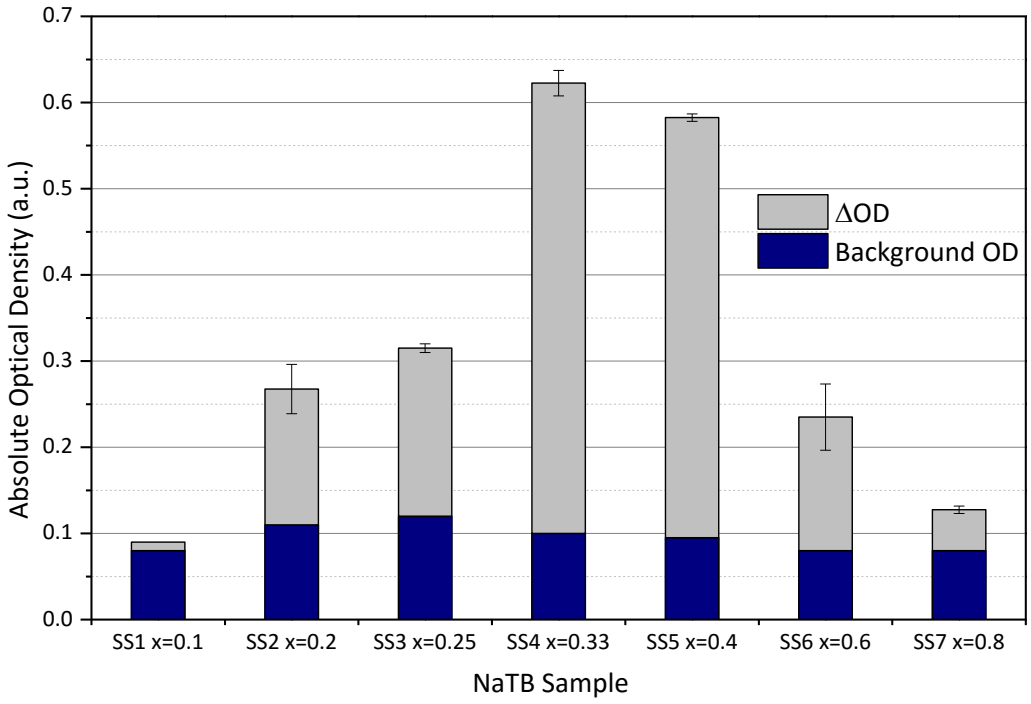

Figure 3.17 - Optical density values resulting from laser imaging tests of solid state Na_xWO_3 samples with different nominal values of x. All samples reached the highest ΔOD at 4.6 Jcm^{-2}.

There are clear differences in performance with varying *x* with a definite peak in ΔOD at x = 0.33. SS1 has the lowest Na content and shows the lowest ΔOD. Since the addition of Na causes W atoms to reduce from 6+ to 5+ and donate an electron to the conduction band,

the is perhaps too little Na in this sample to reduce a sufficient amount of W^{6+} for good NIR absorption. SS2 and SS3 show slightly higher ΔOD values but also have higher background OD values. There is a clear 'jump' in performance between SS3 and SS4. SS4 is the first sample to form the tetragonal II crystal structure and it seems this makes a difference to the performance because the two samples containing it (SS4, SS5) significantly outperform those of other crystal structures.

The laser imaging results correlate reasonably well with the optical spectra seen in Figure 3.10. The mixed tetragonal/cubic SS4 and SS5 samples absorb significantly more NIR radiation than the pure cubic SS6 and SS7 phases and so have much higher ΔOD values. NIR data is not available for NaTB-SS1, SS2 and SS3 samples so cannot be commented on. There could also be a particle size effect, as it was seen with the solvothermal samples that KTB-ST with the smallest particle size gave the best performance. NaTB-SS6 and SS7 have high Na content but, as was seen in Figure 3.14, they are composed of particles nearly an order of magnitude larger than those of SS4 and SS5. It is probable that small particle size aids even distribution within the ink and ensures a high level of contact between the absorber and pigment.

The laser imaging results of KTB-SS1, SS2 and RbTB-SS samples are shown in Figure 3.18. There is no real trend with composition seen for the KTB-SS samples as was seen for the NaTB-SS samples. The KTB-SS1, SS2 and RbTB-SS samples all give low background OD values but they have similar ΔOD values which are not particularly high or low. For KTB-SS1 the ΔOD value is lower than that of its solvothermal counterpart whereas RbTB-SS performs considerably better than RbTB-ST. Compared to the KTB-ST and RbTB-ST samples, the optical absorbance spectra of the SS samples have lower absorbance in the NIR region so lower ΔOD values could be expected.

As mentioned for the SS NaTB's, the larger particle size of KTB-SS1, SS2 and RbTB-SS samples could also be a factor. It would be interesting in future to see if the particle size of the solid state samples can be reduced, e.g. by milling, and if this would lead to an improvement in performance.

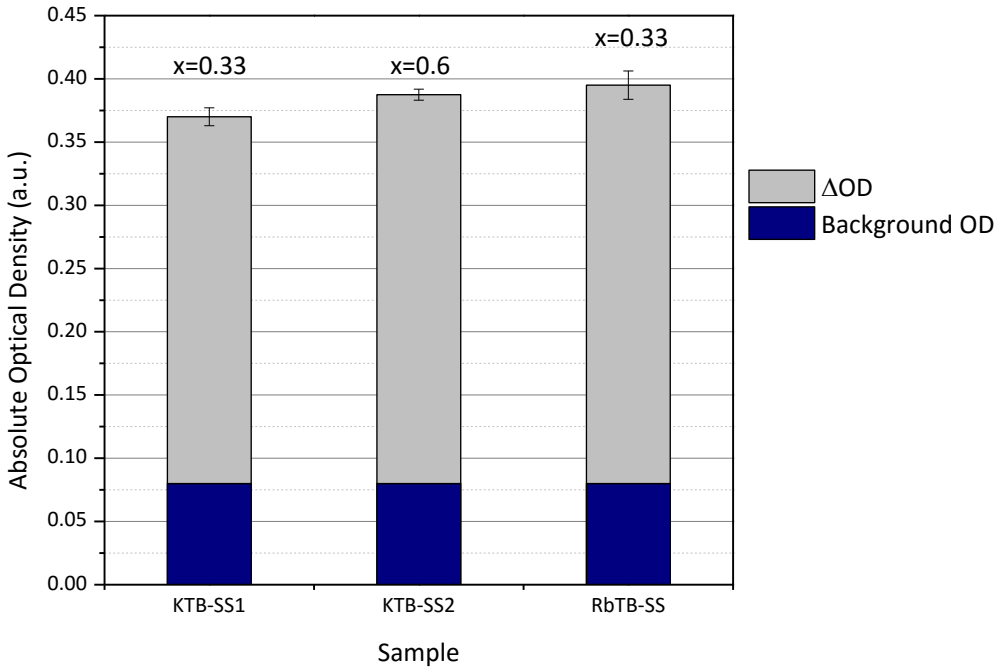

Figure 3.18 - Optical density values resulting from laser imaging tests of solid state NaxWO3 samples with different nominal values of x. All samples reached the highest ΔOD at 4.6Jcm^{-2}.

For ease of comparison the best solvothermal sample (KTB-ST) is shown next to the best solid state sample (NaTB-SS4) and BTO1 in Figure 3.19. These samples show high enough ΔOD and low enough background OD to be used commercially as NIR absorbers.

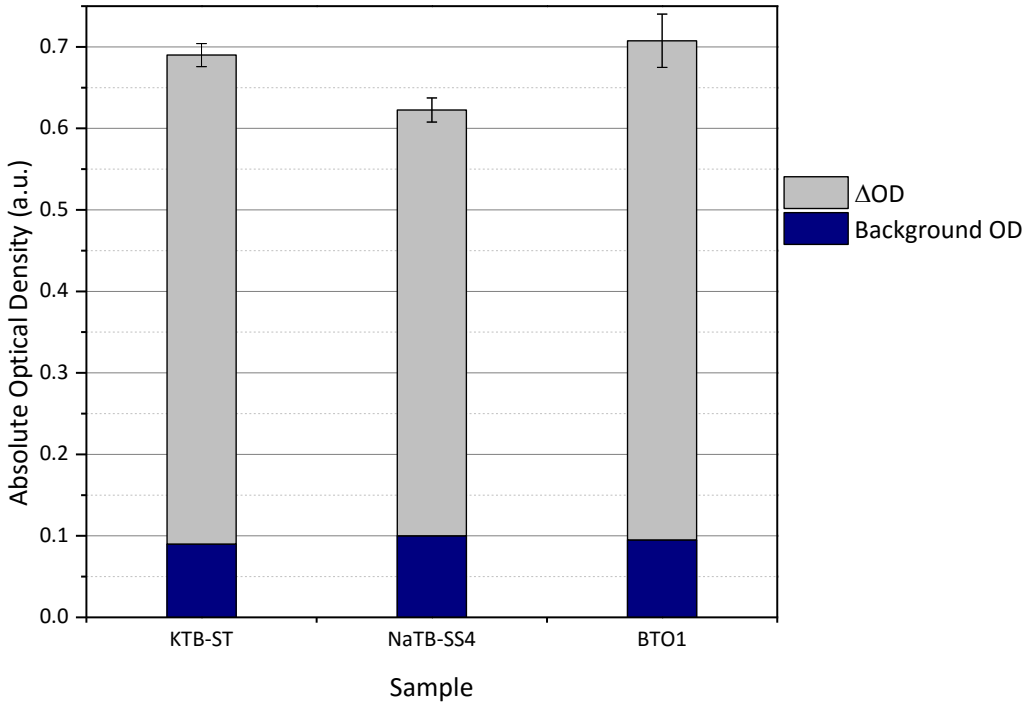

Figure 3.19 - Optical density values of the best solvothermal and solid state M_xWO_3 samples compared to commercial sample BTO1.

3.5 Conclusion

As a family, the tungsten bronzes generally perform well as near infrared absorbers in the Datalase imaging process compared to commercial samples analysed in Appendix 1. It is clear that synthesis conditions make a significant difference to properties with samples made by solvothermal routes having much higher NIR absorbance than samples made by solid state routes. Despite this NaTB-SS sample with x = 0.33 performs well. This is the optimum value of x for the NaTB-SS samples. With less Na present there is not enough W^{6+} reduced to W^{5+} to cause sufficient absorbance but at higher values of x the optical absorbance is shifted too much into the visible region to absorb enough NIR radiation.

There is no clear trend seen in performance as the alkali metals increase in size but the choice of M species and the value of x affects the resulting crystal structure. Using a divalent metal cation (Sn^{2+}) offered no benefit over the monovalent alkali metal samples because its high visible absorbance resulted in very dark coatings. Particle size is a factor that could be investigated further since all the samples that perform well are composed of relatively small particles.

3.6 References

1. Wohler, F., *Pogg. Ann.* **1824,** *2*, 350.
2. (a) Magneli, A., Crystal structure of tetragonal potassium bronze. *Arkiv foer Kemi* **1949,** *1*; (b) Straumanis, M. E., *Journal of the American Chemical Society* **1949,** *71*; (c) Magneli, A., studies on the Hexagonal Tungsten Bronzes of Potassium, Rubidium and Cesium. *Acta Chem. Scand.* **1953,** *7*.
3. Takeda, H.; Adachi, K., Near Infrared Absorption of Tungsten Oxide Nanoparticle Dispersions. *J Am Ceram Soc* **2007,** *90* (12), 4059-4061.
4. (a) Guo, C.; Yin, S.; Dong, Q.; Sato, T., Simple route to $(NH_4)_xWO_3$ nanorods for near infrared absorption. *Nanoscale* **2012,** *4* (11), 3394-3398; (b) Guo, C.; Yin, S.; Zhang, P.; Yan, M.; Adachi, K.; Chonan, T.; Sato, T., Novel synthesis of homogenous Cs_xWO_3 nanorods with excellent NIR shielding properties by a water controlled-release solvothermal process. *J Mater Chem* **2010,** *20* (38), 8227-8229; (c) Guo, C.; Yin, S.; Huang, L.; Sato, T., Synthesis of One-Dimensional Potassium Tungsten Bronze with Excellent near-Infrared Absorption Property. *ACS Applied Materials & Interfaces* **2011,** *3* (7), 2794-2799.
5. Wang, L.; Zhan, J.; Fan, W.; Cui, G.; Sun, H.; Zhuo, L.; Zhao, X.; Tang, B., Microcrystalline sodium tungsten bronze nanowire bundles as efficient visible light-responsive photocatalysts. *Chemical Communications* **2010,** *46* (46), 8833-8835.
6. Guo, C.; Yin, S.; Dong, Q.; Sato, T., Near-infrared absorption properties of Rb_xWO_3 nanoparticles. *CrystEngComm* **2012,** *14* (22), 7727-7732.
7. McColm, I. J.; Steadman, R.; Howe, A., Preparation, structure, and Mössbauer spectra of tin tungsten bronzes. *J Solid State Chem* **1970,** *2* (4), 555-562.
8. (a) Xu, X.-L.; Günter, J. R., Cubic and hexagonal tin tungsten bronzes synthesized from peroxo-polytungstic acid. *Solid State Ionics* **1994,** *74* (1–2), 1-3; (b) Xu, X.-L.; Schmalle, H. W.; R. Günter, J., Crystal structure of a hexagonal tin tungsten bronze prepared by a mild reaction. *Solid State Ionics* **1995,** *76* (3–4), 221-228.
9. Leonova, L. S.; Levchenko, A. V.; Moskvina, E. I.; Tkacheva, N. S.; Aleshina, T. N.; Nadkhina, S. E.; Kolesnikova, A. M.; Dobrovol'skii, Y. A.; Bukun, N. G., Tungsten oxide bronzes with alkali metals. *Russ J Electrochem* **2009,** *45* (5), 593-601.
10. Bartha, L.; Kiss, A. B.; Szalay, T., Chemistry of tungsten oxide bronzes. *International Journal of Refractory Metals and Hard Materials* **1995,** *13* (1–3), 77-91.
11. A. S. Ribnick, B. P., E. Banks, Phase Transitions in Sodium Tungsten Bronzes. In *Nonstoichiometric Compounds*, American Chemical Society: 1963; Vol. 39, pp 246-253.
12. Magneli, A., Blomberg, B., Contribution to the Knowledge of the Alkali Tungsten Bronzes. *Acta Chem. Scand.* **1951,** *5*.
13. Gerand, B.; Nowogrocki, G.; Guenot, J.; Figlarz, M., Structural study of a new hexagonal form of tungsten trioxide. *J Solid State Chem* **1979,** *29* (3), 429-434.
14. Reis, K. P.; Prince, E.; Whittingham, M. S., Rietveld analysis of sodium tungstate hydrate $Na_xWO_{3+x/2}.yH_2O$, which has the hexagonal tungsten bronze structure. *Chem Mater* **1992,** *4* (2), 307-312.
15. Pye, M. F.; Dickens, P. G., A structural study of the hexagonal potassium tungsten bronze, $K_{0.26}WO_3$. *Mater Res Bull* **1979,** *14* (11), 1397-1402.
16. Goreaud, M.; Labbe, P.; Raveau, B., A mixed-valence tungsten oxide of divalent tin: $Sn_{10}W_{16}O_{46}$. II. Analysis of the structure and stereoactivity of the Sn^{2+} lone pair. *Acta Crystallographica Section B* **1980,** *36* (1), 19-22.
17. Takusagawa, F.; Jacobson, R. A., Crystal structure studies of tetragonal sodium tungsten bronzes, Na_xWO_3. I. $Na_{0.33}WO_3$ and $Na_{0.48}WO_3$. *J Solid State Chem* **1976,** *18* (2), 163-174.

18. Gier, T. E.; Pease, D. C.; Sleight, A. W.; Bither, T. A., New lithium, ammonium, and tin hexagonal tungsten bronzes prepared hydrothermallly. *Inorganic Chemistry* **1968,** *7* (8), 1646-1647.
19. Brown, B. W.; Banks, E., The Sodium Tungsten Bronzes1,2. *Journal of the American Chemical Society* **1954,** *76* (4), 963-966.
20. Dickens, P. G.; Whittingham, M. S., The tungsten bronzes and related compounds. *Quarterly Reviews, Chemical Society* **1968,** *22* (1), 30-44.
21. Simon, A.; Ravez, J., Solid-state chemistry and non-linear properties of tetragonal tungsten bronzes materials. *Comptes Rendus Chimie* **2006,** *9* (10), 1268-1276.
22. Hussain, A., Phase Analyses of Potassium, Rubidium and Cesium Tungsten Bronzes. *Acta Chem Scand A* **1978,** *32* (6), 479-484.
23. Adachi, K.; Asahi, T., Activation of plasmons and polarons in solar control cesium tungsten bronze and reduced tungsten oxide nanoparticles. *J Mater Res* **2012,** *27* (06), 965-970.
24. Xue, Y.; Zhang, Y.; Zhang, P., Theory of the color change of Na_xWO_3 as a function of Na-charge doping. *Physical Review B* **2009,** *79* (20), 205113.

Chapter 4

Caesium Tungsten Bronzes

4.1 Introduction

After analysis of commercial samples in Appendix 1, the family of tungsten bronzes M_xWO_3 were chosen as promising candidates for near infrared (NIR) absorbers in laser imaging applications. The alkali metal tungsten bronzes M_xWO_3 (where M = Na, K, Rb, NH_4 and Sn) were dealt with in Chapter 3. This chapter reports on the synthesis, characterisation, testing and subsequent modification of the caesium tungsten bronzes, Cs_xWO_3.

4.2 Synthesis of Caesium Tungsten Bronzes

A caesium tungsten bronze was first prepared via a solid state route by heating appropriate amounts of caesium polytungstate and WO_2 under vacuum for periods of several days[1]. Electrolytic reduction of tungstates has also been widely used[2] to produce single crystals of the bronze phase. Caesium tungsten bronze was first synthesised solvothermally by Guo *et.al.* in 2010[3] using a so-called 'water controlled-release solvothermal process'. In this method, WCl_6 is dissolved in C_2H_5OH and an appropriate amount of $CsOH.H_2O$ added. It is acidified with CH_3COOH and heated for 20 h at 200 ^oC. It is thought that the esterification reaction between the ethanol and acetic acid releases water molecules slowly during the reaction which controls particle morphology. Both solvothermal and solid state routes have been used in this work and are detailed below.

4.2.1 Solvothermal Synthesis

Unless otherwise specified, heating and cooling rates of 10 ^oC/min were used. Distilled water and absolute ethanol were used as solvents/reactants. Starting materials were used as purchased and purities are given on a trace metals basis.

Initially the method of Guo *et. al.* was followed[3]. WCl_6 (Sigma Aldrich ≥ 99.9%, 0.3569 g, 9 x 10^{-4} mol) was dissolved in 50 ml C_2H_5OH to form a clear yellow solution and an appropriate amount of $CsOH.H_2O$ added (Alfa Aesar 99.9%, 0.0307 g, 3 x 10^{-4} mol). 12 ml CH_3COOH was added then the liner was transferred to a steel autoclave and heated for 20 h at 200 ^oC. The

blue product was collected by centrifugation, washed with H_2O and C_2H_5OH and dried at 60 ^oC in air.

The above method was successful but, similar to the method used for ammonium tungsten bronze (see Chapter 3), gave small amounts of product with each synthesis. It was made more concentrated to try to make more product for testing in one synthesis. Also it was noted that adding water caused a dark blue precipitate to form so this was explored by adding different amounts of water to the reaction mixture. The as-formed precipitate was also dried without heating and analysed. The finalised general synthesis was as follows.

ST1, ST2: WCl_6 (Sigma Aldrich ≥ 99.9%, 3.569 g, 9 x 10^{-3} mol) was dissolved in 25 ml C_2H_5OH to form a clear yellow solution. $CsOH.H_2O$ (Alfa Aesar 99.9%, 0.3071 g, 3 x 10^{-3} mol) was added along with 25 ml H_2O. At this stage a sample was centrifuged, dried and analysed. For other samples, the reaction mixture was transferred to Teflon-lined autoclaves (using a little extra H_2O for rinsing) and heated to 200 ^oC for 24 h. They were then centrifuged, washed with H_2O and dried in air.

ST3-6: To change the sample morphology benzyl alcohol C_6H_7OH was added into the solvent mixture. WCl_6 (Sigma Aldrich ≥ 99.9%, 3.569 g, 9 x 10^{-3} mol) was dissolved in C_2H_5OH to form a clear yellow solution. $CsOH.H_2O$ (Alfa Aesar 99.9%, mole ratio of WCl_6 to $CsOH.H_2O$ is 3:1) was added along with H_2O and C_6H_7OH. The reaction mixture was transferred to Teflon-lined autoclaves and heated to 180 ^oC for 24 h. They were then centrifuged, washed with H_2O and dried in air. The ratios of C_2H_5OH:H_2O: C_6H_7OH were varied but the overall solvent volume was kept constant at 75 ml. The amounts of WCl_6 and $CsOH.H_2O$ were also kept the same throughout. Once an optimum ratio was reached the benzyl alcohol was replaced with other organic species – see section 4.3.3.5.

ST7: Cs_2WO_4 (Alfa Aesar 99.9%, 3.0820 g, 6 x 10^{-3} mol) and Cs_2SO_4 (Alfa Aesar 99.99%, 4.3424 g, 0.012 mol) were dissolved in 60 ml water in a 125 ml Teflon liner. 70% HNO_3 was added dropwise until the pH=1.5. The liner was placed in a steel autoclave and heated to 200 ^oC for 24 h. Once separated by centrifugation, washed with H_2O and dried at 60 ^oC in air the yellowish product was ground with a pestle and mortar. It was heated in an Al_2O_3 crucible in a tube furnace to 500 ^oC for 2 h under flowing 5% H_2 in N_2 with a heating rate of 5 ^oC/min. The dark blue product was ground once more before analysis.

ST8: WCl_6 (Sigma Aldrich ≥ 99.9%, 3.569 g, 9 x 10^{-3} mol) was dissolved in 25 ml C_2H_5OH to form a clear yellow solution. $CsOH.H_2O$ (Alfa Aesar 99.9%, 3 x 10^{-3} mol, mole ratio of WCl_6 to $CsOH.H_2O$ is 3:1) was added along with 25 ml H_2O. The dark blue precipitate was centrifuged, dried and ground with a pestle and mortar. In an Al_2O_3 crucible, it was heated in a tube furnace to 500 ^oC for 2 h under flowing 5% H_2 in N_2 with a heating rate of 5 ^oC/min.

4.2.2 Solid State Synthesis

In order to get pure products, different combinations of starting materials were used but the most successful route is described below.

SS1, SS2: H_2WO_4 (Sigma Aldrich 99.99%) was placed in a planetary milling pot with an appropriate amount of $CsCO_3$ (Sigma Aldrich 99.9%), 8x5 mm zirconia balls and propan-2-ol then milled overnight. This mixture was heated in an evaporating dish to remove the solvent then the dry mixture placed in an Al_2O_3 boat crucible. This was heated in an electric tube furnace at 500 ^oC for 1 h under flowing 5% H_2 in N_2. It was cooled naturally then ground briefly using a pestle and mortar before analysis. Nominal sample compositions had several values of x in Cs_xWO_3, namely 0.15, 0.2, 0.25 and 0.33 and the reaction was carried out on a 1 g scale.

Sample names to be used subsequently are listed in Table 4.1.

Table 4.1 – Summary of Cs_xWO_3 samples

Sample	Synthesis	Comments
CsTB-ST1	Precipitation	EtOH + H_2O; No heating step
CsTB-ST2	Solvothermal	EtOH + H_2O; 200 ^oC 24 h
CsTB-ST3	Solvothermal	EtOH:H_2O:BnOH 1:1:1; 180 ^oC 24 h
CsTB-ST4	Solvothermal	EtOH:H_2O:BnOH 4:1:2.5; 180 ^oC 24 h
CsTB-ST5	Solvothermal	EtOH:H_2O:BnOH 1:2.5:4; 180 ^oC 24 h
CsTB-ST6	Solvothermal	EtOH:H_2O:Hydroquinone 4:1:2.5; 180 ^oC 24 h
CsTB-ST7	Solvothermal + solid state	KTB method with Cs precursors
CsTB-ST8	Solvothermal + solid state	Precipitate reduced in tube furnace
CsTB-SS1	Solid state	x = 0.25

CsTB-SS2	Solid state	x = 0.33

4.3 Characterisation and Results

4.3.1 Effect of Sample Crystallinity

4.3.1.1 Powder X-ray Diffraction (PXRD)

The PXRD patterns of the precipitated sample CsTB-ST1 and the CsTB-ST2 sample which was heated at 200 °C for 24 h are shown in Figure 4.1.

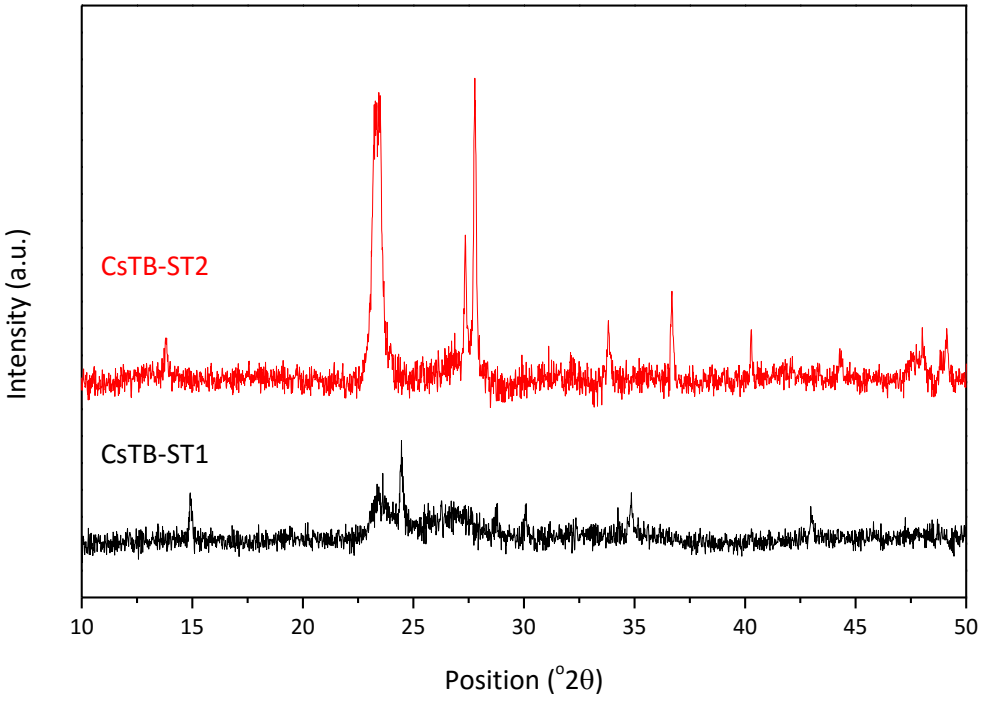

Figure 4.1 - PXRD diffractograms of Cs_xWO_3 samples CsTB-ST1 and CsTB-ST2.

It is clear that the heating step is essential for product crystallisation as the dry unheated precipitate sample gives a poorly crystalline product with 'peaks' that are difficult to distinguish from background noise. Although it also has a noisy background, CsTB-ST2 has discernible peaks which match well to the pattern of hexagonal $Cs_{0.32}WO_3$ (JCPSD number 01-083-1334, from Kihlborg and Hussain[4]) in space group $P6_3/mcm$. The structure of the caesium tungsten bronze is the same as that of the other hexagonal bronzes discussed in Chapter 3 – WO_6 octahedra corner-linked in an arrangement that forms hexagonal channels along the c-axis in which the Cs atoms reside, shown in Figure 4.2. The caesium atoms lie out-of-plane with regards to the tungsten atoms.

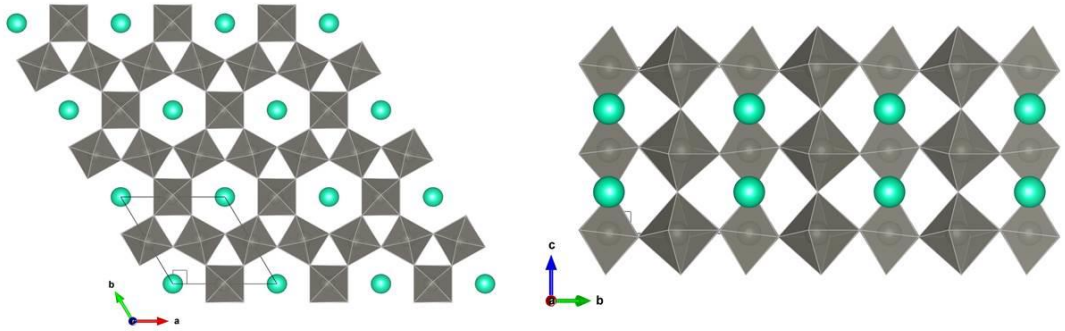

Figure 4.2 - Polyhedral representation of the hexagonal crystal structure of Cs_xWO_3. W=grey, Cs=green.

4.3.1.2 UV-vis-NIR spectroscopy

The optical absorption spectra of CsTB-ST1 and CsTB-ST2 are shown in Figure 4.3. It can be seen that both samples exhibit a broad absorbance peak in the near infrared region, extending partway into the visible region. The absorbance of visible red and orange wavelengths accounts for the blue colour of the samples. The more crystalline CsTB-ST2 sample has increased absorbance intensity across the spectrum but the features of the profiles do not differ significantly between samples.

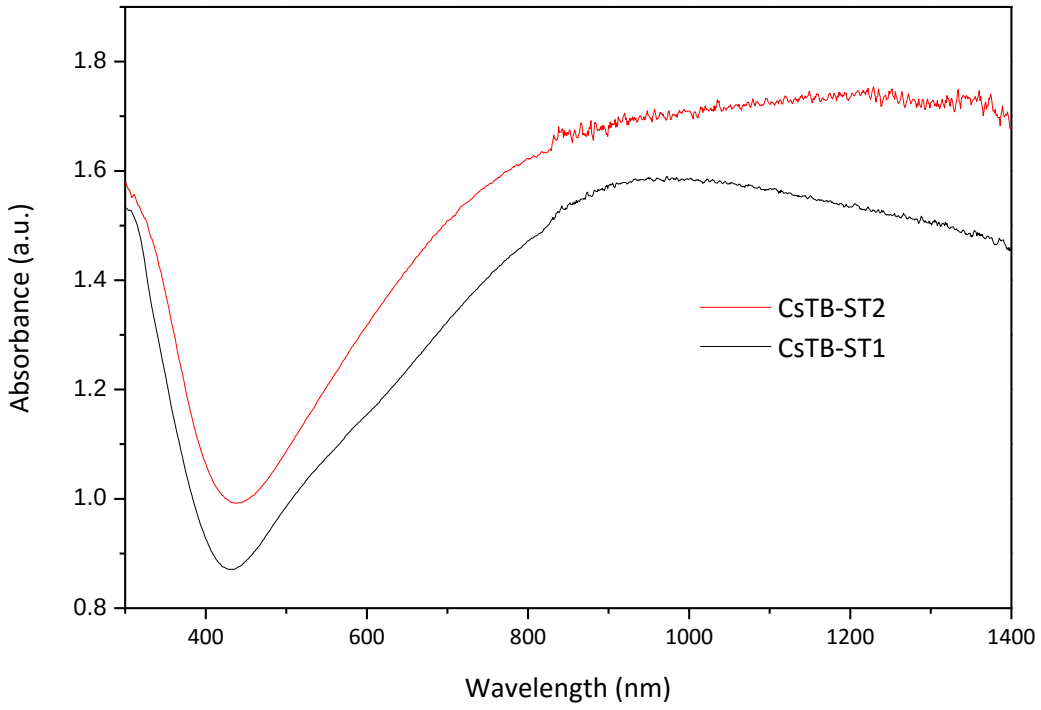

Figure 4.3 - Optical absorbance profiles of Cs_xWO_3 samples made by solvothermal synthesis.

As discussed in Chapter 3, the mechanism of NIR absorbance in tungsten bronzes is a combination of polaron hopping and localised surface plasmon resonance. As there is little observed difference in the optical absorbance profiles it would seem that both mechanisms are present in both samples.

4.3.1.3 Results of laser imaging

Both samples were tested at Datalase for laser imaging performance following the testing procedure described in Chapter 2.4. Optical density values are indicators of performance - the darker the created image compared to the background colour, the better the performance. The results are shown in Figure 4.4 with the commercial caesium tungsten bronze based sample BTO1 for comparison.

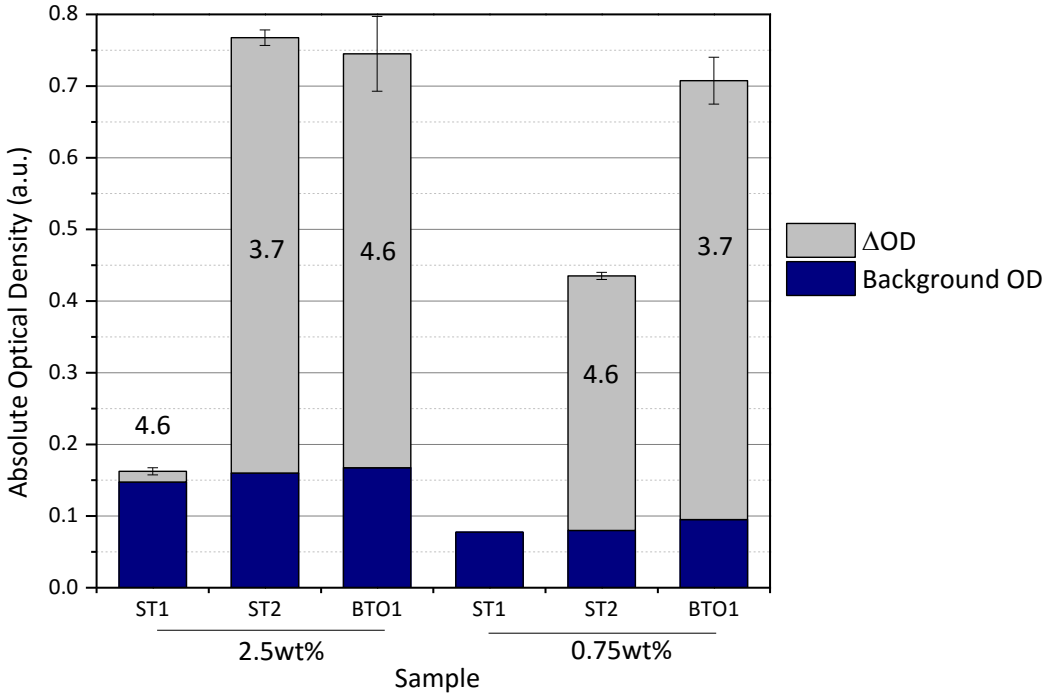

Figure 4.4 - Optical density values resulting from laser imaging tests for Cs_xWO_3 samples made by solvothermal synthesis compared to commercial sample BTO1. The numbers on the bars are the laser fluences in Jcm^{-2} at which the highest ΔOD was reached for each sample.

Two loading concentrations of absorber in ink were used – 2.5 wt% and 0.75 wt%. It can be seen that the background OD is similar for both CsTB-ST samples at both concentrations but the OD values are lower at 0.75 wt% loading as might be expected. However the optical density of images formed under laser irradiation (ΔOD) differs significantly between samples. The amorphous CsTB-ST1 sample has very low ΔOD values, particularly at 0.75 wt% where it does not image at all. The crystalline hexagonal CsTB-ST2 sample gives a much

higher maximum ΔOD at both concentrations, although again the value is lower at 0.75 wt% than 2.5 wt%.

From these results it can be surmised that a crystalline atomic structure is necessary for laser image creation. Since the optical absorbance profiles for both samples are quite similar they should absorb similar amounts of NIR radiation therefore the crystal structure must aid the process of heat transfer from the NIR absorber to the pigment particles distributed through the ink coating. The commercial BTO1 sample shows similar performance to the CsTB-ST2 sample at 2.5wt% loading however at 0.75 wt% it performs better than either CsTB sample. This suggests that performance of these samples can still be improved. However the error values of the BTO1 sample are larger than for CsTB-ST2 which suggests that its performance is less reproducible.

4.3.2 Effect of Pyrochlore Tungstate Phase

From the analysis in Appendix 1, it was seen the BTO1 sample contains the hexagonal caesium tungsten bronze phase but also an amount of a cubic pyrochlore caesium tungstate CsW_2O_6. The crystal structure of this phase is shown in Figure A.1.4. In order to see if the pyrochlore phase plays a role, it was also synthesised. The same route used to make CsTB-ST2, above, was used but the pH was raised to obtain the cubic pyrochlore product. Reis *et. al*.[5] give the relationship between pH and structure formed for sodium analogues. The pyrochlore product forms in the range 3.5-4.5. The PXRD diffractogram is shown in Figure 4.5.

The cubic phase shows no impurity peaks. The diffractograms of commercial sample BTO1 and a mixture of CsTB-ST2 and the pyrochlore tungstate are shown. Although the peaks are sharper for BTO1, it can be seen that the positions of the cubic pyrochlore match those of the secondary phase in BTO1 well and all the peaks of the mixed hexagonal and cubic phases correspond to those of BTO1.

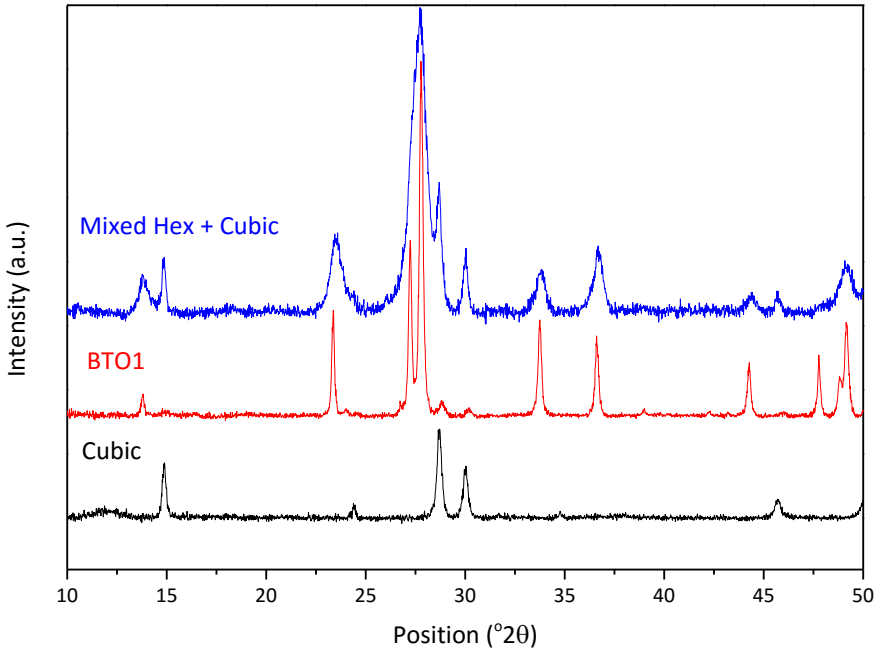

Figure 4.5 - PXRD diffractograms of cubic pyrochlore CsW_2O_6, mixed phase commercial sample BTO1 and a physically mixed sample of hexagonal Cs_xWO_3 and Cs_2WO_6.

When the optical absorbance profile of the mixed hexagonal and cubic phase was measured, the only effect of the pyrochlore phase was to reduce the absorbance intensity compared to the hexagonal phase alone (see Figure A.3.1). Since the pyrochlore phase alone does not show significant absorbance in the visible-NIR region it has 'diluted' the CsTB sample. The BTO1 optical absorbance profile does not match either the pyrochlore or the mixed hexagonal bronze and pyrochlore profiles. Its main peak is shifted towards the visible region and is more in keeping with samples synthesised by solid state routes (see section 4.3.4, below).

4.3.3 Modification of morphology

The sample morphology affects the amount of surface area available for localised surface plasmon resonance (LSPR) interaction with incident radiation from the laser so could alter the plasmon frequency and intensity. Smaller particles have been found to increase visible transparency due to a decrease in the amount of light scattering[5]. Guo *et. al.* in particular found that tungsten bronzes in nanorod form are highly effective NIR absorbers[3, 6].

4.3.3.1 Synthesis

In order to investigate effects of sample morphology on performance, the basic solvothermal synthesis outlined above was modified by changing the solvent mixture. From the literature it was noted that benzyl alcohol C_6H_5OH has been used as a structure directing agent in syntheses of WO_3[8] so could also have an effect in tungsten bronze synthesis. The total solvent volume was kept at 75ml but the ratio of water-ethanol-benzyl alcohol was varied and the ratios are shown in a ternary diagram in Figure 4.6. WCl_6 and $CsOH.H_2O$ were used as starting materials in all cases. Although the points are difficult to discern, samples were also prepared using 100% of each solvent (indicated by numbers 11, 12 and 13).

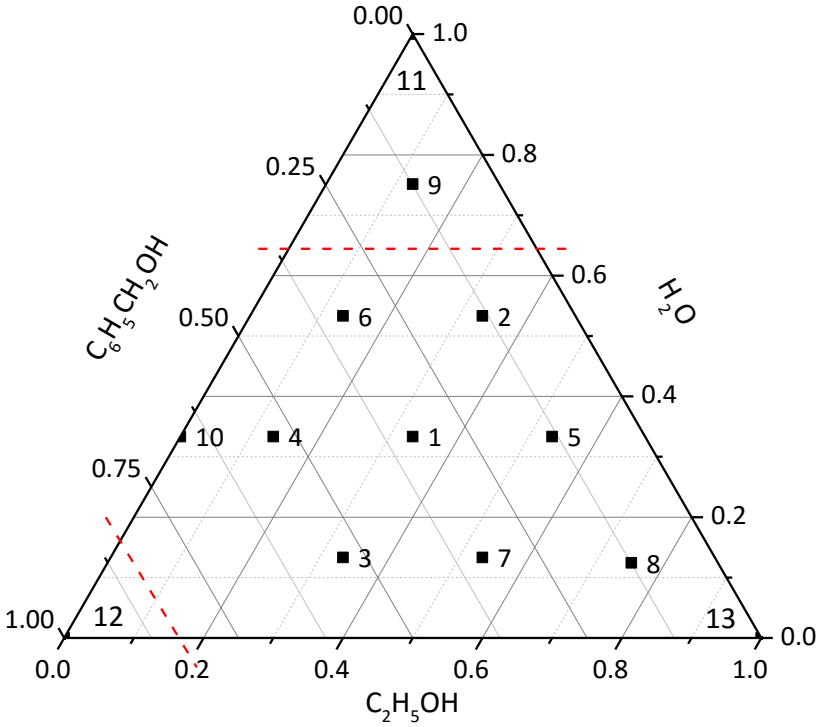

Figure 4.6 - Ternary diagram representing the reaction space explored by varying the ratio of water:ethanol:benzyl alcohol in Cs_xWO_3 solvothermal synthesis using WCl_6 and CsOH. The total solvent volume was 75ml.

The areas of the diagram separated by red dashed lines were samples which did not yield Cs_xWO_3 as the main phase (points 9, 11 and 12), mostly resulting in formation of WO_3. This is unsurprising as the ethanol in the solution acts as the reducing agent so its presence is required to make the reduced tungsten bronze phase and these samples had little to no ethanol present. Point 10 resulted in a dark blue product but it could not be dried sufficiently to analyse and was extremely 'sticky'. PXRD was used for product identification and the reactions corresponding to the remaining points on the diagram all resulted in the

formation of hexagonal Cs_xWO_3 with no significant impurity phases (see Figure A.3.2). Samples low in ethanol (points 4 and 6) were difficult to dry after synthesis and the sample morphology was amorphous as can been seen in the SEM images in Figure 4.7.

Replacing the ethanol in synthesis 13 with other alcohols – methanol, 2-propanol and 1-butanol – did not improve upon the morphology of the product seen using ethanol so other alcohols were not used when varying the ratio of solvent mixtures.

4.3.3.2 Scanning electron microscopy (SEM)

SEM images of Cs_xWO_3 samples are shown in Figure 4.7.

Of all the Cs_xWO_3 samples from the diagram in Figure 4.6, it can be seen that numbers 1, 5, 7 and 8 have defined morphologies. All four samples show agglomerates of small nanorods. Anisotropic growth of tungsten bronzes has been noticed in other works[3, 9] and the growth direction is parallel to the channel direction within the structure i.e. along [001]. Numbers 1 and 7 were chosen for testing with morphologically amorphous 4 for comparison. They will be referred to as CsTB-ST3, ST4 and ST5 respectively. A close up view of the SEM images of the nanorod samples ST3 and ST4 is shown in Figure 4.8 and it can be seen that ST3 consists of longer rods than those of ST4 which have a smaller aspect ratio. The approximate particle sizes from SEM images are ST3 ≈ 50 x 300 nm and ST4 ≈ 50 x 200 nm.

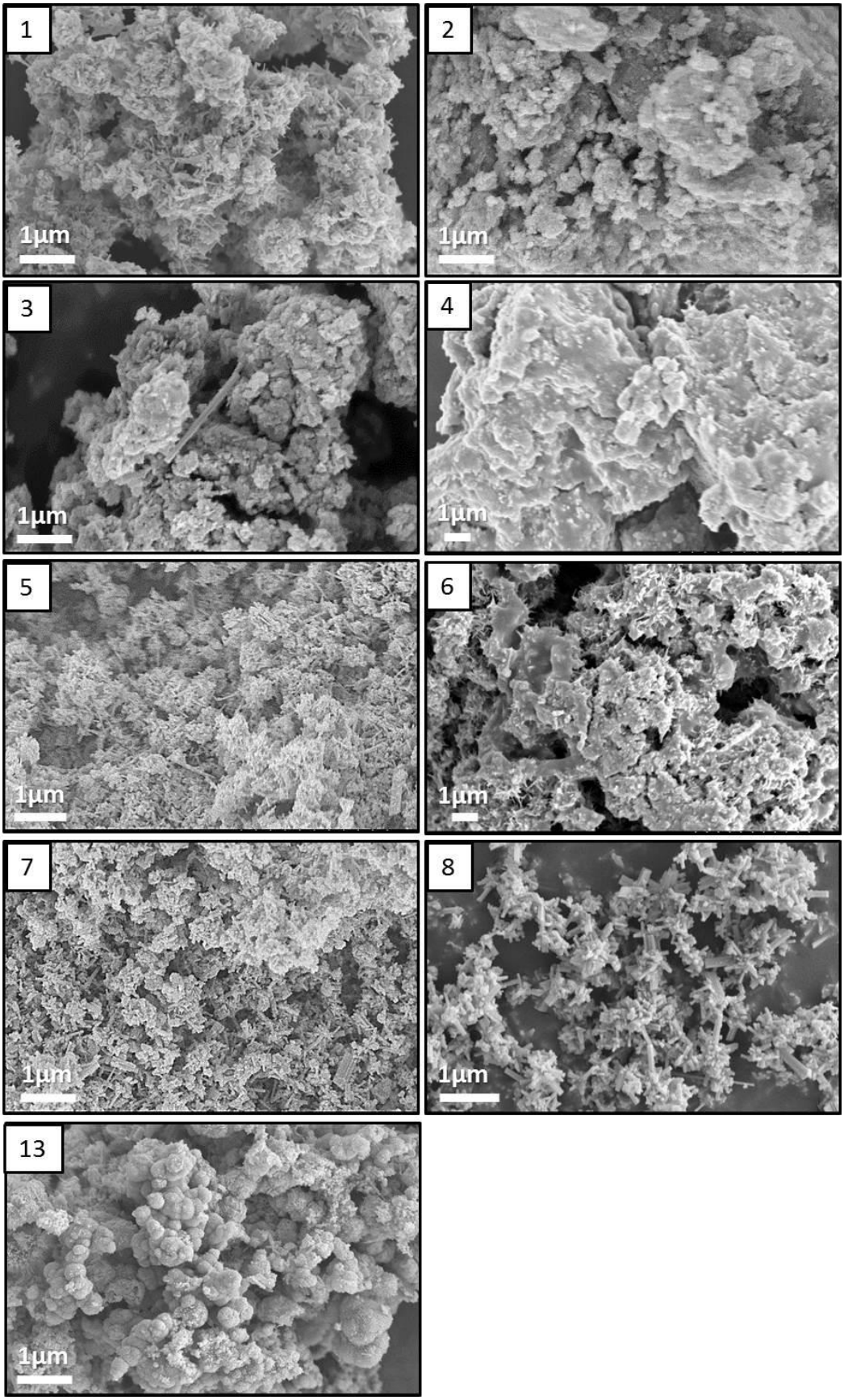

Figure 4.7 – SEM images of Cs_xWO_3 samples synthesised solvothermally using different solvent mixtures. The image numbers correspond to points of ternary diagram Figure 4.6.

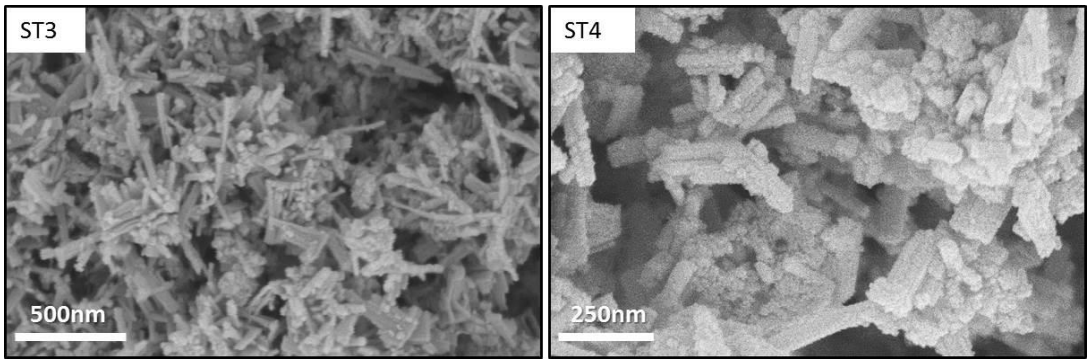

Figure 4.8 - Close-up SEM images of nanorod Cs_xWO_3 samples CsTB-ST3 and ST4.

4.3.3.3 UV-vis-NIR spectroscopy

The optical absorbance spectra of these samples are shown in Figure 4.9.

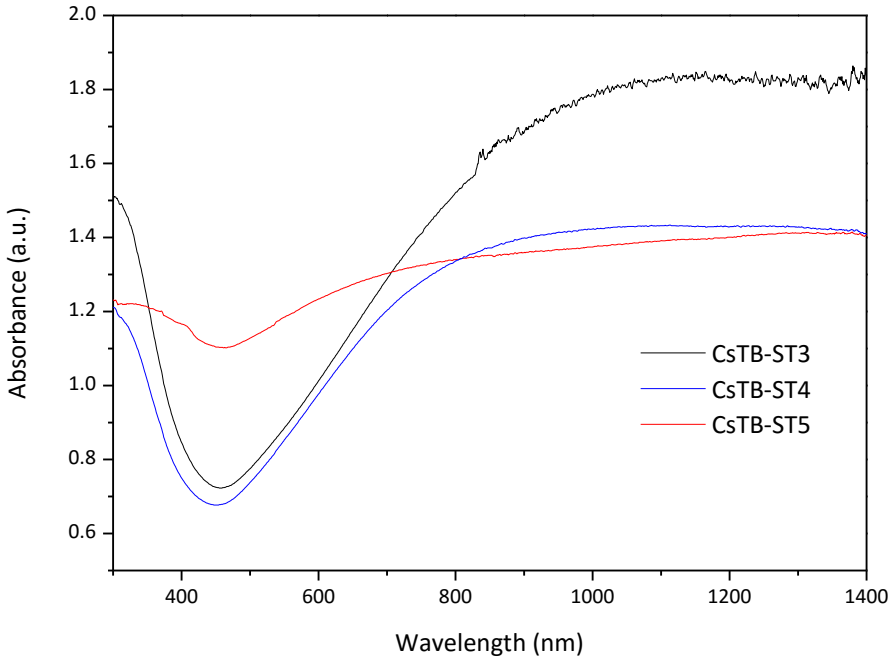

Figure 4.9 - Optical absorbance profiles of Cs_xWO_3 samples made by solvothermal synthesis with different solvent mixtures.

The morphologically amorphous CsTB-ST5 sample has higher absorbance in the visible region than ST3 or ST4 which is consistent with the work of Adachi and co-workers who found that NIR absorbers with smaller particles gave higher visible transmittance[6]. All samples show broad absorbance in the NIR region but the intensity of the CsTB-ST3 peak is the highest. The reason for this is not clear – the longer nanorod shapes perhaps give rise to more longitudinal plasmon resonance than the shorter rods of ST4. As for ST1 and ST2,

both polaron hopping and LSPR absorption mechanisms are thought to be present with LSPR dominant.

4.3.3.4 Results of laser imaging

CsTB-ST3, ST4 and ST5 were tested for laser imaging performance as described in Chapter 2.4. The results are shown in Figure 4.10.

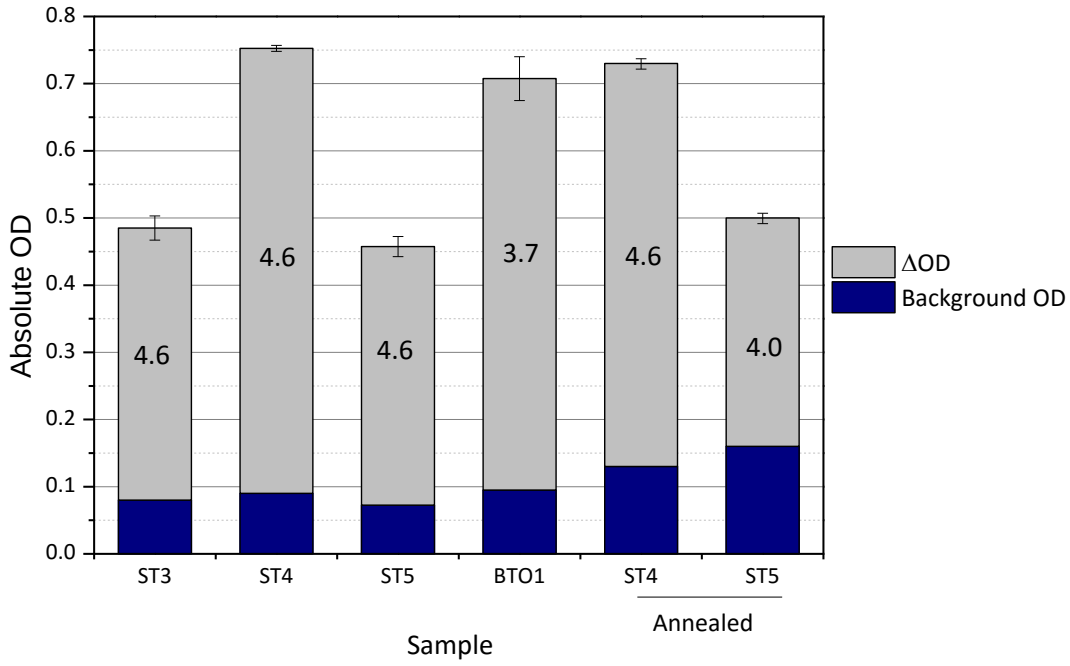

Figure 4.10 - Optical density values resulting from laser imaging tests for Cs_xWO_3 samples made by solvothermal synthesis compared to commercial sample BTO1. The numbers on the bars are the laser fluences in Jcm^{-2} at which the highest ΔOD was reached for each sample.

The samples were tested at 0.75 wt% loading and the commercial BTO1 sample is shown for comparison. The background colours (OD) of all samples are similar and acceptably low for commercial use. It should be noted that the OD of the uncoated PET substrate is 0.09 so coatings of these samples show little deviation from this. However the nanorod ST4 sample shows a significantly higher ΔOD value than the ST3 and ST5 samples. The fact that ST4 and ST5 had similar NIR absorbance shows that the nanorod morphology of ST4 has had an effect. In fact its performance is comparable with that of the commercial sample BTO1 with smaller error margins in ΔOD values.

The only difference the in synthesis of ST3 and ST4 is that ST4 had proportionally more ethanol in the solvent mixture. Despite lower NIR absorbance, ST4 significantly outperforms

ST3. This is unexpected but it is possible that the nanorods of ST4 with their smaller aspect ratio disperse better in the ink formulation and so it is more evenly distributed in the ink coating. In future it would be interesting to test nanosized spherical particles to see how performance compares to the nanorod samples.

The ST4 and ST5 samples were also annealed at 500 ^{o}C in flowing N_2 in a tube furnace for 1 h to see how morphology and performance were affected. Both samples became more crystalline with sharper peaks in the PXRD patterns and well defined nanorod morphologies, despite no nanorods being present in the as-made ST5 sample (see Figures A.3.3 and A.3.5). However the visible absorbance increased for both samples while the NIR absorbance decreased slightly (see Figure A.3.4). It can be seen in Figure 4.10 that this has negatively affected the performance. The background OD values for both samples are significantly higher than for the non-annealed samples. This leads to lower contrast between the background coating and the images so the ΔOD values are lower, although the combined absolute OD remains similar.

4.3.3.5 Further modification of Cs_xWO_3 synthesis

When using benzyl alcohol as a structural directing agent in the synthesis of WO_3, Polleux *et. al.*[7] proposed an interaction of the organic species with the inorganic one to create anisotropic ordering. To see if the morphology could be varied further, benzyl alcohol was replaced with other structurally related organics. The ratio of solvents used to synthesise CsTB-ST4 gave the best performing sample so that value (4:1:2.5 EtOH:H_2O:BnOH) was used. The number of moles of the organic species was kept the same as for the benzyl alcohol sample. Synthetic conditions were also kept the same. The compounds used are shown in Table 4.2.

Table 4.2 - Names and structures of organic compounds used as alternatives to benzyl alcohol in the solvothermal synthesis of Cs_xWO_3.

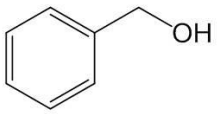	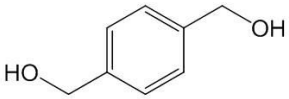	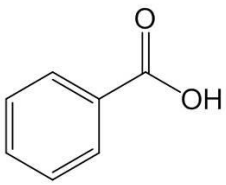
Benzyl alcohol (Phenylmethanol)	1,4-benzenedimethanol	Benzoic acid
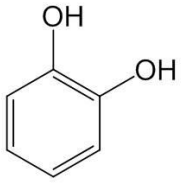	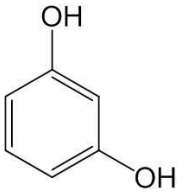	
Pyrocatechol (Benzene-1,2-diol)	Resorcinol (Benzene-1,3-diol)	Hydroquinone (Benzene-1,4-diol)

PXRD was the first technique used for product identification. The sample made using 1,4-benzenedimethanol could not be isolated or analysed. Benzoic acid gave pure hexagonal Cs_xWO_3 as did the reaction containing hydroquinone. The pyrocatechol product was difficult to identify due to the broadness of the peaks in the PXRD pattern but appears to be a WO_{3-x} phase rather than a tungsten bronze. The resorcinol sample was almost amorphous although had a few small peaks that indicate the formation of Cs_xWO_3.

Of the samples that resulted in crystalline Cs_xWO_3, the benzoic acid and resorcinol samples showed some inhomogenous nanorods in SEM images. The hydroquinone sample however takes the form of relatively homogeneous nanorods which are agglomerated into round ball-like clumps (see Figure 4.11c and 4.11d) with occasional large particles present such as the hexagon clearly visible in Figure 4.11c. This sample was selected for testing and called CsTB-ST6.

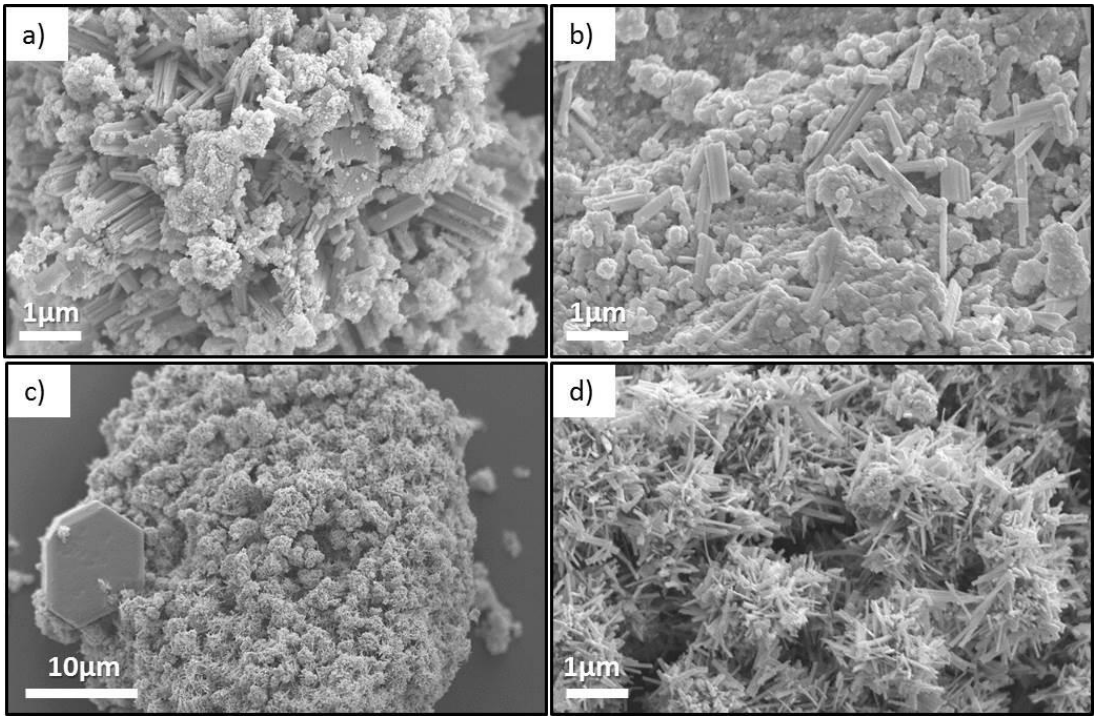

Figure 4.11 - SEM images of Cs_xWO_3 samples synthesised solvothermally using a) benzoic acid, b) resorcinol, c) and d) hydroquinone in the reaction solvent mixture.

NIR data for CsTB-ST6 is unavailable due to instrument breakdown but the optical absorbance of the visible region is shown in Figure 4.12 and compared to ST4. Although NIR region cannot be seen, the profile of CsTB-ST6 looks similar to that of ST4 at around 800 nm. However the profiles are quite different in the visible region with ST6 absorbing significantly more than ST4 at around 450 nm. It is possible this is caused by the large agglomerates of nanorods.

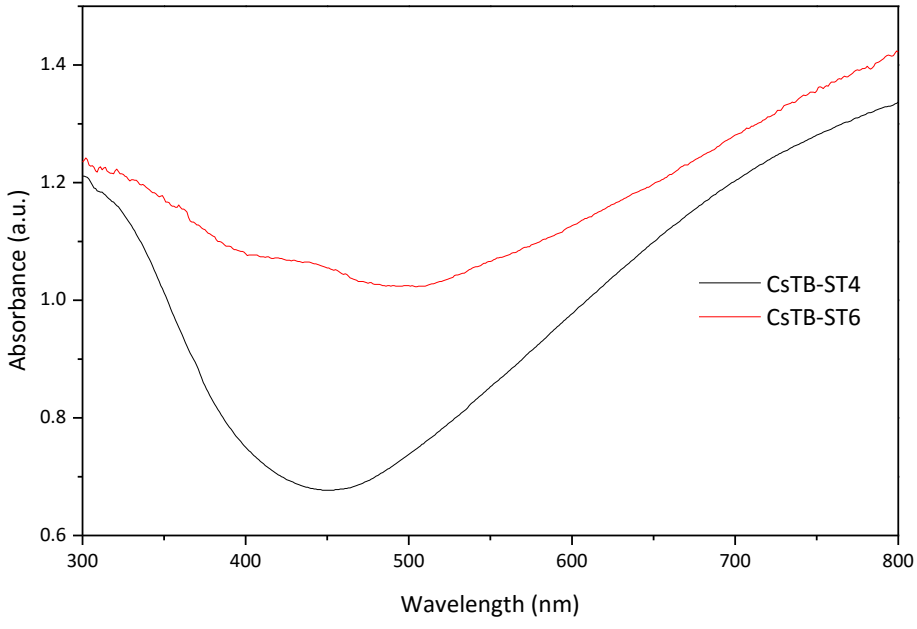

Figure 4.12 - Optical absorbance profiles of Cs_xWO_3 samples CsTB-ST4 and ST6.

To see what effect this has on laser imaging, ST6 was also tested at Datalase (results in Figure 4.13) and it performed poorly compared to ST4 although both samples gave similar background OD values. It was concluded that using other organics in Cs_xWO_3 synthesis offers no benefits over using benzyl alcohol.

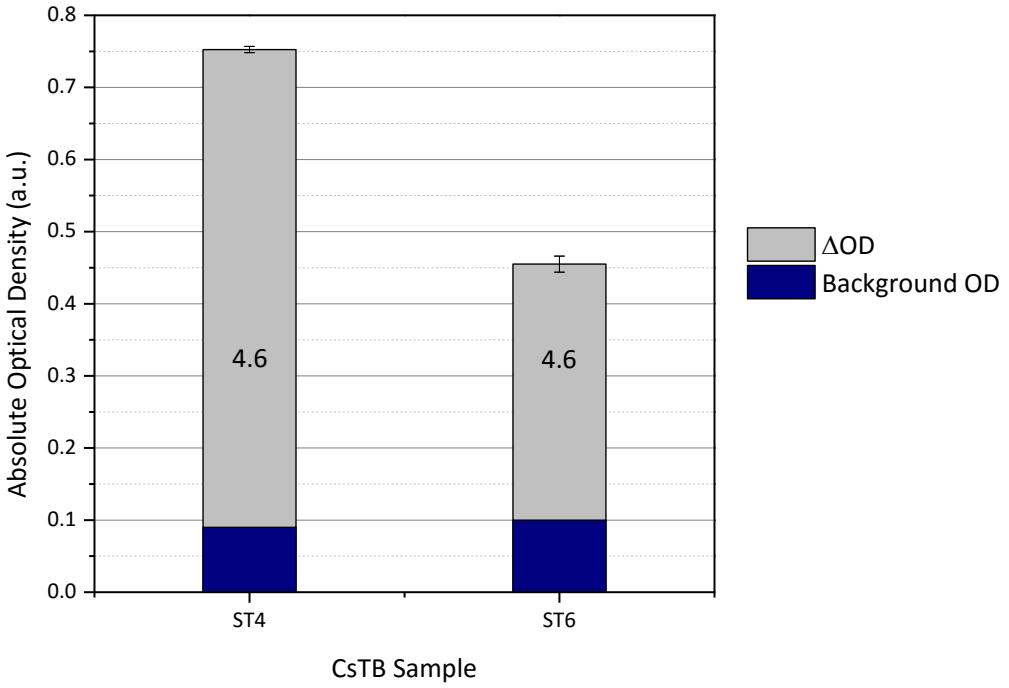

Figure 4.13 - Optical density values resulting from laser imaging tests for Cs_xWO_3 samples made by solvothermal synthesis. The numbers on the bars are the laser fluences in Jcm^{-2} at which the highest ΔOD was reached for each sample.

During the course of this work another research group have published the synthesis of Cs_xWO_3 using a benzyl alcohol route[8]. Eyassu and co-workers obtain small nanorods and investigate the effect of adding different amounts of oleic acid as a capping agent to control particle size. When using pure benzyl alcohol with no oleic acid, they obtain the bronze mixed with WO_3 but as the oleic acid amount increases so does the product purity and caesium content of the bronzes while particle size decreases[8]. The smaller particles give rise to higher NIR absorbance although this is also partially attributed to their higher Cs content. They have very short reaction times of 2 h.

4.3.4 Solid State Synthesis

The solvothermal Cs_xWO_3 samples are tuneable and some perform well but how do they compare to samples prepared by a more traditional solid state route? Solid state syntheses typically give products which are highly crystalline but have relatively large particle sizes. Commercial sample BTO1 was likely prepared by a solid state route and performs well. The

solid state tungsten bronzes in Chapter 3 showed mixed performance so the caesium counterparts have been synthesised for comparison.

4.3.4.1 PXRD

PXRD diffractograms of samples with different nominal values of *x* in Figure 4.14 show that the products are highly crystalline with sharp narrow peaks. The x = 0.33 and x = 0.25 samples are phase pure but it was not possible to make samples with lower values of x (0.15, 0.2) that did not contain WO_{3-x} impurity phases (peaks marked with *). Like RbTB-SS in Chapter 3, CsTB is not known to form any tetragonal or cubic phases due to the large size of the Cs^+ ion so no higher values of *x* were used. Samples with x = 0.25 and x = 0.33 will be referred to as SS1 and SS2 respectively.

Like their solvothermal counterparts, CsTB-SS1 and SS2 adopt the hexagonal tungsten bronze crystal structure shown in Figure 4.2 with a space group of $P6_3/mcm$. Compared to the solvothermal samples, the peaks are sharper and more intense, indicating a higher degree of crystallinity.

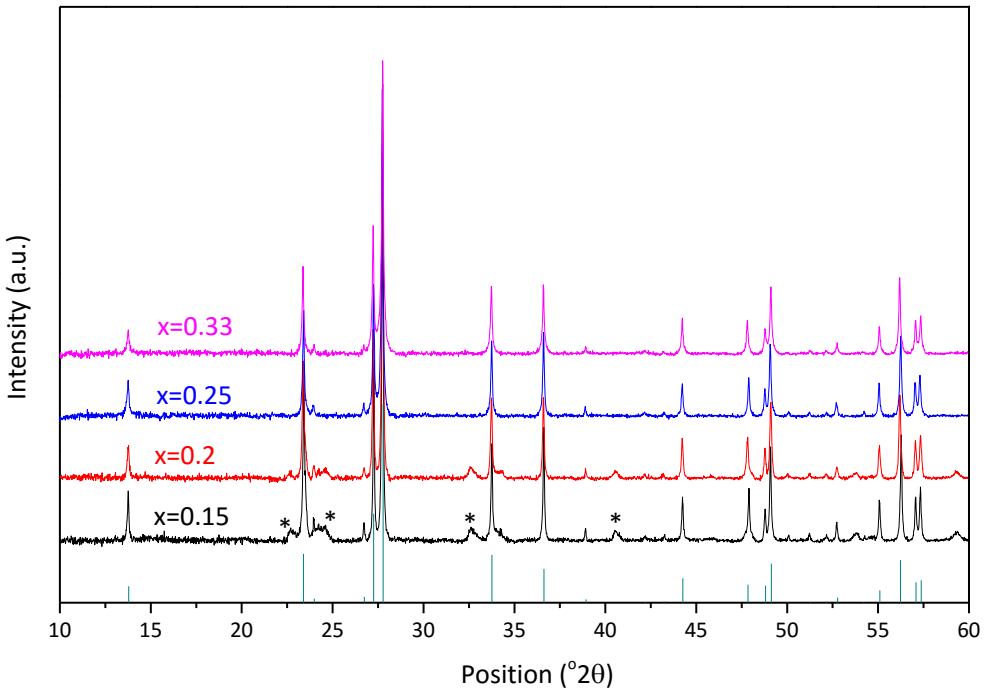

Figure 4.14 - PXRD diffractograms of Cs_xWO_3 samples prepared by a solid state route using different values of x. * denotes WO_3 peaks and the vertical lines show the expected peak positions and intensities of the hexagonal Cs_xWO_3 phase.

4.3.4.2 UV-vis-NIR spectroscopy

The optical absorbance of the x = 0.25 and x = 0.33 samples was measured and spectra are shown in Figure 4.15 and compared to the best performing solvothermal sample CsTB-ST4.

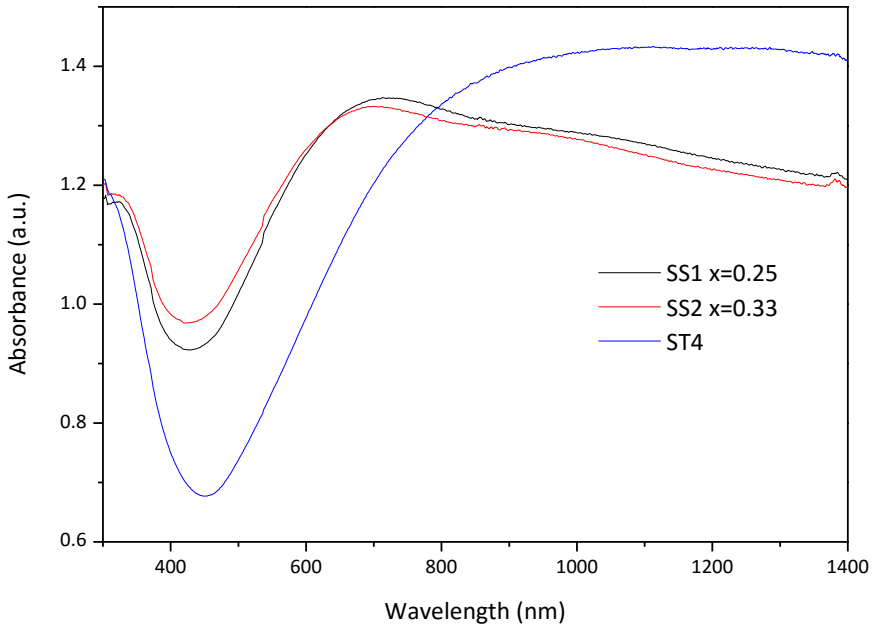

Figure 4.15 - Optical absorbance profiles of solid state Cs_xWO_3 samples compared to solvothermal CsTB-ST4.

There is little difference between the two solid state samples. The x = 0.33 sample, SS2, has slightly decreased NIR absorbance and slightly increased visible absorbance with a small red-shift of the absorbance peak compared to SS1 with x = 0.25. The absorption edge shift is in accordance with the results of Takeda and Adachi[9] although they observe increased NIR absorbance with increased Cs content which is not observed here. However they do not present any experimental evidence for the phase purity or the Cs content of their samples. This also follows the trend seen for solid state NaTB samples in Figure 3.10 – as the value of *x* increased, the absorbance peak shifted towards the UV end of the spectrum.

To see if the samples do vary in *x*, the Cs content was measured using SEM EDX and the results shown in Table 4.3. The values are within error of the nominal compositions. The *x* value is an average over a range of points and the error is the corresponding standard deviation.

Table 4.3 - Cs content x in CsTB-SS samples measured by EDX

Sample	Nominal x	EDX x	Error
CsTB-SS1	0.25	0.265	±0.021
CsTB-SS2	0.33	0.316	±0.025

The difference between the optical absorbance profiles of the solid state and solvothermal samples is more pronounced. The absorbance peaks of the solid state profiles are significantly shifted towards the visible region and the NIR absorbance is lower than for ST4. However a second less intense peak can be seen for the SS samples in this region at around 1000 nm. The origin of absorbance in the tungsten bronzes has been discussed in Chapter 3. Both polaron absorbance and localised surface plasmon resonance (LSPR) mechanisms are present.

The SS samples have larger particles and so the LSPR effect is less prominent than it is in the ST samples which have a much higher surface-to-bulk ratio. However solid state samples have greater bulk character so can host more polarons. The primary peak due to interaction of free electrons is shifted in energy to around 700 nm compared to nanoparticle size samples and a second less intense polaron peak at around 1000 nm appears. This 'double peak' profile was also seen for solid state hexagonal KTB samples in Figure 3.12 but is not observed in solid state bronzes of other crystal structures. This suggests that it is characteristic of the hexagonal tungsten bronze structure. It is possible that this framework can accommodate an optimum amount of alkali metal ($x < 0.33$) to for polaron effects to be suitably balanced with free electron effects for each to be visible as a double peak.

The laser image testing results are shown in Figure 4.19 below.

4.3.5 Combining Solvothermal and Solid State routes

Two samples were made using 'hybrid' routes. Firstly the same route used to make KTB-ST in Chapter 3 was used with caesium precursors – a solvothermal step to make a tungstate followed by reduction in a furnace under a hydrogen atmosphere. Secondly the amorphous precipitate made during the CsTB synthesis was heated in a furnace under reducing conditions instead of being heated in a solvothermal autoclave. They will be called CsTB-ST7 and CsTB-ST8 respectively.

4.3.5.1 PXRD

The PXRD diffractograms are shown in Figure 4.16 with the hexagonal caesium tungsten bronze pattern. Both samples adopt the hexagonal structure and show no evidence of impurity phases. The peaks in the CsTB-ST8 diffractogram are sharper than those of ST7.

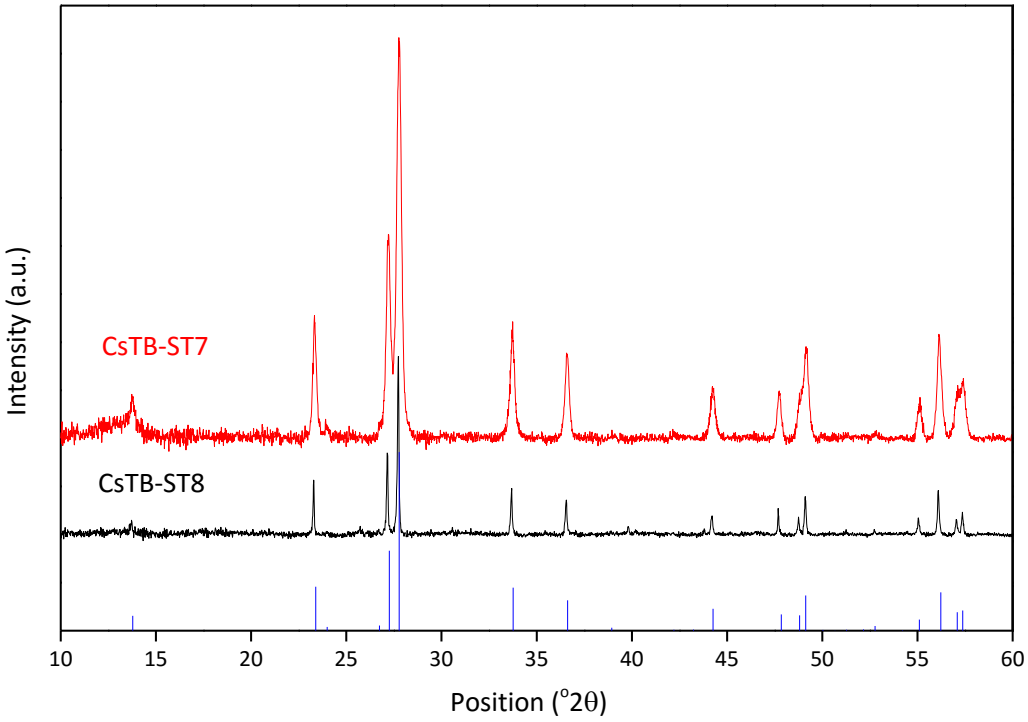

Figure 4.16 - PXRD diffractograms of Cs_xWO_3 samples made by hybrid solvothermal-solid state routes. The expected peak positions and intensities of hexagonal Cs_xWO_3 are shown in blue.

4.3.5.2 UV-vis spectroscopy

NIR data is not available for CsTB-ST7 or ST8 due to an instrument breakdown but the optical spectra in the visible region is shown in Figure 4.17.

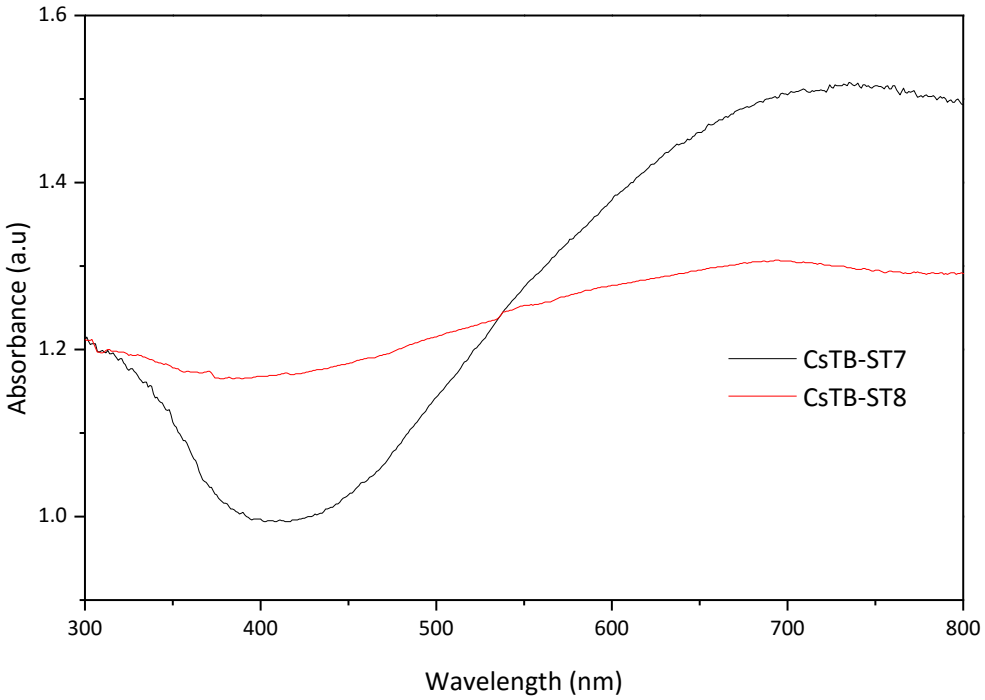

Figure 4.17 - Optical absorbance profiles of Cs_xWO_3samples CsTB-ST7 and ST8.

The spectrum for CsTB-ST8 is flatter than that of ST7 i.e. it is more absorbing at around 400 nm but less absorbing towards the NIR region at 700-800 nm.

4.3.5.3 Scanning electron microscopy (SEM)

The SEM images of ST7 and ST8 are shown in Figure 4.18 and they are strikingly different.

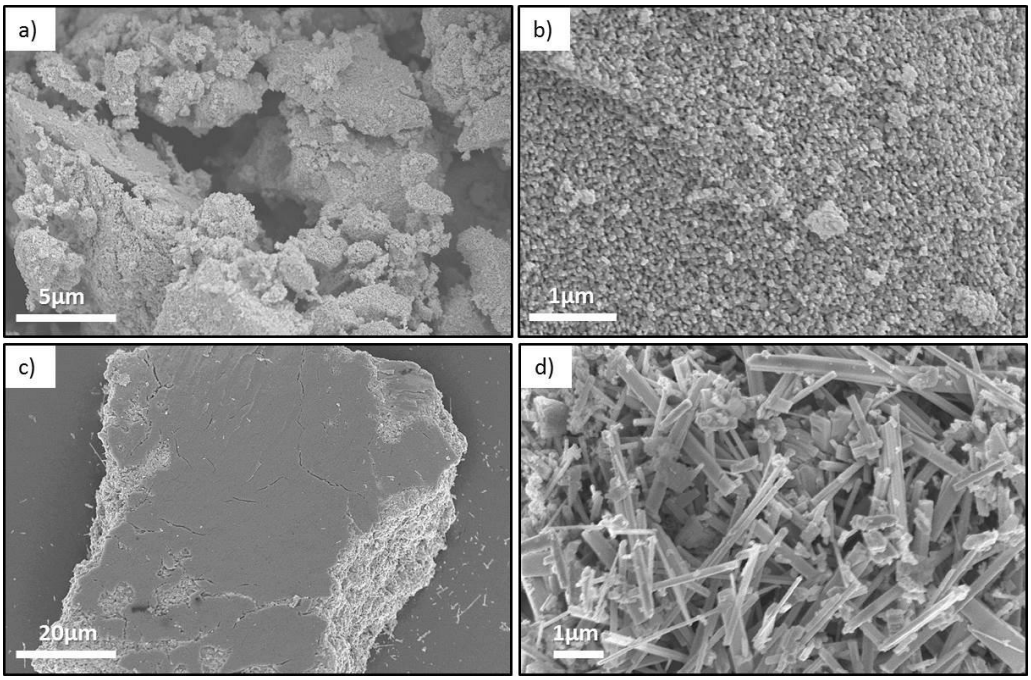

Figure 4.18 - SEM images of Cs_xWO_3 samples a) and b) CsTB-ST7 and c) and d) CsTB-ST8

CsTB-ST7 was made using a solvothermal route to a tungstate precursor which was reduced at 500°C and has resulted in large agglomerates of small spherical particles. CsTB-ST8 however consists of a mixture of relatively large 'blocks' and rod-like particles. The rods are almost an order of magnitude larger than those of CsTB-ST3 or ST5 with dimensions of ~200 x 3000 nm with some rods as long as 10µm. Some small amorphous particles are also seen – the sample morphology is highly inhomogeneous unlike ST7 which exhibits the same small particles throughout. The smaller particle size of ST7 is the cause of its broader PXRD peaks and decreased visible absorbance compared to ST8.

4.3.5.4 Results of laser imaging

CsTB-ST7 and ST8 were tested for laser imaging performance and the results are shown in Figure 4.19 along with those of CsTB-SS1 and SS2. Firstly it can be seen that all samples show similar low background OD values, all of which would be suitable for commercial applications. However there is some variation in the ΔOD values of images produced.

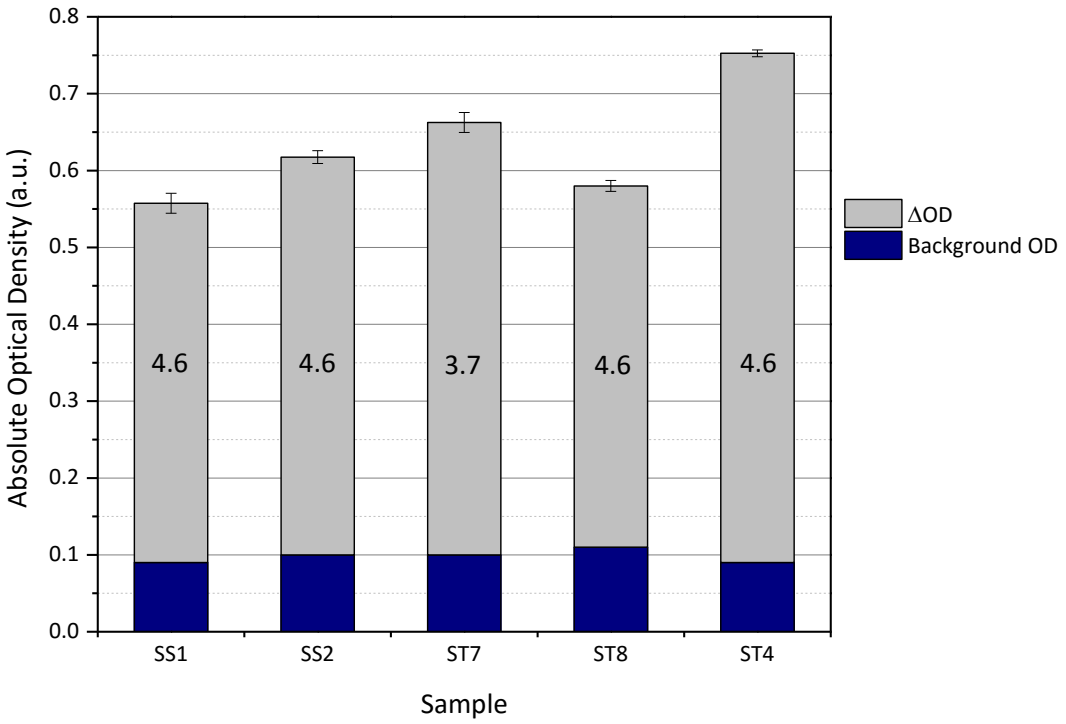

Figure 4.19 – Optical density values resulting from laser imaging tests of Cs_xWO_3 samples made by solid state (SS) and solvothermal-solid state (ST) routes compared to pure solvothermal sample ST4. The numbers on the bars are the laser fluences in Jcm^{-2} at which the highest ΔOD was reached for each sample.

Of the two solid state samples, CsTB-SS1 shows a slightly lighter background colour than SS2. This could be expected from the optical absorbance profiles in Figure 4.15 – that of SS1

is slightly more transparent in the visible region compared to SS2. However despite this lighter background OD of SS1, the maximum ΔOD value of the images created is lower than those of SS2. The difference in the samples is the value of x in Cs_xWO_3 with SS1 = 0.25 and SS2 = 0.33. Each Cs^+ added to the tungsten bronze donates an electron to the conduction band which can act as a free charge carrier and interact with electromagnetic radiation. For this application the advantage of increased transparency of the SS1 sample was outweighed by the higher amount of charge carriers available for NIR absorbance in SS2 and so SS2 ultimately performed better. The best performing CsTB-ST4 sample is shown for comparison and the testing results for CsTB-SS2 are still lower than this value.

Of the hybrid samples CsTB-ST7 and ST8, ST7 shows a slightly lighter background and a higher maximum ΔOD than ST8. This improved performance can be attributed to the smaller particle size seen in the SEM images in Figure 4.18 and the probable lower NIR absorbance of CsTB-ST8 (see Figure 4.17). Neither hybrid samples CsTB-ST7 or ST8 out-perform CsTB-ST4 although ST7 has a higher ΔOD than the SS samples. From these results it can be concluded that hybrid solvothermal/solid state routes offer no benefit over pure solvothermal synthesis routes to caesium tungsten bronze NIR absorbers. However the route used to make ST7, namely synthesising caesium tungstate solvothermally then reducing it to the bronze in a tube furnace, offers improved performance over pure solid state synthesis. This was the same route used to make the best performing sample in Chapter 3, the KTB-ST potassium tungsten bronze.

4.4 Discussion

4.4.1 Sample Composition

The amount of caesium in the solvothermal Cs_xWO_3 samples has not yet been discussed. While it was apparent from Chapter 3 that the crystal structure affects the optical absorbance profiles of tungsten bronze samples, within the subset of hexagonal tungsten bronzes the nature of the cation does not greatly affect the optical absorbance. Each metal cation donates one electron to the conduction band so the orbitals of metal ion do not form part of the overall band structure. However the amount of cation present will affect the electronic and optical properties and therefore could affect the laser imaging performance.

As for the samples in Chapter 3, the Cs content was measured using the atomic ratio of Cs:W from SEM EDX data and is plotted against the highest ΔOD values for each sample in Figure 4.20. The nominal value of x = 0.33 (which was used for all samples apart from CsTB-SS1) is marked by the dashed blue line. A number (~10) of areas was measured for each sample and the error bars represent the standard deviation of the range of values.

It can be seen that there is a general positive correlation of Cs content with performance with some outlying points. The CsTB-ST8 sample (which was made by one of the solvothermal-solid state hybrid routes) has a very high Cs content but there are enormous errors associated with the value so it is perhaps not as reliable as the others. The poorly crystalline CsTB-ST1 sample has close to the nominal amount of Cs present which reinforces the conclusion from section 4.3.1.3 that crystallinity is a key property of tungsten bronze NIR absorbers since the relatively high absorbance and Cs content of this sample do not result in formation of images whereas the crystalline samples all result in at least some imaging.

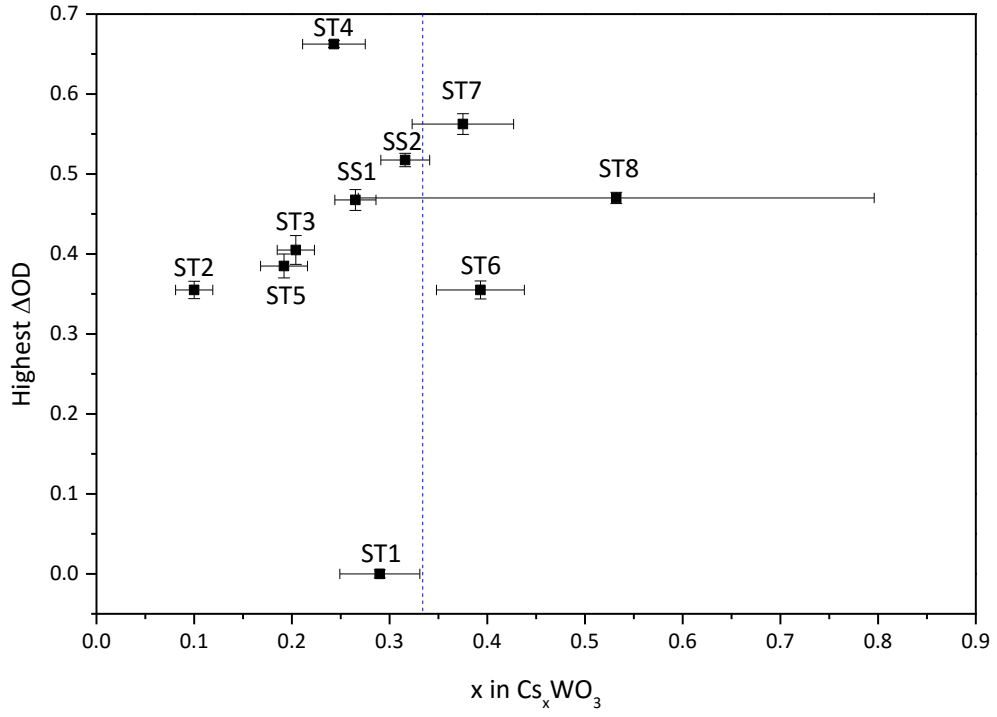

Figure 4.20 - Plot of Cs content vs ΔOD of images created during laser irradiation for all Cs_xWO_3 samples. Cs content is the ratio of Cs:W atomic percent measured by SEM EDX. Error bars show the standard deviation of the range of values measured for each sample.

CsTB-ST3 and ST4 differed in synthesis in that ST4 had proportionally more ethanol in the reaction mixture. The increased amount of reducing agent has resulted in a slightly higher Cs content (ST3 = 0.204±0.019, ST4 = 0.243±0.032). This could help explain the better performance of CsTB-ST4 although the NIR absorbance of ST3 was higher. The solid state samples contain the expected amount of Cs as discussed in section 4.3.4. The solid state routes offer more direct control over composition than do the solvothermal routes.

Although there is no clear explanation for samples that have higher-than-nominal Cs contents and closely related samples that show very different performance, the Cs content is clearly a factor to be considered, and if possible controlled, when synthesising Cs_xWO_3 samples to act as NIR absorbers.

4.4.2 Heat Transfer

The selection and assessment of NIR absorbers for the Datalase imaging process is not straightforward. Sample crystallinity, composition and morphology are all variable factors. The synthetic route used to make the samples clearly has a significant effect on properties. Something that has not been considered up to this point is the second step in the imaging process i.e. the transfer of heat from the absorber to the pigment particles.

This is difficult to measure directly. The laser imaging itself takes less than 0.01 seconds so in-situ measurements are experimentally challenging, especially since placing equipment or sensors in the path of the beam could damage them. Characterisation of the absorbers' inherent physical properties such as thermal conductivity were considered but practically these measurements require dense pellets of the material and the sintering and pressurisation required to achieve this would alter the microstructure, and possibly composition of the samples and therefore change the properties in the process.

Nevertheless an infrared pyrometer[†] was employed to attempt to record the local temperature during laser imaging. The pyrometer could detect temperatures of 250-1800 ^{o}C and had a spot size of 1.5 mm with a focussing distance of 450 mm. The infrared beam was focussed onto the 5x5 mm imaging area beneath the 1070 nm laser and the temperature reached during irradiation at 4.6 Jcm^{-2} was recorded a number of times for each sample. Data is not available for all samples discussed however measurements were

[†] Micro Epsilon pyrometer, model number CTM-3CF4-300X1H3-C3

taken for 0.75 wt% coatings of CsTB samples ST1-ST5. The average temperatures are plotted against the highest ΔOD values in Figure 4.21.

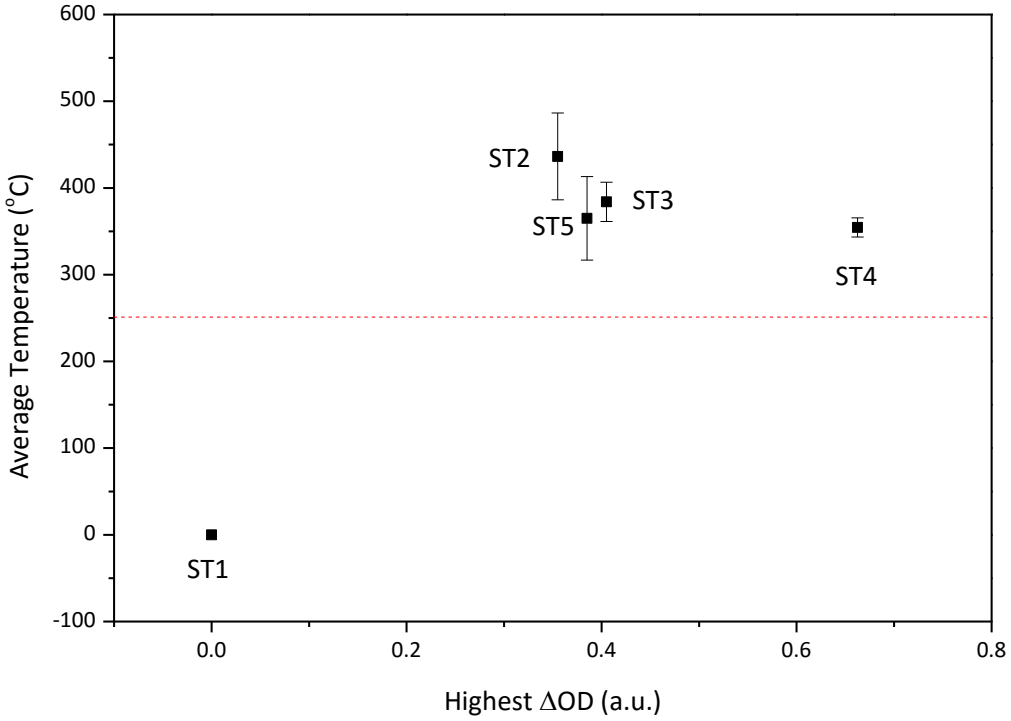

Figure 4.21 - Temperature reached during laser irradiation vs highest ΔOD for CsTB samples ST1-ST5. The dashed red line indicates the minimum detection temperature of the pyrometer.

Although there is no clear trend in this data, it still provides some interesting information. CsTB-ST1 which did not image at 0.75 wt% failed to reach the minimum temperature that the pyrometer can detect (250 °C, marked in red). The pigment colour change occurs at around 310 °C so the reason this sample was not successful is now clear – it failed to heat up enough. The fact that sample crystallinity is important for the heat transfer step was suggested in section 4.3.1.3 and this now seems to be the case. The remaining crystalline samples all formed images during radiation and it can be seen that they all reach temperatures of above 300 °C, up to 450 °C for CsTB-ST2. However there is no direct correlation between temperature reached and ΔOD of images created.

4.4.3 Mixing samples with different alkali metals

It was thought that mixing tungsten bronze samples with different alkali metal cations could have an effect on laser imaging performance. A solvothermal K_xWO_3 sample was

mixed into the ink formulation with a solvothermal Cs_xWO_3 sample in different ratios. Coatings were prepared and tested and the results shown in Figure 4.22.

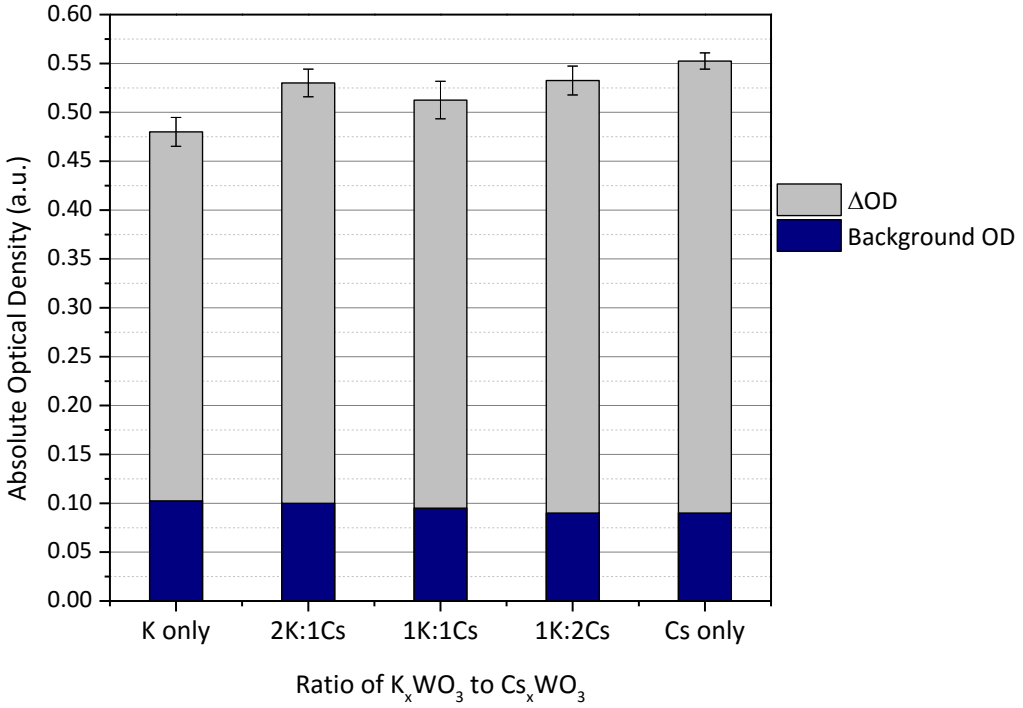

Figure 4.22 - Optical density values resulting from laser imaging tests of K_xWO_3 mixed with Cs_xWO_3 in different ratios. The highest ΔOD was reached at 4.6 Jcm^{-2} for each sample.

The first point to note is that the background OD is similar for all the samples and for the mixed samples it lies between that of the K_xWO_3 sample and the Cs_xWO_3 sample as could be expected. The Cs_xWO_3 sample performs better alone than the K_xWO_3 but it has slightly higher NIR absorbance (see Figure A.3.6) so this is not surprising.

The two tungsten bronzes were mixed in ratios of 2:1, 1:1 and 1:2 while keeping the overall loading at 0.75 wt%. It can be seen that there are small variations in the ΔOD of images created on mixed coatings but no overall trend. None of the mixed samples outperforms the Cs_xWO_3 sample on its own so there is no inherent benefit in having two tungsten bronzes present.

There is recent evidence in the literature of tungsten bronzes that contain more than one alkali metal within their structure[11]. Preliminary attempts were made to synthesise these compounds in this work without much success so it remains to be seen whether they would outperform ternary tungsten bronzes. However this could be an avenue available for future exploration.

4.4.4 Comparison to other tungsten bronzes (TB's)

The CsTB-ST4 sample shows the best performance of the caesium TBs and in Figure 4.23 it is compared to the best Na and K TBs from Chapter 3.

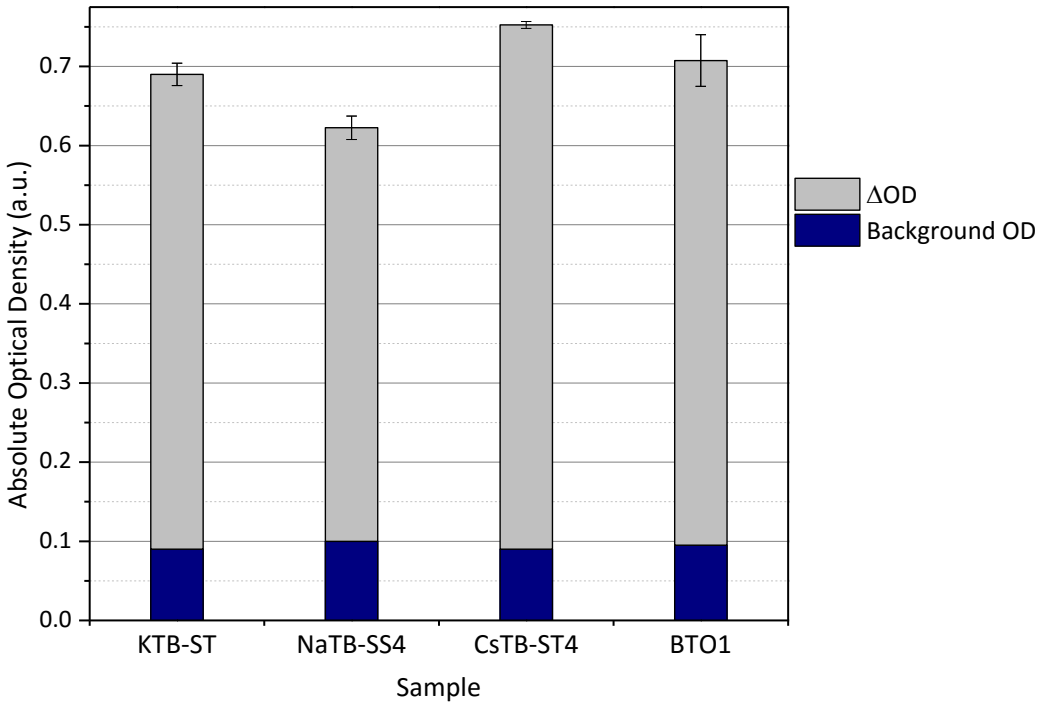

Figure 4.23 - Optical density values resulting from laser imaging tests of the best tungsten bronze samples. The highest ΔOD was reached at 4.6 Jcm^{-2} for each sample.

It can be seen that the CsTB-ST4 sample outperforms the other TBs and also the commercial caesium TB sample BTO1. However the KTB-ST and NaTB-SS4 ΔOD values still have sufficient contrast with the low background OD values to be used as NIR absorbers. Any of these samples are viable candidates for use in the Datalase imaging process.

4.5 Conclusion

Caesium tungsten bronzes perform well as near-infrared absorbers in the Datalase laser imaging process. The samples need to be crystalline in order to create images during laser irradiation. Within the set of samples with hexagonal crystal structure, those with a nanorod morphology show improved imaging compared to those which are morphologically amorphous. Samples made via solid state synthesis have reasonable performance compared to those made by solvothermal routes despite different optical absorbance profiles. However the sample made by an initial solvothermal step followed by

reduction in a furnace showed improved performance over the solid state synthesised samples.

Thermal measurements indicate that samples need to heat up to a threshold temperature in order to create images. Mixing together two tungsten bronzes containing different alkali metals offered no improvement in performance compared to using a single tungsten bronze. A solvothermally synthesised sample with nanorod morphology (CsTB-ST4) showed the best performance of all the caesium tungsten bronzes, and indeed of all the tungsten bronze samples.

4.6 References

1. Magneli, A., Blomberg, B., Contribution to the Knowledge of the Alkali Tungsten Bronzes. *Acta Chem. Scand.* **1951,** *5*.
2. Bevolo, A. J.; Shanks, H. R.; Sidles, P. H.; Danielson, G. C., Heat capacity of hexagonal tungsten bronzes. *Physical Review B* **1974,** *9* (8), 3220-3228.
3. Guo, C.; Yin, S.; Zhang, P.; Yan, M.; Adachi, K.; Chonan, T.; Sato, T., Novel synthesis of homogenous Cs_xWO_3 nanorods with excellent NIR shielding properties by a water controlled-release solvothermal process. *J Mater Chem* **2010,** *20* (38), 8227-8229.
4. Kihlborg, L.; Hussain, A., Alkali metal location and tungsten off-center displacement in hexagonal potassium and cesium tungsten bronzes. *Mater Res Bull* **1979,** *14* (5), 667-674.
5. Reis, K. P.; Ramanan, A.; Whittingham, M. S., Hydrothermal synthesis of sodium tungstates. *Chem Mater* **1990,** *2* (3), 219-221.
6. Adachi, K.; Miratsu, M.; Asahi, T., Absorption and scattering of near-infrared light by dispersed lanthanum hexaboride nanoparticles for solar control filters. *J Mater Res* **2010,** *25* (03), 510-521.
7. Guo, C.; Yin, S.; Huang, L.; Sato, T., Synthesis of One-Dimensional Potassium Tungsten Bronze with Excellent near-Infrared Absorption Property. *ACS Applied Materials & Interfaces* **2011,** *3* (7), 2794-2799.
8. Polleux, J.; Antonietti, M.; Niederberger, M., Ligand and solvent effects in the nonaqueous synthesis of highly ordered anisotropic tungsten oxide nanostructures. *J Mater Chem* **2006,** *16* (40), 3969-3975.
9. (a) Guo, C.; Yin, S.; Huang, L.; Yang, L.; Sato, T., Discovery of an excellent IR absorbent with a broad working waveband: Cs_xWO_3 nanorods. *Chemical Communications* **2011,** *47* (31), 8853-8855; (b) Tsehaye, E.; Tun-Jen, H.; Chhiu-Tsu, L., Facile solvothermal synthesis of NIR absorbing Cs_xWO_3 nanorods by benzyl alcohol route. *Materials Research Express* **2015,** *2* (1), 015016.
10. Takeda, H.; Adachi, K., Near Infrared Absorption of Tungsten Oxide Nanoparticle Dispersions. *J Am Ceram Soc* **2007,** *90* (12), 4059-4061.
11. Adachi, K.; Asahi, T., Activation of plasmons and polarons in solar control cesium tungsten bronze and reduced tungsten oxide nanoparticles. *J Mater Res* **2012,** *27* (06), 965-970.
12. (a) Choi, J.; Moon, K.; Kang, I.; Kim, S.; Yoo, P. J.; Oh, K. W.; Park, J., Preparation of quaternary tungsten bronze nanoparticles by a thermal decomposition of ammonium metatungstate with oleylamine. *Chemical Engineering Journal* **2015,** *281*, 236-242; (b) Moon, K. C., Jin-Ju ; Lee, Ye-Bin ; Yoo, Pil J. ; Bark, Chung Wung ; Park, Juhyun, Near Infrared Shielding Properties of Quaternary Tungsten Bronze Nanoparticle $Na_{0.11}Cs_{0.22}WO_3$. *Bulletin of the Korean Chemical Society* **2013,** *34* (3), 731.

Chapter 5

Sub-stoichiometric Tungsten Trioxide WO_{3-x}

5.1 Introduction

A series of compositions similar to the tungsten bronzes are formed by oxygen-deficient WO_3. The commercial sample BTO2 analysed in Appendix 1 was one of these phases. Rather than doping metal cations into the WO_3 lattice, oxygen vacancies are introduced in these compounds giving compositions of WO_{3-x} with varying *x*. They are often called 'blue tungsten oxides' due to their characteristic colour which, like the tungsten bronzes, is caused by the presence of W^{5+} species and is strikingly different from the pale greenish-yellow stoichiometric WO_3. Tungsten cations are reduced from 6+ to 5+ in order to maintain charge neutrality on the removal of O^{2-} ions from the bulk material. They are named "Magneli phases" after Arne Magneli who was the first to propose a crystallographic shear arrangement of octahedra to account for the oxygen deficiencies[1], structures which are discussed in Chapter 1.

The literature can be contradictory on the dominant optical absorption mechanism present in WO_{3-x} phases. The $W_{18}O_{49}$ phase displays polaronic conductivity[2] according to Viswanathan *et. al.* with significant electron-phonon coupling. Inequivalent tungsten sites and defects such as the hexagonal tunnels scatter electrons and reduce the charge carrier mobility compared to that of WO_3[3]. However the maximum carrier density possible without significant overlap of polaronic functions was calculated by Iguchi, Salje and Tilley[4] to correspond to a composition of $WO_{2.9}$. At greater degrees of reduction when x>0.1 the wavefunctions will overlap and lead to free electron like character and metallic behaviour[5]. As the crystallinity increases, more free-electron-like behaviour is observed by Schrimer *et. al.*[6] yet they see polaron absorption at around 1 eV in electrolytically coloured amorphous WO_3 films. Adachi and Asahi[7] have measured the absorption coefficient of $WO_{2.72}$ which suggests that polaron absorption occurs in the solid state sample. However the dielectric functions and reflectivity profiles of the same sample are indicative of the presence of free electrons[7]. Salje and Guttler[5] also find that polarons and quasi-free carriers are present simultaneously in metallic WO_{3-x}. Similar behaviour is seen in the tungsten bronzes in the preceding chapters. In those samples, polaron absorption is more significant for samples with greater bulk character whereas localised surface plasmon resonance is the dominant

mechanism in nanostructured samples. The same effects will be investigated in binary WO_{3-x} phases.

5.1.1 Synthesis

Like the tungsten bronzes, a range of synthetic routes can be used to make WO_{3-x} phases with different values of x. High temperature vapour phase routes were used by Berak and Sienko in 1970 to produce single crystals of WO_{3-x} phases by heating tungsten trioxide at 1320 ^{o}C for eight days then at 1022 ^{o}C for a further five days under a reducing atmosphere in sealed platinum crucibles[8]. A similar method was used by Sundberg[9].

The effect of particle size on optical properties was discussed in section 1.3.3 and nano-structured $W_{18}O_{49}$ has been of interest for use in a range of applications. Solvothermal methods have been developed in recent years as mild routes to nanostructured $W_{18}O_{49}$ samples. In 2003 Lou and Zeng used an hydrothermal route to obtain single crystalline $W_{18}O_{49}$ nanorods[10] with diameters of 3-10 nm. Choi *et. al.* also made $W_{18}O_{49}$ nanorods using a simple route in which WCl_6 was dissolved in ethanol and heated to 200 ^{o}C for 10 h[11]. Guo *et. al.* used a two-step hydrothermal process[12] by synthesising ammonium tungsten oxide at 200 ^{o}C then annealing the product at 500 ^{o}C under a reducing atmosphere to get $W_{18}O_{49}$. More recently they have developed a simpler route using alcohols and the morphology of the $W_{18}O_{49}$ products was controlled by adjusting the amount and nature of the reactants[13]. Bai *et. al.* have also used a one-pot alcohol-based route combined with a cooling step to give networks of $W_{18}O_{49}$ nanowires[3]. These mild, simple one-step synthetic routes are extremely promising for larger scale applications and are more environmentally friendly. They also allow for facile nanostructure tuning – as well as the common nanorods, nanospheres and even 'nanourchins' have been made. For example see the range of morphologies synthesised by Guo *et. al.* by changing the composition of the reaction mixture[13]. In this work, a solvothermal route was used in order to obtain nanoparticles of $W_{18}O_{49}$. The properties are compared to samples obtained by solid state synthesis.

5.1.1.1 Solvothermal Synthesis of $W_{18}O_{49}$

A number of routes were tried but the one-pot route outlined by Bai *et. al.*[3] gave the best results. WCl_6 (Sigma Aldrich ≥ 99.9%, 0.2506 g, 6.32 x 10^{-4} mol) was dissolved in 80 ml absolute ethanol C_2H_5OH to form a yellow solution. This was placed in a freezer at -5 ^{o}C for 20 h before transfer to Teflon-lined autoclave of 125 ml internal volume. This was heated

for 24 h at 180 °C with a ramp rate of 10 °C/min. The blue product was centrifuged, washed with ethanol and dried in air at 60 °C before characterisation.

5.1.1.2 Solid State Synthesis of $W_{18}O_{49}$

A solid state route was also used to tune the composition with more accuracy following the method of Adachi and Asahi[7]. WO_3 (Sigma Aldrich 99.995%, 1 g, 4.3 x 10^{-3} mol) was ground briefly with a pestle and mortar before being placed in an alumina crucible and heated in a tube furnace to 500 °C under flowing 5% H_2 in N_2. The ramp rate was 5 °C/min and the heating time was varied in order to vary the degree of reduction in the samples. The dark blue products were ground again with a pestle and mortar before analysis. Reaction times used were 0.1, 0.5, 1 and 1.5 h. The resulting compositions were analysed by thermogravimetric analysis.

5.2 Characterisation

5.2.1 Powder X-ray Diffraction (PXRD)

The PXRD diffractogram of the solvothermal $W_{18}O_{49}$ product from 20-50° 2θ is shown in Figure 5.1a and it can be seen that it is very poorly crystalline. However this is also the case in the literature[3] and the single discernible peak at around 2θ = 23° is the (010) peak. Bai and co-workers also identify other small peaks as being indicative that the nanowire crystals grow along the [010] direction[3]. The broadness of the peaks is caused by the small particle size which will be discussed further below.

The pattern of a solid state sample (annealed for 1 h) is also shown in Figure 5.1b and it can be noted that the peaks are much sharper and well-defined indicating a highly crystalline product. The most intense peak is also the (010) one as for the solvothermal product. The peaks correspond well to the pattern of $W_{18}O_{49}$ (JCPDS PDF number 00-036-0101) from the work of Booth *et. al.*[14] which has a monoclinic space group P2/m and is shown below the diffractogram in blue. The small unassigned peak at around 2θ = 26° is due to the presence of a small amount of WO_2. The patterns for all the solid state samples are the same and match the $W_{18}O_{49}$ pattern – see Figure A.4.1.

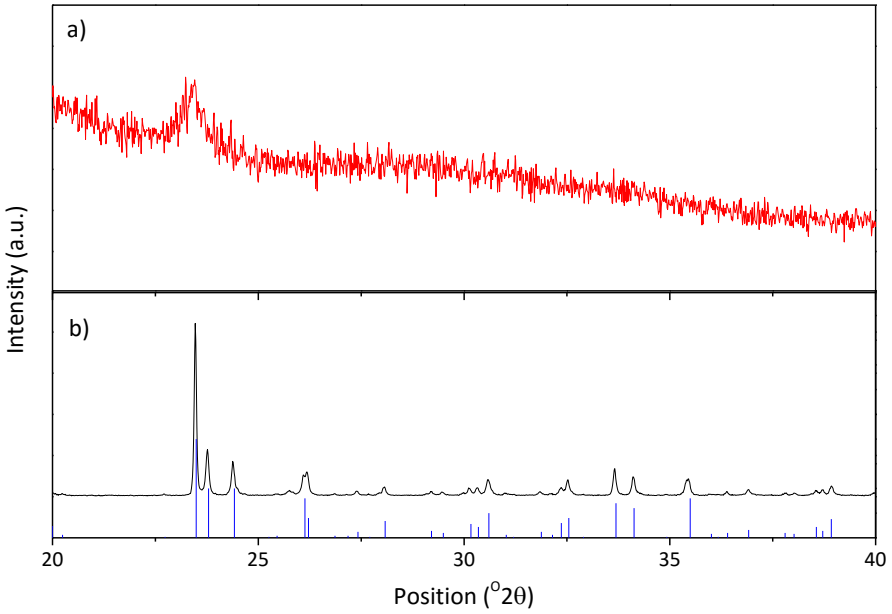

Figure 5.1 - PXRD diffractograms of WO_{3-x} samples made by a) solvothermal and b) solid state routes. Expected peak positions and intensities of monoclinic $W_{18}O_{49}$ are shown in blue.

5.2.2 Fourier Transform Infrared Spectroscopy (FTIR)

Due to the amorphous nature of the PXRD pattern of the solvothermal product, further steps were taken to confirm that the desired phase had formed. FTIR spectroscopy was carried out on a powder sample from 600-4000 cm^{-1} to see if expected W-O modes are present. The resulting spectrum is shown in Figure 5.2.

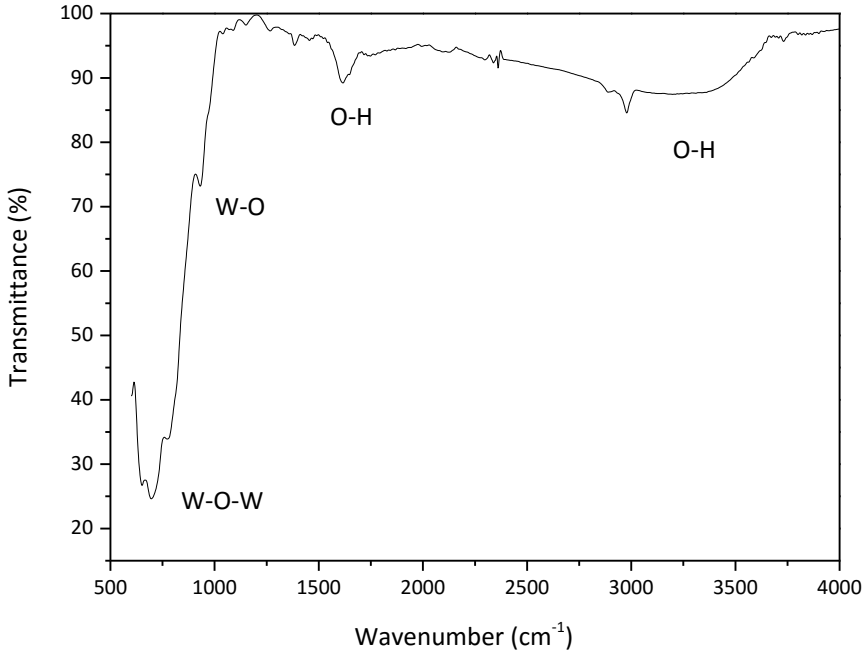

Figure 5.2 - FTIR spectrum of solvothermal WO_{3-x}.

The spectrum shows intense absorption peaks in the 1000-500 cm^{-1} region which arise from W-O interactions. The W-O-W stretches are found in the 800-700 cm^{-1} region[15] and the W-O stretching vibration is visible at around 900cm^{-1}. This is in agreement with the features found by Bai and co-workers[3]. The only other features of the spectrum are a small absorption just above 1500 cm^{-1} and a broad feature at around 3500 cm^{-1} which are both caused by the presence of O-H and result from in-plane bending vibrations and stretching vibrations respectively. The absence of organic features indicates that the product is clean and no solvent remains.

5.2.3 Thermogravimetric Analysis (TGA)

Despite the PXRD data showing that the solid state samples all consist of the same phase, the difference in annealing time is expected to result in differences in composition. Longer time in the reducing 5% H_2/N_2 atmosphere of the tube furnace should have removed a larger amount of oxygen from the WO_3 starting material. TGA measurements were carried out from room temperature to 800 ^{o}C in air to confirm this.

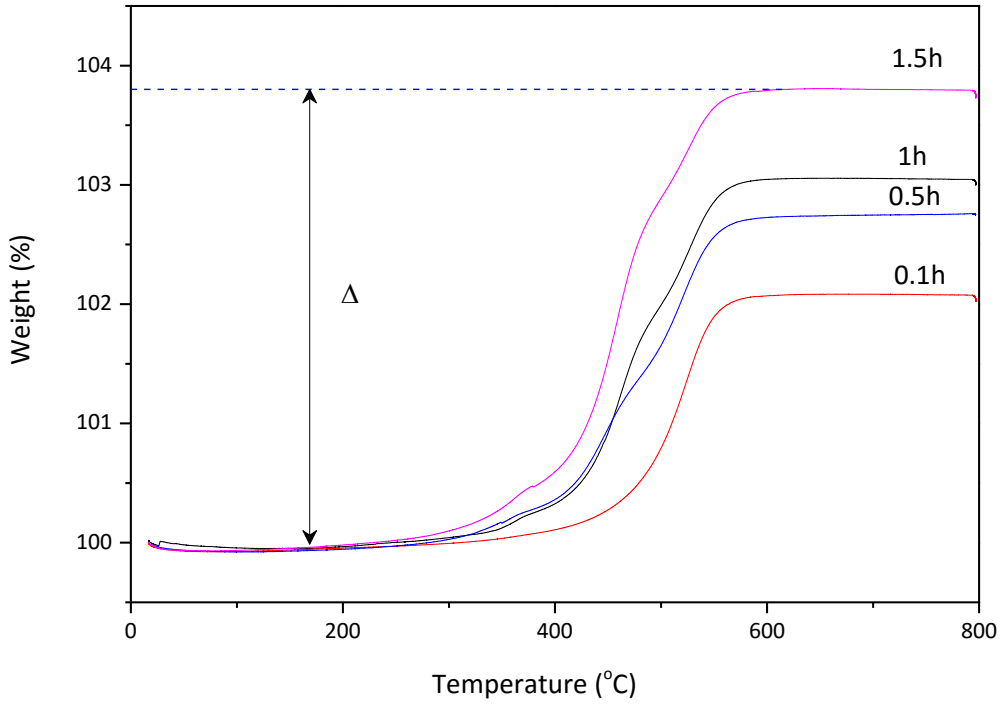

Figure 5.3 - Thermogravimetric profiles of solid state WO_{3-x} samples annealed for different times.

The observed gain in mass was assumed to be oxygen taken up because the product remaining after heating was stoichiometric WO_3 (see Figure A.4.2) and a colour change occurred from dark blue to pale green. This was the case for all 4 samples. The final mass in

grams (y) was used to calculate the number of moles of WO_3 present. The difference in initial mass and final mass (Δ) was divided by the molecular mass of O_2 to find the number of moles of oxygen taken up. The molar ratio of WO_3:O_2 was used to find the value of x in WO_{3-x}. This is summarised in the equation below.

$$x = \frac{mol\ O_2}{mol\ WO_3} = \frac{\Delta/31.988}{y/231.847}$$

The calculated compositions are shown in Table 5.1.

Table 5.1 - Compositions of WO_{3-x} samples made via solid state route

Annealing Time (h)	x	Composition
0.1	0.15	$WO_{2.85}$
0.5	0.19	$WO_{2.81}$
1	0.21	$WO_{2.79}$
1.5	0.27	$WO_{2.73}$

The expected trend of level of reduction increasing with annealing time is observed. It can be seen in Figure 5.3 that the samples annealed for longer had a greater increase of weight with heating because they took up more oxygen. The sample reduced for 1.5 hours is close to the theoretical maximum level of reduction of $WO_{2.72}$ ($W_{18}O_{49}$). The solvothermal sample does not show the same behaviour – it loses mass overall which represents loss of the water present in the sample (see Figure A.4.3). Because of this, the composition cannot be determined in the same way although the final product is also WO_3.

5.2.4 Scanning Electron Microscopy (SEM)

SEM was used to examine the microstructure of the solvothermal (ST) and solid state (SS) samples of $W_{18}O_{49}$. Images of the ST sample are shown in Figure 5.4 and it can be seen that a hierarchical nanostructure has formed. In Figure 5.4a and 5.4b, 'urchins' can be seen composed of small 1D nanowires which measure approximately 30 nm in width and are aggregated together into roughly round shapes which are 1-2 μm in diameter. This is very similar to the morphologies seen in the literature by Bai *et. al.* which they describe as "nanowire networks"[3].

SEM images of the SS samples are also shown in Figure 5.4c and 5.4d and are representative of the SS samples annealed for all different time values. It can be seen that defined large nanorod 'bundles' are formed. They are homogenous with no other morphologies evident. They are 300-400 nm wide and around 2 µm long. The anisotropic growth direction of $W_{18}O_{49}$ can clearly be seen from these elongated rods and the growth direction according to Bai *et. al.* is along the b-axis, parallel to the direction of the pentagonal columns and hexagonal tunnels present in the crystal structure[3].

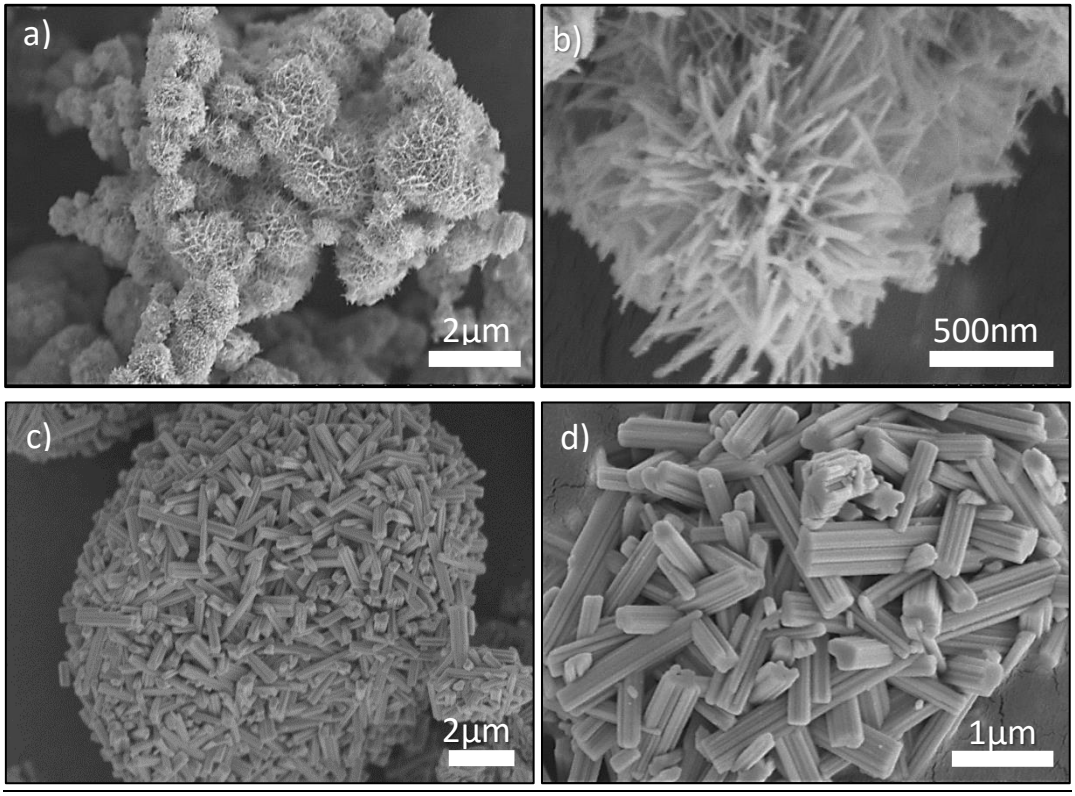

Figure 5.4 - SEM images of WO_{3-x} samples made by a, b) solvothermal and c, d) solid state routes.

The nanowires of the ST sample are much smaller than the structures visible in the SS sample, by around an order of magnitude. This correlates with the PXRD patterns shown in Figure 5.1 in which the SS sample shows much sharper peaks indicative of a more crystalline sample. The peak broadening of the ST sample is caused by the smaller particle size.

The Scherrer equation is commonly used to estimate crystallite size[16]. It takes the form:

$$\tau = \frac{K\lambda}{\beta cos\theta} \qquad (22)$$

τ is the crystallite size, K is a shape factor, usually 1; λ is the wavelength of the incident X-rays, β is the line broadening in radians at the full-width half maximum point of the peak and θ is the Bragg angle. The equation is limited to use on samples with nanosized domains. Although using the Scherrer equation to calculate particle size of the ST is difficult due to the lack of defined peaks, a rough value of 52.86 nm is calculated using the main peak. It indicates that the crystallite size is around half of that for the SS sample which was calculated to be 118.08 nm. These values should not be taken as accurate since significant assumptions such as spherical particle shape have been made. However they serve as a numerical representation of the differences that can be seen in the PXRD and SEM data.

5.2.5 UV-vis-NIR Spectroscopy

The optical absorbance spectra of the solvothermal (ST) and solid state (SS) $W_{18}O_{49}$ samples are shown in Figure 5.5. The SS profile is representative of the SS samples annealed for all time values as there was no significant variation across the series. As was the case with the PXRD diffractograms, the difference between the two is striking. The ST profile again matches that of Bai *et. al.*[3] and shows a broad NIR absorbance peak with a maximum at around 1200 nm and a large dip in the visible region. The SS sample has almost the opposite form with an absorbance peak in the visible region at around 500 nm and dip in absorbance in the NIR region.

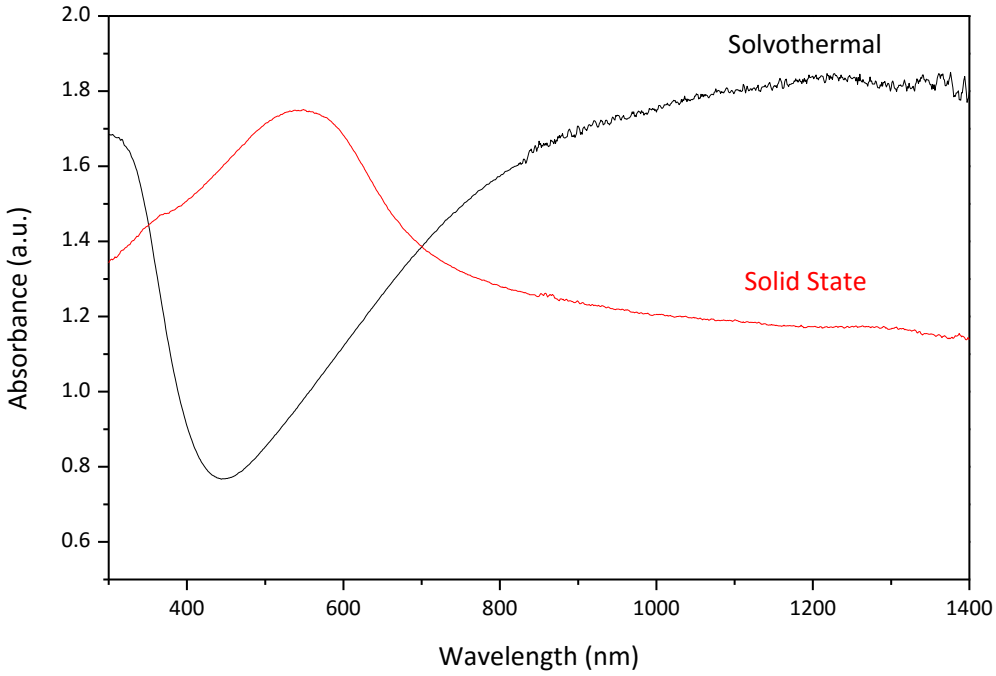

Figure 5.5 - UV-vis-NIR absorbance spectra for WO_{3-x} samples made by solvothermal and solid state routes

The mechanism of NIR absorption by tungsten oxides has been discussed in the literature, the main theories proposed being *local surface plasmon resonance* (LSPR) and *small polaron hopping*. Both phenomena are discussed in detail in Chapter 1. In the ST and SS samples it can be assumed that both polarons and LSPR are present to some extent as discussed in section 5.1. However due to their differences in particle size and crystallinity they exhibit different dominant absorption mechanisms. The solid state sample has greater bulk character and so can host more polarons. The ST has smaller particles and therefore much larger surface area to accommodate strong LSPR effects. This accounts for the difference in energy of the absorbance peaks seen in Figure 5.5 and is in accordance with the conclusions of Bai *et. al.*[3] as well as the work of Manthiram and Alivisatos[17]. A profile with two peaks is not seen for the solid state sample as was the case with the solid state tungsten bronzes (Figure 3.12 and 4.15). This reinforces the theory that this is a distinct feature of the hexagonal tungsten bronze crystal structure. However the SS profile is similar to that of NaTB-SS4 (Figure 3.10) in which the peak was assigned to plasmon absorption.

The blue colouration of these compounds is caused by W^{5+} colour centres which are created on the removal of oxygen atoms to maintain charge neutrality of the complex. Temporary colouration can be caused in WO_3 by mechanical milling due to the appearance of W^{5+} at the surfaces of freshly cracked crystals[18]. In studies of lightly reduced phases ($x < 0.1$), W^{5+} was found to be the dominant reduced species and little evidence of W^{4+} was found[19]. However in the more reduced phases some W^{4+} is also seen[20].

5.3 Results of Laser Imaging

The WO_{3-x} samples were tested for laser imaging performance at the Datalase laboratories as detailed in section 2.4. Optical density (OD) values were used to judge the quality of the images formed. The darker the image compared to the background colour, the better the performance – i.e. high contrast is desirable. Results are shown in Figure 5.6.

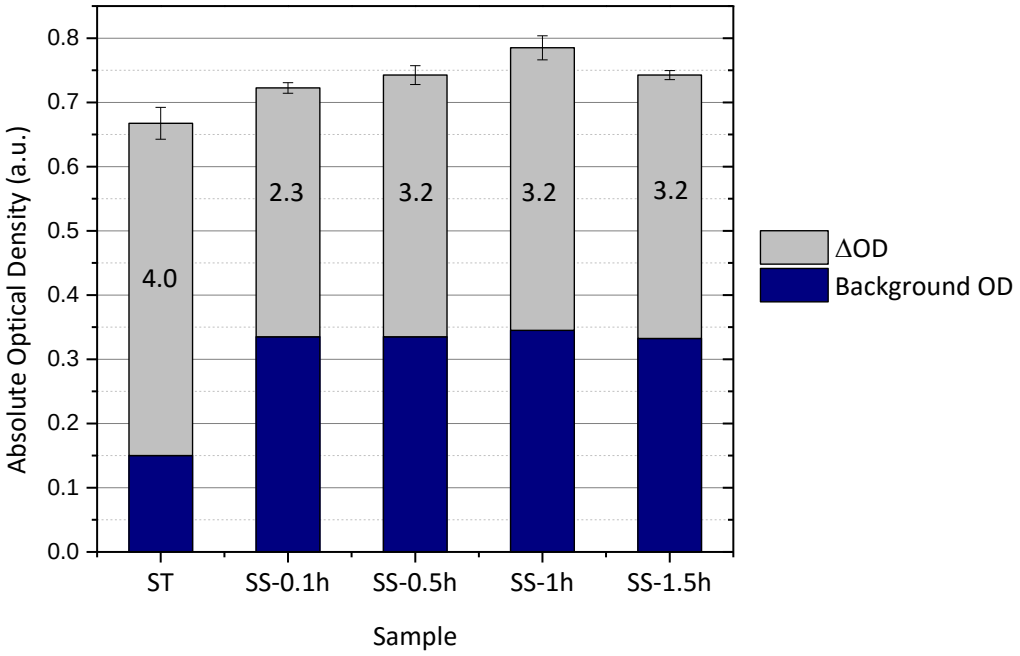

Figure 5.6 - Optical density values of laser images on films coated in ink containing different NIR absorbers ST=solvothermal, SS=solid state; Values on bars=the laser fluence value at which the highest OD was reached for each sample in Jcm^{-1}.

Unlike the tungsten bronzes, the WO_{3-x} samples were first loaded into the ink at 2.5 wt%. The solvothermal sample (ST) is on the left of the figure and the remaining four bars show results for solid state (SS) samples annealed for increasing amounts of time. As could be expected from the optical absorbance plots, the background OD of the ST sample is much lower than that of the SS samples. The SS absorbance peak was located in the visible region of the electromagnetic spectrum making them darker in colour and therefore darker when formulated into coatings. The absolute OD of the SS samples is higher than that of the ST sample largely due to their higher background OD. The ST sample has a higher ΔOD than any of the SS samples.

Across the range of SS samples there are slight fluctuations in background coating OD and a peak in ΔOD at the SS-1h sample. The background OD of these samples at this loading concentration is too dark for commercial use. The OD of uncoated PET substrate is 0.09 and values should be as close to this as possible for effective imaging. The fluence values marked on the bars correspond to the fluence at which the highest ΔOD is reached. In general the ΔOD values increase with increasing fluence however the highest fluences can sometimes ablate the coating off the substrate which causes a decrease in ΔOD at the

highest fluence(s). This is seen for the SS samples. The highest ΔOD values are reached at lower laser fluences than the ST sample because the coatings are so dark that some is ablated off above these fluences. The absorber has absorbed so much of the NIR radiation that some of the coating is essentially burned off. As long as the working fluence remains below 5Jcm^{-1} then it is commercially viable, which is the case for all samples in this range.

The ST and SS-1h samples were also tested at a lower loading of 0.75 wt% to see if a lower concentration would give good imaging with a lighter background colour. The results compared to the corresponding 2.5 wt% samples are shown in Figure 5.7.

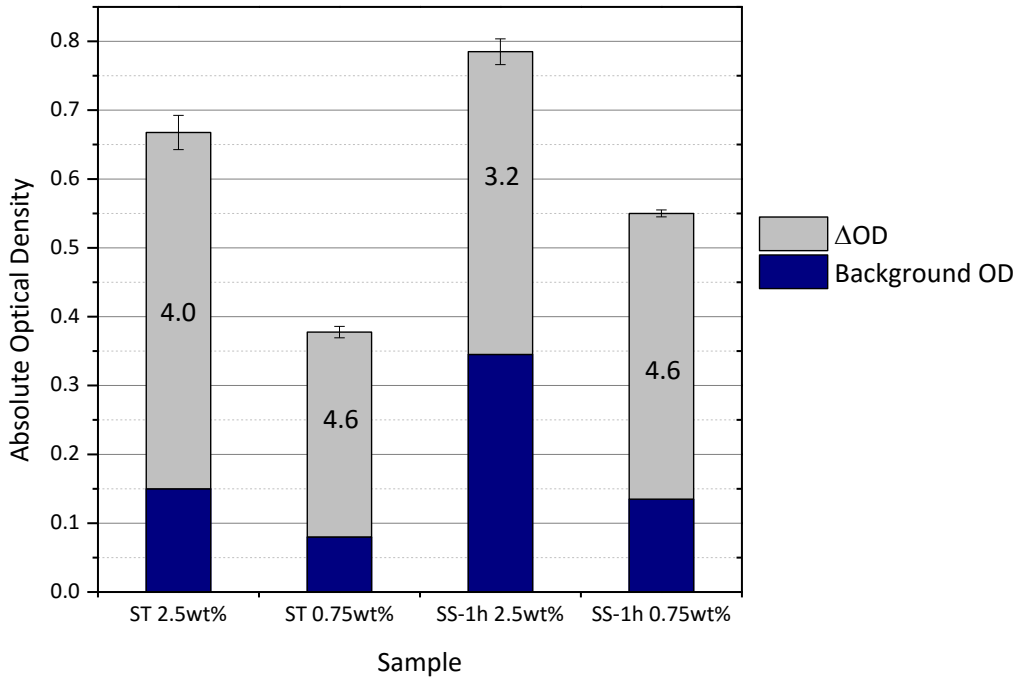

Figure 5.7 - Optical density values of laser images on films coated in ink containing NIR absorbers used in different concentrations. ST=solvothermal, SS=solid state. Values on bars=the laser fluence value at which the highest OD was reached for each sample in Jcm^{-1}.

It can be seen immediately that the background optical densities of the coatings are much lighter at lower concentrations, particularly for the SS sample. The background OD of the ST sample at 0.75 wt% is very close to that of uncoated PET. The ΔOD values decrease slightly due to the reduced amount of absorber present but the decrease is not directly proportional to the decrease in concentration. The samples at lower wt% loadings both achieve their highest ΔOD values at the highest fluence used (4.6 Jcm^{-1}) – no laser ablation occurs, because the reduced amount of absorber means that not enough of the laser radiation can be absorbed for this to occur. The error values of the 0.75 wt% results are

also smaller indicating that the results are more consistent than for the samples loaded at 2.5 wt%. The commercial WO_{3-x} sample (BTO2, see Appendix A.1) did not form images at all under these conditions – it needs to be added in higher concentrations. Also its larger particle size hinders good distribution through the ink.

Over time (around 1 year) the $W_{18}O_{49}$-ST sample changed colour from blue to green. This indicates that the sample has oxidised to form WO_3 although the PXRD pattern remains as amorphous as that in Figure 5.1 and no new features are seen. The small particle size, water present and poorly crystalline nature of the sample could all aid this process. This instability makes it undesirable for commercial purposes since the absorbers could be stored for periods of time before use.

5.4 Thermal Measurements

The UV-vis-NIR spectra can explain the difference in background coating colour but the ST and SS samples show similar ΔOD values when irradiated despite the SS sample absorbing less NIR radiation in the optical absorbance spectrum than the ST sample. The images are the result of a two-step process – the NIR laser irradiation is absorbed by the absorber particles which are excited then transfer the energy non-radiatively to the pigment particles as heat to cause the colour change. The second heat-transfer step is difficult to measure quantitively although an attempt was made using a pyrometer in Chapter 4. For the WO_{3-x} samples pellets of pure NIR absorber (ST and SS-1h WO_{3-x} in this case) were irradiated directly with the 1070 nm laser and the temperature increase on the same side of the pellet was recorded with a thermocouple 5 seconds after irradiation. The temperature increase on the opposite side of the pellet was also recorded 5 seconds after irradiation. The measurements were repeated three times and the values measured on the opposite side of the pellet from the laser were adjusted to account for the pellets width. The results for the solvothermal sample and the solid state sample annealed for 1 hour are shown in Table 5.2.

Table 5.2 - Temperature increase on NIR absorber pellets 5 seconds after 1070nm laser irradiation measured with a thermocouple.

Sample	Same side (^{o}C)	Opposite side (^{o}C)
Solvothermal	0.5 ± 0.08	0.2 ± 0.07
Solid state (1h)	1.1 ± 0.08	1.5 ± 0.08

While these measurements are fairly rudimentary, nevertheless they give an indication that the solid state sample is a more effective conductor of heat than the ST sample. The opposite side of the SS pellet is hotter than the irradiated side after 5 seconds showing fast

conduction of heat. This could help explain the similar ΔOD values obtained during laser imaging. The ST sample can absorb NIR radiation more strongly but is not a good at transferring the energy to the pigment particles. The SS sample absorbs less radiation but passes on the energy it does absorb more efficiently causing a similar level of imaging. The improved thermal conductivity could be linked to the more crystalline nature of the SS sample, as was discussed for CsTB samples in Chapter 4. Larger continuous areas of uninterrupted structural units with fewer grain boundaries provide a faster conduction pathway.

5.5 Conclusion

Despite some interesting particle morphologies, ultimately the solvothermal WO_{3-x} sample proved to be unstable in air and oxidised over time so is not suitable for industrial applications. In any case the ΔOD of the images formed is not as large as for other NIR absorber samples like the tungsten bronzes. As discussed previously, the SS samples were too dark after formulation into ink coatings for commercial laser imaging applications. The greater crystallinity of the SS samples improved image formation by transferring heat effectively while the smaller particle size of the ST sample gave it higher optical absorbance in the NIR region. If these two properties could be combined in a single $W_{18}O_{49}$ sample then it is likely a more successful absorber would be the result but the synthetic routes used in this work yield distinctly different products. Further modification of synthetic routes, like that undertaken for the Cs_xWO_3 samples in Chapter 4, is outside the scope of this project but could be something for future consideration.

5.6 References

1. Magneli, A., Structures of the ReO_3-type with recurrent dislocations of atoms: `homologous series' of molybdenum and tungsten oxides. *Acta Crystallographica* **1953,** *6* (6), 495-500.
2. Viswanathan, K.; Brandt, K.; Salje, E., Crystal structure and charge carrier concentration of $W_{18}O_{49}$. *J Solid State Chem* **1981,** *36* (1), 45-51.
3. Bai, H.; Su, N.; Li, W.; Zhang, X.; Yan, Y.; Li, P.; Ouyang, S.; Ye, J.; Xi, G., $W_{18}O_{49}$ nanowire networks for catalyzed dehydration of isopropyl alcohol to propylene under visible light. *Journal of Materials Chemistry A* **2013,** *1* (20), 6125-6129.
4. Iguchi, E.; Salje, E.; Tilley, R. J. D., Polaron interaction energies in reduced tungsten trioxide. *J Solid State Chem* **1981,** *38* (3), 342-359.
5. Salje, E.; Güttler, B., Anderson transition and intermediate polaron formation in WO_{3-x} Transport properties and optical absorption. *Philosophical Magazine Part B* **1984,** *50* (5), 607-620.
6. Schirmer, O. F.; Wittwer, V.; Baur, G.; Brandt, G., Dependence of WO_3 Electrochromic Absorption on Crystallinity. *J Electrochem Soc* **1977,** *124* (5), 749-753.
7. Adachi, K.; Asahi, T., Activation of plasmons and polarons in solar control cesium tungsten bronze and reduced tungsten oxide nanoparticles. *J Mater Res* **2012,** *27* (06), 965-970.
8. Berak, J. M.; Sienko, M. J., Effect of oxygen-deficiency on electrical transport properties of tungsten trioxide crystals. *J Solid State Chem* **1970,** *2* (1), 109-133.
9. Sundberg, M., Structure and "oxidation behavior" of $W_{24}O_{70}$, a new member of the {103} CS series of tungsten oxides. *J Solid State Chem* **1980,** *35* (1), 120-127.
10. Lou, X. W.; Zeng, H. C., An Inorganic Route for Controlled Synthesis of $W_{18}O_{49}$ Nanorods and Nanofibers in Solution. *Inorganic Chemistry* **2003,** *42* (20), 6169-6171.
11. Choi, H. G.; Jung, Y. H.; Kim, D. K., Solvothermal Synthesis of Tungsten Oxide Nanorod/Nanowire/Nanosheet. *J Am Ceram Soc* **2005,** *88* (6), 1684-1686.
12. Guo, C.; Yin, S.; Huang, Y.; Dong, Q.; Sato, T., Synthesis of $W_{18}O_{49}$ Nanorod via Ammonium Tungsten Oxide and Its Interesting Optical Properties. *Langmuir* **2011,** *27* (19), 12172-12178.
13. Guo, C.; Yin, S.; Yan, M.; Kobayashi, M.; Kakihana, M.; Sato, T., Morphology-Controlled Synthesis of $W_{18}O_{49}$ Nanostructures and Their Near-Infrared Absorption Properties. *Inorganic Chemistry* **2012,** *51* (8), 4763-4771.
14. Booth, J.; Ekström, T.; Iguchi, E.; Tilley, R. J. D., Notes on phases occurring in the binary tungsten-oxygen system. *J Solid State Chem* **1982,** *41* (3), 293-307.
15. Pfeifer, J.; Guifang, C.; Tekula-Buxbaum, P.; Kiss, B. A.; Farkas-Jahnke, M.; Vadasdi, K., A reinvestigation of the preparation of tungsten oxide hydrate WO_3,$^1/_3H_2O$. *J Solid State Chem* **1995,** *119* (1), 90-97.
16. Patterson, A. L., The Scherrer Formula for X-Ray Particle Size Determination. *Phys Rev* **1939,** *56* (10), 978-982.
17. Manthiram, K.; Alivisatos, A. P., Tunable Localized Surface Plasmon Resonances in Tungsten Oxide Nanocrystals. *Journal of the American Chemical Society* **2012,** *134* (9), 3995-3998.
18. Kuzmin, A.; Purans, J.; Cazzanelli, E.; Vinegoni, C.; Mariotto, G., X-ray diffraction, extended x-ray absorption fine structure and Raman spectroscopy studies of WO_3 powders and $(1-x)WO_{3-y}.xReO_2$ mixtures. *J Appl Phys* **1998,** *84* (10), 5515-5524.
19. Salje, E.; Carley, A. F.; Roberts, M. W., The effect of reduction and temperature on the electronic core levels of tungsten and molybdenum in WO_3 and $W_xMo_{1-x}O_3$—A photoelectron spectroscopic study. *J Solid State Chem* **1979,** *29* (2), 237-251.
20. Guo, C.; Yin, S.; Dong, Q.; Sato, T., The near infrared absorption properties of $W_{18}O_{49}$. *RSC Advances* **2012,** *2* (12), 5041-5043.

Chapter 6

Other Bronze Compounds

6.1 Phosphate Tungsten Bronzes

6.1.1 Introduction

Following the success of the tungsten bronzes M_xWO_3 as near infrared absorbers (Chapters 3 ad 4), other compounds were sought with an overall tungsten oxidation state of between 5.5 and 6. The presence of some W^{5+} is necessary for NIR absorption but if all the W^{6+} is reduced the sample will be very darkly coloured. After elimination of compounds containing undesirable toxic elements, two families of compounds remained: polyoxotungstates and phosphate tungsten bronzes (PTBs). As there was little optical data available for the polyoxotungstates and questions of their stability, they were not pursued. However the phosphate tungsten bronzes $A_x(PO_2)_4(WO_3)_{2m}$ or $A_x(P_2O_4)_2(WO_3)_{2m}$ were considered viable candidates.

The first PTB was discovered in 1978, over 150 years after the first Na_xWO_3 sample, and even then it was by chance rather than design[1]. It was composed of diphosphate $P_2O_7^{4-}$ units and in the following years samples with monophosphate PO_4^{3-} units were also prepared[2]. Magneli recognised the structural similarity with γ-Mo_4O_{11} that he had worked on and the PTBs were examined for similar low-dimensional conductivity and charge density wave (CDW) properties[3] seen in molybdenum bronzes (see section 6.2 below). The conductivity along the *c*-axis is much higher than in other directions and CDW behaviour is observed. The transition temperature to a CDW state increases as *m* increases.

Despite the similarity in name, they are not isostructural with any of the alkali metal tungsten bronze phases. The larger size of the phosphate unit means it cannot simply be inserted into channels in a WO_6 framework like the alkali metal cations - rather they need to form part of the framework itself. Three main types exist with three different structures:

1. MPTBp: Monophosphate PTB with pentagonal channels (A = vacancy)
2. MPTBh: Monophosphate PTB with hexagonal channels (A = K, Na, Pb)
3. DPTBh: Diphosphate PTB with hexagonal channels (A = K, Rb, Tl, Ba)

The basic structure is made up of perovskite layers of WO_6 octahedra linked by phosphate tetrahedra layers. The corner-sharing layers of WO_6 octahedra are tilted in a zigzag arrangement in the MPTB structures but have a non-tilted linear arrangement in the DPTB structure. The WO_6 octahedra are corner-linked together to form slabs of width *m* octahedra (hence the general formulae $A_x(PO_2)_4(WO_3)_{2m}$ and $A_x(P_2O_4)_2(WO_3)_{2m}$) and these are axially corner-linked to other slabs to form infinite ribbons. The ribbons are linked by diphosphate P_2O_7 units in the DPTBh structure to form a three dimensional network with octagonal channels running along the [001] direction of the orthorhombic unit cell and hexagonal channels running along the [010] direction.

The MPTB structures differ only in the way the WO_6 ribbons are linked together by PO_4 tetrahedra. Parallel linkage, in which the layers are related by translation, results in the formation of hexagonal channels and the MPTBh structure. Anti-parallel linkage in which the layers are related by a rotation axis gives the MPTBp structure with pentagonal channels. The channels can more accurately be described as cavities linked by hexagonal or pentagonal windows. Guest cations can reside in the larger cavities of the MPTBh structure. These structures are similar to the Magneli phases discussed in Chapter 5. The MPTBp phase with m = 4 was chosen for initial synthesis (as it is the simplest since the A species is a vacancy) with the possibility of attempting an MPTBh phase containing an alkali metal guest as the next step. The formation of the different PTB structures from the basic octahedral and tetrahedral building blocks is shown in Figure 6.1.

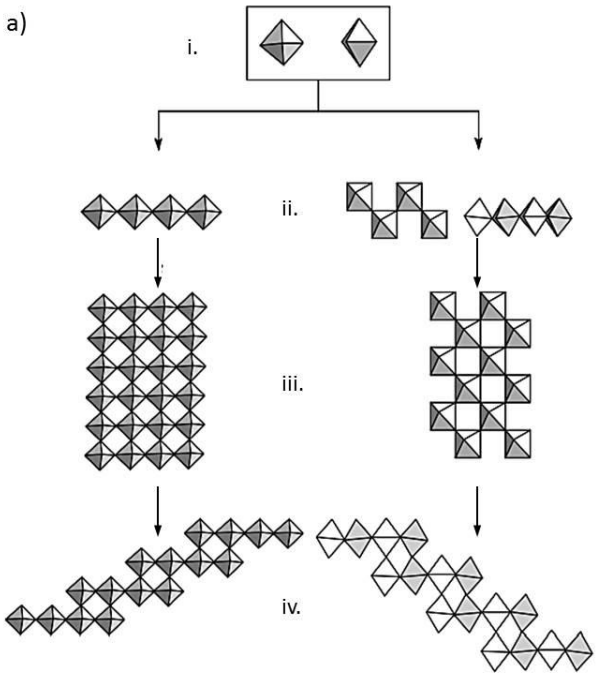

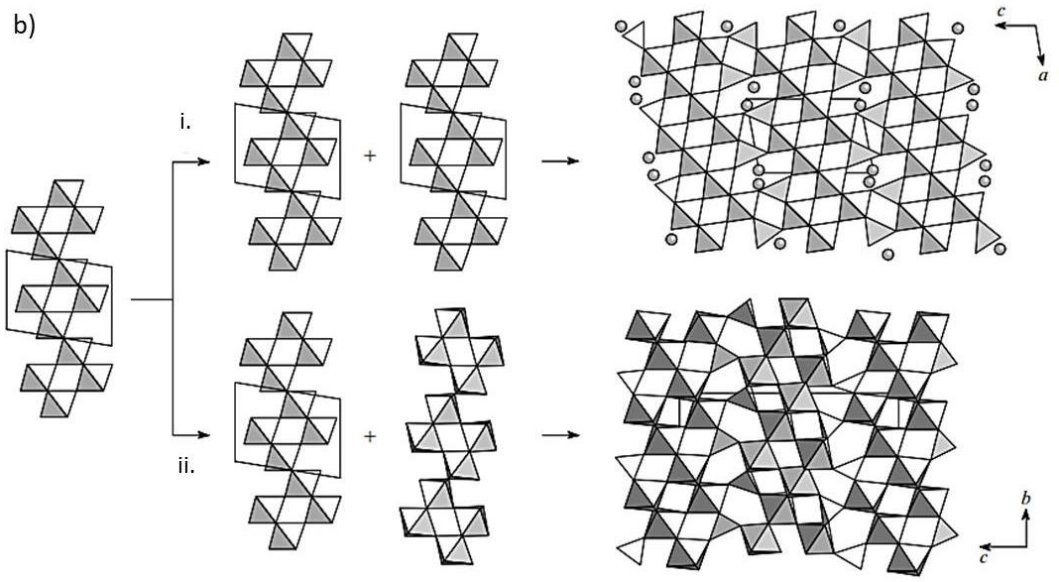

***Figure 6.1 – a) Step-wise arrangement of WO_6 octahedra into slabs in the DPTBh structure (left) and MPTB structures (right) and b) i) parallel and ii) antiparallel joining of WO_6 layers to form the MPTBh and MPTBp structures respectively. Adapted from Skopeko* et. al.[4]**

In Figure 6.1ai the isolated octahedral are shown assembling into blocks of four (Figure 6.1aii) in a straight (left) or tilted (right) arrangement. The blocks then assemble into slabs (Figure 6.1aiii) before linking with other slabs to form a three dimensional layered structure. Figure 6.1b shows the possible parallel (Figure 6.1bi) and anti-parallel (Figure 6.1bii) linkages of the tilted layers to form the MPTBh and MPTBp structures respectively.

Changes of symmetry occur for different values of *m* so phases with four different space groups are known. The value of *m* ranges from 2-12 and even numbers are more common than odd, although samples have been made with m = 5 and m = 7[5].

6.1.2 Synthesis

Unfortunately, considering their interesting physical properties, PTBs are not straightforward to synthesise. They are very sensitive to reaction conditions and often form intergrowth phases. Despite this, many attempts have been made and the full list of starting materials, conditions and relevant references can be consulted in reference 4. Chemical vapour transport and flux melt systems have been used to grow single crystals. Polycrystalline samples are generally made by solid state routes in a two-step process. The first is to decompose an ammonium orthophosphate starting material with tungsten trioxide then, in the second step, metallic tungsten is added and the mixture heated to high temperatures for relatively long times. The non-equilibrium nature of reduction by

transition metals leads to co-existence of regions in which co-crystallisation of different phases occurs within narrow temperature and concentration ranges. Skopenko *et. al.* note that:

> *"often crystallisation of compounds differing in composition and structure occurs under identical experimental conditions."*[4].

In this work the route used by Roussel *et. al.* was used as a starting point[6] for synthesis of monophosphate $(PO_2)_4(WO_3)_{2m}$ with m = 4 i.e. $P_4W_8O_{32}$ on a 1 g scale. Appropriate amounts of diammonium hydrogen phosphate $(NH_4)_2HPO_4$ (Alfa Aesar 98% min) were mixed with WO_3 (Sigma Aldrich 99.995%) using a pestle and mortar then heated in to 200, 400 and 600 ^oC for 12 h each in a platinum crucible. The resulting mixture was ground and weighed. The intermediate product mixture was identified by PXRD. In the second step of the synthesis appropriate amounts of tungsten powder were added according to the equation:

$$6WO_3 + 4(NH_4)_2HPO_4 \rightarrow 2WO_3 + 2W_2O_3(PO_4)_2 + 2W \rightarrow P_4W_8O_{32}\ (+side\ products)$$

The W (Sigma Aldrich 99.9%) was mixed with the intermediate product using a pestle and mortar then the powder was pressed into a rectangular pellet. The pellet was sealed into a quartz tube under vacuum and heated to 950 ^oC for 48 h. The tube was cut open, the pellet ground with a pestle and mortar then reformed, sealed into a tube again and reheated to 1150 ^oC for 48 h. The second heating step was repeated twice.

The method described above gave the best product although several other variations were used which resulted in impure mixtures of products. Reheating temperatures of 950 and 1050 ^oC and using 5 and 10 atomic percent excess of the $(NH_4)_2HPO_4$ starting material made little difference to results. Using H_2WO_4 instead of WO_3 as a starting material also had no significant effect. Chemical vapour transport was also attempted with a 200 ^oC temperature gradient but the result was single crystals of an impurity diphosphate phase $P_8W_{12}O_{52}$. All in all it took several months of work to achieve a sample for testing and so synthesis of further phosphate tungsten bronze samples was not attempted.

6.1.3 Characterisation

6.1.3.1 Powder X-ray diffraction (PXRD)

PXRD was used to determine the crystallinity and phase composition of the products. The diffractogram of the PTB sample is shown in Figure 6.2.

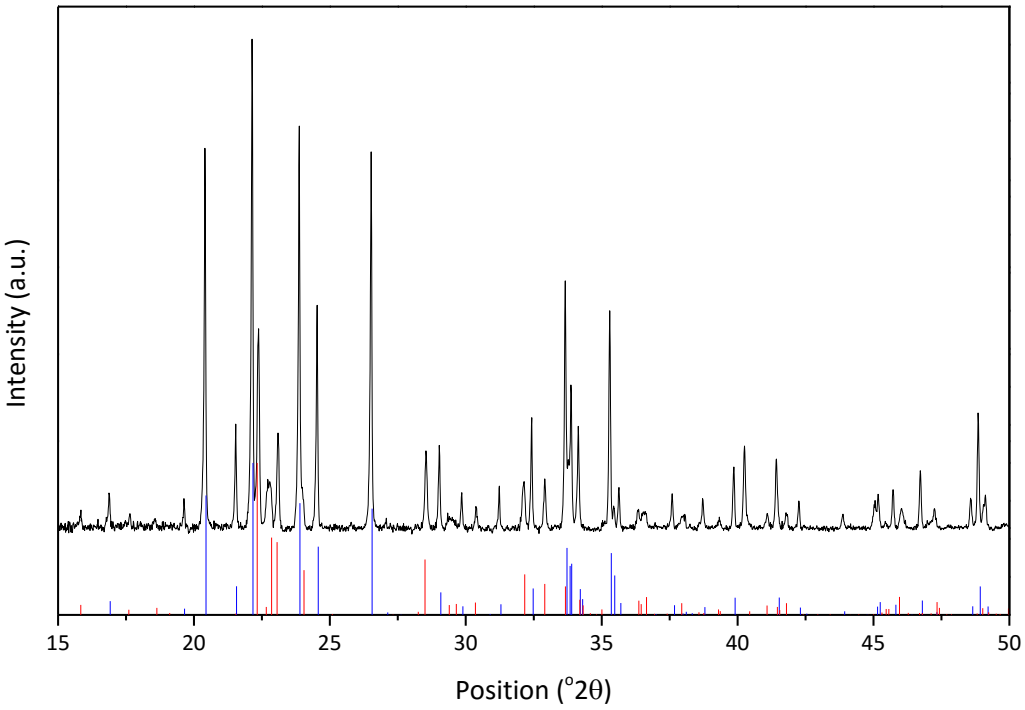

Figure 6.2 - PXRD diffractogram of phosphate tungsten bronze sample. The blue lines show expected peak positions and intensities for $P_4W_8O_{32}$ and the red lines $P_8W_{12}O_{52}$.

The sample is composed of two phases – the target compound $P_4W_8O_{32}$ and an impurity diphosphate $P_8W_{12}O_{52}$ phase. This was an improvement on earlier samples which had a third WO_2 phase. Removal of this phase was important for optical properties since WO_2 is black and therefore strongly absorbing. A small amount of cubic elemental tungsten is also present, indicated by the peak at around $2\theta = 40.5^{\circ}$.

The crystal structure of $P_4W_8O_{32}$ is in orthorhombic space group $P2_12_12_1$and is shown in Figure 6.3. The anti-parallel arrangement of WO_6 slabs can clearly be seen and each slab is 4 octahedra wide since m = 4. The PO_4 tetrahedra corner-link the WO_6 layers together forming pentagonal channels.

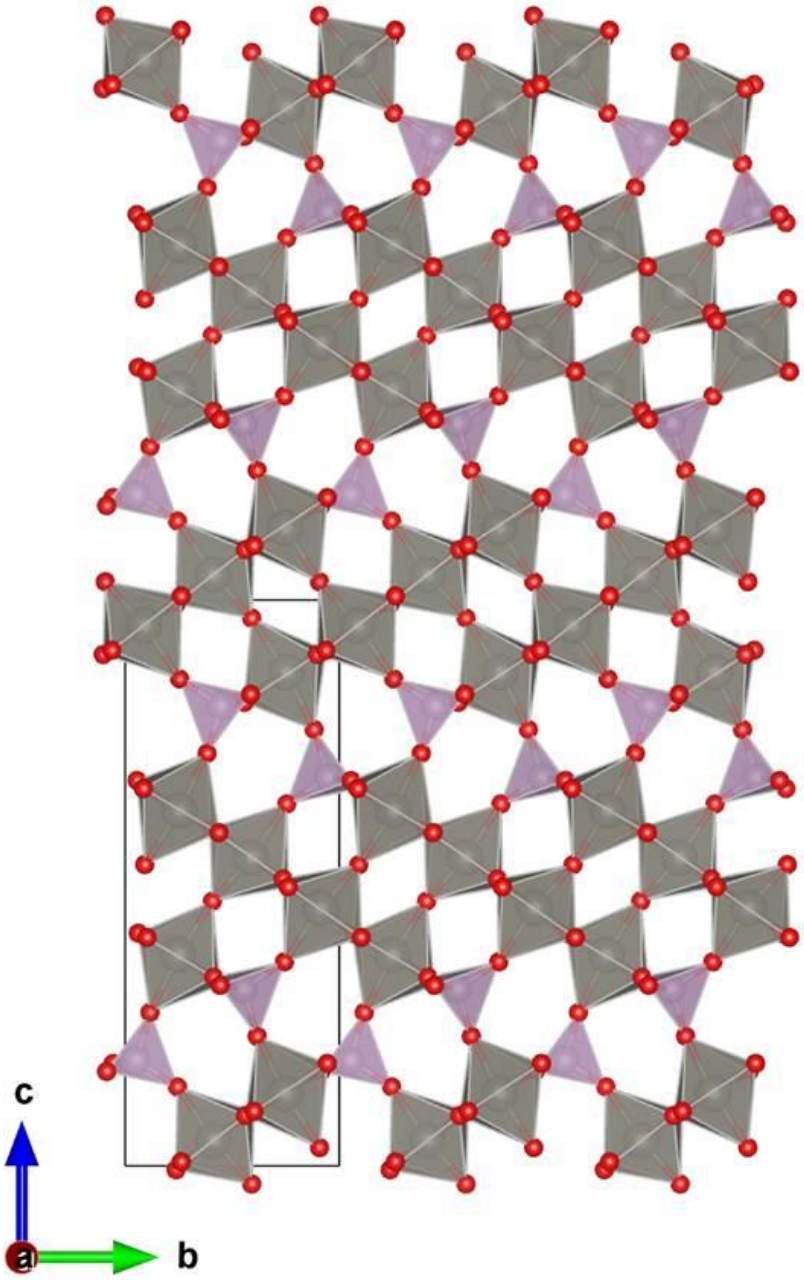

Figure 6.3 - Polyhedral representation of the crystal structure of $P_4W_8O_{32}$ viewed along the a axis. W=grey, P=purple and O=red.

The impurity $P_8W_{12}O_{52}$ diphosphate phase is in a different family of compounds and contains P_2O_7 diphosphate units instead of isolated PO_4 tetrahedra[7]. Its orthorhombic Pnam structure is shown in Figure 6.4.

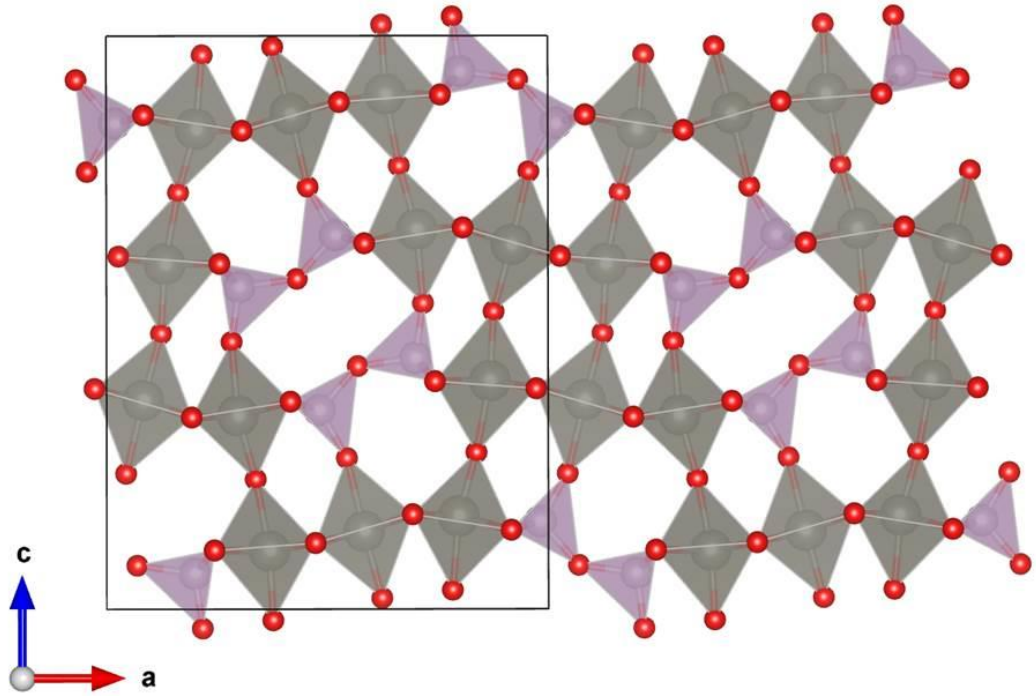

Figure 6.4 - Polyhedral representation of the crystal structure of $P_8W_{12}O_{52}$ viewed along the* b *axis. W=grey, P=purple and O=red.

The framework of this structure is similar to that of $P_4W_8O_{32}$ which is perhaps why it is difficult to isolate them. Both are built up of layers of tilted WO_6 octahedra linked by phosphate units and have channels in the structure – pentagonal in $P_4W_8O_{32}$ and both pentagonal and hexagonal in $P_8W_{12}O_{52}$. Rietveld refinement of the PXRD data (see Figure A.5.1 and Table 6.1) shows that 70.2% of the sample is the phosphate bronze $P_4W_8O_{32}$ and 27.8% the $P_8W_{12}O_{52}$ phase. The remaining 2% is tungsten.

Table 6.1 - Parameters calculated from Rietveld refinement of PXRD data for PTB sample.

Phase	Space Group	%of sample	a	b	c	Volume
$P_4W_8O_{32}$	$P2_12_12_1$	70.15	5.28997(7)	6.58597(9)	17.385(2)	605.6(1)
$P_8W_{12}O_{52}$	Pnam	27.84	11.9755(8)	15.6098(7)	5.3083(4)	992.3(1)
W	Im-3m	2.01	3.16662(9)	-	-	31.753(3)

Although stoichiometric amounts of starting materials were used, and the W amount was adjusted according to the yield of the decomposition step of the synthesis, there seems to be a deficiency in phosphorous. The reason for this is not clear and, as mentioned above, using 5 and 10% excess phosphate starting material did not resolve this issue.

6.1.3.2 UV-vis-NIR Spectroscopy

The optical absorbance profile for the PTB sample is shown in Figure 6.5.

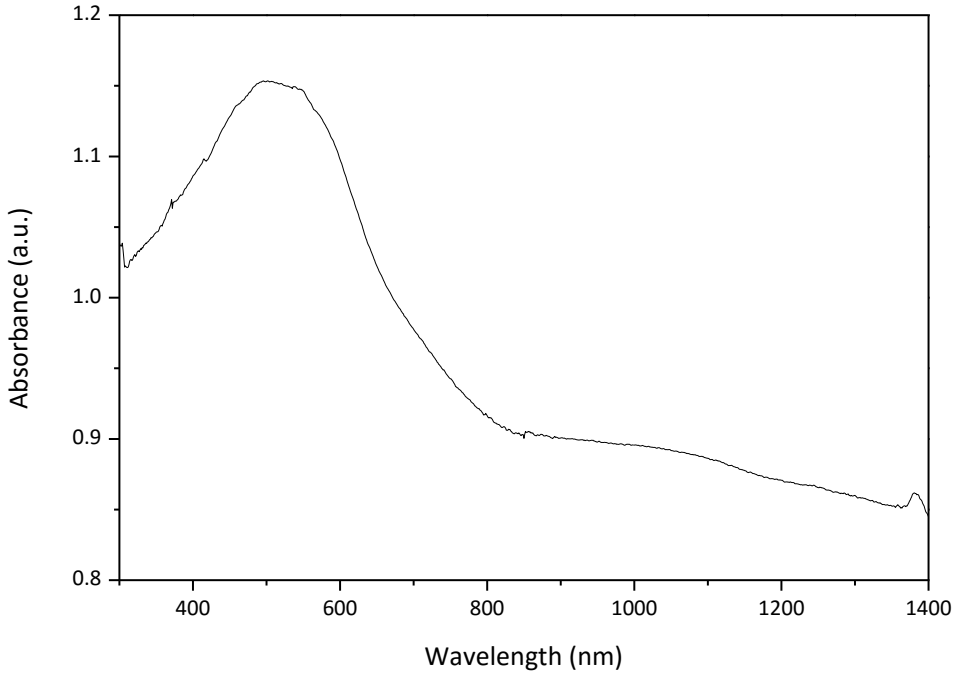

Figure 6.5 - Optical absorbance profile of PTB sample.

There is a peak in absorbance at around 500 nm in the visible region. It should be noted that Figure 6.5 shows a "zoomed in" view of the absorbance profile and it is relatively absorbing across the whole spectrum. The powder is a dark blue-ish red colour. Both the $P_4W_8O_{32}$ and $P_8W_{12}O_{52}$ phases contain mixed valence W^{5+} and W^{6+} species. Although optical properties are not often discussed directly in the literature, there is evidence that both localised and delocalised electrons are present in the monophosphate tungsten bronzes[8]. The delocalised electrons can be restricted to certain pathways depending on the crystal structure so PTB's are known to be 1D, 2D and 3D metallic conductors[4]. $P_4W_8O_{32}$ is a 2D conductor[5] so there are free electrons present to interact with incident radiation. The simultaneous presence of W^{5+} and W^{6+} also makes polaron hopping possible. There could be a second less intense absorbance feature at around 1100 nm in Figure 6.5 which would indicate that absorptions arise from two different mechanisms, or transitions with different energies. The alkali metal tungsten bronzes (Chapters 3 and 4) also exhibited a combination of plasmon and polaron absorbance mechanisms.

6.1.3.3 Scanning electron microscopy (SEM)

SEM was used to examine the particle size and morphology. As can be seen in Figure 6.6, the PTB sample is composed of a mixture of large and small featureless particles. There is no surface texture or defined particle shape which is common when using high temperature synthesis routes.

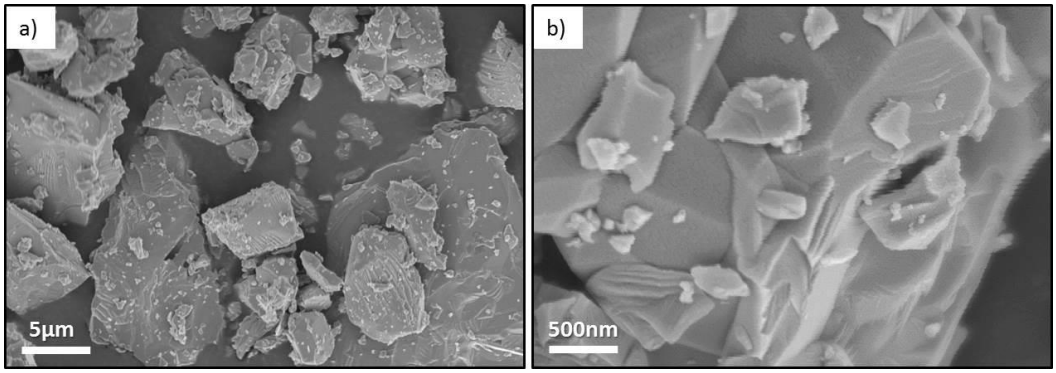

Figure 6.6 - SEM images of PTB sample. Scale bars are given.

The PTB sample was tested for laser imaging performance and the results are shown in section 6.3 below.

6.2 Molybdenum Bronzes

6.2.1 Introduction

The molybdenum analogues of alkali metal tungsten bronzes have also been investigated. They were discovered more recently than the tungsten bronzes but long before the phosphate tungsten bronzes with the first phase reported by Stavenhagen and Engels in 1895[9] but then no further work until the 1930's. However it wasn't until the 1960's that the compounds were more fully understood and characterised. They became well known for displaying charge density wave phenomena[10]. Like the alkali metal tungsten bronzes they have a general formula of M_xMoO_3 and are non-stoichiometric, however they do not adopt the same crystal structures as their tungsten counterparts. The structure adopted is also much more sensitive to composition with 'red' 'blue' and 'purple' molybdenum bronzes known with x = 0.33, 0.3 and 0.15 respectively.

Unlike the tungsten bronzes which are structurally built up of corner-sharing WO_6 octahedra, the molybdenum bronzes (MBs) contain MoO_6 octahedra which are both corner- and edge-sharing. These form two dimensional sheets which are arranged in layers held together by the M cations. In this respect they are more similar to the phosphate tungsten bronzes, discussed in section 6.1, that also adopt a layered structure. The nature

of the linkages determines whether the MB adopts the red, blue or purple structure. The three structural types are outlined below.

6.2.1.1 Red bronze

The red bronzes have a general composition of $M_{0.33}MoO_3$ and their crystal structure was first determined by Stephenson and Wadsley[11] in 1965. It is made up of clusters of six edge-sharing MoO_6 octahedra which are corner-linked to others along the *b*-axis forming infinite two dimensional sheets. The alkali metal sites lie between the layers, have irregular eight-fold coordination with distorted trigonal prismatic geometry and are in a zigzag chain arrangement relative to each other. The ratio of Mo atoms to M sites is 3:1 so a composition of $M_{0.33}MoO_3$ represents full M site occupation. The phase has monoclinic space group C2/m and the MoO_6 octahedra are distorted so there is considerable variation in Mo-O bond lengths and two distinct Mo sites.

The red bronze shows the electronic properties of a semi-conductor. Unlike the tungsten bronzes, Bang and Sperlich[12] found that the d electrons are localised on the octahedral clusters. Isostructural analogues are known with M = K, Rb, Cs and Tl but the M = Li phase forms a completely different three dimensional triclinic network[13].

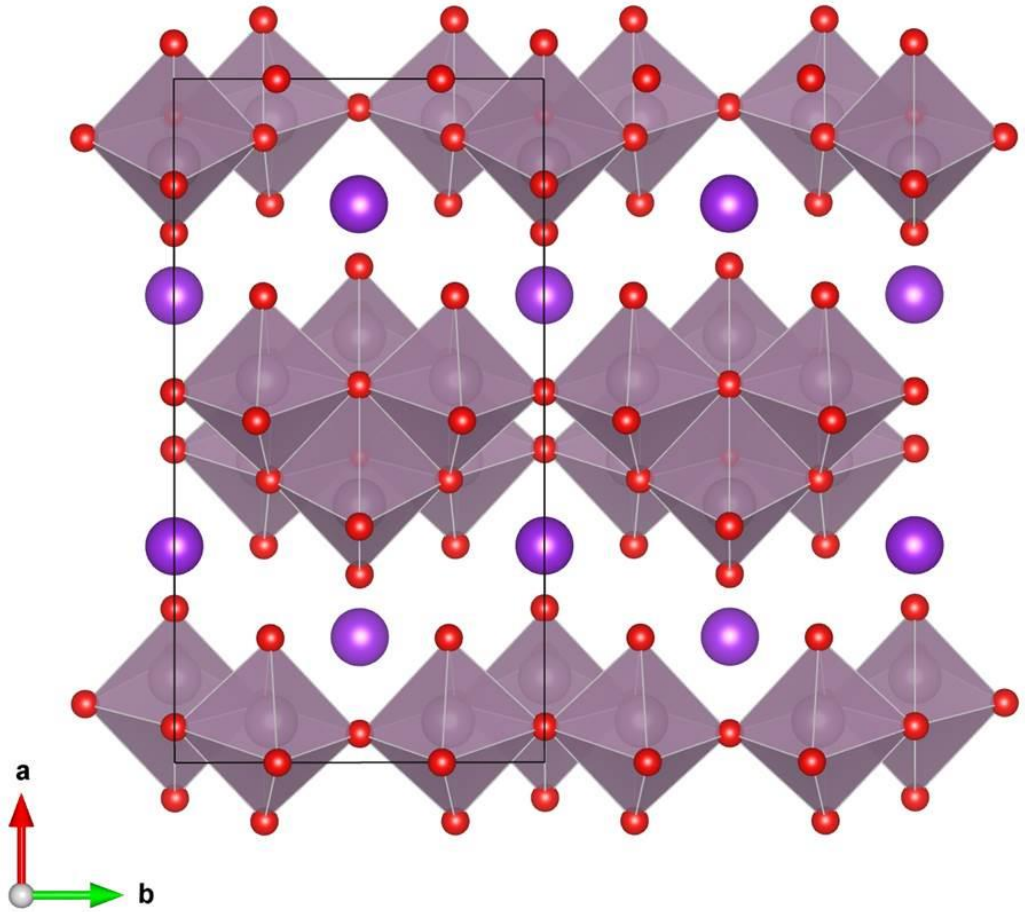

Figure 6.7 - Polyhedral representation of the red molybdenum bronze structure $M_{0.33}MoO_3$ viewed along the* c *axis. Mo=grey, O=red, M=purple.

6.2.1.2 Blue bronze

The crystal structures of the blue MB $M_{0.3}MoO_3$ is similar to that of the red bronze and also has monoclinic symmetry in space group C2/m[14]. However in this case clusters of ten rather than six MoO_6 octahedra form which are then linked by corners in the *b* direction to form infinite two dimensional sheets. As is the case for the red bronze, the available M sites are located between these sheets and the occupying cations hold the layers together. There are three independent Mo sites, one more than in the red bronze. The MoO_6 octahedra are distorted by Mo-Mo repulsion although not as strongly as in the red bronze. The red and blue MBs have been found to exist in parallel domains within crystals, unsurprising due to their structural similarity.

The blue bronzes exhibit anisotropic conductivity and are quasi-one-dimensional metals. The majority of the electron density is found on the Mo atoms that make up the chains along the *b*-axis in the layers. Metallic conductivity is seen along the *b* direction whereas semi-conducting behaviour is seen along the [102] direction and in the [201] direction

perpendicular to the layers. The electrons are not localised as in the red bronze but located in a π* conduction band originating from the overlap of Mo 4d(t_{2g}) orbitals with O p(π) orbitals. The nature and behaviour of a charge density wave in these phases has been widely studied[15]. Isostructural analogues exist with M = K, Rb and Tl.

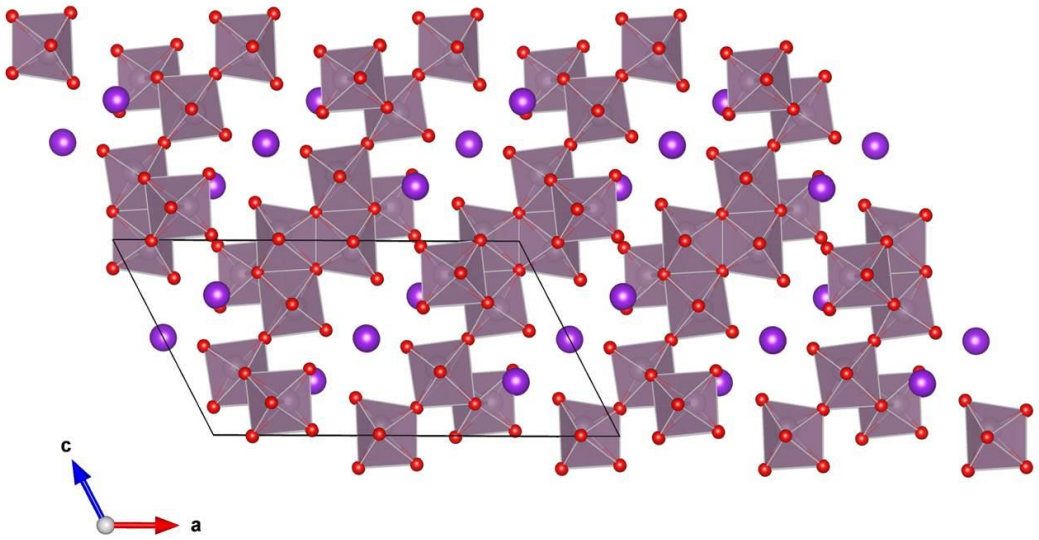

Figure 6.8 - Polyhedral representation of the blue molybdenum bronze structure $M_{0.3}MoO_3$ viewed along the* b *axis. Mo=grey, O=red, M=purple.

6.2.1.3 Purple Bronze

The purple molybdenum bronzes have the general formula $M_{0.9}Mo_6O_{17}$ and also adopt a layered structure like their red and blue counterparts. Analogues with M = Li, Na, K, and Tl are known but each have different space groups so the K structure will be discussed[16]. The framework in this case is built up of both MoO_6 octahedra and MoO_4 tetrahedra. Four layers of octahedra are corner-sharing to form ReO_3-like slabs which are terminated by a layer of tetrahedra on either side which are corner-linked to the octahedra. The slabs are infinite in the *a* and *b* directions and linked by a layer of K sites which are 12 coordinate icosahedra. The structure has trigonal symmetry in space group P-3.

This phase is a quasi-two-dimensional metallic conductor due to the anisotropy of the structure[15]. The 4d electrons are located in the slabs and can move freely within them along the *a* and *b* directions but not easily between slabs along the *c* direction. The Na and Tl purple bronzes are similar in structure but as with the red bronzes, the Li phase is structurally quite different and so exhibits different behaviour. Charge density waves are known in the M = Na, K and Tl phases but are less stable than those seen in the blue bronzes.

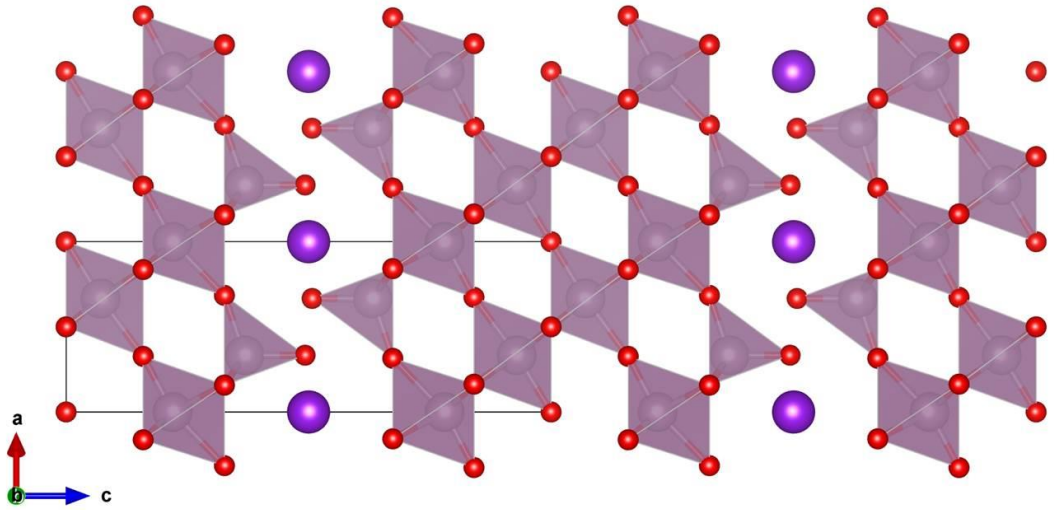

Figure 6.9 - Polyhedral representation of the purple molybdenum bronze structure $K_{0.9}Mo_6O_{17}$ viewed along the* b *axis. Mo=grey, O=red, K=purple.

6.2.2 Synthesis

The first MBs were generally prepared by electrolytic reduction. This method was used by Stavenhagen and Engels in 1895[9], Cannert in 1930[17] and Wold e*t .al.* in 1964[18] and many others since[19] to produce MB's with M = Li, Na, K, Rb Cs and also Tl[20] with red, blue and purple structural types, usually in single crystal form. Vapour phase transport or routes with temperature gradients have also been used extensively[21]. Uncommon phases have been prepared at high pressure[22] Polycrystalline samples have been made by traditional solid state synthesis from stoichiometric amounts of M_2MoO_4, MoO_3 and MoO_2 heated in evacuated quartz tubes[23].

More recently solution-based routes have been used. Thomas and McCarron[24] made a hydrated sodium molybdenum bronze by reducing a buffered solution of MoO_3 with $Na_2S_2O_4$. This phase was used as a starting material for ion exchange by Sotani *et. al.*[25] to make the potassium analogue. It was also used by Eda *et. al.*[26] for ion exchange to the caesium bronze. Sotani *et. al.*[27] also prepared H_xMoO_3 by reducing an acidic solution of $MoO_3$with Zn powder. Eda *et. al.*[28] successfully exchanged the H_xMoO_3 phase with KCl hydrothermally to give K_xMoO_3. Adding ethanol to this route produced K_xMoO_3 'nanoribbons'. Tsang *et. al.*[29] used KBH_4 to reduce solutions of K_2MoO_4 then crystallised the amorphous products by heating to 350 ^oC. Tsang and Manthiram[30] used the same procedure to make potassium analogues.

As for the tungsten bronzes in Chapter 3 and 4, both solvothermal and solid state synthetic routes were used in this work to prepare samples to test as NIR absorbers.

6.2.2.1 Solution-based Synthesis

1. H_xMoO_3 was made using the method from Sotani *et. al.*[27]. MoO_3 (Alfa Aesar 99.95%, 30 g, 0.208 mol) was added to 100 ml of 2 M HCl solution. Zn (Alfa Aesar 99,9%, 5 g, 0.076 mol) was added and caused a suspension colour change from pale green to dark blue. After stirring for 15 minutes, the suspension was filtered and the solid product washed with further HCl and water then dried.

2. The method used by Thomas and McCarron[24] was followed in order to make a sodium molybdenum bronze $Na_xMoO_3.yH_2O$. Pre-dried MoO_3 (Alfa Aesar 99.95%, 5 g, 0.035 mol) was added to 250 ml H_2O and N_2 bubbled through the solution for 30 minutes. $Na_2MoO_4.2H_2O$ (Sigma Aldrich 99.5%, 60 g, 0.25 mol) was added with $Na_2S_2O_4$ (Sigma Aldrich 85%, 2 g, 0.011 mol). A colour change from pale green to dark blue was observed. After 3 h stirring with on-going N_2 bubbling, the suspension was filtered and the solid blue product dried.

3. The product from synthesis 1 above was used as a starting material for hydrothermal ion exchange following the method by Eda *et. al.*[28]. 0.9 M KCl solution was deaerated using the freeze-pump-thaw method using liquid N_2 and a vacuum line. In a glove bag which had been purged with N_2 for several hours, 35 ml of the KCl solution was added to 0.43 g H_xMoO_3 in a 125 ml Teflon liner. The liner was sealed into a steel autoclave and heated to 180 ^oC for 48 h with heating and cooling rates of 10 ^oC/min. This was repeated using RbCl and CsCl solutions although the reaction with CsCl did not result in the formation of a product. Time constraints prevented optimisation of this reaction.

6.2.2.2 Solid State Synthesis

Only the potassium analogue was made by a solid state route. All heating rates were 5 ^oC/min. The method used by Hirata and Yagisawa[23] in 1990 was followed. K_2MoO_4 (Alfa Aesar 99.8%, 0.2505 g, 1.052 x 10^{-3} mol) was added to MoO_3 (Alfa Aesar 99.95%, 0.6149 g, 4.27 x 10^{-3} mol) and MoO_2 (Sigma Aldrich 97%, 0.1346 g, 1.052 x 10^{-3} mol) according to the following equation:

$$^x/_2\, K_2MoO_4 + (1-x)MoO_3 + \,^x/_2\, MoO_2 \rightarrow\ K_xMoO_3$$

MoO_2 was found to be of low purity so was replaced in subsequent reactions with appropriate amounts of MoO_3 and Mo. The reactants were ground together using a pestle and mortar then pressed into pellets. These were sealed into evacuated pyrex tubes and heated to 435 ^oC for 98 h. The tubes were cut open, the pellet ground using a pestle and mortar, re-pressed and reheated under the same conditions. The resulting dark blue product was ground again before characterisation.

Molten salt ion exchange routes were tried using several different salts and heating conditions without success.

A list of sample names is given in Table 6.1.

Table 6.2 - Summary of molybdenum bronze samples

Sample	Composition	Synthesis Route
HMB	H_xMoO_3	Reduction of MoO_3 in acid
NaMB	Na_xMoO_3	Reduction of MoO_3 with $Na_2S_2O_4$
KMB-ST	K_xMoO_3	Solvothermal ion exchange of HMB with KCl
KMB-SS	K_xMoO_3	Solid state
RbMB	Rb_xMoO_3	Solvothermal ion exchange of HMB with RbCl

6.2.3 Characterisation

6.2.3.1 Powder X-ray Diffraction (PXRD)

The PXRD diffractogram of HMB is shown in Figure 6.10. Although primarily made as a starting material for ion exchange to other molybdenum bronzes, the hydrogen analogues are molybdenum bronzes in their own right with 4 possible structural types which are dependent on the amount of H in the structure from $0 < x < 2$. When H is intercalated into the layered MoO_3 structure there are two possible sites for occupation. Phase I exists when $0.23 < x < 0.4$, phase II at $0.85 < x < 1.04$, phase III at $1.55 < x < 1.72$ and phase IV is the stoichiometric H_2MoO_3[31]. From Figure 6.10 it can be seen that the HMB sample forms the phase I structure which is monoclinic with space group $P2_1b$, shown in Figure 6.11.

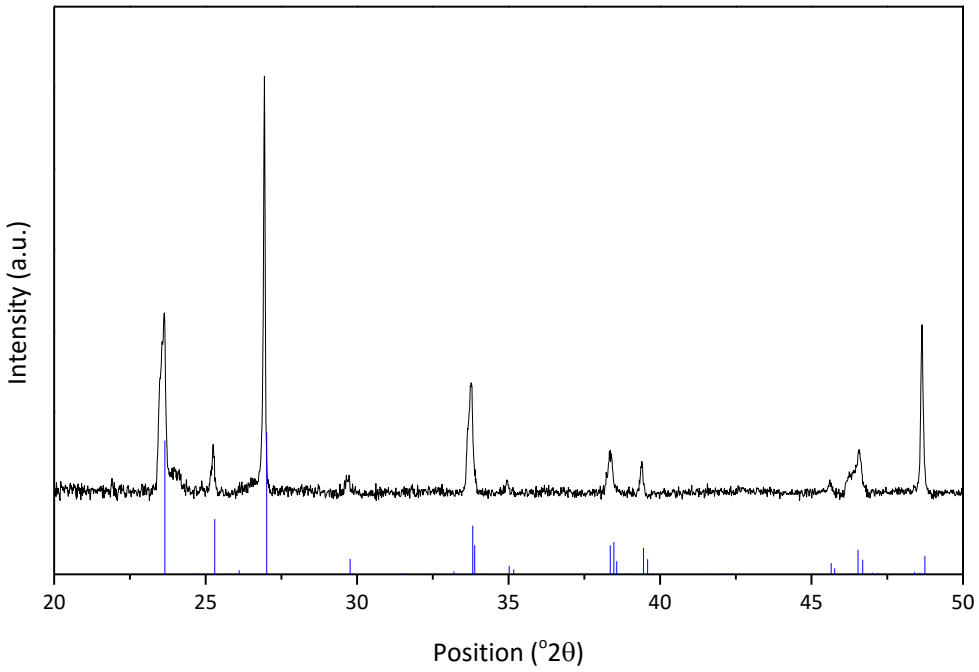

Figure 6.10 - PXRD diffractogram of H_xMoO_3. Expected peak positions and intensities are shown by blue lines.

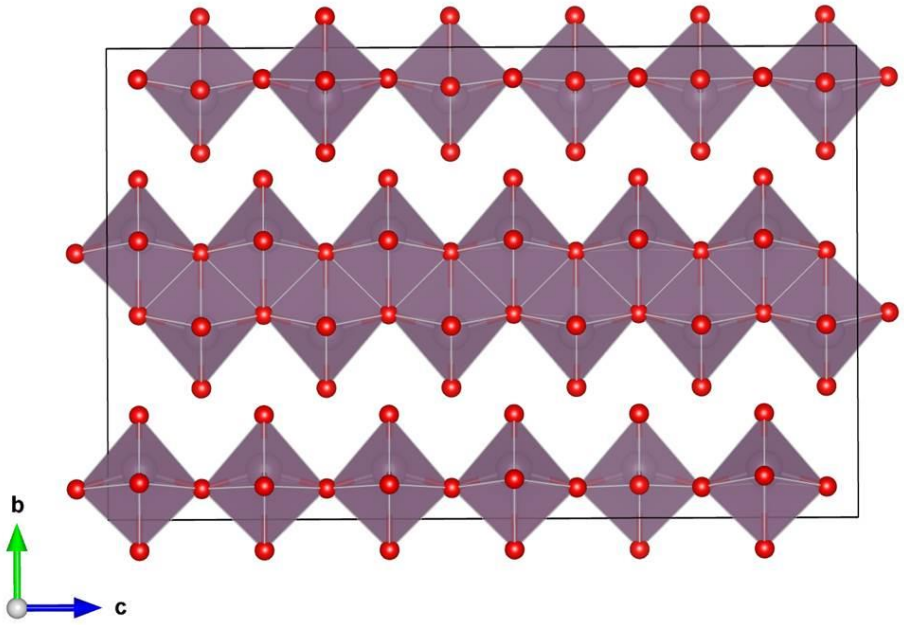

Figure 6.11 - Polyhedral representation of Phase I H_xMoO_3 structure. Mo=purple, O=red, H is not shown.

The proton sites are not shown but Adams *et. al.*[31] found that they are located between the Mo-O layers and exhibit long-range order.

The NaMB PXRD diffractogram is shown in Figure 6.12.

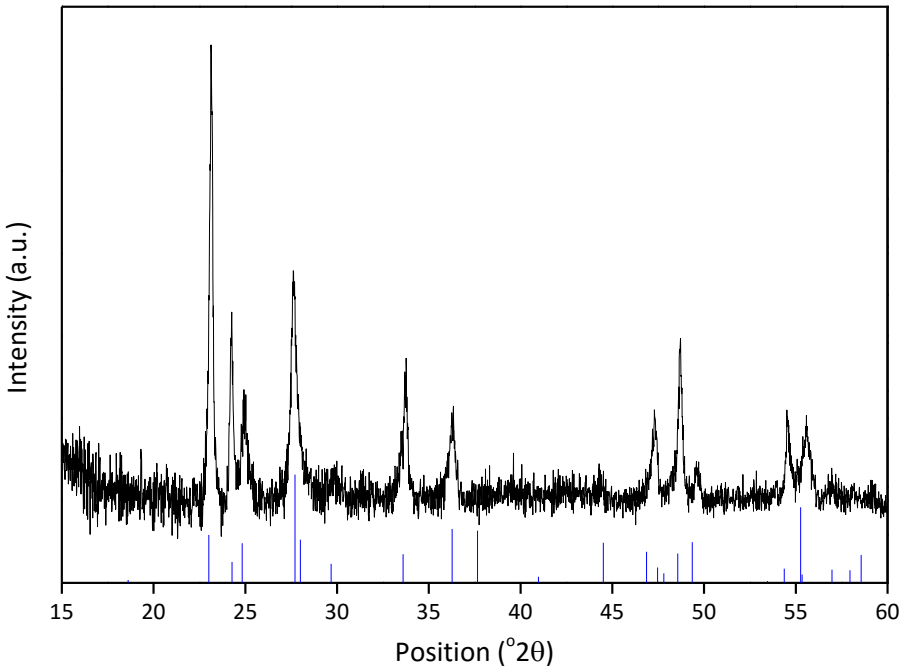

Figure 6.12 - PXRD diffractogram of $Na_xMoO_3.yH_2O$. Expected peak positions and intensities are shown in blue.

The diffractogram has a noisy background which obscures some of the smaller peaks. The crystal structure of the NaMB sample (Figure 6.13) is similar to that of HMB (Figure 6.11) consisting of two dimensional layers of edge- and corner-sharing MoO_6 octahedra with Na^+ cations situated in between the layers. Compared to the HMB structure, that of NaMB has larger inter-layer spacing to accommodate the larger Na^+ cations. Although not shown, water molecules are also present in the channels, which was also the case for the sodium tungsten bronze NaTB-ST2 in chapter 3.

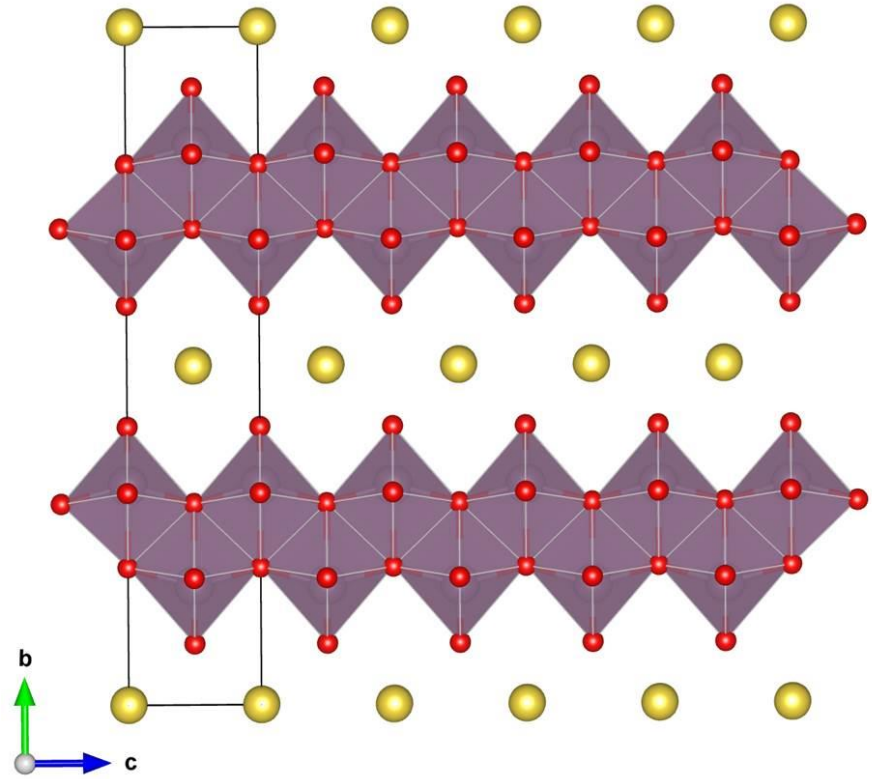

Figure 6.13 - Polyhedral representation of the crystal structure of Na_xMoO_3. Mo=purple, O=red and Na=yellow.

The diffractogram of the KMB-ST sample is shown in Figure 6.14.

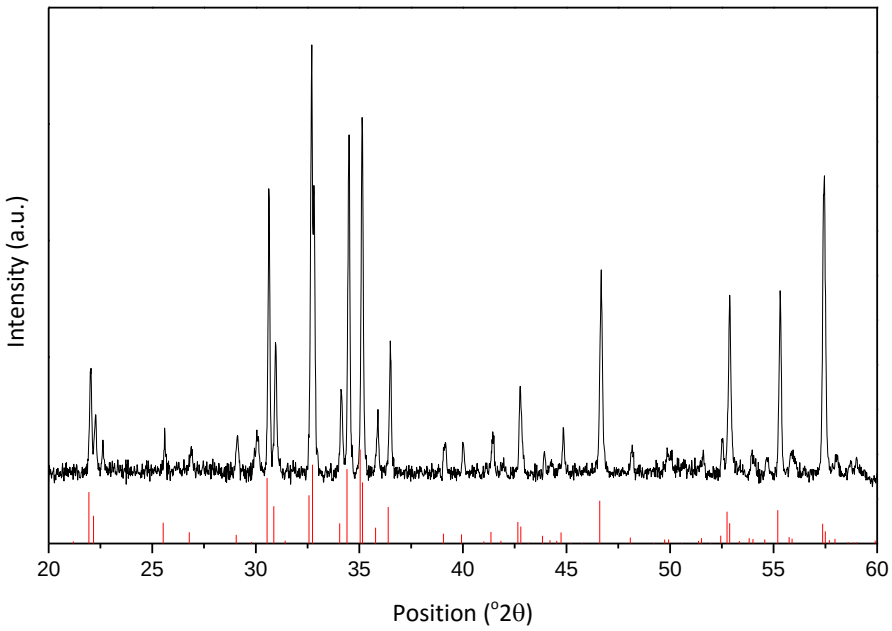

Figure 6.14 - PXRD diffractogram of K_xMO_3 made via solvothermal synthesis. Expected peak positions and intensities of the red bronze $K_{0.33}MoO_3$are shown in red.

The ion exchange of HMB with KCl solution has resulted in the formation of the red bronze structure despite following the route that Eda *et. al.* gave for the blue bronze. The structure is shown in Figure 6.7 and is closely related to the blue bronze phase in Figure 6.8. It is likely that the synthesis is dependent on the value of *x* in the H_xMoO_3 starting material and this was not studied in detail.

The diffractogram of the KMB-SS sample is shown in Figure 6.15.

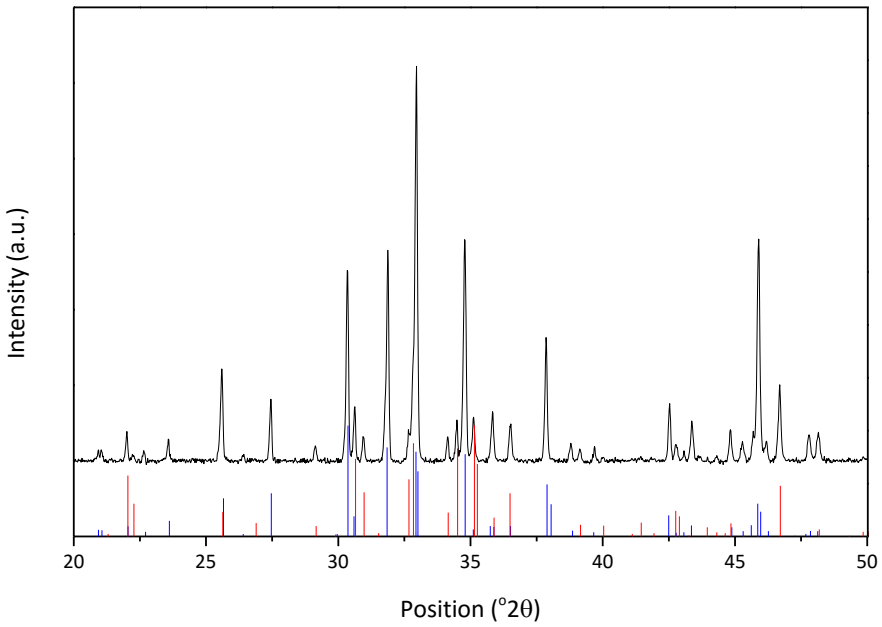

Figure 6.15 - PXRD diffractogram of K_xMO_3 made via solid state synthesis. Expected peak positions and intensities of blue bronze phase $K_{0.3}MoO_3$ are shown in blue and those of the red bronze $K_{0.33}MoO_3$ in red.

It is composed of both the blue and red bronze crystal structures discussed in section 6.2.1. The similarity in structure and closeness in composition of these structures makes them relatively difficult to separate but no other impurity phases were present. Although the blue and red bronze structures are closely related, the red bronze is a semi-conductor whereas the blue bronze displays metallic conductivity.

The RbMB diffractogram is shown in Figure 6.16. Like the NaMB pattern in Figure 6.12, there is a significantly noisy background however the peaks can still be identified as arising from the red bronze structure like the KMB-ST sample. Since these samples were synthesised by the same route from the same starting material (HMB) this is not surprising.

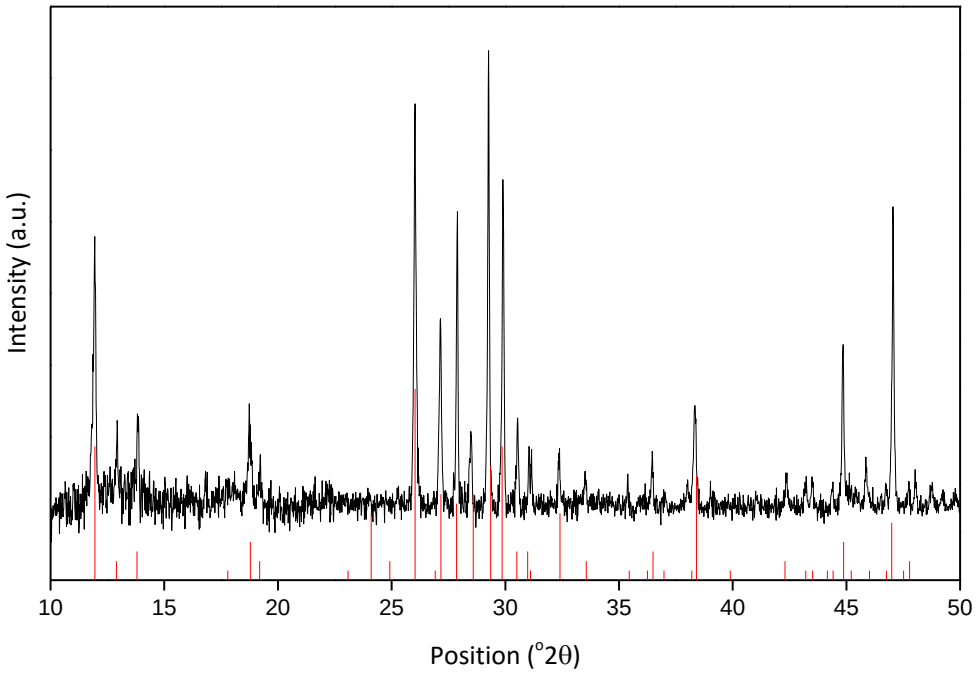

Figure 6.16 - PXRD diffractogram of molybdenum bronze Rb_xMoO_3. Expected peak positions and intensities of the red bronze $Rb_{0.33}MoO_3$ are shown below in red.

6.2.3.2 UV-vis-NIR spectroscopy

The optical absorbance profiles of HMB and NaMB are shown in Figure 6.17.

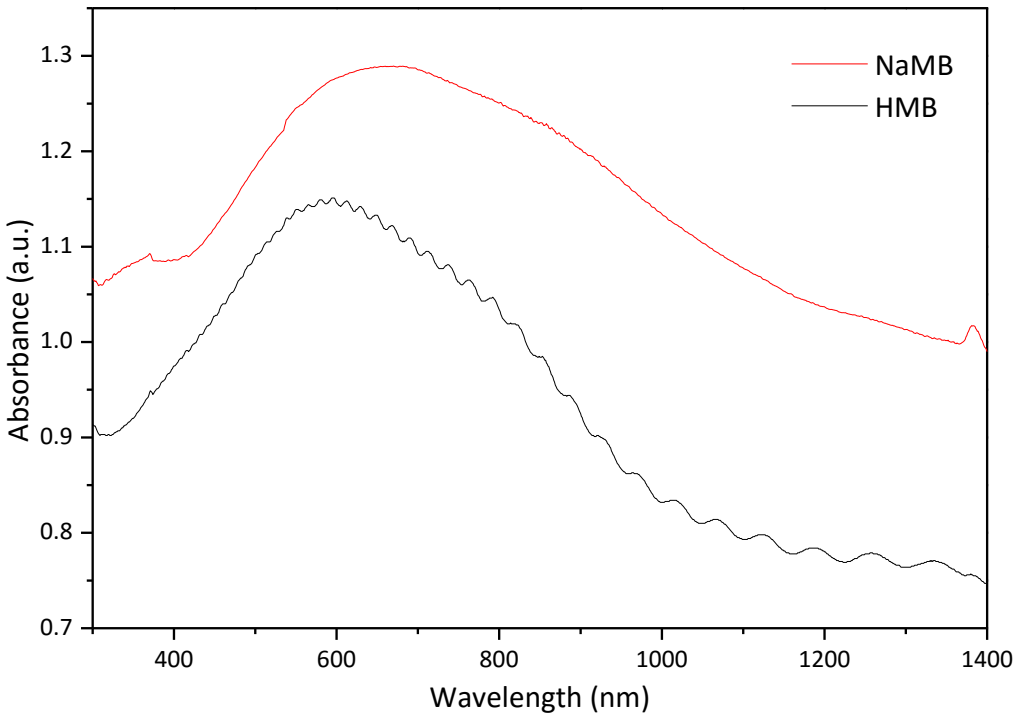

Figure 6.17 - Optical absorbance profiles of molybdenum bronzes HMB and NaMB.

They both take a similar form with a single broad absorbance peak across most of the visible region but the intensity of the NaMB profile is higher across the spectrum. Hussain[32] attributes the absorbance of H_xMoO_3 films to small polaron hopping rather than absorption of free electrons (both mechanisms are discussed in Chapter 1). Wang *et, al.*[33] also attribute the dark blue colour of Li analogues to an intervalence Mo^{5+}-Mo^{6+} couple. This absorption mechanism was also seen for the tungsten bronzes (Chapters 3 and 4). It is likely that the intensity depends on the amount of Mo^{5+} present and therefore the value of *x* in M_xMoO_3. Unfortunately this data is not available for these samples and the origin of the unusual 'rippled' appearance of the HMB profile is unknown.

The optical absorbance profiles of the KMB samples are shown in Figure 6.18.

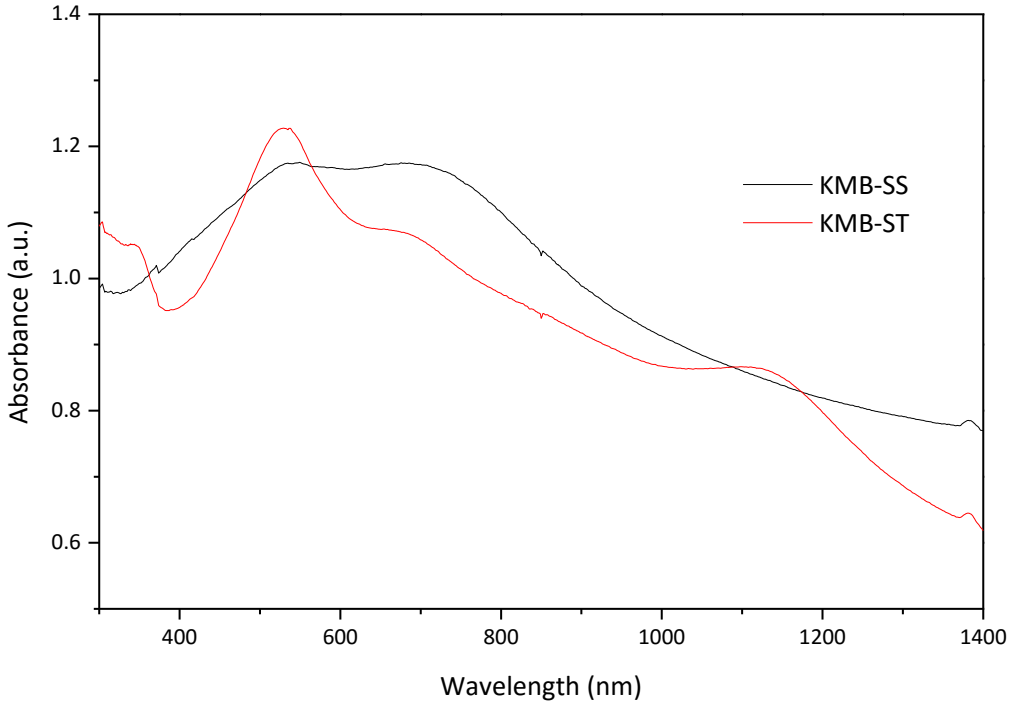

Figure 6.18 - Optical absorbance profiles of potassium molybdenum bronzes KMB made by solvothermal (ST) and solid state (SS) syntheses.

It can be seen that the KMB profiles differ from those of HMB and NaMB by having double absorbance peaks, although the peaks seen for HMB and NaMB are so broad they could incorporate more than one peak. For example it could be argued that there is a shoulder in the NaMB profile at around 900 nm.

Soriano *et. al.*[34] and Aritani *et. al.*[35] assign higher energy visible peaks (~400 nm) to the presence of Mo^{6+} and lower energy visible peaks (~600 nm) to the presence of Mo^{5+}

species, in other reduced molybdenum compounds. This is consistent with the double peak seen in the visible region in both the KMB-SS and KMB-ST optical spectra as both Mo^{5+} and Mo^{6+} cations are present in the reduced bronzes. Dickens and Neild[36] also see a double absorbance peak for red potassium bronzes however it is centred at slightly lower energy in the NIR region. They attribute the absorbances to promotion of electrons from donor bands into the conduction band. The Mo^{5+} donor bands contain electrons from the potassium atoms. The origin of the double peak is not discussed.

Travaglini and co-workers[37] have measured optical spectra of a $K_{0.33}MoO_3$ red bronze single crystal and found that measuring perpendicular to the layer direction *b* gave different spectral features than measuring parallel to *b*. They assign different optical features to the presence of both localised electrons and electrons delocalised within the clusters of MoO_6 octahedra. In a similar study of the blue bronze[10a] $K_{0.3}MoO_3$ they assign features at 4.7 and 3.5 eV (~265 and 350 nm respectively) to interband transitions from π and pπ orbitals to unoccupied π* and σ*orbitals. However these features are at higher energy than those seen in Figure 6.18 at ~500 and 700 nm. They also assign a feature at 1.5 eV (~825 nm) to the presence of free electrons which gives blue molybdenum bronzes metallic conductivity in the *b* direction.

Sing *et. al.*[38] give evidence for plasmon propagation along 1D axis in blue bronze. There is a third peak in the NIR region of the KMB-ST sample at around 1100 nm which is not present in the spectrum of the KMB-SS sample. This peak could be due to surface plasmon absorption, especially because the particles are rod-shaped (see section 6.2.3.3 below). It is possible that the peak is also present for KMB-SS but hidden under the more intense main broad absorbance peak.

It is likely that that absorbance of these samples is a combination of polaron hopping and surface plasmon resonance similar to the tungsten bronzes. There is evidence for the presence of both free electrons and electrons localised within the structural Mo-O clusters. There are two Mo crystallographic sites in the red bronze structure and three in the blue bronze and polaron hopping between sites with different energies could lead to the double peaks seen in Figure 6.18. Further fundamental study would be required to definitively assign each peak.

NIR optical data was not available for RbMB due to instrument breakdown but the visible absorbance is shown in Figure 6.19 compared to that of the red bronze KMB-ST. It can be seen that the optical absorbance profiles are almost identical only differing slightly in the intensity of the features. The alkali metals do not contribute directly to the electronic and therefore the optical properties so it is not surprising that these two red bronzes have such similar spectra.

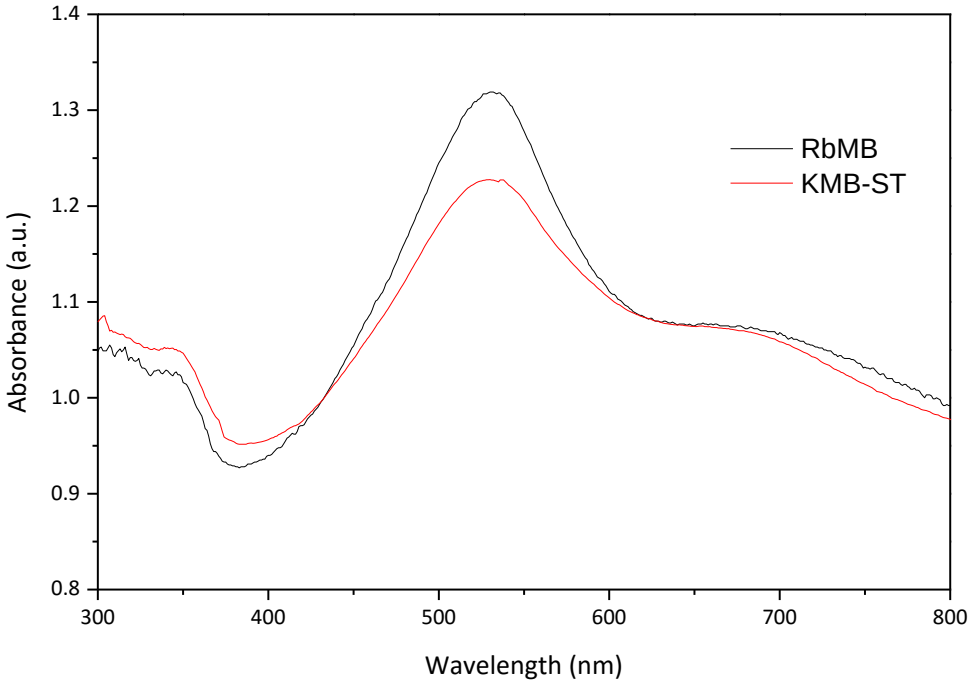

Figure 6.19 - Optical absorbance profile of red bronze Rb_xMoO_3 RbMB compared to KTB-ST.

6.2.3.3 Scanning electron microscopy (SEM)

SEM images of the MB samples are shown in Figure 6.20. The underlying 2D layered crystal structures of HMB and NaTB are clearly seen in their microstructure (Figure 6.20a and 6.20b) which consists of large particles made up of flaky layers. The KMB-ST and RbMB samples were made via ion exchange of HMB but their morphology is more rod-like with agglomerations of rods around 10 µm in length and 2 µm in diameter (Figure 6.20c and 6.20e). The RbMB rods are fairly smooth and homogenous whereas some smaller particles are seen on the surface of the KMB-ST ones. The solid state KMB-SS sample (Figure 6.20d) has notably different morphology than the solvothermal samples, composed of relatively large blocky particles with no defined shape. This is similar to the morphology seen for the PTB sample seen in Figure 6.6 and this sample was also made by a solid state route.

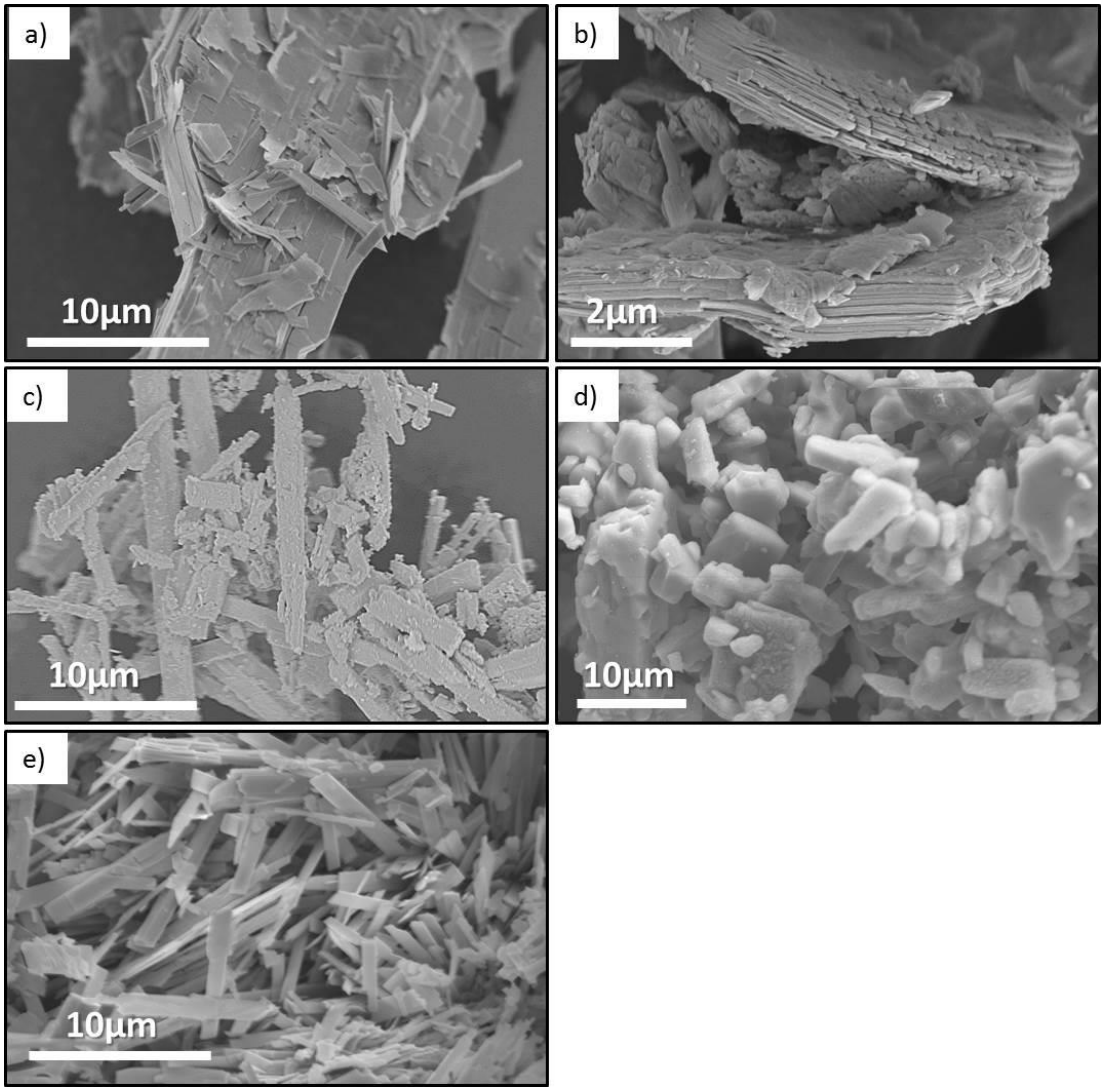

Figure 6.20 - SEM images of molybdenum bronze samples a) HMB, b) NaMB, c) KMB-ST, d) KMB-SS and e) RbMB. Scale bars are given.

6.3 Results of Laser Imaging

The phosphate tungsten bronze sample and all the molybdenum bronzes were tested for laser imaging performance according to the protocol described in Chapter 2.4. During testing of RbMB there was a problem with the Datalase bead mill which broke down with the sample inside and it could not be recovered without significant contamination. Another RbMB sample could not be prepared within the timeframe of the project so testing data is not available. The results for the other samples are shown in Figure 6.20.

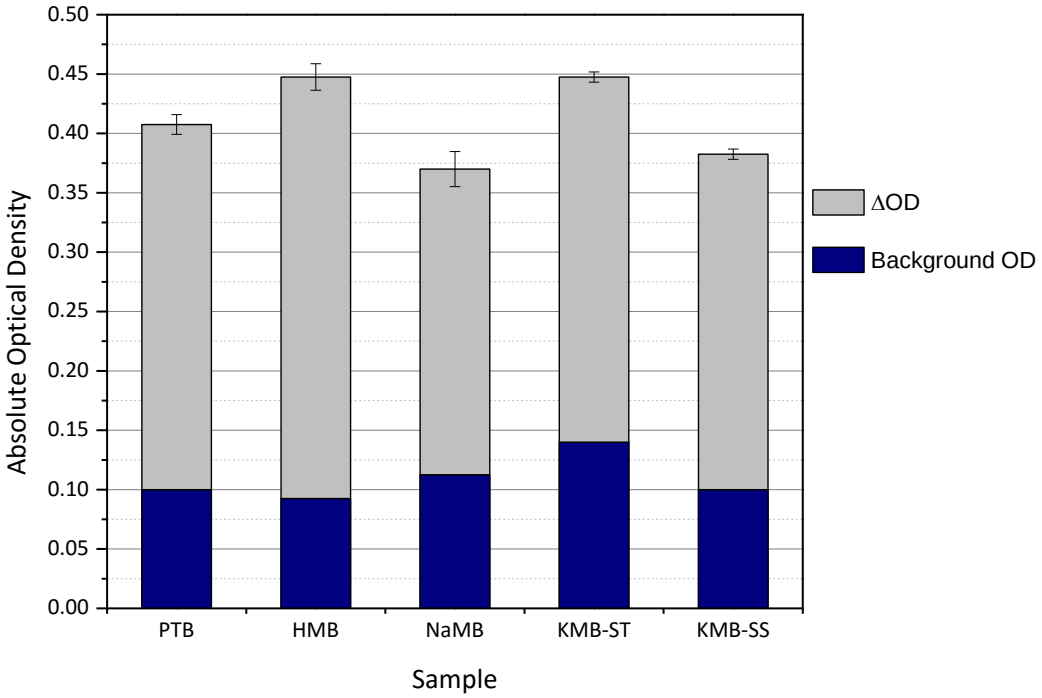

Figure 6.21 - Optical density values resulting from laser imaging tests of $P_4W_8O_{32}$ and M_xMoO_3 samples. All samples reached the highest ΔOD at 4.6Jcm^{-2}.

It can be seen that the samples do not vary as widely in performance as the tungsten bronzes did in Chapter 3. All show relatively low background OD values apart from the KMB-ST sample which is noticeably higher. It is unclear why this is as both the KMB-SS and ST samples had similar absorbance in the visible region (Figure 6.18). The PTB sample shows very similar performance to the MB's despite being composed of different elements arraged in a different structure. However the optical spectrum of the PTB sample (Figure 6.5) is not dissimilar to those of the MB samples (Figures 6.17 and 6.18) with the main absorbance peak for all samples located in the visible region between 400-600 nm and decreased absorbance intensity towards the NIR region.

The HMB sample shows the highest ΔOD value of all the samples and NaMB the lowest. Despite having similar absorbance mechanisms, the best performance of the MB samples is poorer than that of most of the tungsten bronze (TB) samples from Chapters 3 and 4. One factor in this could be the particle size of the samples. The best-performing TB samples were all composed of relatively small particles (~100 nm) whereas these are at least an order of magnitude larger. For comparison KMB-SS results are shown with those of its tungsten counterpart, solid state KTB-SS1, in Figure 6.22.

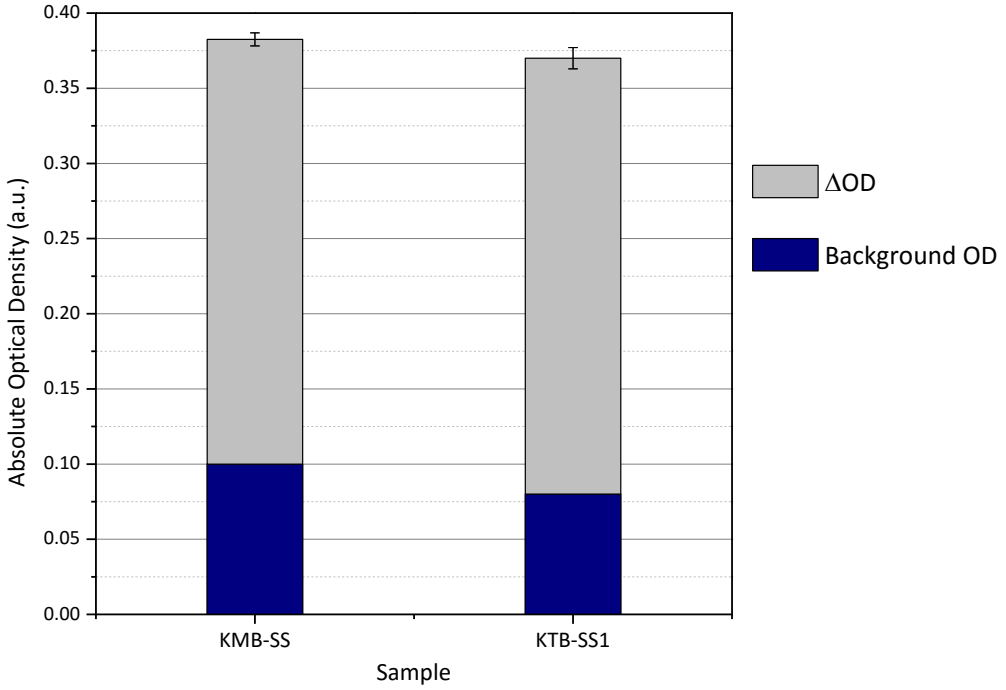

Figure 6.22 - Optical density values resulting from laser imaging tests of K_xMoO_3 and K_xWO_3 samples made by solid state synthesis. Both samples reached the highest ΔOD at 4.6Jcm-2.

The performance of KMB-SS and KTB-SS1 during laser imaging is almost identical apart from a slightly higher background OD for KMB-SS. This suggests that the MB's have potential for further development. If a route could be found that yields nanoparticles and gives good control over composition then the performance could be improved to TB-like levels. Future work could be to develop and modify the synthetic procedures as was done for CsTB samples in Chapter 4 to achieve different particle morphologies. It would also be interesting to see if results for Rb and Cs MB analogues would be similar to those of the other samples in Figure 6.21. The difficulty in obtaining phase pure PTB samples or MB's with the desired phase by the routes used mean that full synthetic exploration is outside the scope of this project due to time constraints.

6.4 Conclusion

The monophosphate tungsten bronze family had the potential to act as an alternative NIR absorber to the alkali metal tungsten bronzes presented in Chapters 3 and 4. However these samples have the drawback of being difficult to synthesise and performance was not as good as the alkali metal tungsten bronzes. The molybdenum bronzes were chosen as a tungsten-free set of candidate absorbers but, like the phosphate tungsten bronzes, it proved relatively difficult to synthesise phase pure samples. Again, the performance of

samples in laser imaging tests was intermediate. None of the commercial samples from Appendix 1 are directly comparable to these materials but it can be seen that their performance is not as good as that of the other tungsten bronze samples in preceding chapters.

Both of these sets of samples would benefit from more detailed study and either modification of synthetic routes or exploration of new ones in order to obtain samples with different properties. In particular, altering particle morphology could have a beneficial effect of performance as it did for the CsTB samples in Chapter 4. Overall the PTB and MB samples have potential – they do form images under laser irradiation – but need to be developed further to be commercially viable as NIR absorbers in the Datalase process.

6.5 References

1. Giroult, J. P.; Goreaud, M.; Labbe, P.; Raveau, B., $Rb_xP_8W_{32}O_{112}$: a tunnel structure built up from ReO_3-type blocks and P_2O_7 groups. *Acta Crystallographica Section B* **1980,** *36* (11), 2570-2575.
2. Giroult, J. P.; Goreaud, M.; Labbe, P.; Raveau, B., $P_4W_8O_{32}$: a mixed-valence tunnel structure built up of ReO_3-type slabs connected through PO_4 tetrahedra. *Acta Crystallographica Section B* **1981,** *37* (12), 2139-2142.
3. Canadell, E.; Whangbo, M.-H., Charge-density-wave instabilities expected in monophosphate tungsten bronzes. *Physical Review B* **1991,** *43* (3), 1894-1902.
4. Skopenko, V. V.; Lisnyak, V. V.; Stus, N. V.; Slobodyanik, N. S., Phosphate tungsten bronzes. *Russian Chemical Reviews* **2004,** *73* (8), 753.
5. Roussel, P.; Perez, O.; Labbe, P., Phosphate tungsten bronze series: crystallographic and structural properties of low-dimensional conductors. *Acta Crystallographica Section B* **2001,** *57* (5), 603-632.
6. Roussel, P.; Foury-Leylekian, P.; Domengès, B.; Groult, D.; Labbé, P.; Pouget, J. P., Structural investigation of a new variety of the low dimensional conductor with 2 m = 5 + 5: $P_4W_{10}O_{38}$. *Eur. Phys. J. B* **1999,** *12* (4), 497-508.
7. Domenges, B.; Goreaud, M.; Labbe, P.; Raveau, B., $P_8W_{12}O_{52}$: a mixed-valence tungsten oxide built up from WO_6 octahedra and P_2O_7 groups. *Acta Crystallographica Section B* **1982,** *38* (6), 1724-1728.
8. Canadell, E.; Whangbo, M. H., Conceptual aspects of structure-property correlations and electronic instabilities, with applications to low-dimensional transition-metal oxides. *Chemical Reviews* **1991,** *91* (5), 965-1034.
9. Stavenhagen, A.; Engels, E., Ueber Molybdänbronzen. *Berichte der deutschen chemischen Gesellschaft* **1895,** *28* (2), 2280-2281.
10. (a) Travaglini, G.; Wachter, P.; Marcus, J.; Schlenker, C., The blue bronze $K_{0.3}MoO_3$: A new one-dimensional conductor. *Solid State Communications* **1981,** *37* (7), 599-603; (b) Brun, C.; Girard, J. C.; Wang, Z. Z.; Marcus, J.; Dumas, J.; Schlenker, C., Charge-density waves in rubidium blue bronze $Rb_{0.3}MoO_3$ observed by scanning tunneling microscopy. *Physical Review B* **2005,** *72* (23), 235119; (c) Ren, Y.; Lüpke, G.; Xu, Z. a., Photoinduced charge-density-wave dynamics in $K_{0.3}MoO_3$. *Appl Phys Lett* **2004,** *84* (12), 2169-2171; (d) Rai, R. C.; Bondarenko, V. A.; Brill, J. W., Electro-reflectance spectra of blue bronze. *Eur. Phys. J. B* **2003,** *35* (2), 233-238.
11. Stephenson, N. C.; Wadsley, A. D., The crystal structure of the red potassium molybdenumbronze, $K_{0.26}MoO_3$. *Acta Crystallographica* **1965,** *19* (2), 241-247.
12. Bang, G.; Sperlich, G., Localized d-electrons in the semiconductor $K_{0.33}MoO_3$ (ESR measurements). *Physics Letters A* **1974,** *49* (1), 21-23.
13. Tsai, P. P.; Potenza, J. A.; Greenblatt, M.; Schugar, H. J., Crystal structure of $Li_{0.33}MoO_3$, a stoichiometric, triclinic, lithium molybdenum bronze. *J Solid State Chem* **1986,** *64* (1), 47-56.
14. Graham, J.; Wadsley, A. D., The crystal structure of the blue potassium molybdenum bronze, $K_{0.28}MoO_3$. *Acta Crystallographica* **1966,** *20* (1), 93-100.
15. Greenblatt, M., Molybdenum oxide bronzes with quasi-low-dimensional properties. *Chemical Reviews* **1988,** *88* (1), 31-53.
16. Vincent, H.; Ghedira, M.; Marcus, J.; Mercier, J.; Schlenker, C., Structure cristalline d'un conducteur métallique bidimensionnel: Le bronze violet de potassium et molybdene K0.9Mo6O17. *J Solid State Chem* **1983,** *47* (1), 113-121.
17. Cannert, C., *Gazzetta Chimica Italiana* **1930,** *60*, 113.

18. Wold, A.; Kunnmann, W.; Arnott, R. J.; Ferretti, A., Preparation and Properties of Sodium and Potassium Molybdenum Bronze Crystals. *Inorganic Chemistry* **1964,** *3* (4), 545-547.
19. (a) Bouchard, G. H.; Perlstein, J. H.; Sienko, M. J., Solid-state studies of potassium molybdenum bronzes. *Inorganic Chemistry* **1967,** *6* (9), 1682-1685; (b) Mumme, W. G.; Watts, J. A., The crystal structure of the molybdenum bronze Cs_xMoO_3 (x ≈ 0.25). *J Solid State Chem* **1970,** *2* (1), 16-23; (c) Strobel, P.; Greenblatt, M., Crystal growth and electrical properties of lithium, rubidium, and cesium molybdenum oxide bronzes. *J Solid State Chem* **1981,** *36* (3), 331-338; (d) Buder, R.; Devenyi, J.; Dumas, J.; Marcus, J.; Mercier, J.; Schlenker, C.; Vincent, H., Two-dimensional electronic properties of the purple potassium molybdenum bronze $K_{0.9}Mo_6O_{17}$. *J. Physique Lett.* **1982,** *43* (2), 59-65; (e) Schneemeyer, L. F.; DiSalvo, F. J.; Fleming, R. M.; Waszczak, J. V., Sliding charge-density wave conductivity in potassium molybdenum bronze. *J Solid State Chem* **1984,** *54* (3), 358-364; (f) Schneemeyer, L. F.; Spengler, S. E.; Di Salvo, F. J.; Waszczak, J. V.; Rice, C. E., Electrochemical crystal growth in the cesium molybdate-molybdenum trioxide system. *J Solid State Chem* **1984,** *55* (2), 158-164.
20. Ganne, M.; Boumaza, A.; Dion, M.; Dumas, J., The blue bronze $Tl_{0.30}MoO_3$ structure and physical properties. *Mater Res Bull* **1985,** *20* (11), 1297-1308.
21. (a) McCarroll, W. H.; Greenblatt, M., Preparation of lithium molybdenum oxide bronzes by a temperature gradient flux growth technique. *J Solid State Chem* **1984,** *54* (2), 282-290; (b) Ramanujachary, K. V.; Greenblatt, M.; McCarroll, W. H., Crystal growth of alkali metal molybdenum bronzes by a temperature gradient flux technique. *J Cryst Growth* **1984,** *70* (1–2), 476-483.
22. Bither, T. A.; Gillson, J. L.; Young, H. S., Synthesis of Molybdenum and Tungsten Bronzes at High Pressure. *Inorganic Chemistry* **1966,** *5* (9), 1559-1562.
23. Hirata, T.; Yagisawa, K., Infrared reflectivity spectra of the reaction products K_xMoO_3 (x=0.1-0.5) prepared by a solid state reaction. *Journal of Physics: Condensed Matter* **1990,** *2* (23), 5199.
24. Thomas, D. M.; McCarron Iii, E. M., The composition and proposed structure of the alkali metal layered molybdenum bronzes. *Mater Res Bull* **1986,** *21* (8), 945-960.
25. Sotani, N.; Suzuki, T.; Eda, K.; Yanagi-ishi, M.; Takagi, S.; Hatayama, F., Preparation of Hydrated Potassium Molybdenum Bronzes and Their Thermal Decomposition. *J Solid State Chem* **1997,** *132* (2), 330-336.
26. Eda, K.; Miyazaki, T.; Hatayama, F.; Nakagawa, M.; Sotani, N., Cesium–Sodium Ion Exchange on Hydrated Molybdenum Bronze and Formation of New Cesium Molybdenum Bronze by a Low-Temperature Synthesis Route. *J Solid State Chem* **1998,** *137* (1), 12-18.
27. Sotani, N.; Eda, K.; Sadamatu, M.; Takagi, S., Preparation and Characterization of Hydrogen Molybdenum Bronzes, H_xMoO_3. *Bulletin of the Chemical Society of Japan* **1989,** *62* (3), 903-907.
28. Eda, K.; Chin, K.; Sotani, N.; Stanley Whittingham, M., Hydrothermal synthesis of potassium molybdenum oxide bronzes: structure-inheriting solid-state route to blue bronze and dissolution/deposition route to red bronze. *J Solid State Chem* **2005,** *178* (1), 158-165.
29. Tsang, C.; Dananjay, A.; Kim, J.; Manthiram, A., Synthesis of Lower Valent Molybdenum Oxides by an Ambient Temperature Reduction of Aqueous K_2MoO_4 by KBH_4. *Inorganic Chemistry* **1996,** *35* (2), 504-509.
30. Fo Tsang, C.; Manthiram, A., Synthesis of lower-valent molybdenum oxides in aqueous solutions by reducing Na_2MoO_4 with $NaBH_4$. *J Mater Chem* **1997,** *7* (6), 1003-1006.
31. Adams, S.; Ehses, K. H.; Spilker, J., Proton ordering in the Peierls-distorted hydrogen molybdenum bronze $H_{0.33}MoO_3$: structure and physical properties. *Acta Crystallographica Section B* **1993,** *49* (6), 958-967.

32. Hussain, Z., Dopant-dependent reflectivity and refractive index of microcrystalline molybdenum–bronze thin films. *J Appl Phys* **2002,** *91* (9), 5745-5759.
33. Wang, L.; Schindler, J.; Kannewurf, C. R.; Kanatzidis, M. G., Lamellar polymer-Li_xMoO_3 nanocomposites via encapsulative precipitation. *J Mater Chem* **1997,** *7* (7), 1277-1283.
34. Soriano, M. D.; Concepción, P.; Botella, P.; López Nieto, J., Partial Oxidation of H_2S to Sulfur Over Mo and/or W-Containing Bronzes with a TTB-Structure. *Top Catal* **2011,** *54* (10-12), 729-736.
35. Aritani, H.; Tanaka, T.; Funabiki, T.; Yoshida, S.; Eda, K.; Sotani, N.; Kudo, M.; Hasegawa, S., Study of the Local Structure of Molybdenum−Magnesium Binary Oxides by Means of Mo L3-Edge XANES and UV−Vis Spectroscopy. *The Journal of Physical Chemistry* **1996,** *100* (50), 19495-19501.
36. Dickens, P. G.; Neild, D. J., Some electronic properties of the molybdenum bronzes. *Transactions of the Faraday Society* **1968,** *64* (0), 13-18.
37. Travaglini, G.; Wachter, P.; Marcus, J.; Schlenker, C., Optical properties of the red bronze $K_{0.33}MoO_3$. *Solid State Communications* **1982,** *42* (6), 407-410.
38. Sing, M.; Grigoryan, V. G.; Paasch, G.; Knupfer, M.; Fink, J.; Lommel, B.; Aßmus, W., Plasmon excitations in quasi-one-dimensional $K_{0.3}MoO_3$. *Physical Review B* **1999,** *59* (8), 5414-5425.

Chapter 7

Copper Phosphates

7.1 Introduction

One of the commercial samples analysed in Appendix 1 was a copper hydroxyphosphate $Cu_2(PO_4)(OH)$ and so copper phosphates were identified as promising candidates for use as near infrared (NIR) absorbers. Synthesis, characterisation and testing of several copper phosphate compounds is discussed in this chapter.

The d-d transitions (discussed in section 1.3.3) found in transition metals could provide an alternative NIR absorption mechanism to the polaron hopping and plasmon resonance mechanisms found in the tungsten-based materials in Chapters 3-6. The phosphate building blocks can either be single (PO_4^{3-}) or double ($P_2O_7^{4-}$) units linked together through polyhedral corners to form different structural families. This results in a range of different copper sites available for occupancy. Following the principles of crystal field theory, the five 3d orbitals of copper ions have different energies depending on the character of the local environment. Different numbers and co-ordination geometries of nearest neighbours will split the degenerate d orbitals of a free copper ion into different energy levels, as shown in Figure 7.1.

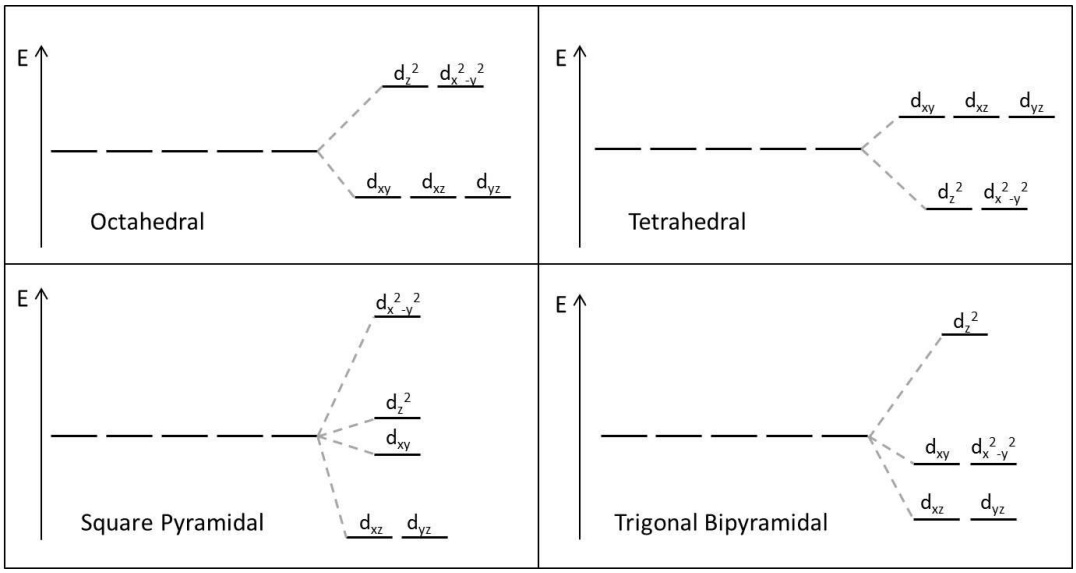

Figure 7.1 - Crystal field splitting diagrams for different ligand environments.

The total energy of the orbitals is unchanged but electrons residing in orbitals that have strong interactions with nearby ligands will be at a higher energy level than those which have weaker interactions or are farther away from the influence of the ligands. This happens in order to stabilise the compound by minimising electrostatic repulsion between electrons in the d orbitals and electrons of the ligand. When incident radiation is applied to transition metal compounds, a photon can be absorbed and excite an electron to a higher energy d orbital since the orbitals are no longer degenerate. The crystal field splitting parameter of copper (II) d orbitals in a regular octahedral environment[1] is known to be 13000 cm^{-1} which corresponds to an absorption peak at around 770 nm.

When the copper environment is more distorted, the d orbitals shift in energy and the transition energy can be between 6000 and 15000 cm^{-1} (~1670-670 nm). Distorted environments are more common in copper (II) complexes than in those of other transition metals due to the Jahn-Teller effect. The d^9 electron configuration of Cu^{2+} has a degenerate ground state since the ninth electron can enter either of the e_g orbitals. According to the Jahn-Teller theorem, this arrangement is not stable so the d-orbitals distort to reduce the symmetry and remove the degeneracy to lower the overall energy of the system. Typically this results in an elongation of the z axis to reduce electrostatic repulsion between the ligands and the orbitals that point directly at them. Therefore the position of an absorbance peak in these compounds depends on the splitting energy of the d orbitals which in turn depends on the valence state and co-ordination environment of the copper species. This makes them interesting to study as potential NIR absorber candidates.

Three different phosphates were chosen as candidates for synthesis and testing: $CuZr_2(PO_4)_3$, $Ca_{10-x/2}Na_xCu_{0.5}(PO_4)_7$ and $SrZn_{1-x}Cu_xP_2O_7$.

7.2 $CuZr_2(PO_4)_3$

The potential of Nasicon-type Cu(I) compound $CuZr_2(PO_4)_3$ was noticed in a paper by Mbandza *et. al.* from 1985[2], particularly the optical absorbance spectrum number 5 shown in Figure 7.2.

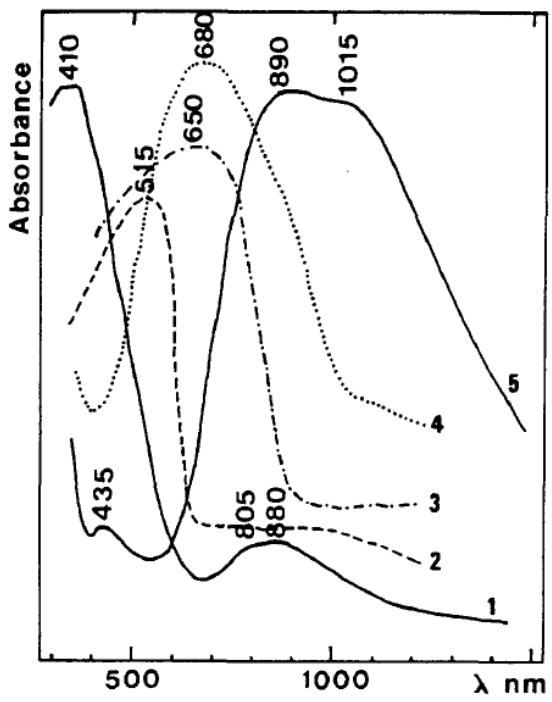

FIG. 1
Visible spectra of
(1) $CuTi_2(PO_4)_3$
(2) Cu_2O
(3) CuO
(4) $Cu_3(PO_4)_2$
(5) $CuZr_2(PO_4)_3$

Figure 7.2 - UV-vis-NIR spectra of copper compounds taken from Mbandza et. al.[2]

The $CuZr_2(PO_4)_3$ phase (CZP) shows a double absorbance peak in the NIR region combined with low visible absorbance which is an ideal profile for NIR absorbers for this project.

7.2.1 Synthesis

First prepared by Yao and Fray[3], it was synthesised in this work following the method used by Christiansen and Warner[4]. Heating was carried out in electric furnaces and all heating and cooling rates were 5 °C/min unless otherwise specified. CuO (Sigma Aldrich 99.999%), ZrO_2 (Sigma Aldrich 99.99%) and $NH_4H_2PO_4$ (Sigma Aldrich 99.999%) were mixed in appropriate amounts according to the equation:

$$CuO + 2ZrO_2 + 3NH_4H_2PO_4 \rightarrow CuZr_2(PO_4)_3 + 1\,{}^1/_2\,N_2 + 4H_2O + 5H_2$$

The mixture was ball milled overnight using a planetary mill with acetone as a dispersion agent. After drying, the mixture was ground using a pestle and mortar then placed in an Al_2O_3 crucible and heated to 400 °C for 12 h in air with a heating rate of 2 °C/min to decompose the phosphate starting material. The resulting product was ground in a pestle and mortar and heated in an Al_2O_3 crucible in a tube furnace under flowing argon for 16 h at 1200 °C. The product was re-ground and re-fired at 1250 °C under the same conditions. The white product was ground once more before analysis.

7.2.2 Characterisation

The Rietveld refinement of the PXRD data of the CZP sample is shown in Figure 7.3.

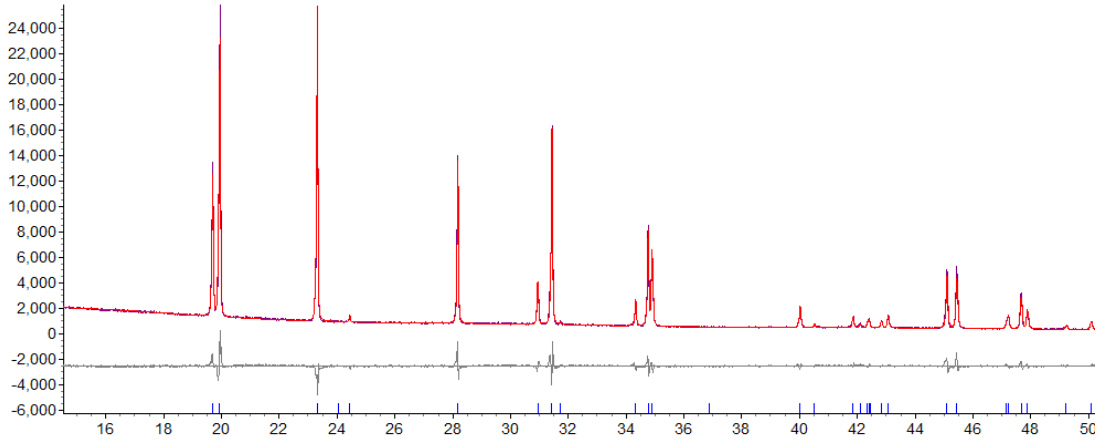

Figure 7.3- Rietveld fit of PXRD data of $CuZr_2(PO_4)_3$.The grey line is the difference curve and the blue tick marks show the allowed peak positions.

The pattern was fitted using data from the neutron and powder diffraction study by Bussereau and co-workers[5] (ICSD file number 71881). Lattice parameters were refined and are close to literature values from Bussereau *et. al.*, shown in Table 7.1.

Table 7.1 – Calculated lattice parameters for $CuZr_2(PO_4)_3$ compared to literature values

Lattice Parameter:	a (Å)	c (Å)	V (Å^3)
This work	8.8977(5)	22.1942(2)	1521.7(2)
Literature	8.9018(2)	22.2021(6)	1523.6(1)

No impurity peaks are seen and the crystal structure is rhombohedral with space group R-3c. The three-dimensional Nasicon framework is composed of PO_4 tetrahedra and ZrO_6 octahedra which are corner-sharing and leave two interstitial metal cation sites M(1) and M(2) available for occupation. There is a three dimensional ionic conduction pathway between these two metal sites. Cu cations are distributed evenly between 6 off-centre positions at the M(1) site, giving a 'daisy wheel' appearance to those sites in Figure 7.4 while the M(2) sites are vacant. The local geometry takes the form of an elongated octahedron[6]. The M(1) site is in fact large enough to accommodate 2 Cu^+ ions and doubly occupied sites are thought to be the origin of the strong green fluorescence observed in this phase under UV light[4].

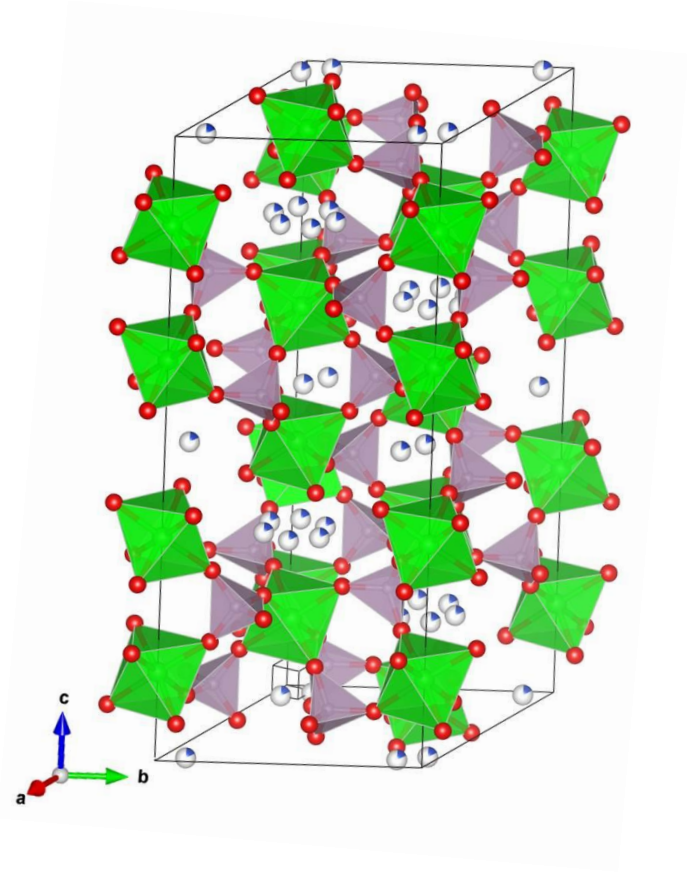

Figure 7.4 - Crystal structure of $CuZr_2(PO_4)_3$ showing PO_4 tetrahedra (purple), ZrO_6 octahedra (green) and interstitial Cu^{2+} ions (blue and white). The 6 off-centre positions at the Cu site can be seen.

The white colour of the powder is to be expected from the optical absorbance profile shown in Figure 7.5 as the sample absorbs very little radiation across the whole spectrum.

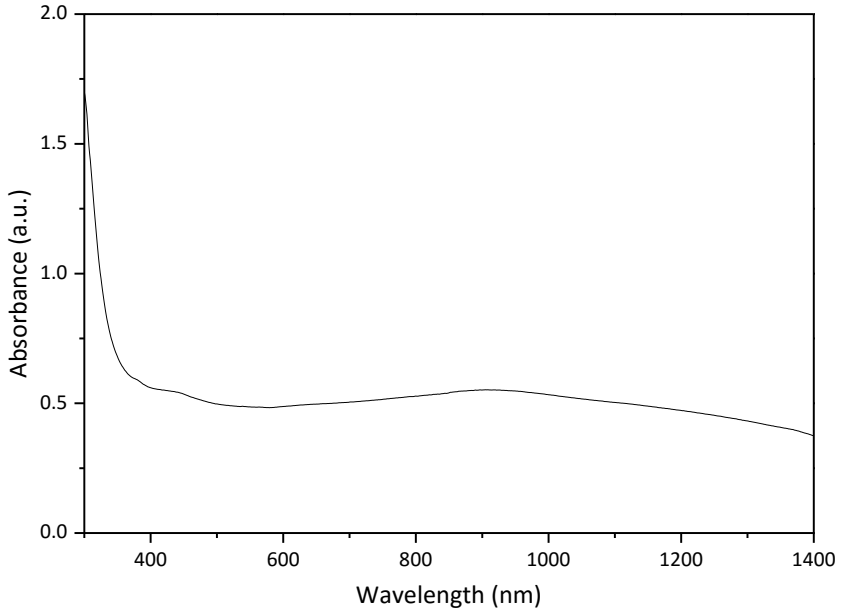

Figure 7.5 - UV-vis-NIR absorbance spectrum of $CuZr_2(PO_4)_3$

It is also an indication that only Cu^{+} species are present since the phases of this structure containing Cu^{2+} are pale green[7]. The absorbance 'peak' at around 900 nm in the NIR region is very low and broad. The elongated octahedral shape of the Cu(I) environment removes the degeneracy of the e_g orbitals that exists in a regular octahedral environment (see Figure 7.1). The d_z^2 orbital is shifted to a lower energy than the d_x^2-$_y^2$ orbital because the oxygen anions in the z axis are now farther away from the metal centre and so will have a weaker interaction with the lobes of the d_z^2 orbital that lie on that axis. Since the lobes of the d_x^2-$_y^2$ orbital lie along the x and y axes they still have strong direct interactions with the oxygen anions bonded along these directions. This is similar to the effect of a Jahn-Teller distortion but is not caused by electronic considerations in this case since the d^{10} configuration means there would be no energetic advantage to removing orbital degeneracy. The d orbitals are fully occupied so d-d transitions are not expected to be observed. Mbanza *et. al.* attribute their peak in Figure 7.2 to "hybridisation of $d^9s"^2$. It is possible that an electron is excited from the highest occupied d_x^2-$_y^2$ to the next empty energy level, the 4s. Testing results are shown below in section 7.5.

7.3 $\underline{Ca_{10-x/2}Na_xCu_{0.5}(PO_4)_7}$

Copper-doped calcium orthophosphates (CSCP) were chosen because of the promising absorbance profile in Figure 7.6 from work by Benarafa *et. al.*[8]. It is interesting to note that the visible absorbance peak decreases with increasing amounts of sodium doping while the NIR peak remains – the reason for this is discussed below.

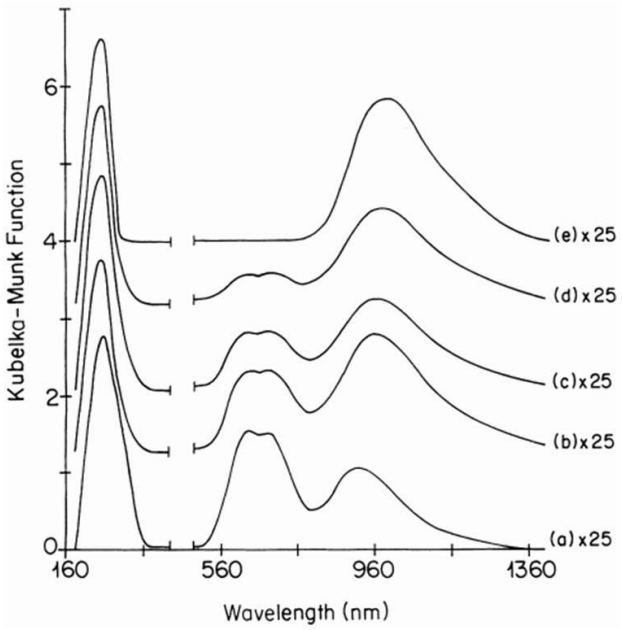

Figure 7.6 - Effect of calcium substitution by Na+ in Ca(4) sites on the diffuse reflectance spectra of $Ca_{10-x/2}Na_xCu_{0.5}(PO_4)_7$ for x = 0, 0.25, 0.5, 0.75 and 1; taken from Benarafa et .al.[8].

7.3.1 Synthesis

The synthetic route from the same paper was followed[8]. Heating was carried out in electric furnaces and all heating and cooling rates were 5 °C/min. Appropriate amounts of $CaCO_3$ (Sigma Aldrich ≥ 99.999%), Na_2CO_3 (Alfa Aesar 99.997%) CuO (Sigma Aldrich 99.99%) and $NH_4H_2PO_4$ (Sigma Aldrich 99.999%) were measured using the following equation:

$$10 - {}^{x}/_{2}\, CaCO_3 + {}^{x}/_{2}\, Na_2CO_3 + 0.5CuO + 7NH_4H_2PO_4 \rightarrow Ca_{10-{}^{x}/_{2}}Na_xCu_{0.5}(PO_4)_7 + 7NH_3 + H_2O + CO_2$$

These were mixed using a pestle and mortar, placed in an Al_2O_3 crucible lined with Al foil and heated in air to 200, 400 and 600 °C for 12 h each with intermittent grinding. The resulting products were pressed into pellets of 20mm diameter and heated in air to 940 °C for 48 h in Al_2O_3 crucibles. They were ground using a pestle and mortar, re-pelletised then reheated under the same conditions. Samples were prepared with compositions of x = 0, 0.5 and 1.

7.3.2 Characterisation

The PXRD diffractograms of the three CSCP samples are shown in Figure 7.7.

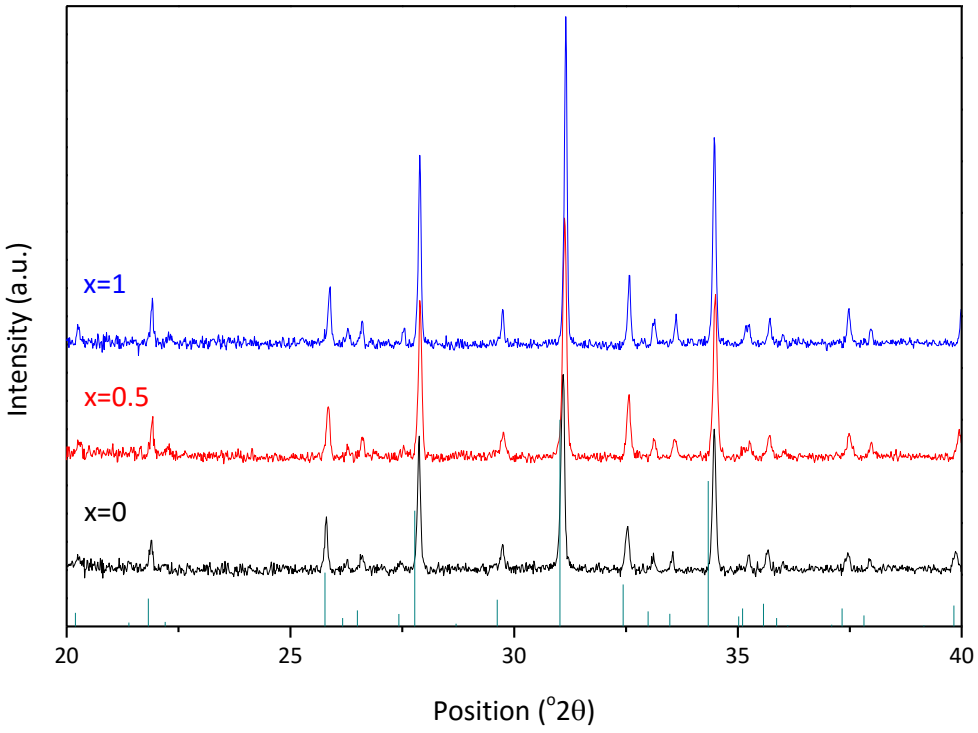

Figure 7.7 - PXRD diffractograms of $Ca_{10-x/2}Na_xCu_{0.5}(PO_4)_7$ with x = 0, 0.5 and 1.

All three samples were phase pure and isostructural with rhombohedral β-$Ca_3(PO_4)_2$ (peak positions shown). The lack of impurity phases indicates that both the copper and the added sodium have been incorporated into sites in the calcium phosphate structure, shown in Figure 7.8. The unit cell is relatively complex so it is difficult to identify features clearly but the PO_4 tetrahedra can be seen and the corner linking of polyhedra is evident.

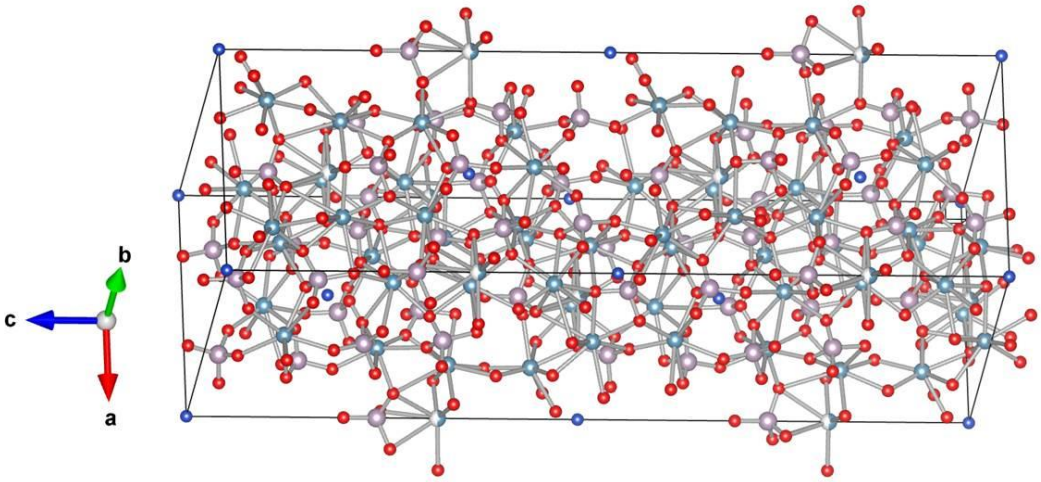

Figure 7.8 - Crystal structure of $Ca_{19}Cu_2(PO_4)_{14}$ showing calcium (blue), oxygen (red), phosphorus (purple) and copper (darker blue) ions.

There are 5 crystallographically different calcium sites in this structure. Ca(1), Ca(2) and Ca(3) have no symmetry elements but Ca(4) and Ca(5) have three-fold symmetry axes. The co-ordination numbers vary from 6 to 9 and the Ca(4) site is only half filled. When the tricalcium phosphate is doped with copper, it has been found in previous studies[9] to occupy Ca(4) and Ca(5) sites. Due to the smaller ionic radius of Na^+ compared to Cu^{2+}, the c lattice parameter decreases with increasing Na content in good agreement with the values obtained by Benarafa and co-workers (see Table 7.2).

Table 7.2 - Lattice parameters (c) of $Ca_{10-x/2}Na_xCu_{0.5}(PO_4)_7$ samples compared to literature values from Benarafa et. al.[8]

x	c (experimental)	c (literature)
0	37.341(1)	37.310(2)
0.5	37.273(1)	37.273(1)
1	37.210(1)	37.253(2)

The optical absorbance spectra of the three CSCP compositions are shown in Figure 7.9. The same features seen by Benarafa *et. al.* are present i.e. the NIR peak and the visible peak which decreases in intensity with increasing Na content. Due to the decrease of the visible

peak, the sample colour progresses from blue (x = 0) to white (x = 1) with increasing Na content.

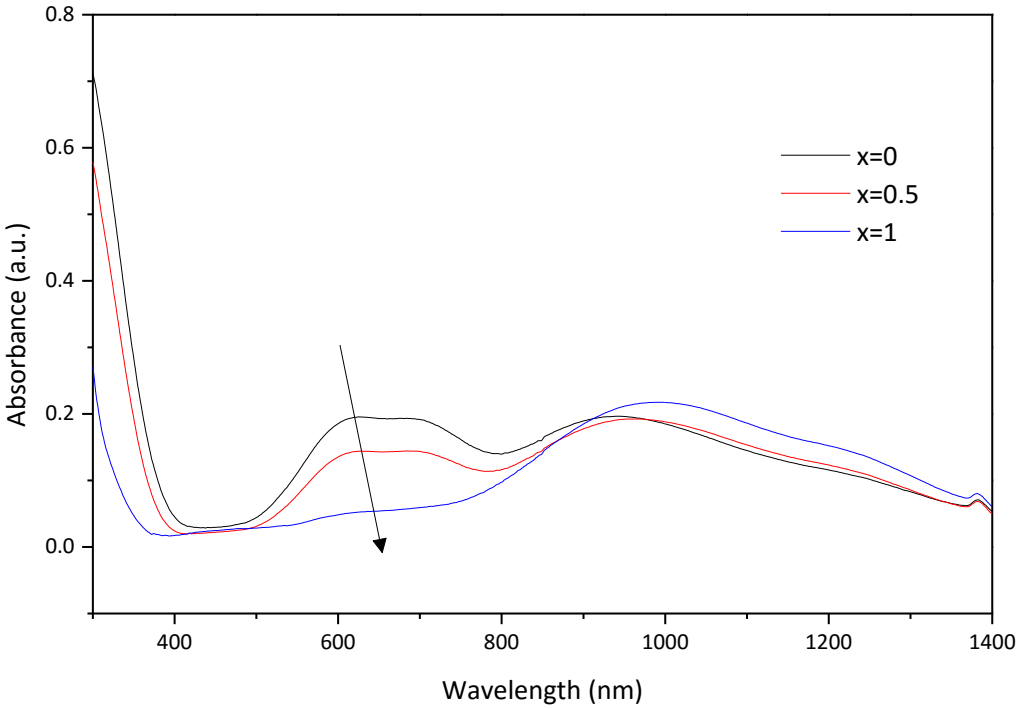

Figure 7.9 - UV-vis-NIR absorbance spectra of $Ca_{10-x/2}Na_xCu_{0.5}(PO_4)_7$ samples with x=0, 0.5 and 1.

Both absorbance peaks are caused by d-d transitions in the Cu^{2+} ions. The d^9 electronic configuration means that the d_{x2-y2} orbital is only half-filled so electrons from the other lower energy orbitals can be excited into it by absorbing incident radiation. The peak at ~1000 nm is due to Cu^{2+} d-d transitions in a trigonal copper environment and shows that some Cu^{2+} occupies the Ca(5) sites in all three samples. The Ca(5) site is octahedral but with trigonal distortion. The ~650 nm peak in the x=1 sample is attributed to d-d transition from Cu^{2+} in the octahedral Ca(4) site. As sodium is introduced into the structure it replaces the copper at this site and so in the $Ca_{9.5}NaCu_{0.5}(PO_4)_7$ sample the copper ions are all located on the Ca(5) site with Na^+ only on the Ca(4) sites. All three samples have similar NIR absorbance intensity so the x = 1 sample was chosen for testing due to its low visible absorbance. Testing results are shown below in section 7.5

7.4 $SrZn_{1-x}Cu_xP_2O_7$

The potential of copper-doped strontium zinc diphosphate (SZCP) as an NIR absorber was seen in a paper by El Jazouli *et. al.*[1], particularly in the figure shown in Figure 7.10. An absorbance peak is seen in the NIR region with little absorbance across the visible region.

The compounds are investigated by El Jazouli and co-workers for application as pigments so the optical properties are well characterised.

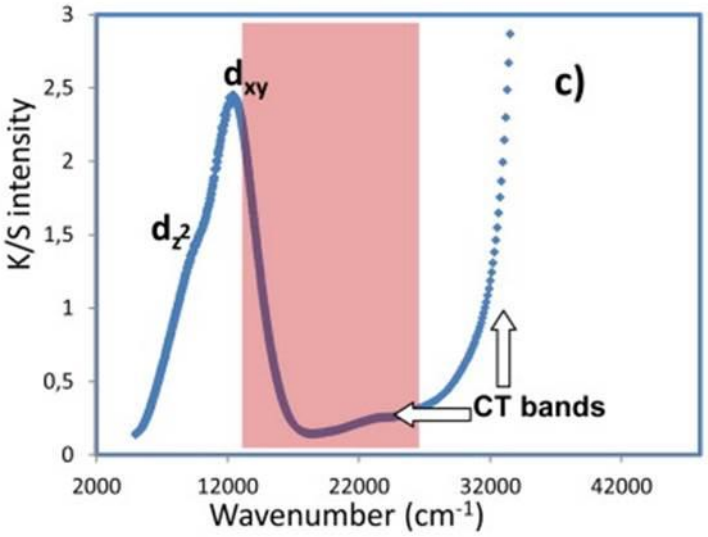

Figure 7.10 - Kubelka-Monk transformation of the absorption spectrum of $SrZn_{0.5}Cu_{0.5}P_2O_7$ taken from El Jazouli et. al.[1].

7.4.1 Synthesis

The synthetic procedure from the same work was used[1]. Heating was carried out in electric furnaces with heating and cooling rates of 5 °C/min. Appropriate amounts of ZnO (Alfa Aesar 99.99%), CuO (sigma Aldrich 99.99%), $SrCO_3$ and $(NH_4)_2HPO_4$ (Alfa Aesar 98% min) were weighed out according to the following equation:

$$1 - xZnO + xCuO + SrCO_3 + 2(NH_4)_2HPO_4 \rightarrow SrZn_{1-x}Cu_xP_2O_7 + 4NH_3 + 3H_2O + CO_2$$

They were mixed using a pestle and mortar and heated in an Al_2O_3 crucible lined with Al foil to 200, 400 and 600 °C for 12 h each with intermittent grinding. The resultant powders were ground again, pressed into pellets of 13 mm diameter and heated to 900 °C in an Al_2O_3 crucible for 12 h. After grinding they were re-pressed into pellets and reheated to 950 °C for 12 h. Compositions corresponding to x = 0, 0.25, 0.5, 0.75 and 1 were synthesised.

7.4.2 Characterisation

The PXRD data are shown in Figure 7.11. As the copper content increases, the structure progresses from that of $SrZnP_2O_7$ to the fully doped $SrCuP_2O_7$ structure, both of which adopt monoclinic symmetry with space group $P2_1/m$. Phases of this diphosphate family containing transition metals from Mn to Zn are all isostructural[1]. There are no impurity peaks present and the samples are all single phase. This can be seen by the 'merging' of peaks across the series rather than the presence of overlapping peaks of two distinct

phases. Particularly in the x = 0.5 sample there is a single broad peak at around 2θ = 32° instead of 4 peaks which would be present if the x = 0 and x = 1 samples were simply mixed together. The peak positions of $SrZnP_2O_7$ and $SrCuP_2O_7$ are also shown in Figure 7.11.

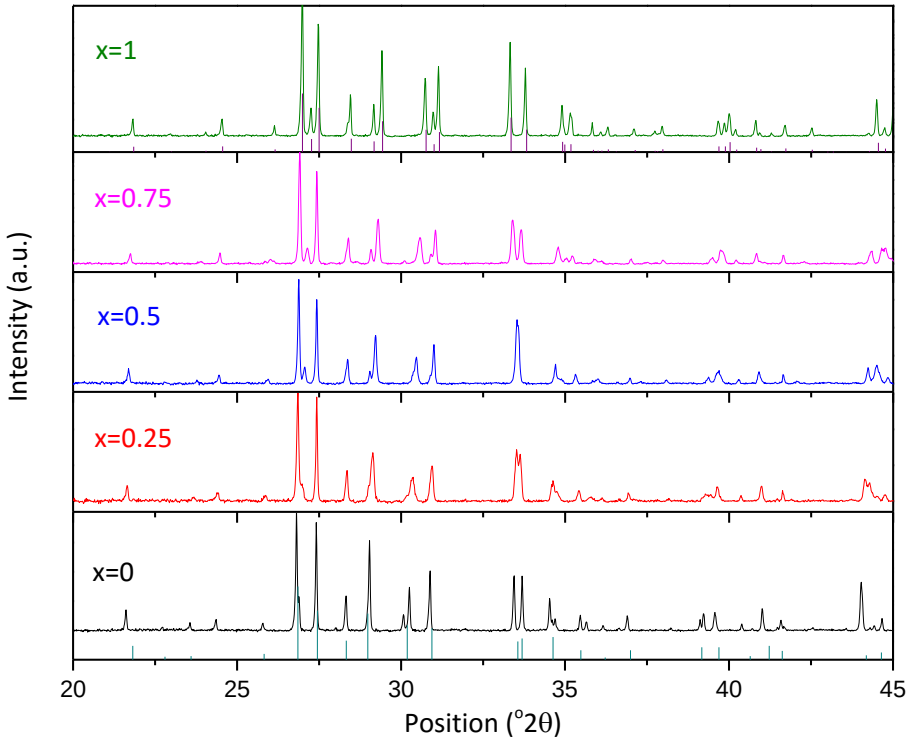

Figure 7.11 - PXRD diffractograms of $SrZn_{1-x}Cu_xP_2O_7$ with x = 0, 0.25, 0.5, 0.75 and 1.The lines under x = 0 show the expected peak positions and intensities of $SrZnP_2O_7$ and those under x = 1, $SrCuP_2O_7$.

The lattice parameters calculated using the Rietveld refinement method, are plotted against copper content x in Figure 7.12 and are in good agreement with literature values found by El Jazouli and co-workers. As x increases, *a* increases linearly while *b* and *c* both decrease. These structural changes are attributed to the distortion of the Zn^{2+} site by Jahn-Teller effect of the Cu^{2+} cations[1], as discussed previously. The crystal structures of the two end members of the solid solution (i.e. x = 0 and x = 1) are shown in Figure 7.13 and the shift of the Cu^{2+} ion towards the square base plane of the pyramidal site in $SrCuP_2O_7$ can be clearly seen in comparison to the Zn^{2+} ions in the same sites in $SrZnP_2O_7$. These phases differ from the CZP and CSCP structures because they are built up of $P_2O_7^{4-}$ diphosphate building blocks rather than the single PO_4^{3-} units found in the other compounds.

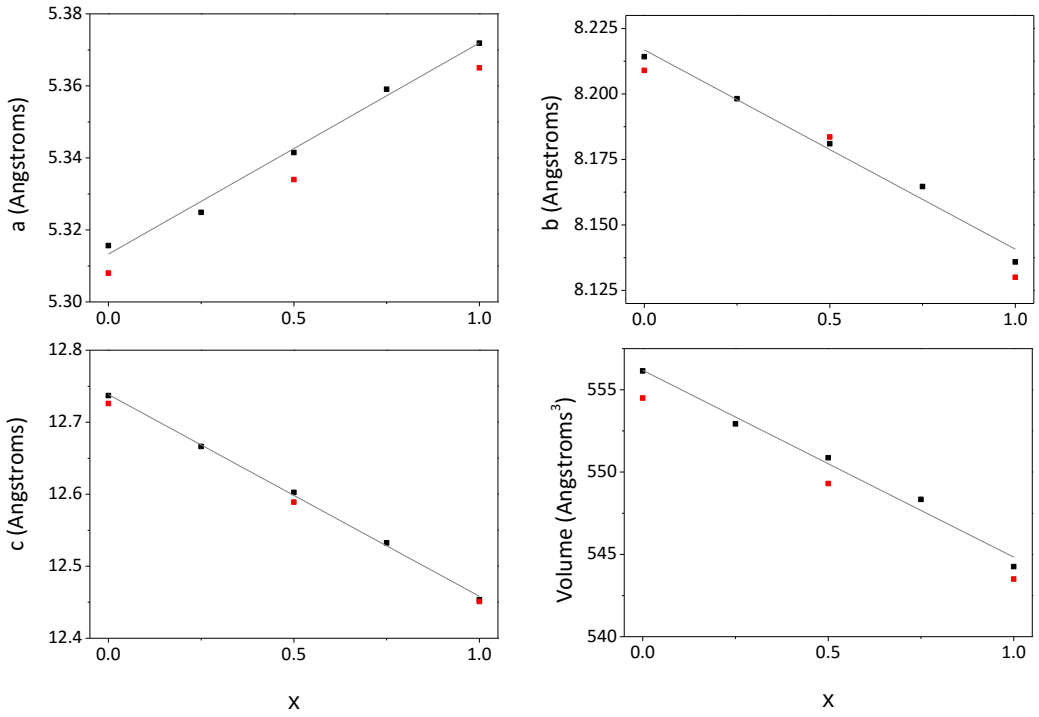

Figure 7.12 - Lattice parameters vs copper content for $SrZn_{1-x}Cu_xP_2O_7$ samples with x = 0, 0.25, 0.5, 0.75 and 1. Lines of best fit shown as a guide to the eye, values from El Jazouli et. al.[1] shown in red.

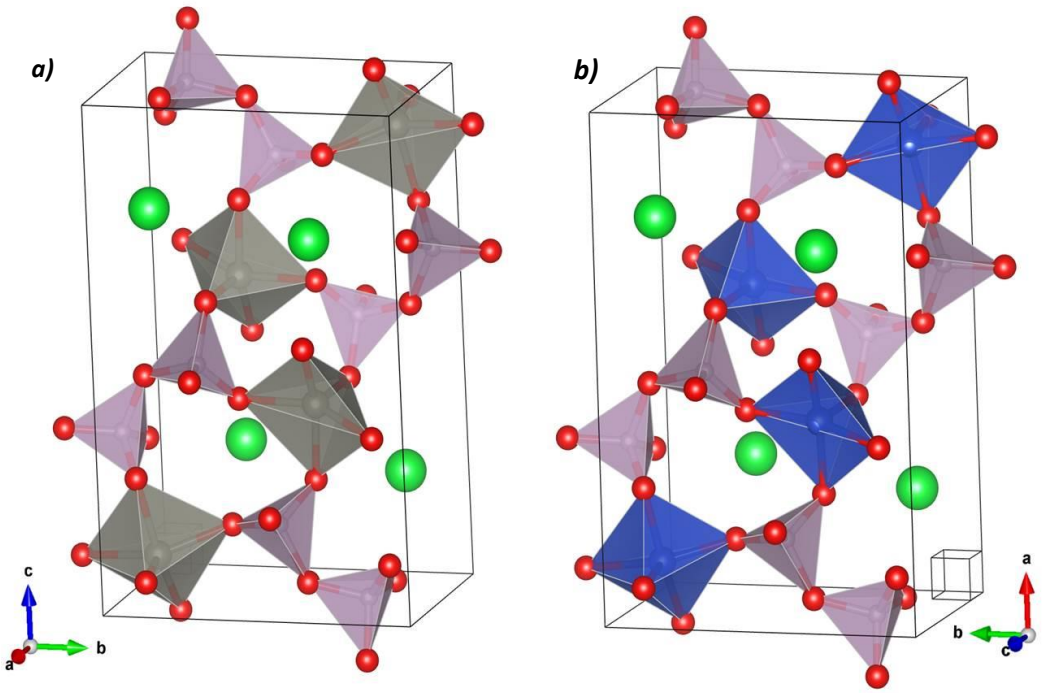

Figure 7.13 - Crystal structures of a) $SrZnP_2O_7$ and b) $SrCuP_2O_7$. Sr=green, Zn=grey, Cu=blue, P=purple and O=red.

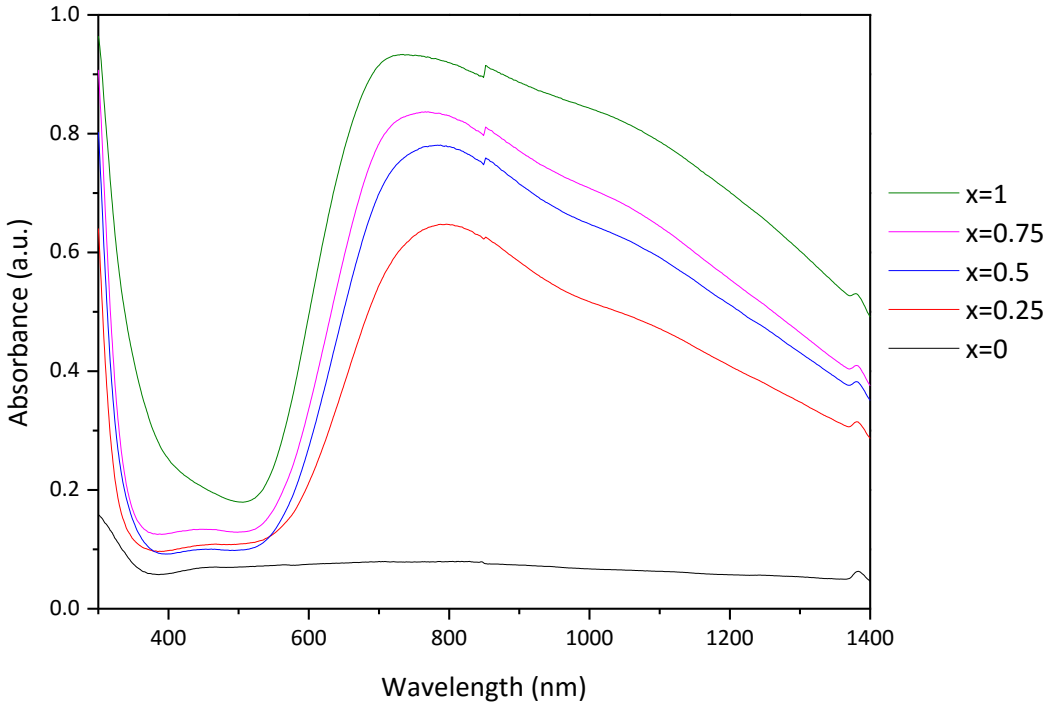

Figure 7.14 - UV-vis-NIR absorbance spectra of $SrZn_{1-x}Cu_xP_2O_7$ samples with x=0, 0.25, 0.5, 0.75 and 1.

The optical absorbance profiles of the SZCP samples are shown in Figure 7.14. Please note that the small 'step' at 850 nm is due to detector switchover and is not an effect of the sample. As was the case for the CSCP samples, the NIR absorbance is caused by Cu^{2+} d-d transitions. Therefore the sample without copper (x = 0) does not show the absorbance peak like the others since Zn^{2+} has a d^{10} electronic configuration so no d-d transitions are possible.

It was seen in the CSCP samples that the Cu^{2+} local environment affects the wavelength of the absorbance peak because the d orbitals have different energies so transitions between them also vary in energy. In these samples the Cu^{2+} environment is a distorted square-based pyramid (see Figure 7.13b). It is more distorted than the site of the Zn^{2+} it is replacing due to the Jahn-Teller effect. The d^9 configuration of the copper means it has one less electron than the Zn^{2+} ion and can move closer to the square plane of the pyramid resulting in the axial Cu-O bond being much longer than the equatorial ones. The energy levels of the d orbitals are also shifted as discussed in section 7.1. This gives the absorbance peak its shoulder – two transitions are possible at slightly different energies (see Figure 7.1). An electronic transition from the d_{xy} orbital to the partially filled $d_{x^2-y^2}$ orbital requires more

energy than the transition from the d_z^2 level which forms the lower energy shoulder in the optical absorption spectra.

There is a systematic increase in the intensity of the NIR absorbance peak with increasing Cu^{2+} content. The absorbance edge gradually shifts into the visible region so the samples change colour across the series from white when x = 0 to bright blue when x = 1 (see Figure 7.15).

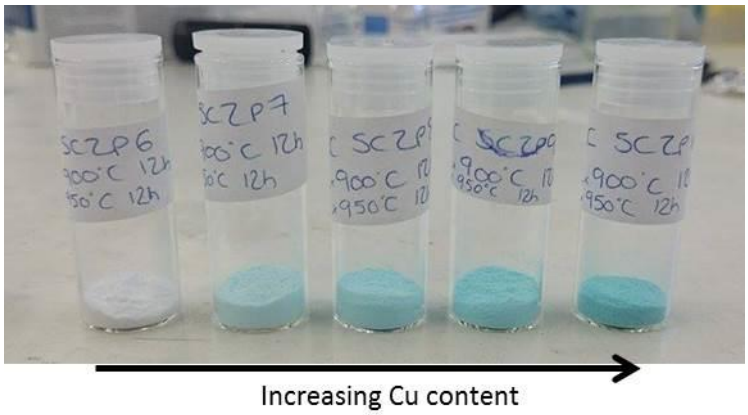

Figure 7.15 - Photograph showing the progressive colour change of $SrZn_{1-x}Cu_xP_2O_7$ samples from white to blue with copper content increasing left to right from x = 0 to x = 1

As expected the samples with the highest value of x show the highest NIR absorbance. The most absorbing sample (x = 1) was chosen for laser image testing as well as the x = 0.75 sample in case the slightly lower visible absorbance makes a difference to coating transparency once the samples are formulated into an ink.

7.5 Results of Laser Imaging

All copper phosphate samples were formulated into inks following the procedure outlined in Chapter 2. Optical density values give an indication of performance – low background OD combined with high image OD is desirable.

Results are shown in Table 7.3. A range of wt% loadings were used, particularly for the samples that weren't strongly coloured because the absorber concentration could be increased without significantly darkening the background colour of the coating. Although the background OD of the coatings was very good (i.e. close to white), none of the copper

phosphate absorbers resulted in any laser imaging during irradiation apart from SZCP x = 1 at very high loading.

Table 7.3 - Results of laser image testing of copper phosphate samples

Sample	Loading (wt%)	Background OD	ΔOD 1070 nm
CZP	3	0.07	0
CSCP x = 1	0.75	0.07	0
CSCP x = 1	12	0.07	0
SZCP x = 0.75	0.75	0.065	0
SZCP x = 1	0.75	0.0625	0
SZCP x = 1	12.5	0.0675	0.215

The CZP sample simply did not have a sufficient level of NIR absorbance (see Figure 7.5) to take up enough laser radiation to result in imaging. For the more strongly absorbing CSCP and SZCP samples the explanation is slightly more complex. It is thought that the absorption of NIR irradiation by these samples via d-d transitions is very much localised on the Cu ions so the energy is not then transferred to the pigment particles as heat to cause a colour change.

When the $SrCuP_2O_7$ sample was tested at a high loading level of 12.5 wt% there was some imaging. The NIR absorbance of the SZCP samples was significantly higher than that of the CSCP samples so it could be expected that SZCP would show better imaging performance. Despite this, the high level of loading results in a strangely 'textured' ink coating and the absorber settles out of the ink easily.

7.6 Conclusion

Due to the generally poor imaging performance of the copper phosphate samples and the poor coating quality of the SZCP sample that did image, these samples were not pursued further nor were any other copper-based materials. The d-d transition absorption mechanism is clearly not as effective in this application as the combined polaron/plasmon absorbance mechanisms seen in the tungsten-based samples in Chapters 3-5.

7.7 References

1. El Jazouli, A.; Tbib, B.; Demourgues, A.; Gaudon, M., Structure and colour of diphosphate pigments with square pyramid environment around chromophore ions (Co^{2+}, Ni^{2+}, Cu^{2+}). *Dyes Pigments* **2014,** *104* (0), 67-74.
2. Mbandza, A.; Bordes, E.; Courtine, P., Preparation and structural properties of the solid state ionic conductor $CuTi_2(PO_4)_3$. *Mater Res Bull* **1985,** *20* (3), 251-257.
3. Yao, P. C.; Fray, D. J., The preparation and properties of the solid state ionic conductor, $CuZr_2(PO_4)_3$. *Solid State Ionics* **1983,** *8* (1), 35-42.
4. Christiansen, R. H. W.; Warner, T. E., A study of copper stoichiometry and phase relationships in the copper-zirconium phosphate system: $CuZr_2(PO_4)_3$–$Cu_{0.5}Zr_2(PO_4)_3$. *Journal of Materials Science* **2006,** *41* (4), 1197-1205.
5. Busserau, I.; Belkhiria, M. S.; Gravereau, P.; Boireau, A.; Soubeyroux, J. L.; Olazcuaga, R.; Le Flem, G., Structure of $CuZr_2(PO_4)_3$ by X-ray and neutron powder diffraction. *Acta Crystallographica Section C* **1992,** *48* (10), 1741-1744.
6. Fargin, E.; Bussereau, I.; Olazcuaga, R.; Le Flem, G.; Cartier, C.; Dexpert, H.; Verdaguer, M., Phosphates with Nasicon-derived structure: an extended X-ray absorption fine structure investigation. *J Alloy Compd* **1992,** *188* (0), 107-109.
7. Warner, T. E.; Skou, E. M., On the thermal stability of the copper–titanium–zirconium phosphate solid-solution series: $CuTi_{2-x}Zr_x(PO_4)_3$ ($0 \le x \le 2$) under air. *Journal of Materials Science* **2011,** *46* (13), 4622-4629.
8. Benarafa, A.; Kacimi, M.; Coudurier, G.; Ziyad, M., Characterisation of the active sites in butan-2-ol dehydrogenation over calcium–copper and calcium–sodium–copper phosphates. *Applied Catalysis A: General* **2000,** *196* (1), 25-35.
9. (a) Yanov, O. V.; Morozov, V. A.; Vieting, B. N.; Ivanov, L. N.; Lazoryak, B. I., A whitlockite-like calcium copper phosphate. *Mater Res Bull* **1994,** *29* (12), 1307-1314; (b) Khan, N.; Morozov, V. A.; Khasanov, S. S.; Lazoryak, B. I., Synthesis and crystal structure of calcium copper phosphate, s-$Ca_{19}Cu_2(PO_4)_{14}$. *Mater Res Bull* **1997,** *32* (9), 1211-1220.

Chapter 8

Transparent Conducting Oxide Materials

8.1 Introduction

Transparent conducting oxides (or TCO's) have revolutionised the opto-electronics industry with their combination of optical transparency and good electrical conductivity. A number of examples are discussed in section 1.8.4. A reduced form of indium tin oxide (rITO), a well-known TCO, was one of the commercial samples analysed in Appendix 1 and it works well as a near infrared (NIR) absorber in the Datalase laser imaging process so other TCO's were investigated. In this chapter the synthesis, characterisation and testing results of N-doped TiO_2 and La-doped $BaSnO_3$ are presented.

8.2 N-doped TiO_2

Titania (TiO_2) is a wide band gap semiconductor with a huge range of applications. Pure TiO_2 is commonly used as a white pigment and as a component of sunscreen since it absorbs UV light strongly. Recently it has been applied to textiles to make self-cleaning clothing[1]. Much work has been done to maximise its potential as a photocatalyst for water-splitting, degradation of organic contaminants and solar energy conversion to name just a few. Excellent reviews exist on the subject, for example reference 2 and references therein.

At room temperature three polymorphs exist named for the minerals in which they are found – rutile, anatase and brookite. Their structures are shown in Figure 8.1. The orthorhombic brookite phase is relatively rare compared to the tetragonal anatase and rutile phases. Anatase has the lowest surface energy of the three phases so small particles tend to be anatase whereas the rutile phase is stable in bulk[3]. However the synthetic routes and precursors used can have a significant effect on the resulting phase(s).

Many different elements have been used to tune the band gap of TiO_2 to optimise it for different applications[4], in particular for photocatalysis using visible light. Again many reviews of current work are available[5].

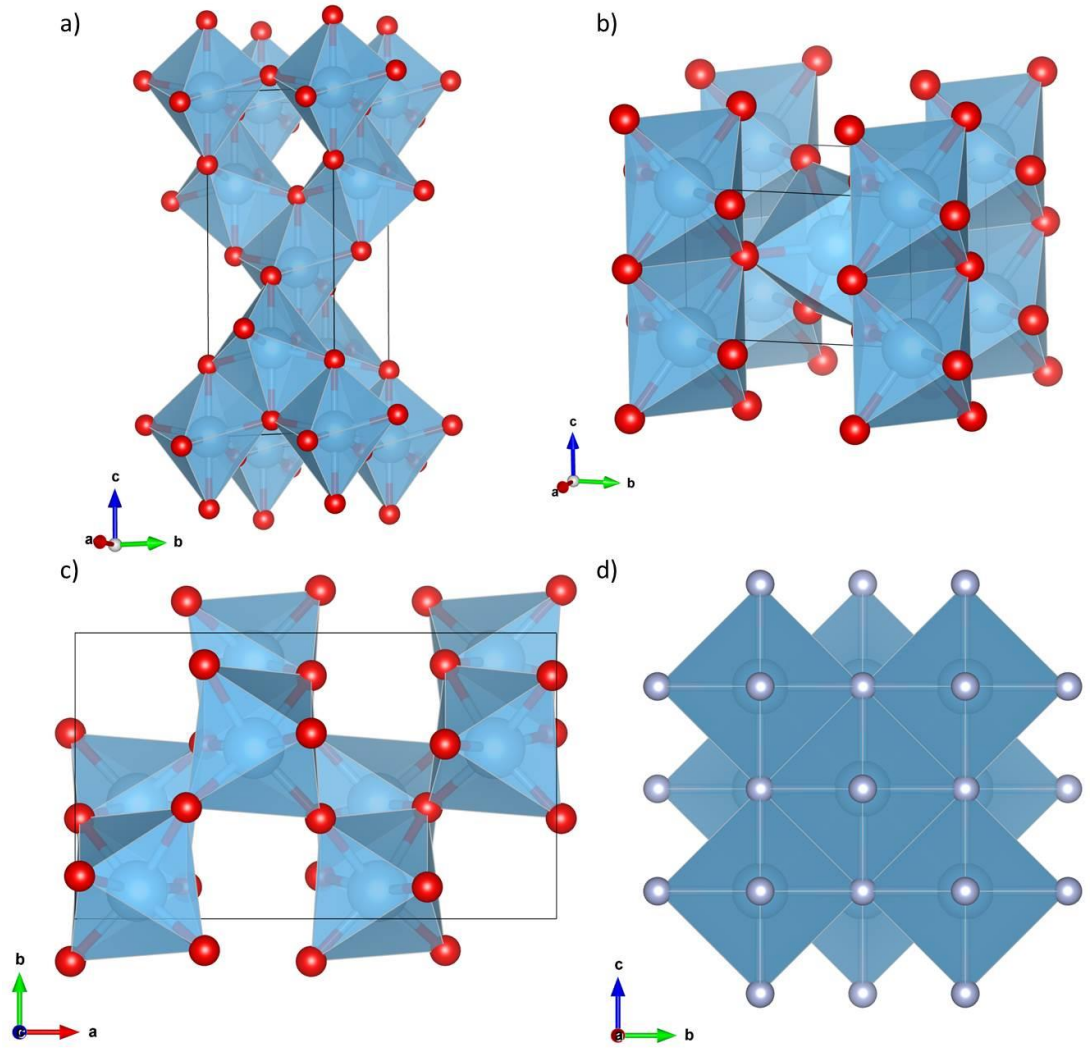

Figure 8.1 - Polyhedral representations of the crystal structures of a) anatase TiO2, b) rutile TiO2, c) brookite TiO2 and d) TiN. Ti=blue, O=red and N=grey.

Asahi *et. al*. first showed that N-doping would shift the optical absorbance into the visible region[6] and these materials have been studied for various applications[7]. Several methods have been used in this work to synthesise $TiO_{2-x}N_x$ samples.

8.2.1 Synthesis

Three routes were used: nitridation of TiO_2 by i)ammoniolysis, ii)a solvothermal route and iii)oxidation of TiN. P25 was used as a starting material – it is a commercially available form of titania with small particle size and an anatase:rutile phase ratio of around 70:30.

TiO_2-AM i) P25 (Sigma Aldrich 99.5%, 1.8 g, 0.0225 mol) was placed in an Al_2O_3 boat crucible and placed in a tube furnace. It was heated to 700 ^oC for under flowing NH_3 with a heating rate of 10 ^oC/min and cooled naturally to room temperature under flowing N_2. Heating times of 4 h and 8 h were used.

TiO_2-ST ii) Following the method used by Peng *et. al.*[8] P25 (Sigma Aldrich 99.5%, 0.5 g, 6.26 x 10^{-3} mol) was added to 40 ml triethanolamine (TEA, $N(C_2H_4OH)_3$) and sonicated for 20 minutes. The mixture was heated in a Teflon-lined autoclave for 24 h or 48 h at 140 ^oC then separated by centrifugation before being washed with water and ethanol then dried at 200 ^oC for 10 h.

TiN-OX iii) From the paper by Zhou *et. al.*[9] 0.5g TiN (Datalase) was dispersed in 80 ml H_2O_2 solution by sonication for 10 minutes. It was heated in a Teflon-lined autoclave for 24 h at 170 ^oC then separated by centrifugation, washed with water and ethanol and dried at 100 ^oC for 24 h. H_2O_2 solutions of 0.5, 1, 2 and 3 weight % were used.

8.2.2 Characterisation

8.2.2.1 PXRD

The diffractograms of the nitrided TiO_2-AM and TiO_2-ST samples are shown in Figure 8.2 and those of the TiN-OX samples in Figure 8.4.

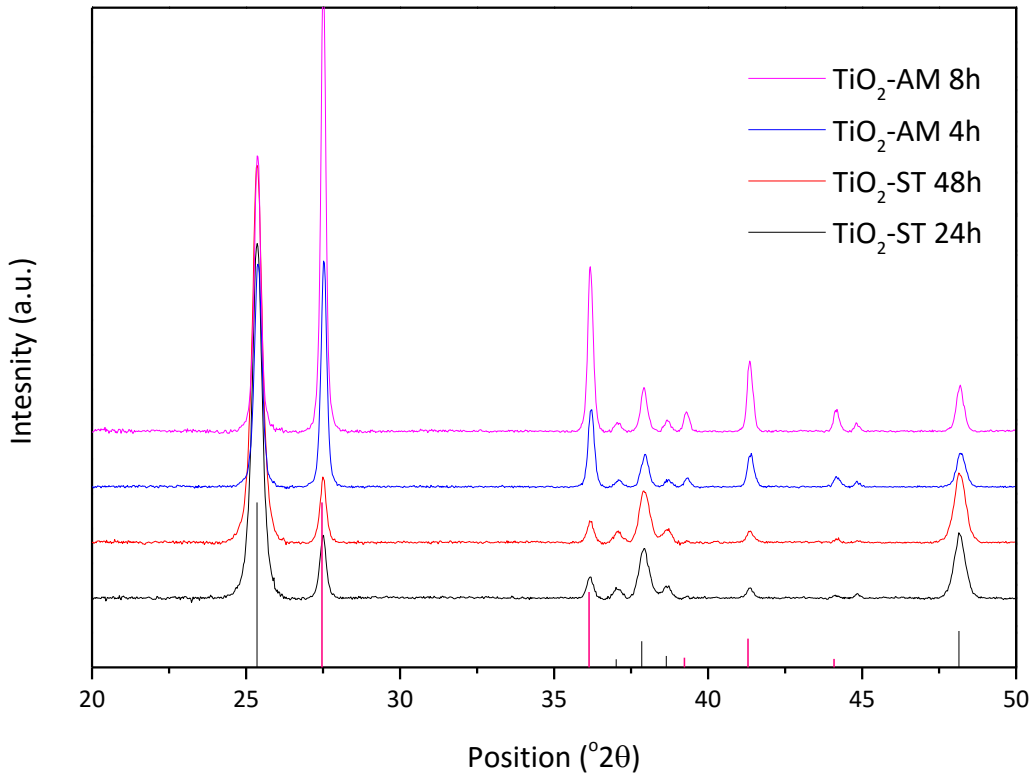

Figure 8.2 - PXRD diffractograms of solvothermally nitrated (ST) TiO_2 samples and ammoniolysed (AM) TiO_2 samples. Expected peak positions and intensities are shown for anatase and rutile TiO_2 phases with black and magenta lines respectively.

Since mixed phase P25 was used as a starting material for the ammoniolysis and the solvothermal nitration all products made using these routes are also mixed phase although

the phase ratio varies. The proportions of the $I4_1/amd$ anatase to $P4_2/mnm$ rutile phase were calculated using Rietveld refinement method of the PXRD data and are shown in Table 8.1.

Table 8.1 - Phase ratios of $TiO_{2-x}N_x$ samples calculated from Rietveld refinement of PXRD data.

Sample	Anatase %	Rutile %
TiO_2-ST 24h	85.0	15.0
TiO_2-ST 48h	85.3	14.7
TiO_2-AM 4h	47.7	52.3
TiO_2-AM 8h	35.7	64.3

It can be seen that the solvothermally nitrided samples have a much higher amount of anatase phase than the ammonionlysis samples. The rutile phase starts to form at around 600 ^{o}C so it is unsurprising that the ammoniolysis route with a temperature of 700 ^{o}C yielded more of this phase than the solvothermal route which was heated to a maximum temperature of 200 ^{o}C.

The lattice parameters were also calculated during the refinement and increase with increasing nitridation time up to the TiO_2-ST 48 h sample which shows a decrease compared to the TiO_2-ST 24 h sample. The same behaviour is seen for the *a* and *c* parameters of both the rutile and anatase phases in each sample, as seen in Figure 8.3.

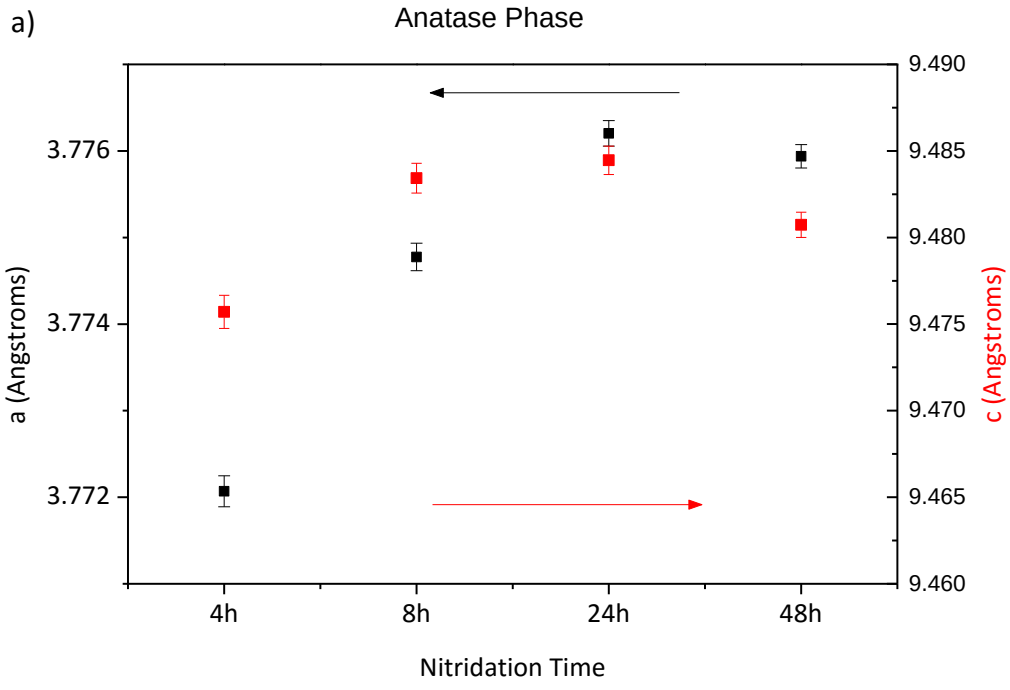

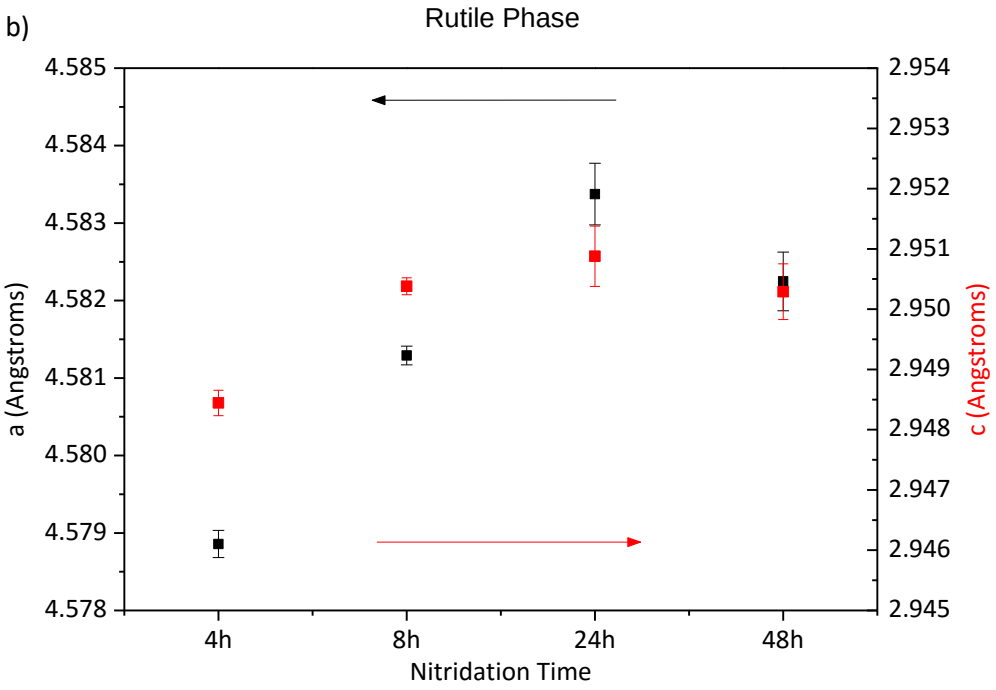

Figure 8.3 - Lattice parameters of a) anatase phase and b) rutile phase of TiO_2 samples nitrided for different amounts of time calculated from Rietveld refinement of PXRD data.

The ionic radius of N^{3-} is slightly larger than O^{2-} so this indicates that N has been incorporated into the TiO_2 framework since no impurity phases are seen.

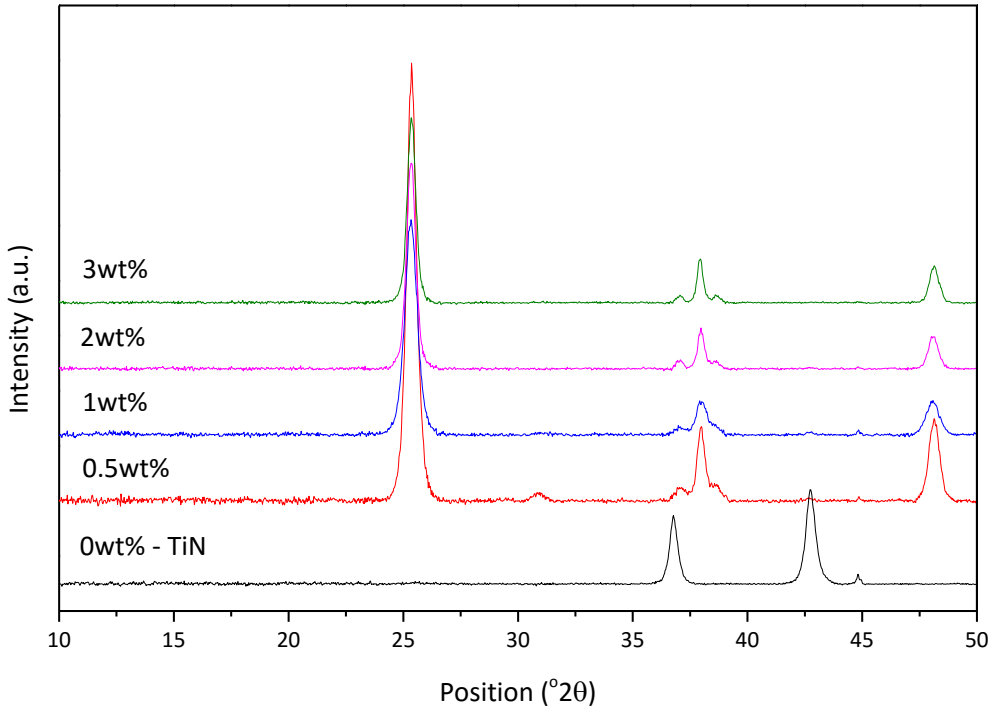

Figure 8.4 - PXRD diffractograms of TiN samples oxidised with H_2O_2 solutions of different concentrations.

It can be seen from Figure 8.4 that the oxidised TiN samples are pure anatase phase with the exception of the 0.5 wt% H_2O_2 sample in which some residual TiN peaks are also visible as well as a peak at around $2\theta = 32^{o}$ that corresponds to the brookite form of TiO_2. The three room temperature crystal structures of TiO_2 are shown in Figure 8.1 with the cubic structure of TiN.

The lattice parameters of the anatase TiN-OX samples are calculated using a Pawley refinement of PXRD data and plotted in Figure 8.5. The impure 0.5 wt% H_2O_2 sample has anomalous *a* and *c* values with large error values. However for the other samples, a trend of decreasing *a* and increasing *c* lattice parameters with increasing oxidation level is seen. Again this indicates that nitrogen has been incorporated into the lattice since no impurity phases are observed.

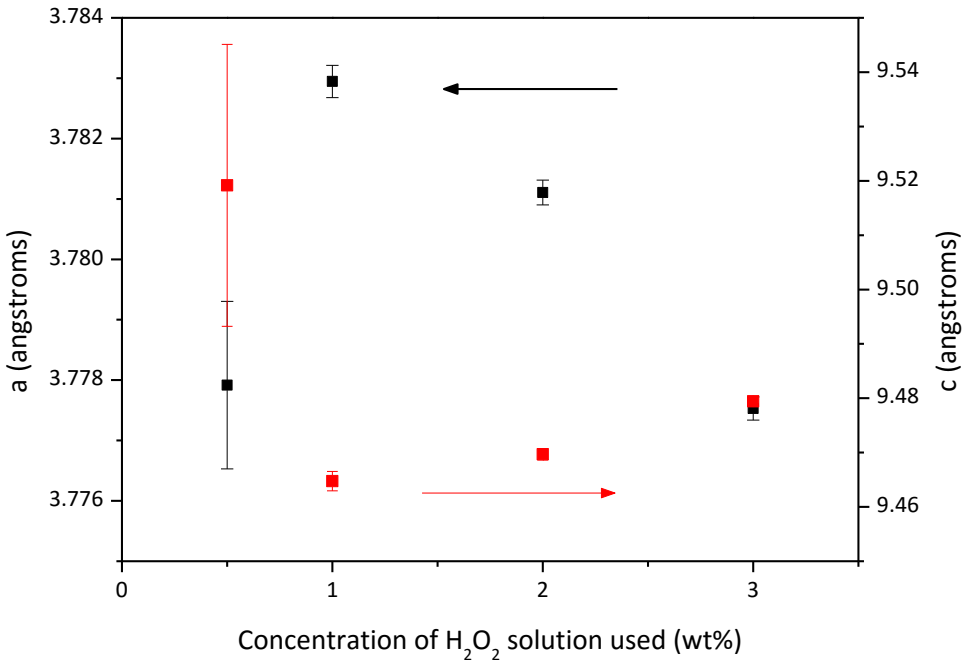

Figure 8.5 - Lattice parameters of TiN samples oxidised with different concentrations of H_2O_2 calculated from Rietveld refinement of PXRD data.

8.2.2.2 UV-vis-NIR spectroscopy

The colour of the samples varied from pale yellow for the TiO_2-AM samples to brown for the TiO_2-ST samples and blue for the TiN-OX samples. The optical absorbance profiles are shown in Figure 8.6 and compared to the white P25 and black TiN starting materials.

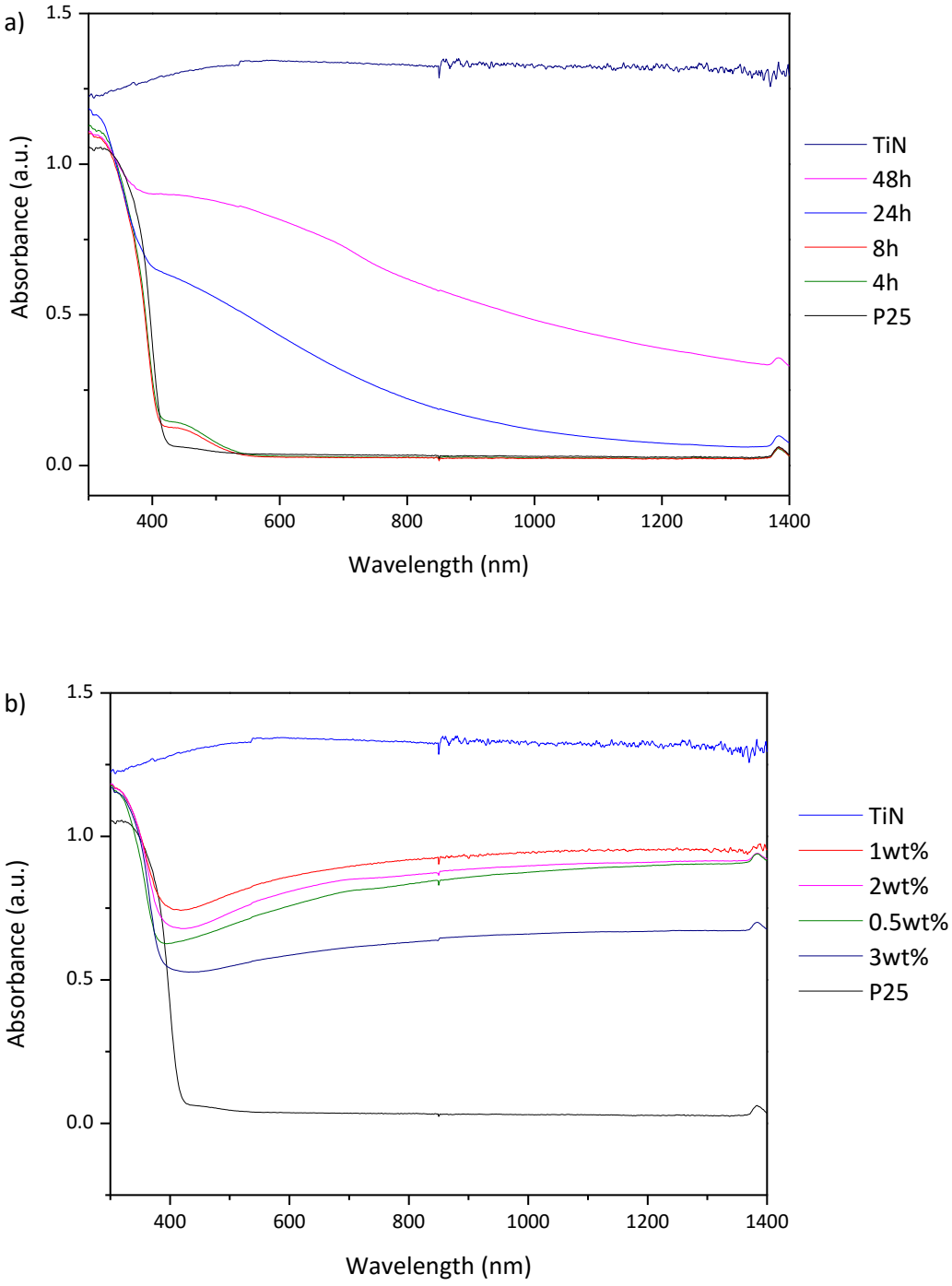

Figure 8.6 - Optical absorbance spectra of a) nitrided TiO_2 and b) oxidised TiN samples.

The effect of the ammoniolysis was to introduce a small absorbance peak between 400-500nm in Figure 8.5a with no effect on the NIR region. The solvothermal nitridation created a broad absorbance across the spectrum which decreased in intensity towards the NIR end but increased in overall intensity with increased reaction time. Peng *et. al.* observed a

similar effect and attributed it to the creation of a narrow band in the band gap by the mixing of N 2p and O 2p orbitals[7b].

The oxidised TiN samples also showed broad absorbance across the whole spectrum, decreasing slightly towards the UV wavelengths. The sample made using a 3 wt% H_2O_2 solution has less intense absorbance than the other samples – greater levels of oxidation makes the samples increasingly TiO_2-like and therefore less coloured. However the absorbance profiles of the other 3 samples do not differ significantly. TiN exhibits metallic behaviour so can form highly reflective coatings. Absorbance arises from plasmon resonance and partial oxidation changes the amount of charge carriers[10]. Based on the optical data, the 1 wt% TiN-OX sample was chosen for laser image testing since it has the highest NIR absorbance of the range of samples. Pure TiN was also tested. The results are shown below in section 8.4.

8.3 La-doped $BaSnO_3$

Cubic perovskite barium stannate $BaSnO_3$ is known as a transparent wide band gap semiconductor in the family of alkaline earth stannates. Doping with non-isovalent cations on the A-site introduces electronic conductivity by creation of donor electronic bands in the band gap. Some visible optical absorbance also arises due to the formation of Sn^{2+} species[11]. This was investigated as a potential NIR absorber.

8.3.1 Synthesis

A solid state synthetic route was used. Appropriate amounts of pre-dried SnO_2 (Sigma Adrich 99.99%), $BaCO_3$ (Sigma Adrich 99.98%) and La_2O_5 (Sigma Aldrich 99.999%) were used according to the equation:

$$SnO_2 + \ 1 - xBaCO_3 + {}^{x}/_{2}\, La_2O_5 \rightarrow La_xBa_{1-x}SnO_3 + CO_2 + 2\,{}^{1}/_{2}\, O_2$$

They were mixed using a pestle and mortar then pressed into a 20 mm pellet. The pellets were heated in a Pt-foil-lined alumina crucible to 1250 ^{o}C in air for 24 h with a heating and cooling rate of 5 ^{o}C/min. The pellet was ground, re-pressed and heated to 1450 ^{o}C for 48 h with the same heating and cooling rate. It was ground again with a pestle and mortar before analysis. Values of x = 0.05 and 0.1 was used i.e. 5 and 10% doping levels.

8.3.2 Characterisation

8.3.2.1 PXRD

The PXRD diffractogram of the LaBSO sample is shown in Figure 8.7.

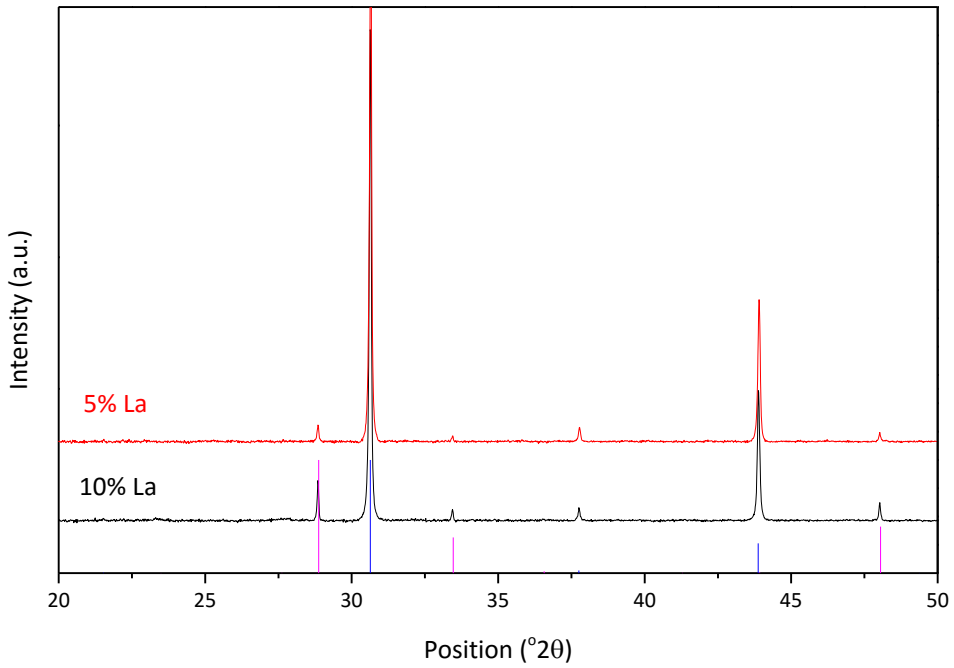

Figure 8.7 - PXRD diffractogram of $Ba_{1-x}La_xSnO_3$. The expected peak positions and intensities of cubic $BaSnO_3$ and cubic pyrochlore $La_2Sn_2O_7$ are shown in blue and red respectively.

Both samples contain two cubic phases – $BaSnO_3$ and pyrochlore $La_2Sn_2O_7$. This is expected as only a small amount ($x < 0.02$) of La substitutes into the $BaSnO_3$ structure[12]. Rietveld refinement gives the relative amounts of each phase and the *a* lattice parameters for each phase, shown in Table 8.2.

Table 8.2 – Phase ratios and lattice parameters of $La_xBa_{1-x}SnO_3$ samples calculated from Rietveld refinement of PXRD data.

Sample	$BaSnO_3$ phase	a (Å)	$La_2Sn_2O_7$ phase	a (Å)
5% La:$BaSO_3$	96.2%	4.112(1)	3.8%	10.703(9)
10% La:$BaSnO_3$	90.9%	4.120(2)	9.1%	10.702(2)

As expected the 10% La-doped sample contains proportionally more of the pyrochlore $La_2Sn_2O_7$ phase than the 5% La-doped sample. There is also a small increase in the *a* lattice parameter of the $BaSnO_3$ phase compared to the 5% La-doped sample. the value for the undoped parent phase in 4.123 Å so the slight decrease from this value for both samples is an indication that a small amount of La^{3+} has been doped onto the Ba site since its ionic

radius is smaller than that of Ba^{2+}. The lattice parameters for the pyrochlore phase are unchanged from that of parent phase. The crystal structures of both structures are shown in Figure 8.8.

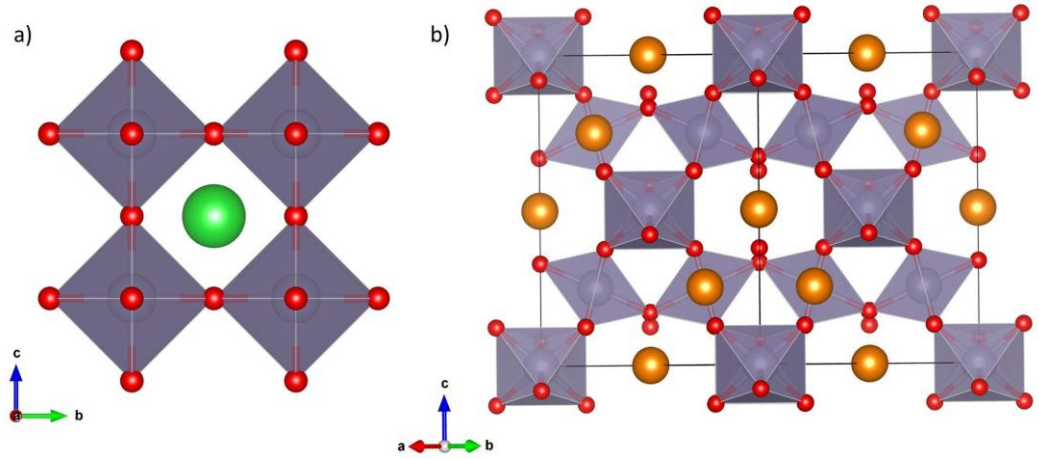

Figure 8.8 – Polyhedral representation of the crystal structures of a) cubic BaSnO3 and b) cubic pyrochlore $La_2Sn_2O_7$. Sn=grey, O=red, Ba=green and La=orange.

8.3.2.2 UV-vis-NIR Spectroscopy

The optical absorbance profile of 5 and 10% La-doped $BaSnO_3$ is shown in Figure 8.9.

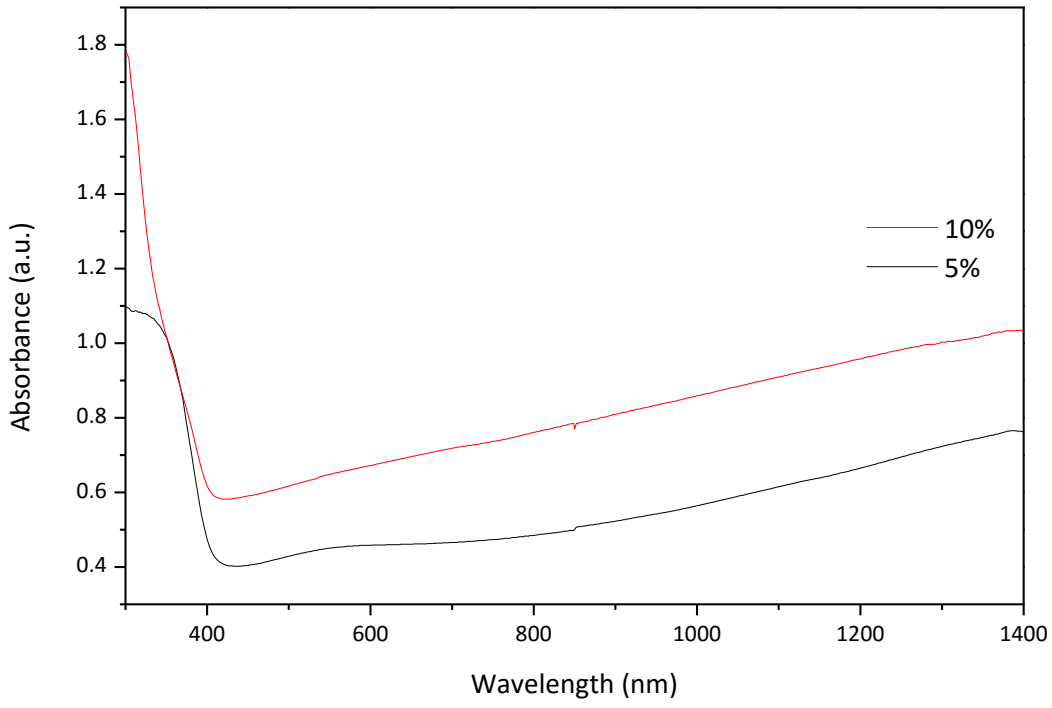

Figure 8.9 – Optical absorbance profiles of 5% and 10% La-doped $BaSnO_3$.

The absorbance gradually increases moving across the spectrum from the visible to the NIR region. The 10% sample has increased intensity across the whole spectrum compared to

the 5% sample but both show the same profile shape. Both samples are light blue in colour. It can be assumed that the absorbance values would continue to increase in the infrared region which is out of the measurement range. The insertion of La^{3+} into the $BaSnO_3$ phase causes reduction of some Sn^{4+} to Sn^{2+} so two electrons are generated per La^{3+}. Although some polarons may be present in the structure[12], at high levels of doping as is the case in the LaBSO sample, electrons reside in the conduction band. These electrons are delocalised and so the absorbance arises from plasmon resonance. The intensity is higher for the 10% doped sample because it has more electrons to participate in the interaction compared to the 5% doped sample. The 10% doped sample was chosen for testing and called LaBSO.

8.4 Results of Laser Imaging

1wt% TiN-OX and 10% LaBSO samples were tested at Datalase. The samples were mixed into inks according to the procedure outlined in Chapter 2.4. The optical density of the unirradiated background coating (OD) and of the irradiated areas (ΔOD) are shown in Table 8.3.

At 0.75 wt% loading in the ink the background optical density was low with near-white coatings for TiN-OX and LaBSO samples (uncoated PET OD = 0.09) but irradiation did not result in the creation of images. Using higher loadings of 2.5 and 5 wt% LaBSO had no effect except to increase the background OD slightly. The pure TiN sample was the only one to result in image creation however it is so absorbing that the background OD was dark even at a very low loading of 0.05 wt%.

Table 8.3 – Results of laser image testing

Sample	Loading (wt%)	Background OD	ΔOD
TiN-OX	0.75	0.07	0
TiN	0.05	0.145	0.3725
LaBSO	0.75	0.0675	0
LaBSO	2.5	0.0825	0
LaBSO	5	0.09	0

It is evident from these results that $TiO_{2-x}N_x$ and $Ba_{1-x}La_xSnO_3$ do not perform well as NIR absorbers in the Datalase imaging process. It is likely that they simply do not absorb sufficient radiation in the NIR region to drive the thermal pigment colour change. TiN is too

absorbing in the visible region to be practical in commercial labelling applications. The contrast between images created and a dark background would be too low for good legibility and dark labels are aesthetically unappealing. These materials were not pursued further.

8.5 Other TCO materials

Over the course of the project a number of other TCO's were looked at but not tested. They will be described here briefly.

8.5.1 Nb-doped $SrTiO_3$

Strontium titanate $SrTiO_3$ is a cubic perovskite (ABO_3) semi-conductor that can be doped to improve conductivity either by using a rare earth element on the A site or a transition metal on the B site. Replacing Ti^{4+} with Nb^{5+} introduces more charge carriers which increases electronic conductivity[13] but more importantly for this project, shifts the optical absorbance from the IR region towards the visible wavelengths.

A solid state route from Karczewski *et. al.*[14] was used to synthesise samples. Reactants were mixed according to the equation:

$$SrCO_3 + (1-x)TiO_2 + {}^{x}/_{2}\,Nb_2O_5 \rightarrow SrTi_{1-x}Nb_xO_3 + CO_2$$

They were ground using a pestle and mortar and pressed into 10 mm pellets. The pellets were heated to 1200 ^{o}C for 12 h in air with heating and cooling rates of 5 ^{o}C/min. They were ground into powder, re-formed into pellets and reheated to 1400 ^{o}C for12 h with heating and cooling rates of 1 ^{o}C/min. the resulting products were ground once more with a pestle and mortar before analysis.

PXRD (Figure 8.10) showed the products to be phase pure and cubic and Rietveld refinements of this data measured using an internal LaB_6 standard showed that the lattice parameters increase with increasing *x* (Figure 8.11). This is in accordance with the literature since Nb^{5+} has a larger ionic radius than Ti^{4+}.

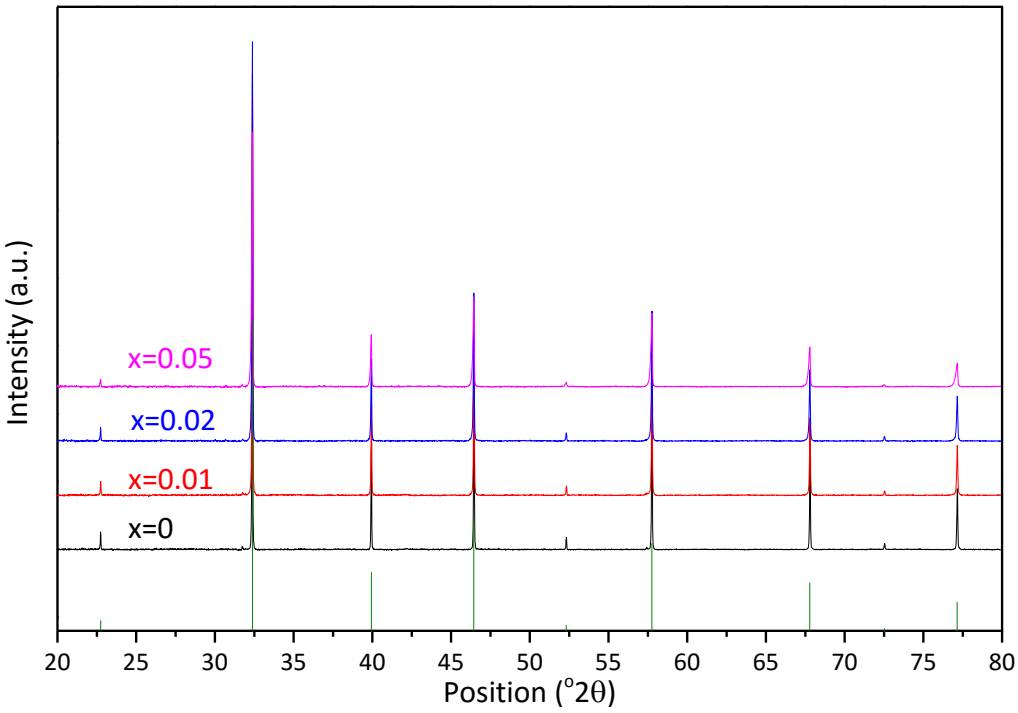

Figure 8.10 - PXRD diffractograms of $SrTi_{1-x}Nb_xO_3$ samples with different values of x. The expected peak positions and intensities of $SrTiO_3$ are shown.

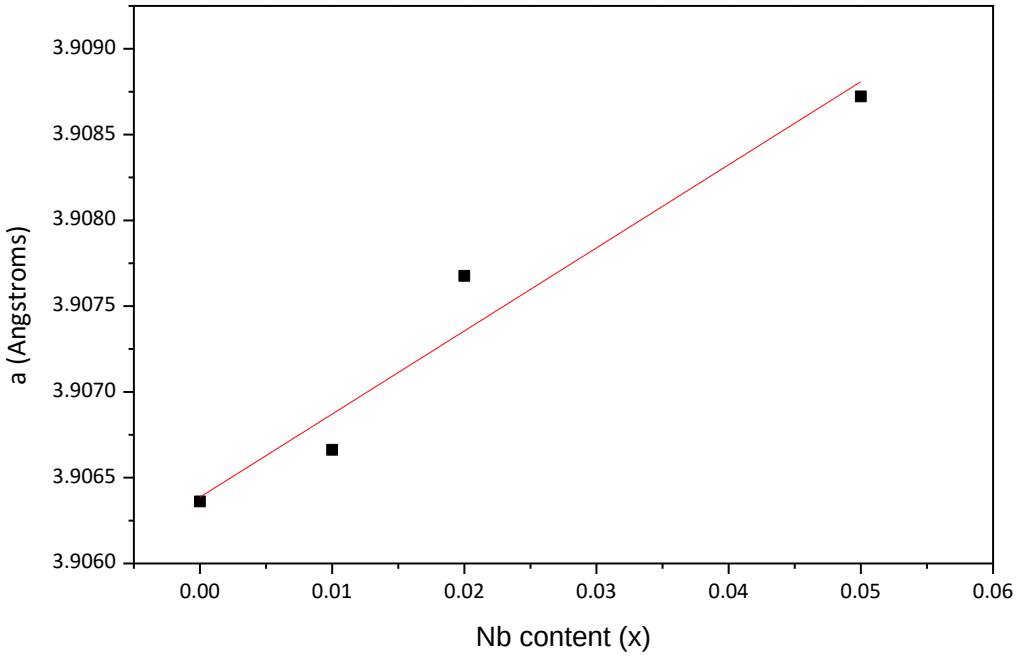

Figure 8.11 - Variation in a lattice parameter in $SrTi_{1-x}Nb_xO_3$ samples with increasing x.

The optical absorbance profiles of the samples are shown in Figure 8.12.

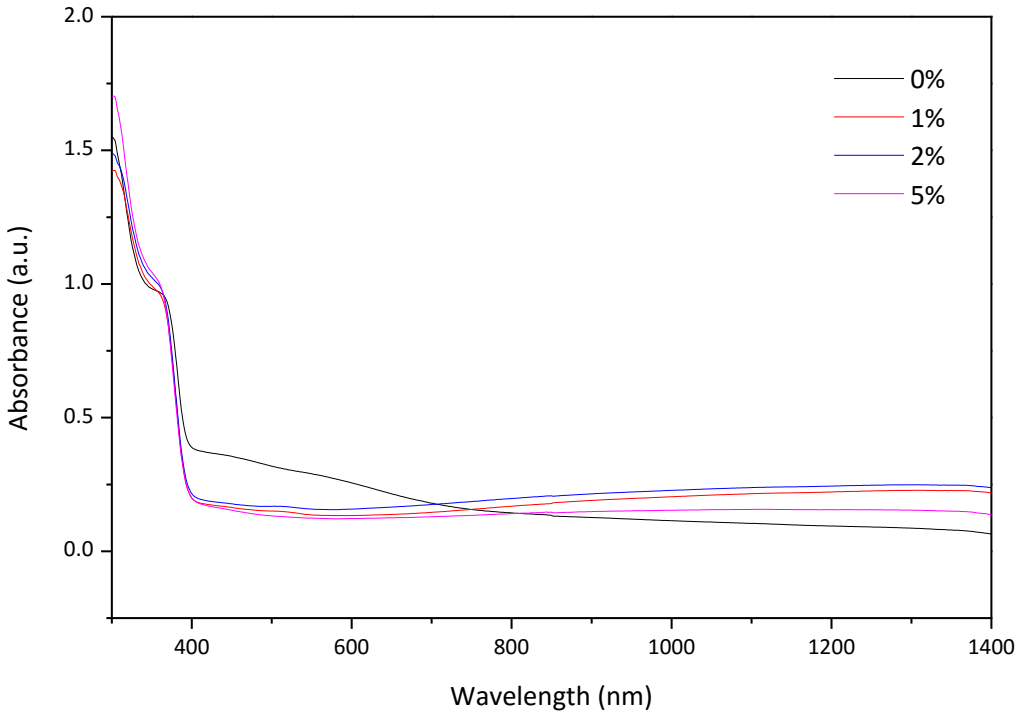

Figure 8.12 - Optical absorbance profiles of $SrTi_{1-x}Nb_xO_3$ samples with different values of x.

It can be seen that the x = 0 sample has some absorbance in the visible rage between 400-600 nm and the reason for this is unclear although it results in light brown colouration of the sample whereas the others are white. For the x = 0.01, 0.02 and 0.05 samples some increased absorbance compared to the x = 0 sample is seen in the NIR region. However even the most absorbing sample (x = 0.02) has a very broad low intensity peak and there is no clear trend of absorbance with increasing *x*. The absorbance was so low that these samples were not tested for laser imaging.

A solvothermal route from a paper by Wang *et. al.*[15] was also used to make Nb-doped $SrTiO_3$ (see Appendix 6) but resulted in samples with very similar optical properties to the solid state ones above (Figure A.6.1). Other synthesis routes such as glycine nitrate combustion[16] have been used to make these samples and it would be interesting to see if different routes affect the optical properties (as in Chapters 3 and 4). The fact that the lattice parameters do not reach a plateau indicates that the doping level could also be increased further. However further work is outside the scope of this project.

Doped ZnO and reduced SnO_2 were discussed in the literature section in Chapter 1. Both were synthesised but low absorbance similar to the $SrTi_{1-x}Nb_xO_3$ samples was seen for Al-doped ZnO (figure A.6.2) so it not tested for laser imaging. One sample of reduced SnO_{2-x}

showed reasonable absorbance across the whole spectrum (Figure A.6.3) and was tested, but the resulting coatings were too dark and irradiation did not form images.

Overall TCO-type materials have performed poorly as NIR absorbers for the Datalase imaging process. It could be that the NIR region is simply too close to the visible region for adequate absorbance since most semi-conductors absorb in the mid-to-far infrared ranges. Their generally good electrical conductivity was thought to give them good thermal conductivity which would aid the heat transfer step of the imaging process but it seems the samples are unable to absorb enough energy in the first place in order to pass it on to the pigment. The commercial sample rITO is a reduced form of ITO so future work could focus on making more reduced forms of the samples discussed above.

8.6 References

1. Montazer, M.; Pakdel, E., Functionality of nano titanium dioxide on textiles with future aspects: Focus on wool. *Journal of Photochemistry and Photobiology C: Photochemistry Reviews* **2011,** *12* (4), 293-303.
2. Henderson, M. A., A surface science perspective on photocatalysis. *Surface Science Reports* **2011,** *66* (6–7), 185-297.
3. Reyes-Coronado, D.; Rodríguez-Gattorno, G.; Espinosa-Pesqueira, M. E.; Cab, C.; Coss, R. d.; Oskam, G., Phase-pure TiO_2 nanoparticles: anatase, brookite and rutile. *Nanotechnology* **2008,** *19* (14), 145605.
4. Li, W., Influence of electronic structures of doped TiO_2 on their photocatalysis. *physica status solidi (RRL) – Rapid Research Letters* **2015,** *9* (1), 10-27.
5. (a) Dozzi, M. V.; Selli, E., Doping TiO_2 with p-block elements: Effects on photocatalytic activity. *Journal of Photochemistry and Photobiology C: Photochemistry Reviews* **2013,** *14*, 13-28; (b) Tatlıdil, İ.; Bacaksız, E.; Buruk, C. K.; Breen, C.; Sökmen, M., A short literature survey on iron and cobalt ion doped TiO_2 thin films and photocatalytic activity of these films against fungi. *J Alloy Compd* **2012,** *517*, 80-86; (c) Rauf, M. A.; Meetani, M. A.; Hisaindee, S., An overview on the photocatalytic degradation of azo dyes in the presence of TiO_2 doped with selective transition metals. *Desalination* **2011,** *276* (1–3), 13-27.
6. Asahi, R.; Morikawa, T.; Ohwaki, T.; Aoki, K.; Taga, Y., Visible-Light Photocatalysis in Nitrogen-Doped Titanium Oxides. *Science* **2001,** *293* (5528), 269-271.
7. (a) Dunnill, C. W. H.; Aiken, Z. A.; Pratten, J.; Wilson, M.; Morgan, D. J.; Parkin, I. P., Enhanced photocatalytic activity under visible light in N-doped TiO_2 thin films produced by APCVD preparations using t-butylamine as a nitrogen source and their potential for antibacterial films. *Journal of Photochemistry and Photobiology A: Chemistry* **2009,** *207* (2–3), 244-253; (b) Irie, H.; Watanabe, Y.; Hashimoto, K., Nitrogen-Concentration Dependence on Photocatalytic Activity of $TiO_{2-x}N_x$ Powders. *The Journal of Physical Chemistry B* **2003,** *107* (23), 5483-5486.
8. Peng, F.; Cai, L.; Huang, L.; Yu, H.; Wang, H., Preparation of nitrogen-doped titanium dioxide with visible-light photocatalytic activity using a facile hydrothermal method. *J Phys Chem Solids* **2008,** *69* (7), 1657-1664.
9. Zhou, X.; Peng, F.; Wang, H.; Yu, H.; Yang, J., Preparation of nitrogen doped TiO_2 photocatalyst by oxidation of titanium nitride with H_2O_2. *Mater Res Bull* **2011,** *46* (6), 840-844.
10. Graciani, J.; Hamad, S.; Sanz, J. F., Changing the physical and chemical properties of titanium oxynitrides $TiN_{x-1}O_x$ by changing the composition. *Physical Review B* **2009,** *80* (18), 184112.
11. Zidi, N.; Omeiri, S.; Hadjarab, B.; Bouguelia, A.; Akroun, A.; Trari, M., Transport properties and photo electrochemical characterization of oxygen-deficient $ASnO_{3-\delta}$ (A=Ca, Sr and Ba). *Physica B: Condensed Matter* **2010,** *405* (16), 3355-3359.
12. Hadjarab, B.; Bouguelia, A.; Benchettara, A.; Trari, M., The transport and photo electrochemical properties of La-doped stannate $BaSnO_3$. *J Alloy Compd* **2008,** *461* (1–2), 360-366.
13. Hashimoto, S.; Poulsen, F. W.; Mogensen, M., Conductivity of $SrTiO_3$ based oxides in the reducing atmosphere at high temperature. *J Alloy Compd* **2007,** *439* (1–2), 232-236.
14. Karczewski, J.; Riegel, B.; Gazda, M.; Jasinski, P.; Kusz, B., Electrical and structural properties of Nb-doped $SrTiO_3$ ceramics. *J Electroceram* **2010,** *24* (4), 326-330.
15. Wang, Y.; Xu, H.; Wang, X.; Zhang, X.; Jia, H.; Zhang, L.; Qiu, J., A General Approach to Porous Crystalline TiO_2, $SrTiO_3$, and $BaTiO_3$ Spheres. *The Journal of Physical Chemistry B* **2006,** *110* (28), 13835-13840.

16. Blennow, P.; Hagen, A.; Hansen, K. K.; Wallenberg, L. R.; Mogensen, M., Defect and electrical transport properties of Nb-doped $SrTiO_3$. *Solid State Ionics* **2008,** *179* (35–36), 2047-2058.

Project Conclusion

The purpose of this project was to investigate potential materials to act as near infrared absorbers to be used in a novel laser imaging process being developed by Datalase Ltd. First a selection of commercial samples was analysed. Based on this analysis, candidate materials were identified, researched, synthesised, characterised and tested. Based on initial results a number of materials were refined by altering synthetic conditions and in turn improving performance. Compounds related to successful samples were then identified and synthesised in turn. A number of other materials were discarded due to poor performance, no performance or difficulty of synthesis. Table 8.3 gives an overview of all the samples tested during the project, rating the performance as good (good imaging, low background), medium (some imaging and/or darker background), poor (little imaging or very dark background) and none (no imaging at all).

Table 8.3 - Overview and assessment of all samples tested.

Sample	Composition	Performance	Comments
NaTB-ST1	Na_xWO_3	Medium	Low background, some imaging
NaTB-ST2	Na_xWO_3	None	No imaging
NaTB-SS1	Na_xWO_3	Poor	Low background, little imaging
NaTB-SS2	Na_xWO_3	Medium	Low background, some imaging
NaTB-SS3	Na_xWO_3	Medium	Low background, some imaging
NaTB-SS4	Na_xWO_3	Good	Low background, good imaging
NaTB-SS5	Na_xWO_3	Good	Low background, good imaging
NaTB-SS6	Na_xWO_3	Medium	Low background, some imaging
NaTB-SS7	Na_xWO_3	Poor	Low background, little imaging
KTB-ST	K_xWO_3	Good	Low background, good imaging
KTB-SS1	K_xWO_3	Medium	Low background, some imaging
KTB-SS2	K_xWO_3	Medium	Low background, some imaging
RbTB-ST	Rb_xWO_3	Poor	Hardly any imaging
RbTB-SS	Rb_xWO_3	Medium	Low background, some imaging
ATB	$(NH_4)_xWO_3$	Medium	Low background, some imaging
TTB	Sn_xWO_3	Medium	Some imaging, dark background
CsTB-ST1	Cs_xWO_3	None	Non-crystalline sample
CsTB-ST2	Cs_xWO_3	Medium	Low background, some imaging

CsTB-ST3	Cs_xWO_3	Medium	Low background, some imaging
CsTB-ST4	Cs_xWO_3	Good	Low background, good imaging
CsTB-ST5	Cs_xWO_3	Medium	Low background, some imaging
CsTB-ST6	Cs_xWO_3	Medium	Low background, some imaging
CsTB-ST7	Cs_xWO_3	Good	Low background, good imaging
CsTB-ST8	Cs_xWO_3	Good	Imaging but not as good as ST7
CsTB-SS1	Cs_xWO_3	Good	Imaging but not as good as SS2
CsTB-SS2	Cs_xWO_3	Good	Low background, good imaging
$W_{18}O_{49}$-ST	WO_{3-x}	Medium	Some imaging, unstable in air over time
$W_{18}O_{49}$-SS	WO_{3-x}	Poor	Some imaging, dark backgrounds
HMB	H_xMoO_3	Medium	Some imaging
NaMB	Na_xMoO_3	Medium	Some imaging
KMB-ST	K_xMoO_3	Medium	Some imaging, darker background than other Mo bronzes
KMB-SS	K_xMoO_3	Medium	Low background, some imaging
RbMB	Rb_xMoO_3	Medium	Low background, some imaging
PTB	$P_4W_8O_{32}$	Medium	Some imaging, difficult synthesis
CZP	$CuZr_2(PO_4)_3$	None	No imaging
CSCP	$Ca_{10-x/2}Na_xCu_{0.5}(PO_4)_7$	None	No imaging
SZCP	$SrZn_{1-x}Cu_xP_2O_7$	Poor	Only images at very high concentrations
TiN	TiN	Poor	Very dark background even at very low concentration
TiN-OX	$TiN_{1-x}O_x$	None	No imaging
LaBSO	$BaSn_{1-x}La_xO_3$	None	No imaging

It became apparent that the Datalase imaging process is a niche application and the only real way of determining the performance of NIR absorbers is to test them in the ink formulation. Attempts at screening samples based on physical characteristics were not successful. A more detailed study would be needed of the interaction between the absorber, the ink and the pigment at a molecular level to be able to choose samples more selectively and avoid time-consuming tests.

There are many parameters which can be controlled or varied when looking for potential NIR absorbers: the crystal structure of the samples, their composition (and therefore level of non-stoichiometry), light absorbance mechanisms, thermal conductivity, presence of secondary phases, stability over time and particle size and shape. A number of these parameters are interlinked and so are often not easy to control. For example the optical behaviour of samples could be easily measured whereas characterising thermal conductivity proved more difficult. Efforts to understand the thermal behaviour of the samples were undertaken but more data would be needed to provide a fuller picture.

Some trends in sample performance became evident. Samples have to be crystalline. Tungsten bronzes M_xWO_3 need to have a sufficient amount of M present for good absorbance but not so much that the absorbance is extremely strong in the visible region. TCO materials and copper phosphates do not absorb enough NIR radiation to cause imaging. The best performing samples were all composed of small particles. However other results are less clear, such as the varying performance of Cs_xWO_3 samples with similar particle morphologies or poor performance of samples that had promising NIR absorbance. The correlation of sample properties to performance in laser imaging tests is not straightforward.

Several synthetic routes were developed during the course of the project. The hydrothermal synthesis of Sn_xWO_3 detailed in Chapter 3 is the first one-pot synthesis of this material and gives a high yield of a phase pure product. Some of the other tungsten bronze routes were also significantly modified to attain more product or different product morphologies. The benzyl alcohol synthesis of Cs_xWO_3 has been published by another research group during the course of this work.

Phosphate-based materials and transparent conducting oxides perform poorly as NIR absorbers in the Datalase process. Molybdenum bronzes M_xMoO_3 do form images but they are not sufficiently dark and the compounds are relatively difficult to synthesise. The most commercially viable NIR absorbers are the tungsten bronzes M_xWO_3. Several samples result in light coloured coatings and dark image formation. The best performing samples KTB-ST (K_xWO_3) and CsTB-ST4 (Cs_xWO_3) have comparable performance to commercial sample BTO1 but with smaller errors on optical density values of images created which indicates more regular reproducible imaging.

Appendices

A.1 Analysis of Commercial Samples

Datalase provided 4 commercially available samples that perform reasonably well as near infrared absorbers so these were thought to be a practical starting point for the research project. The samples were obtained from foreign suppliers so very little was known about their synthesis or composition. The first stage of the project was to characterise these samples and use information thus gained to guide the choice of future candidate materials. Details of techniques and equipment used here can be found in Chapter 2.

The samples are outlined in Table A.1.1.

Table A.1.1 - Summary of commercial NIR absorber compounds

Designated Name	Full name	Colour
rITO	Reduced indium tin oxide	Blue
CHP	Copper hydroxyphosphate	Pale green
BTO1	'Blue tungsten oxide' 1	Dark blue
BTO2	'Blue tungsten oxide' 2	Dark blue

The abbreviations shown in Table A.1.1 will be used in subsequent discussion. It was thought that BTO1 and BTO2 are the same compound with different particle sizes. However since little was known about the synthesis or composition of the samples the first step was analysis by powder X-ray diffraction (PXRD). The diffractograms are shown in Figure A.1.1. It is immediately apparent that each of the four samples has a different crystal structure and that BTO1 and BTO2 are not the same compound as was assumed.

The rITO pattern fits well to the cubic In_2O_3 structure (see A.1.2) in the Ia-3 space group which is isostructural with the mineral bixbyite. This is a good indication that the tin is incorporated into the indium sites and does not exist as a separate phase since no impurity peaks are present. The replacement of In^{3+} with Sn^{4+} results in the donation of an electron to the conduction band and so the conductivity increases with increasing doping level. However the maximum is at is at around 8 atomic percent Sn in the bulk above which impurity phases form[1]. Two indium sites are present in the structure, both with distorted

octahedral geometry. The tin is thought to occupy the In(1) site which is the least distorted of the two[1a]. The reduced phase of ITO has the same crystal structure but has a larger number of charge carriers due to the formation of Sn interstitials and O vacancies.

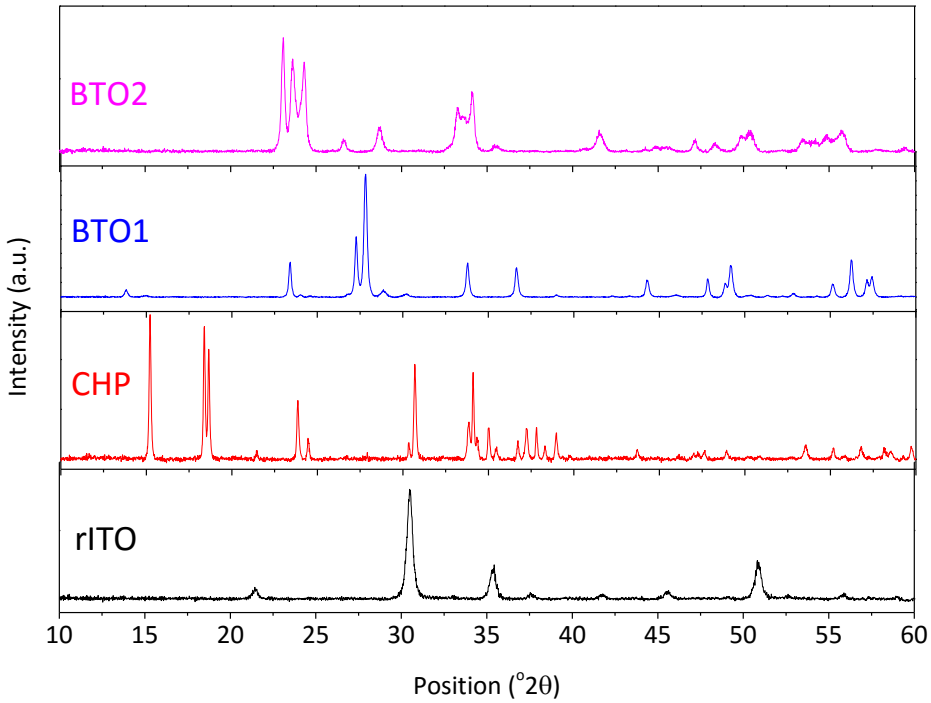

Figure A.1.1 - PXRD diffractograms of commercial samples rITO, CHP, BTO1 and BTO2

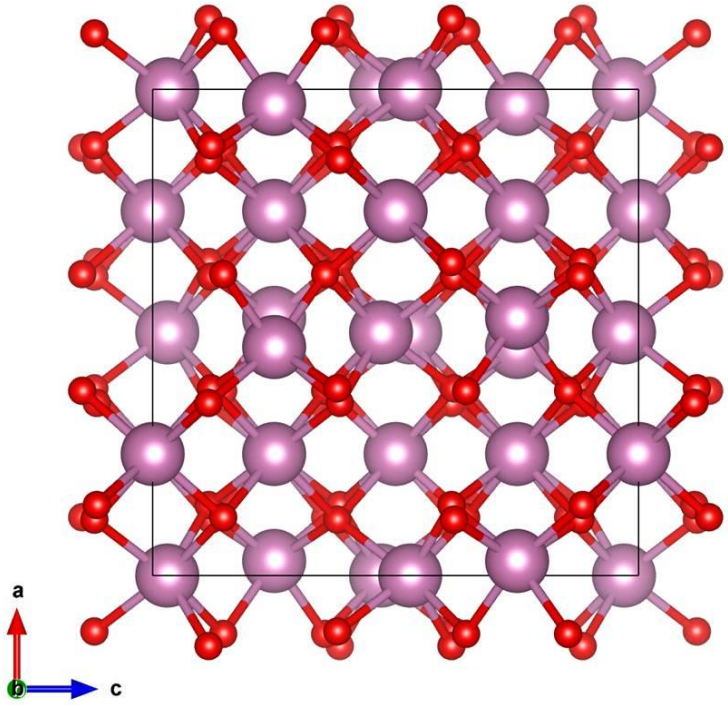

Figure A.1.2 - Representation of the crystal structure of In_2O_3: In=purple, O=red.

The CHP sample is crystalline and there is no evidence of impurity peaks. It matches the orthorhombic copper hydroxyphosphate $Cu_2(OH)(PO_4)$ pattern well (ICSD PDF number 01-077-0922) with space group Pnnm and is also known as the mineral libethenite[2]. The structure is comprised of PO_4 tetrahedra corner-linked in such a way to form two Cu environments, as shown in A.1.3. Cu(1) is an octahedral site and shares edges with its neighbours to form a chain running parallel to the c-axis. These are also corner-sharing with Cu(2) sites which take the form of a trigonal bipyramid. As well as being linked to each other, both sites are corner-linked to the PO_4 tetrahedra.

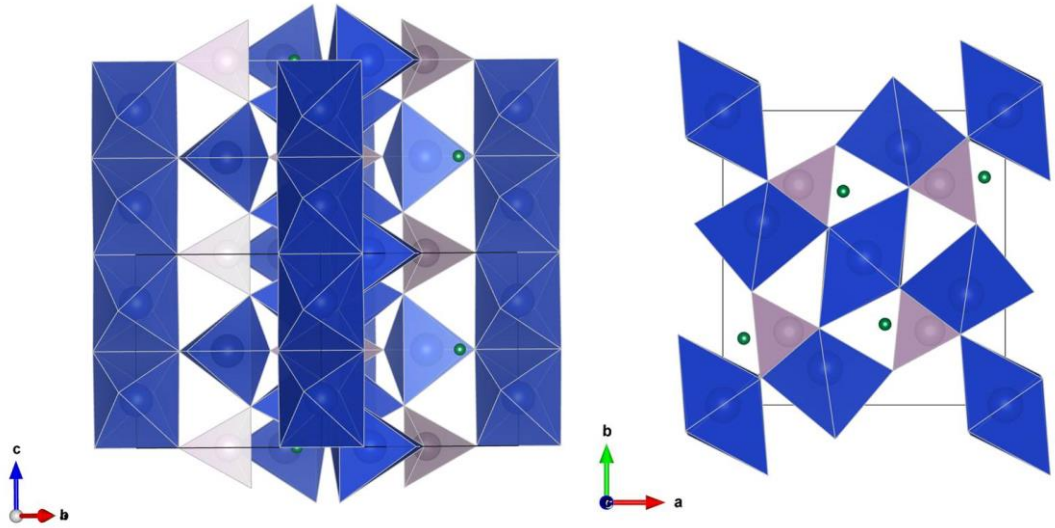

Figure A.1.3 - Polyhedral representation of the crystal structure of $Cu_2(OH)(PO_4)$ viewed along the a and c axes: Cu=blue, P=purple, H=green.

BTO1 was found to be mixed phase with hexagonal caesium tungsten bronze Cs_xWO_3 as the primary phase and a cubic caesium tungstate pyrochlore CsW_2O_6 secondary phase. A Rietveld refinement showed that the cubic phase made up about 12% of the sample. The hexagonal structure is discussed in more detail in section 3.3.1.1 and the pyrochlore structure is shown in Figure A.1.4. Pyrochlores take the general formula $A_2B_2O_6$ where A is an alkali or rare earth metal and B is a transition metal. The cubic structure is face-centred in space group Fd-3m. This phase was discovered by Cava *et. al.* in 1993[3] and is composed of WO_6 octahedra corner-linked in a regular network to form cavities with two sites available for occupation. The Cs atoms occupy the centre of the cavities and the sites located in the centre of hexagonal rings formed by the octahedra are vacant giving the observed stoichiometry. EDX found no other elements present. It is unclear yet whether the pyrochlore phase affects the performance of the BTO1 sample. The formal tungsten valence is 5.5

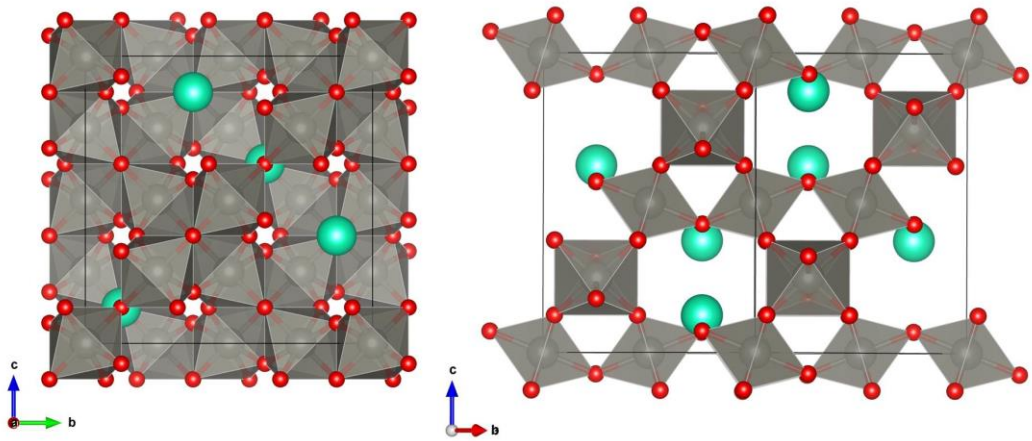

Figure A.1.4 - Polyhedral representation of the pyrochlore crystal structure of CsW_2O_6 viewed along the a axis and along the a-b corner: Cu=green, W=grey, O=red.

BTO2, although thought to be the same as BTO1, is a reduced tungsten oxide WO_{3-x} phase and contains no caesium, a fact confirmed by energy-dispersive X-ray spectroscopy (EDX). Like stoichiometric parent phase WO_3, it adopts the monoclinic $P2_1/n$ space group. This structure is discussed more detail in Chapter 1. Using the weight gained during thermogravimetric analysis (TGA) to calculate x gives a formula of $WO_{2.95}$ so the sample is lightly reduced. The oxygen vacancies cause a number of tungsten cations to be reduced from W^{6+} to W^{5+} to maintain charge neutrality. The W^{5+} cations give the sample its blue colour (hence 'Blue Tungsten Oxide') which is not seen in pale green WO_3 in which all W species are W^{6+}.

Scanning electron micrographs of the four samples are shown in A.1.5. The relatively large fractured particles of rITO, BTO1 and BTO2 indicate that a solid state synthetic route was used for these samples, probably including at least one milling step. rITO and BTO1 have 'textured' particle surfaces, perhaps indicating that they are agglomerates of smaller particles. This feature is not seen in BTO2 which has smooth particles with some small needle-like features on the surface. The CHP sample consists of smaller agglomerates of relatively large crystallites so perhaps a sol-gel or hydrothermal route was used in this case. A number of these wet-chemistry routes to $Cu_2(OH)(PO_4)$ are published in the literature[4]. The surface area measurements of these samples reflect what is seen in the SEM images. The order from largest to smallest is as follows: rITO, BTO1, BTO2 and CHP. The 'textured' surfaces of rITO and BTO1 give rise to greater surface area. Values are shown in Table A.1.2.

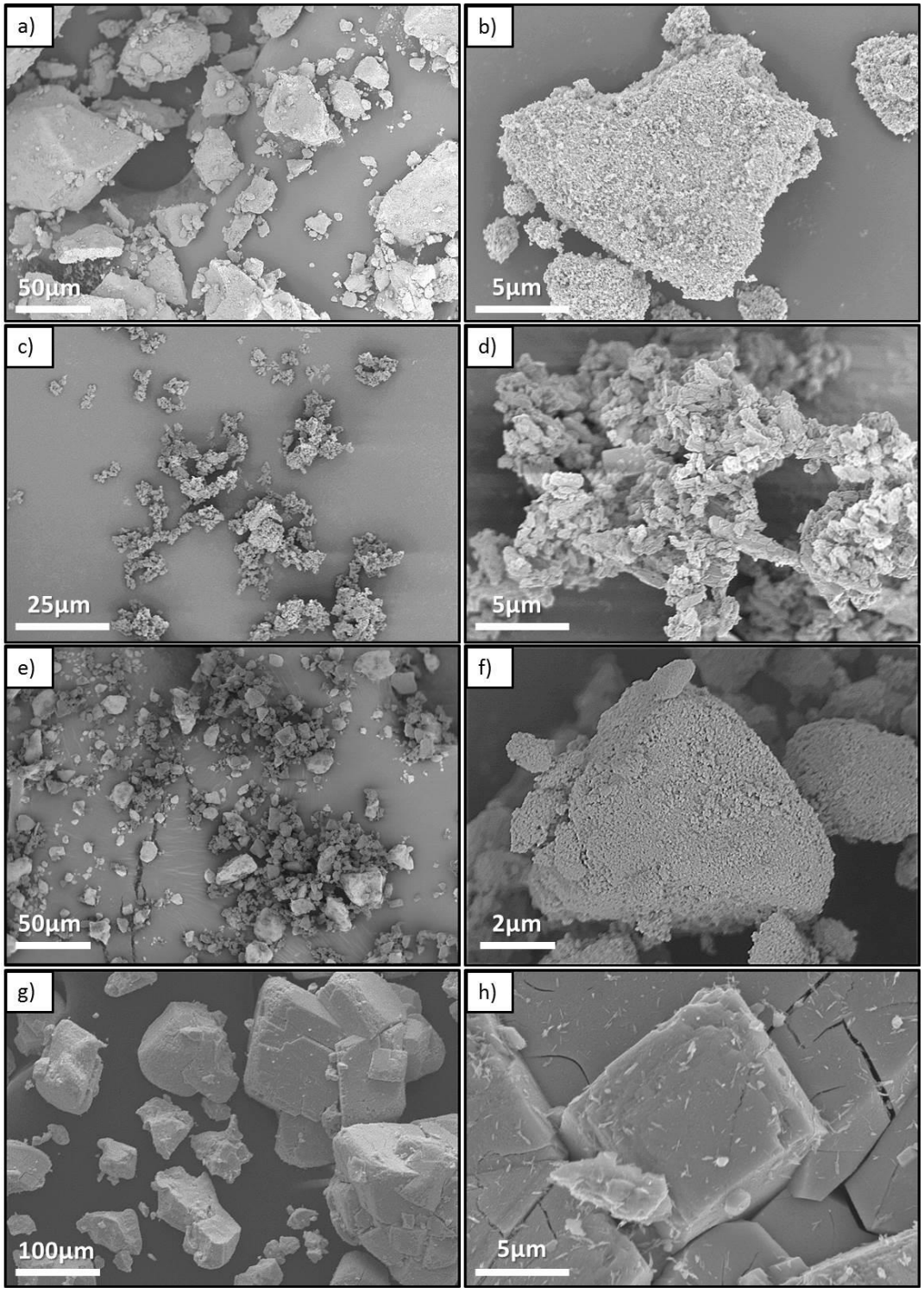

Figure A.1.5 - SEM images of a) and b) rITO; c) and d) CHP; e) and f) BTO1; g) and h) BTO2. Scale bars are given.

Table A.1.2- Surface Area Measurements of commercial samples

Sample	Surface Area (m^2g^{-1})
rITO	33.3
CHP	1.4
BTO1	11.8
BTO2	6.5

The optical absorbance profiles of the commercial samples are shown in A.1.6.

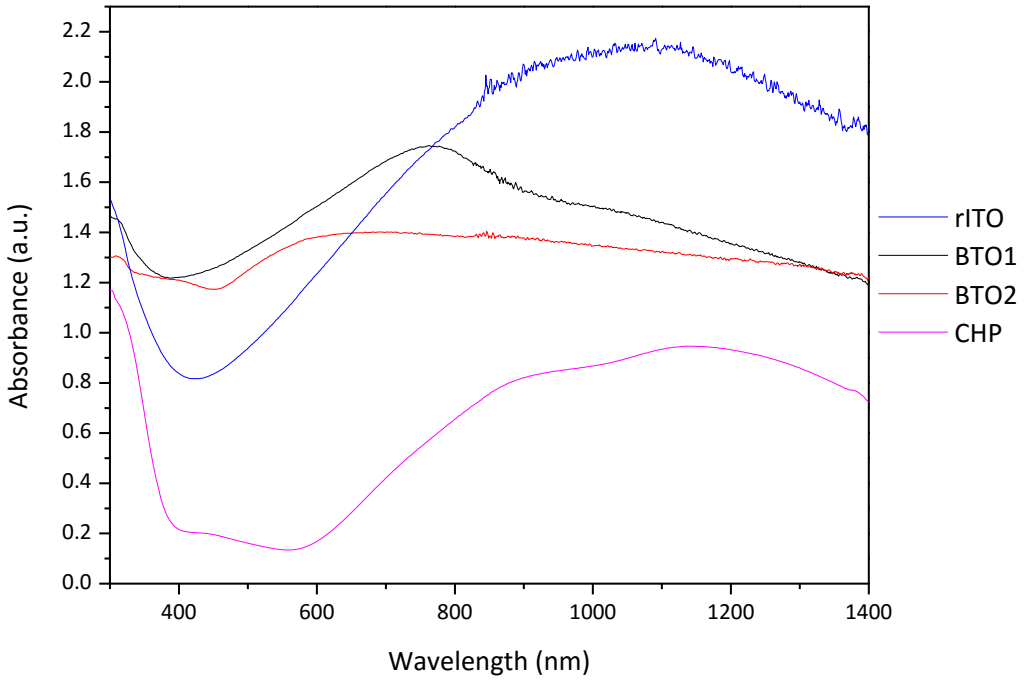

Figure A.1.6 - Optical absorbance spectra of NIR absorbers rITO, CHP, BTO1 and BTO2

All the samples absorb in the NIR region to some extent however the intensity of the absorption differs between samples. rITO has the highest absorption peak, centred at around 1100 nm. The origin of this peak is free carrier absorption and the large amount of charge carriers in the reduced ITO shifts the peak out of the infrared - where it is located for non-reduced ITO - towards the visible region. There is a double absorbance peak for BTO1, or rather a peak with a secondary shoulder. This arises from the occurrence of both polaron and surface plasmon absorption mechanisms in caesium tungsten bronzes. This could also be the case for reduced WO_{3-x} phase BTO2 but the peaks are overlapped to give a broad absorbance. However the relatively low level of reduction of the sample (x = 0.05 from TGA) should mean that only polaron absorption mechanism is present. If this is the case then the single peak is extremely broad.

The CHP sample is less absorbing than the others in the NIR region and when used in ink formulations, is loaded at much higher concentrations. The absorbance in this case arises from electronic d-d transitions in the Cu atoms so there is no strong delocalised contribution to the absorbance profile as for the other samples. The different energies associated with d-d transitions in each of the copper sites gives rise to the double absorbance peak. The low absorbance in the visible region means it can be used at higher concentrations without creating a dark background colour.

Standardised laser imaging conditions outlined Chapter 2.4 were used for testing and the results shown in Figure A.1.7. A high ΔOD with low background OD is desirable.

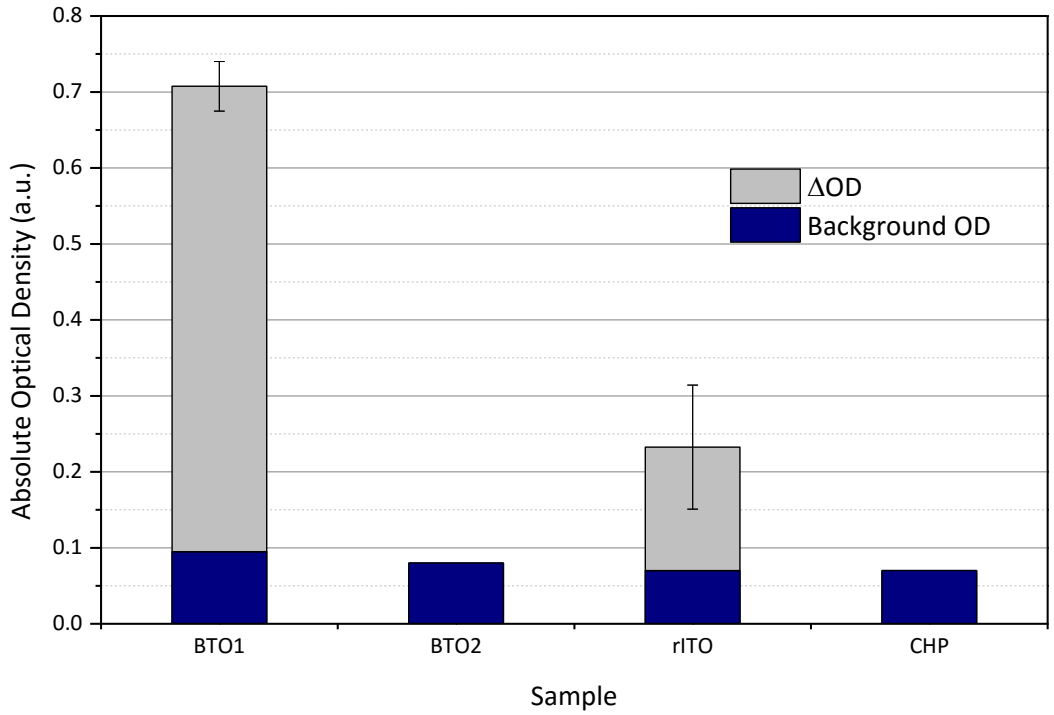

Figure A.1.7 - Results of laser imaging tests of commercial samples.

It can be seen that under these conditions BTO2 and CHP do not image at all. Here they are used at 0.75 wt% in the ink but under optimised conditions they would be used at higher loading concentrations. rITO shows some imaging but the BTO1 sample clearly performs the best under these conditions showing a high ΔOD value combined with low background OD to give good image contrast.

It is clear that choosing potential NIR absorbers for the Datalase imaging process is not simple. These samples all have different compositions, crystal structures, morphologies and

NIR light absorption mechanisms - all factors which will need to be considered during the project. Based on these analyses, four types of compound related to the commercial samples were initially chosen as potential NIR absorber candidates:

1. Tungsten bronzes
2. Sub-stoichiometric tungsten oxides
3. Copper phosphates
4. Transparent conducting oxides.

The existing work on these families of materials is summarised in section 1.8.

A.1.1 References

1. (a) Nadaud, N.; Lequeux, N.; Nanot, M.; Jové, J.; Roisnel, T., Structural Studies of Tin-Doped Indium Oxide (ITO) and In4Sn3O12. *J Solid State Chem* **1998,** *135* (1), 140-148; (b) Kim, S.-M.; Seo, K.-H.; Lee, J.-H.; Kim, J.-J.; Lee, H. Y.; Lee, J.-S., Preparation and sintering of nanocrystalline ITO powders with different SnO_2 content. *Journal of the European Ceramic Society* **2006,** *26* (1–2), 73-80.

2. Cordsen, A., A crystal-structure refinement of libethenite. *The Canadian Mineralogist* **1978,** *16* (2), 153-157.

3. Cava, R. J.; Roth, R. S.; Siegrist, T.; Hessen, B.; Krajewski, J. J.; Peck Jr, W. F., $Cs_{8.5}W_{15}O_{48}$ and CsW_2O_6: Members of a New Homologous Series of Cesium Tungsten Oxides. *J Solid State Chem* **1993,** *103* (2), 359-365.

4. (a) Xu, J. S.; Xue, D. F., Fabrication of copper hydroxyphosphate with complex architectures. *J Phys Chem B* **2006,** *110* (15), 7750-7756; (b) Xu, Y.; Wang, C.; Yang, S., Uniform copper hydroxyphosphate microstructures with tunable size: Synthesis by a facile surfactant-free hydrothermal route and photocatalytic properties. *Mater Lett* **2012,** *78* (0), 46-49.

A.2 Appendix 2 – Supplementary Information for Chapter 3

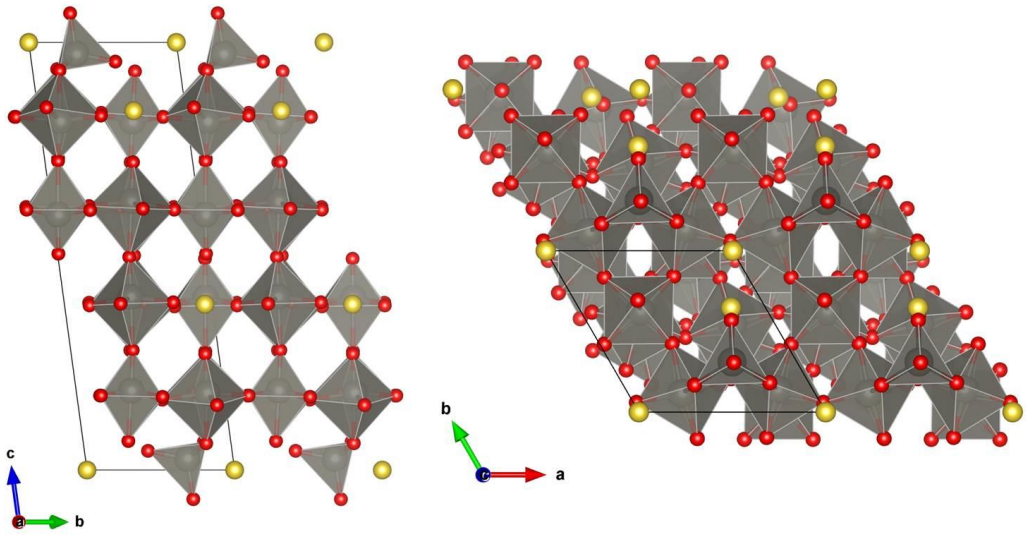

Figure A.2.1 - Polyhedral representation of the crystal structure of $Na_5W_{14}O_{44}$ viewed along a and c axes. W=grey, O=red and Na=yellow.

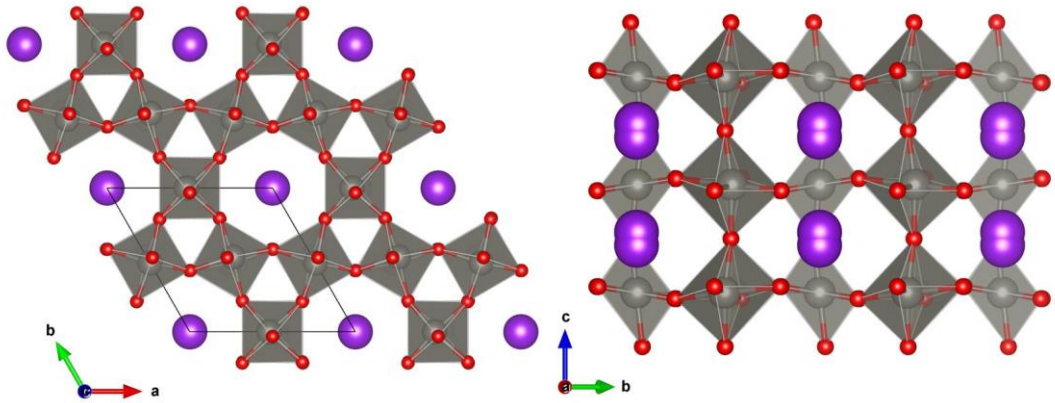

Figure A.2.2 - Polyhedral representation of the $P6_3/22$ hexagonal potassium tungsten bronze structure viewed along a and c axes. W=grey, O=red and K=purple. The double K site and distorted WO_6 octahedra can be clearly seen.

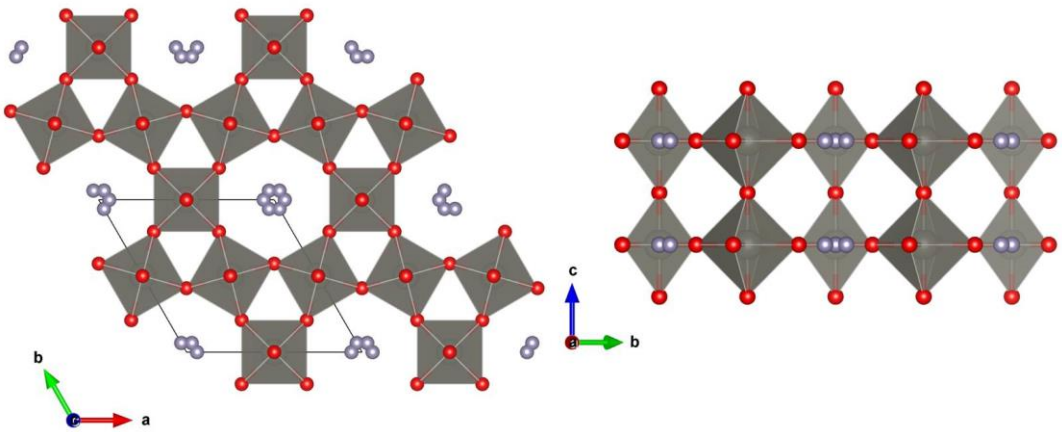

Figure A.2.3 - Polyhedral representation of the P6/mmm hexagonal tin tungsten bronze structure viewed along a and c axes. W=grey, O=red and Sn=purple. The six-fold Sn site can clearly be seen.

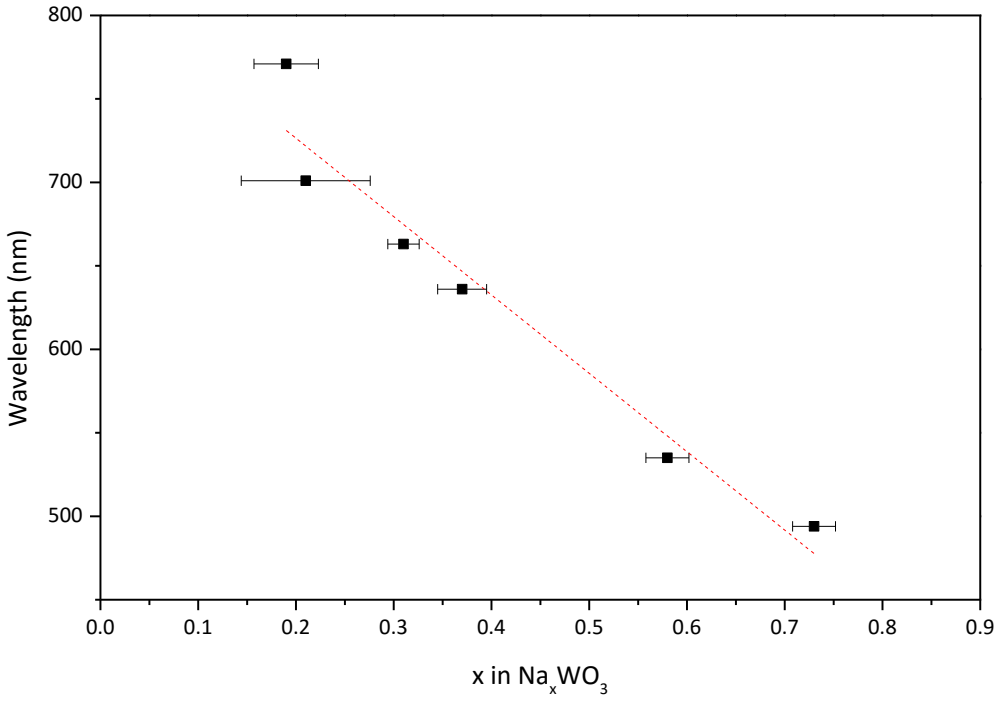

Figure A.2.4 - Dependence of absorbance peak maxima on Na content x in Na_xWO_3 samples made by solid state synthesis. x values are measured by EDX and associated errors shown. No data point exists for x = 0.1 since the absorbance peak was outside the scale of the graph in Figure 3.11.

A.3 Appendix 3 – Supplementary Information for Chapter 4

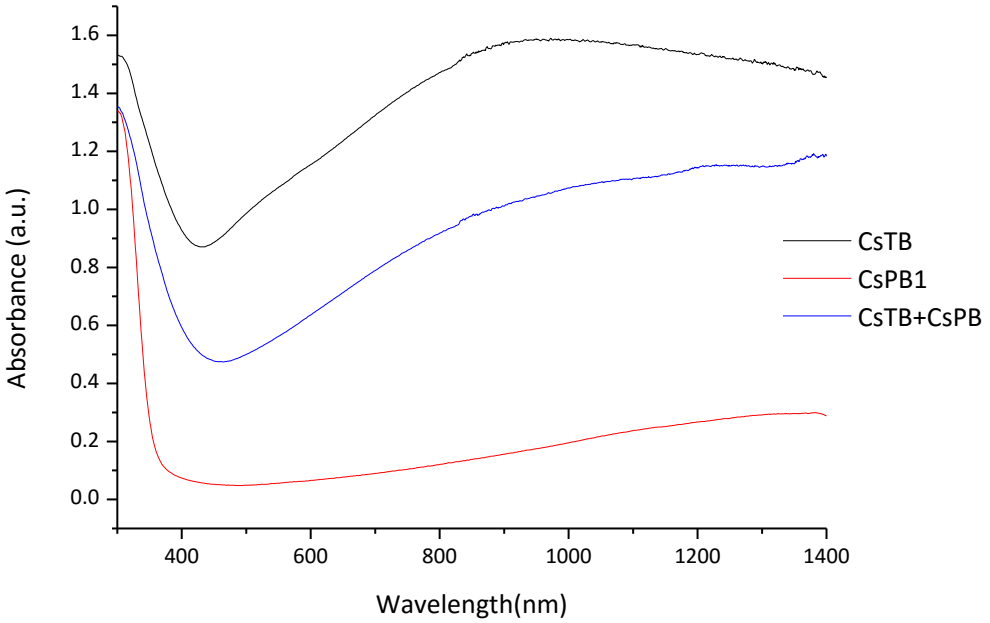

Figure A.3.1 - Optical absorbance spectra of mixed hexagonal Cs_xWO_3 and pyrochlore CsW_2O_6 compared to commercial sample BTO1 from section 4.3.2.

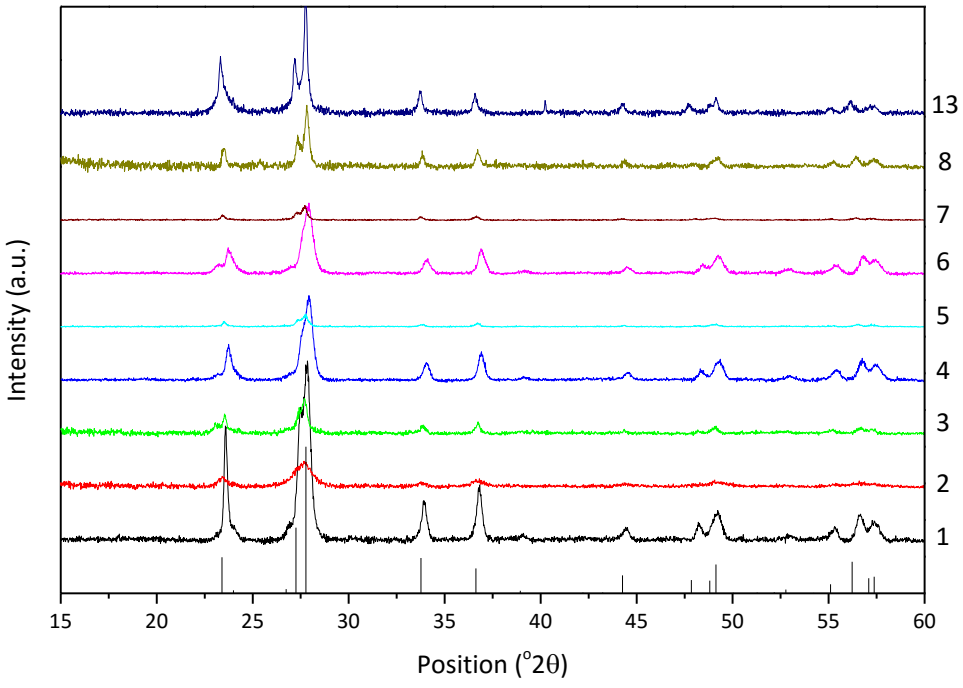

Figure A.3.20.1 - PXRD diffractograms of samples made with varying solvent mixtures in solvothermal CsxWO3 synthesis. Number correspond to points on ternary diagram Figure 4.6. The expected peak positions and intensities of hexagonal Cs_xWO_3 are shown.

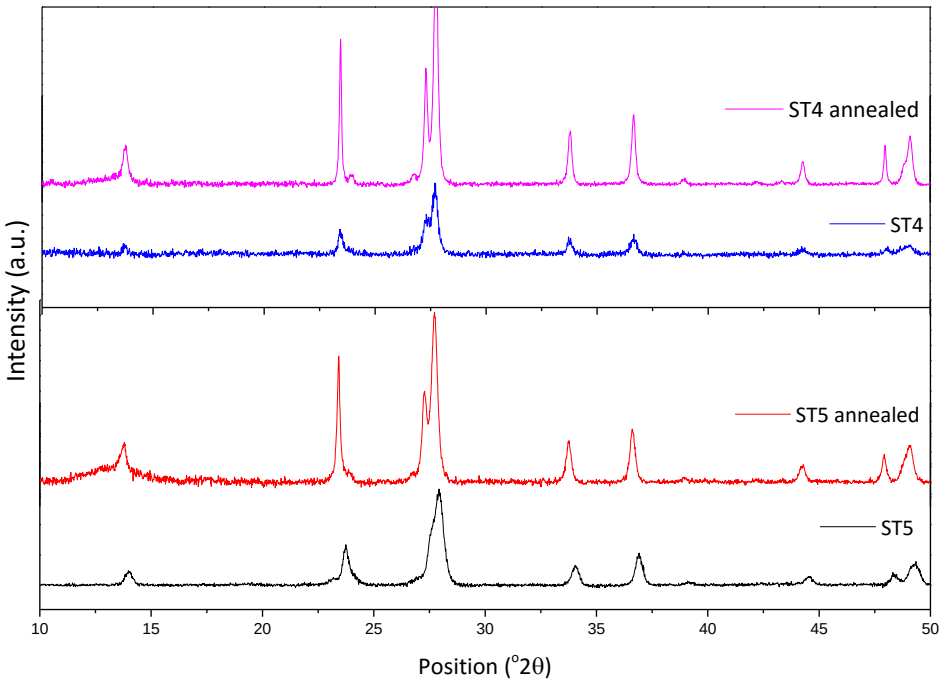

Figure A.3.3 - PXRD of CsTB-ST4 and ST5 before and after annealing in N_2 at 500 °C.

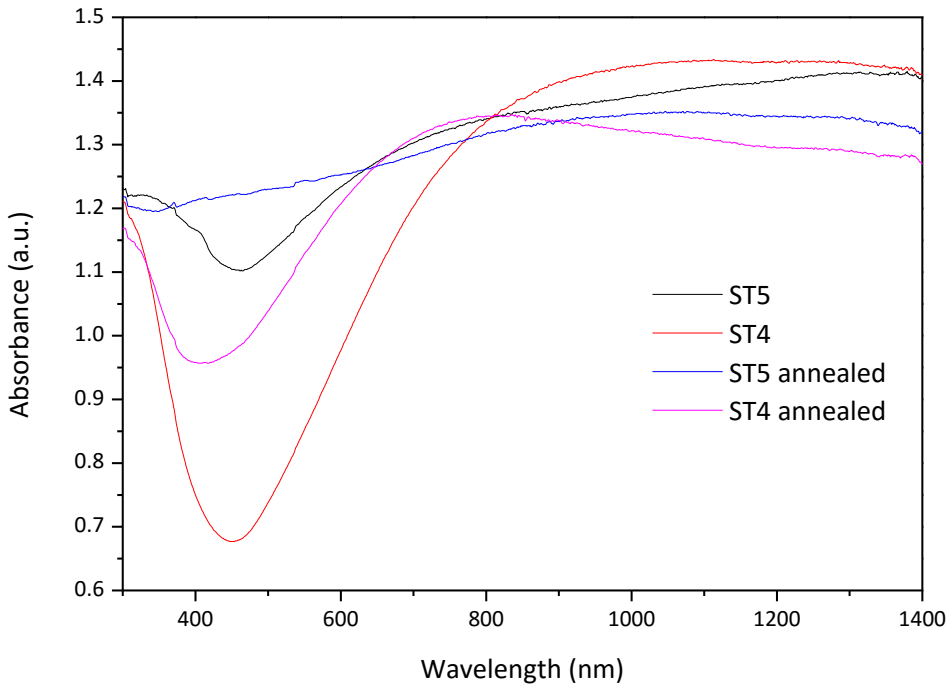

Figure A.3.4 - Optical absorbance of CsTB-ST4 and ST5 before and after annealing in N_2 at 500 °C.

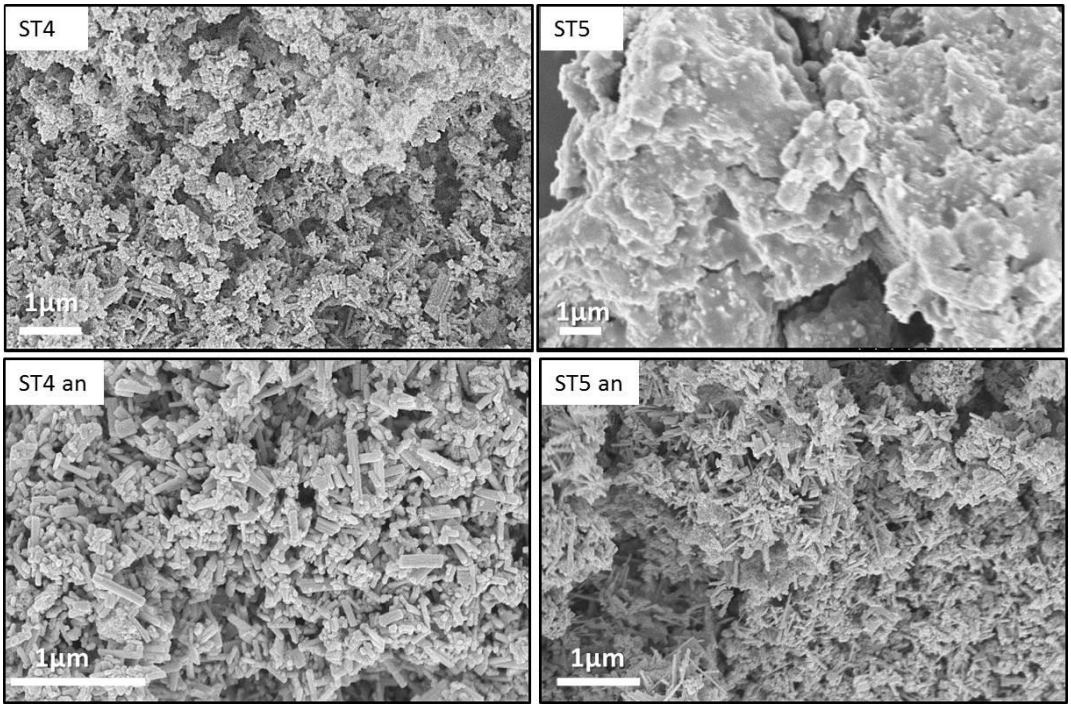

Figure A.3.5 – SEM images of CsTB-ST4 and ST5 particle morphology before and after annealing in N2 at 500 °C.

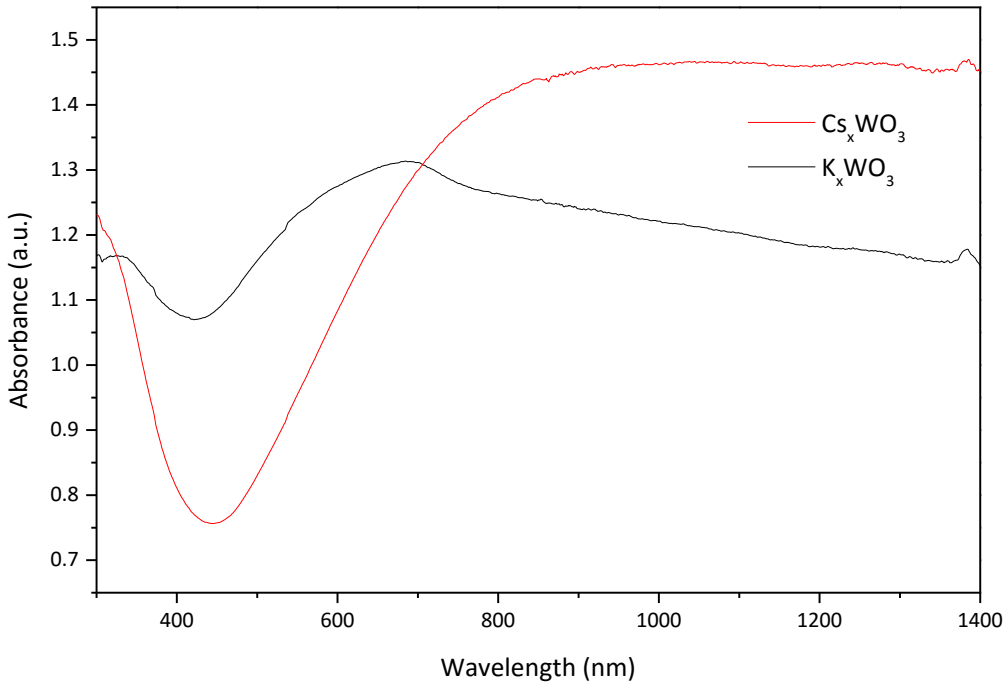

Figure A.3.6 - Optical absorbance spectra of K_xWO_3 and Cs_xWO_3 used for mixing tests in section 4.4.3.

A.4 Appendix 4 –Supplementary Information for Chapter 5

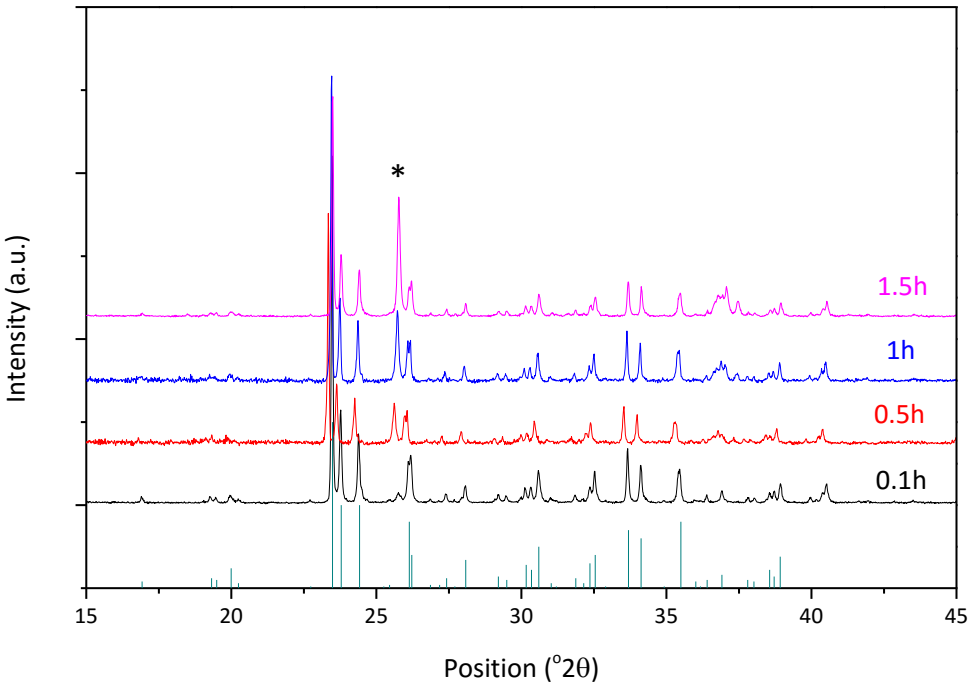

Figure A.4.1 - PXRD diffractograms of WO_{3-x} samples synthesised by a solid state route heated for different amounts of time.$W_{18}O_{49}$ pattern is shown and WO_2 peak marked with *.

Table A.4.1 - Lattice parameters of solid state $W_{18}O_{49}$ samples calculated using a Pawley refinement of PXRD data.

Sample	a	b	c	β
0.1 h	18.3251(4)	3.78367(6)	14.0390(3)	115.21(2)
0.5 h	18.3224(6)	3.78306(9)	14.0378(4)	115.21(3)
1 h	18.3255(5)	3.78406(6)	14.0406(4)	115.21(2)
1.5 h	18.3257(8)	3.7834(1)	14.0382(7)	115.20(4)

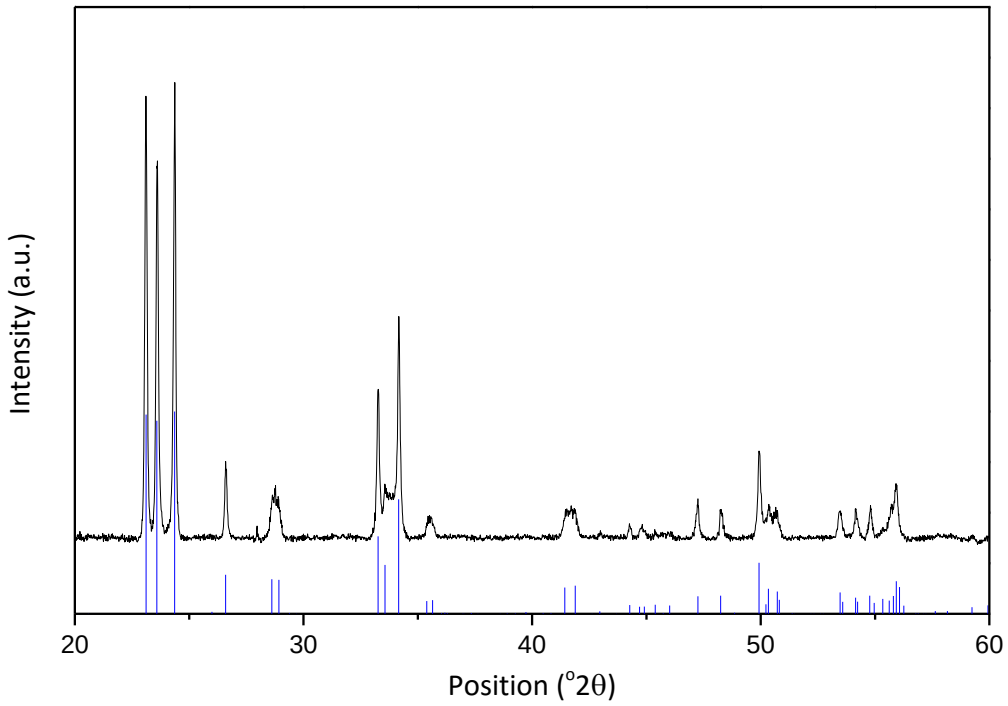

Figure A.4.2 - PXRD diffractogram of $W_{18}O_{49}$ sample after TGA in air. The blue lines indicate the expected peak positions and intensities of monoclinic WO_3. All SS samples showed the same result after heating as did the ST sample.

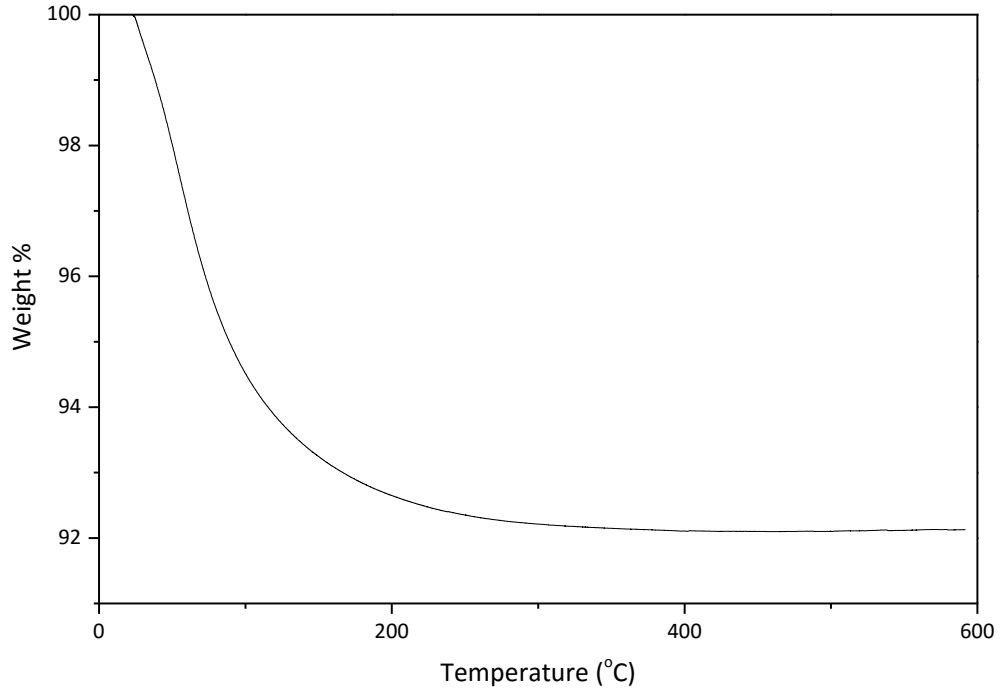

Figure A.4.3 - TGA curve of solvothermal $W_{18}O_{49}$ sample.

A.5 Appendix 5 – Supplementary Information for Chapter 6

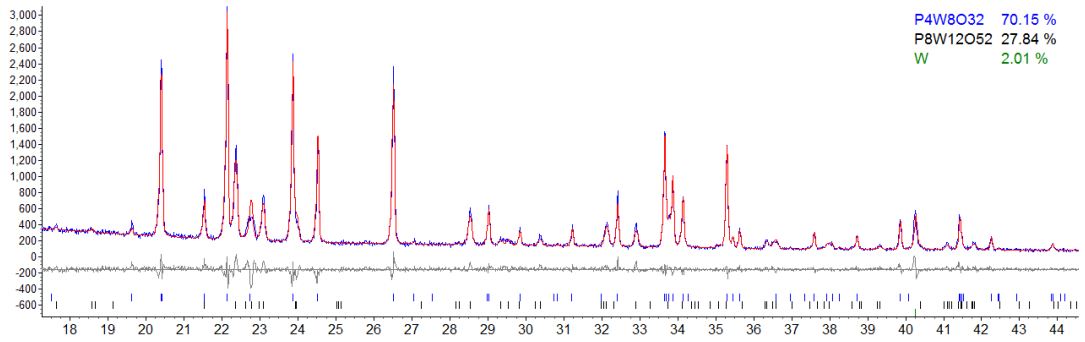

Figure A.5.1 - Rietveld refinement of PXRD data of PTB sample.

A.6 Appendix 6 - Supplementary Information for Chapter 8

Alternative synthesis of Nb-doped $SrTiO_3$

A solvothermal synthesis route from Wang *et. al.*[1] was used to synthesise Nb-doped $SrTiO_3$. Appropriate amounts of Sr(OH), P25 (TiO_2) and Nb_2O_5 were mixed in 60 ml water in a Teflon liner of 125 ml internal volume. These were transferred to steel autoclaves and heated to 180 ^oC for 12 h with a heating rate of 5 ^oC/min and cooling of 2 ^oC/min. Once cool the white products were separated by centrifugation, washed alternately with water and acetic acid then dried in air at 50 ^oC. Doping levels of x = 0, 0.01, 0.02 and 0.05 were used.

Synthesis of Al-doped ZnO

A solvothermal route from Zhou *et. al.*[2] was used. Appropriate amounts of $Zn(CH_3COO)_2.2H_2O$ and $Al(NO_3)_3.9H_2O$ were added to 40 ml C_2H_5OH in a Teflon liner. The liner was placed in a steel autoclave and heated to 140 ^oC for 6 h with a heating rate of 10 ^oC/min and cooling rate of 2 ^oC/min. Once cool the white products were separated by centrifugation, washed alternately with water and methanol then dried in air at 70 ^oC.

Reduction of SnO_2

1 g $SnO_2$was placed in an Al_2O_3boat crucible and placed in a tube furnace. Samples were heated under flowing 5% H_2/N_2 with heating and cooling rates of 5 ^oC/min to 300 ^oC for 1 h and 12 h, 350 ^oC for 1 h and 400 ^oC for 1 h.

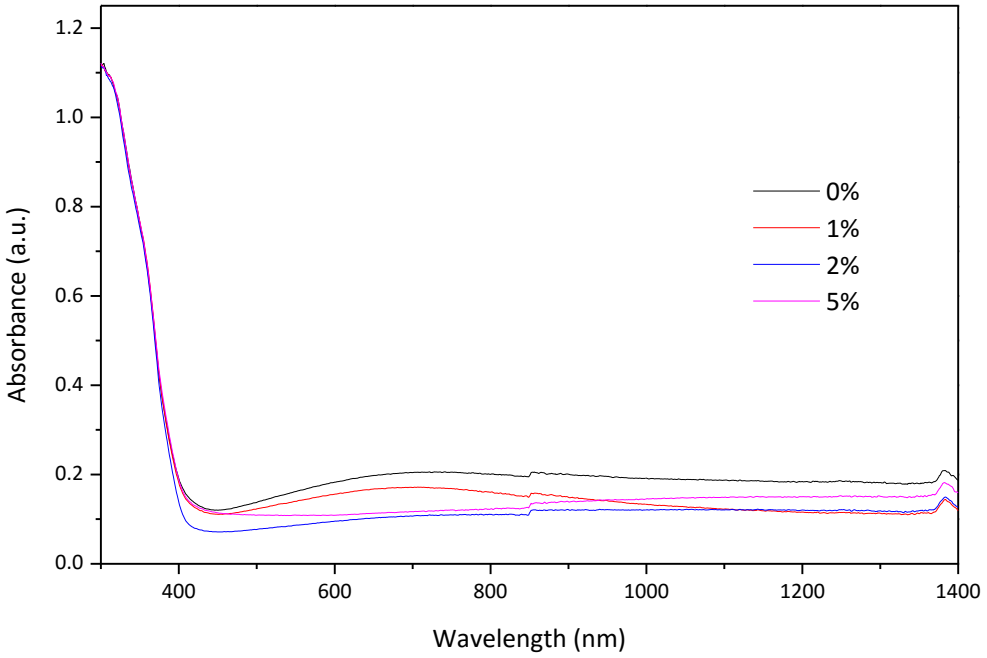

Figure A.6.1 - Optical absorbance profiles of $Sr_{1-x}Nb_xTiO_3$ samples with different Nb doping levels.

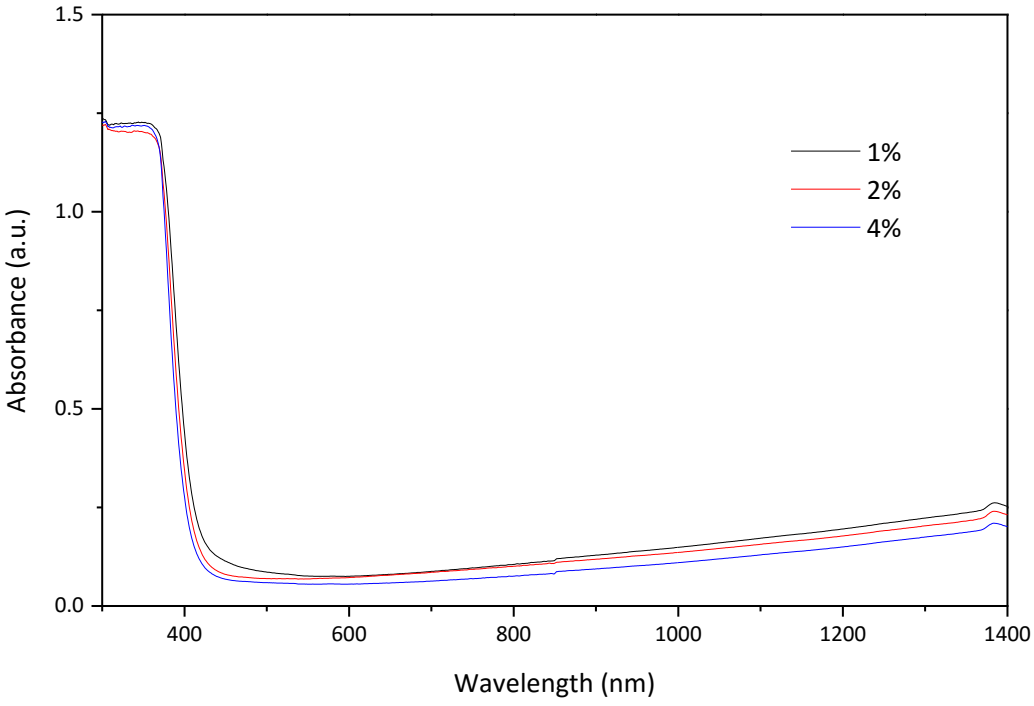

Figure A.6.2 – Optical absorbance profiles of $Zn_{1-x}Al_xO$ samples with different Al doping levels

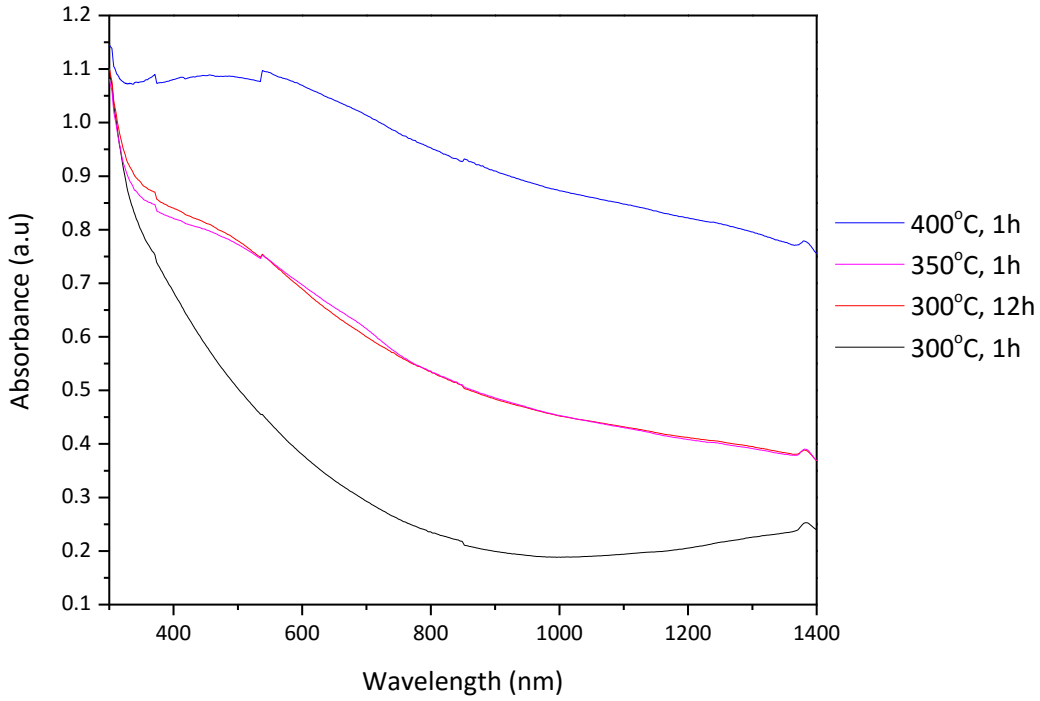

Figure A.6.3 - Optical absorbance profiles of SnO_{2-x} reduced at different times and temperatures. The 400 °C, 1h sample was tested but did not image.

1. Wang, Y.; Xu, H.; Wang, X.; Zhang, X.; Jia, H.; Zhang, L.; Qiu, J., A General Approach to Porous Crystalline TiO_2, $SrTiO_3$, and $BaTiO_3$ Spheres. *The Journal of Physical Chemistry B* **2006,** *110* (28), 13835-13840.

2. Zhou, H., Wang, H., Zheng, K., Gu, Z., Wu, Z., Tian, X.: Aluminum-doped zinc oxide nanoparticles with tunable near-infrared absorption/reflectance by a simple solvothermal process. *RSC Advances*, **2014**, *4* (81), 42758-42763.